CALIFORNIA INSTITUTE OF TECHNOLOGY

EARTHQUAKE ENGINEERING RESEARCH LABORATORY

ON THE MODELING OF ELASTIC AND INELASTIC, CRITICAL- AND POST-BUCKLING BEHAVIOR OF SLENDER COLUMNS AND BRACING MEMBERS

BY

SWAMINATHAN KRISHNAN

REPORT NO. EERL 2009-03

PASADENA, CALIFORNIA

MAY 2009

A REPORT ON RESEARCH SUPPORTED IN PART BY THE SOUTHERN CALIFORNIA EARTHQUAKE CENTER UNDER THE SUPERVISION OF SWAMINATHAN KRISHNAN

Acknowledgements

I am grateful to Prof. Chia-Ming Uang (University of California, San Diego) for providing the data from the pseudodynamic test of a full-scale 6-story structure, conducted in the years 1982–84, to Prof. Robert Tremblay (Ecole Polytechnique, Montreal, Canada) for providing data from his tests on concentrically braced steel frames with tubular braces, to Prof. Amit Kanvinde (University of California, Davis) and Prof. Benjamin Fell (California State University, Sacramento), for extensive discussions on brace behavior and for providing the data from their NEESR brace-testing project, and to the Earthquake Engineering Research Center (University of California, Berkeley), for permission to reproduce figures from the Black et al. EERC report. I wish to thank the National Science Foundation (NSF), the Southern California Earthquake Center (SCEC), and the United States Geological Survey (USGS) for their continued support to my research program.

Abstract

Analyzing tall braced frame buildings with thousands of degrees of freedom in three dimensions subject to strong earthquake ground motion requires an efficient brace element that can capture the overall features of its elastic and inelastic response under axial cyclic loading without unduly heavy discretization. This report details the theory of a modified elastofiber (MEF) element developed to model braces and buckling-sensitive slender columns in such structures. The MEF element consists of three fiber segments, two at the member ends and one at mid-span, with two elastic segments sandwiched in between. The segments are demarcated by two exterior nodes and four interior nodes. The fiber segments are divided into 20 fibers in the cross-section that run the length of the segment. The fibers exhibit nonlinear axial stress-strain behavior akin to that observed in a standard tension test in the laboratory, with a linear elastic portion, a yield plateau, and a strain hardening portion consisting of a segment of an ellipse. All the control points on the stress-strain law are user-defined. The elastic buckling of a member is tracked by updating both exterior and interior nodal coordinates at each iteration of a time step, and checking force equilibrium in the updated configuration. Inelastic post-buckling response is captured by fiber yielding in the nonlinear segments. A user-defined probability distribution for the fracture strain of a fiber in a nonlinear segment enables the modeling of premature fracture, observed routinely in cyclic tests of braces. If the probabilistically determined fracture strain of a fiber exceeds the rupture strain, then the fiber will rupture rather than fracturing. While a fractured fiber can take compression, it is assumed that a ruptured fiber cannot. Handling geometric and material nonlinearity in such a manner allows the accurate simulation of member-end yielding, mid-span elastic buckling and inelastic post-buckling behavior, with fracture or rupture of fibers leading to complete severing of the brace. The element is integrated into the nonlinear analysis framework for the 3-D analysis of steel buildings, FRAME3D. A series of simple example problems with analytical solutions, in conjunction with data from a variety of cyclic load tests, is used to calibrate and validate the element. Using a fiber segment length of 2% of the element length ensures that the elastic critical buckling load predicted by the MEF element is within 5% of the Euler buckling load for box and I-sections with a wide range of slenderness ratios (L/r = 40, 80, 120, 160, and 200) and support conditions (pinned-pinned, pinned-fixed, and fixed-fixed). Elastic post-buckling of the Koiter-Roorda L-frame (tubes and I-sections) with various member slenderness ratios (L/r = 40, 80, 120, 160, and 200) is simulated and shown to compare well against second-order analytical approximations to the solution. The inelastic behavior of struts under cyclic loading observed in the Black et al. and the Fell et al. experiments is numerically simulated using MEF elements. Certain parameters of the model (e.g., fracture strain, initial imperfection, support conditions, etc.) that are not controllable and/or unmeasured during the tests are tuned to realize the best possible fit between the numerical results and the experimental data. A similar comparison is made between numerical results using the MEF element and the experimental data by Tremblay et al. collected from cyclic testing of single-bay braced frames. Finally, a FRAME3D model of a full-scale 6-story braced frame structure that was pseudodynamically tested by the Building Research Institute of Japan subjected to the 1978 Miyagi-Ken-Oki earthquake record, is analyzed

and shown to closely mimic the experimentally observed behavior. To summarize, the MEF element is able to incorporate all the characteristic features of slender columns and braces that significantly affect their elastic and inelastic, critical and post-buckling behavior, and is remarkably effective in capturing the essence of said behavior, even with the vast uncertainty associated with the buckling phenomenon.

To aid in the evaluation of the collapse-prediction capability of competing methodologies, a benchmark problem of a water-tank subjected to the Takatori near-source record from the 1995 Kobe earthquake, scaled down by a factor of 0.32, is proposed. The water-tank is so configured as to have a unique collapse mechanism (under all forms of ground motion), of overturning due to $P-\Delta$ instability resulting from column and brace buckling at the base. A FRAME3D model of the tank reveals severe buckling in the bottom mega-columns and one of the two braces on the west face of the tower when the structure is hit by the Takatori near-source pulse, resulting a tilt in the structure. This is followed by sequential compression buckling of braces on the south and north faces leading to $P-\Delta$ instability and complete collapse of the tank.

Contents

Acknowledgements **iii**

Abstract **iv**

1 Introduction and Motivation **1**

2 The Modified Elastofiber Element and its Integration into the FRAME3D Analysis Framework **3**
2.1 3-D Modified Elastofiber (MEF) Element to Model Slender Columns and Braces 6
2.2 Modeling Considerations 14
2.3 Calibration and Validation 14

3 Elastic Buckling of Struts and the Selection of Middle Segment Length **20**

4 Modeling the Elastic Post-Buckling Behavior of the Koiter-Roorda Frame **22**
4.1 The Koiter-Roorda Frame 22

5 Modeling the Inelastic Buckling of Cyclically Loaded Struts in Pseudodynamic Tests **29**
5.1 Black et al. test data 29
5.2 Fell et al. test data 37
5.3 Tremblay et al. test data 43

6 Analytical simulation of the full-scale pseudodynamic test of a 6-story steel building **52**

7 A Proposed Benchmark Problem to Evaluate the Collapse-Prediction Capability of Competing Methodologies **66**

8 Conclusions **77**

A Koiter-Roorda Frame **79**

B Black et al. Tests **98**

C Fell et al. Tests **121**

D Tremblay et al. Tests **135**

E Benchmark Problem **141**

Bibliography **149**

List of Figures

2.1 Element arrangement in the FRAME3D modeling framework, showing joint nodes, attachment points, beam internal nodes, and the three coordinate systems, XYZ (global), $X'Y'Z'$ (element/segment local), $\bar{X}\bar{Y}\bar{Z}$ (panel zone local). Also shown are the plastic hinge and elastofiber elements for beam/column modeling, the 5-segment modified elastofiber element for brace/slender-column modeling, the panel zone element for joint modeling, and the diaphragm element for floor slab modeling. 4

2.2 Four rotational degrees of freedom of a panel zone element: Joints, comprising of a length of column within the depth of the connecting beams, are modeled using panel zone elements consisting of two rectangular panels which are perpendicular to each other, panel ① in the $\bar{X}-\bar{Z}$ plane and panel ② in the $\bar{X}-\bar{Y}$ plane, forming a cruciform section. The thicknesses of all web plates and web doubler plates of the associated column are combined to form the thickness of panel ①, $t_p^{①}$, while the thicknesses of all flange plates of the associated column are combined to form the thickness of panel ②, $t_p^{②}$. Each panel has two DOF which are also global DOF: $\theta^B_{J\bar{Y}}$ and $\theta^C_{J\bar{Y}}$ for panel ① and $\theta^B_{J\bar{Z}}$ and $\theta^C_{J\bar{Z}}$ for panel ②, where J is the global node at the center of the joint. These rotations deform the two panels into parallelograms. The B and C indicate that the rotating panel edges are connected to columns and beams, respectively. Strain or rotation in one of the panels causes a rigid body rotation but no strain in the orthogonal panel. 5

2.3 (a) Layout of the five-segment modified elastofiber element (fiber arrangement is shown for an I-section and a box section. (b) Axial stress-strain hysteresis model for each fiber. 9

2.4 The incremental beam rotation, $\Delta\theta^B_{J\bar{Y}}$, lead to incremental rotations of the lines connecting the node J to the brace attachment points, corners $a-e$, $a-f$, $b-e$, and $b-f$ of panel ①, in addition to incremental translation of these corners. Shown here is the deformed geometry of the panel, and the derivation of the resulting incremental brace rotations, needed for the construction of the $[T_2]$ transformation for a brace. 16

2.5 The incremental beam rotation, $\Delta\theta^B_{J\bar{Z}}$, lead to incremental rotations of the lines connecting the node J to the brace attachment points, corners $c-e$, $c-f$, $d-e$, and $d-f$ of panel ②, respectively, in addition to incremental translation of these corners. Shown here is the deformed geometry of the panel, and the derivation of the resulting incremental brace rotations, needed for the construction of the $[T_2]$ transformation for a brace. 17

2.6 The column rotation, $\Delta\theta^C_{J\bar{Y}}$, leads to incremental rotations of the lines connecting the node J to the brace attachment points, corners $a-e$, $a-f$, $b-e$, and $b-f$ of panel ①, in addition to incremental translation of these corners. This figure illustrates the deformed geometry of the panel, and the resulting incremental brace rotations, needed for the construction of the $[T_2]$ transformation for a brace. 18

2.7 The column rotation, $\Delta\theta^{C}_{J\bar{Z}}$, leads to incremental rotations of the lines connecting the node J to the brace attachment points, corners $c-e$, $c-f$, $d-e$, and $d-f$ of panel ②, in addition to incremental translation of these corners. This figure illustrates the deformed geometry of the panel, and the resulting incremental brace rotations, needed for the construction of the $[T_2]$ transformation for a brace. 19

3.1 Calibration of fiber segment length for MEF elements: (a) Ratio of elastic critical buckling load, predicted using MEF elements with fiber segment length of 2% of the element length, to the theoretical Euler buckling load plotted as a function of KL/r (four box sections, four wide-flange sections, five slenderness ratios and three support conditions give rise to 120 possible combinations; plotted here are 120 points corresponding to each of these 120 cases). Prediction errors are roughly equally distributed about zero. Except for cases with very small effective slenderness ratios, errors are below 3%. (b) Predicted elastic critical buckling loads plotted against the theoretical Euler buckling load for each of the 120 cases. The diagonal line represents zero prediction error. 21

4.1 (a) Undeformed geometry of the L-shaped Koiter-Roorda frame eccentrically loaded at the corner. Two possible buckling modes, shown in (b) and (c), exist (after Bazant and Cedolin). The force equilibrium at the joint is shown for both cases. Buckling to the left (mode shown in (c)) is favored for the following reasons: the column axial force is smaller than P in (b) whereas it is larger in (c); the beam is in tension in (b) increasing the stiffness whereas it is in compression in (c) lowering its stiffness; and beam curvature in (b) is greater than that in (c). 23

4.2 Comparison of the numerical solution using MEF elements (dashed lines) against a second-order analytical solution (solid lines) for the L-shaped Koiter-Roorda frame with a downward force (P) acting at the corner (black), or at eccentricities of e/L=0.001 (red), 0.01 (green), and 0.05 (blue): Case 1: TS8x8x3/16, L/R=40) – (a) Corner rotation versus P/P_{CR}; (b) Corner in-plane lateral displacement versus P/P_{CR}. 24

4.3 Deformed shape of TS8x8x3/16, L/R=40 frame at various levels of corner loading (zero eccentricity). The applied force history, corner rotation and displacement histories, and column mid-point deflection history for the TS8x8x3/16, L/R=40 case are also shown. . . . 25

4.4 Deformed shape of TS8x8x3/16, L/R=40 frame at various levels of corner loading (zero eccentricity). 26

4.5 Deformed shape of TS8x8x3/16, L/R=40 frame at various levels of corner loading (zero eccentricity). 27

4.6 Deformed shape of TS8x8x3/16, L/R=40 frame at various levels of corner loading (zero eccentricity). 28

5.1 FRAME3D model of the Black et al. and Fell et al. experimental setup, data from which is used to validate the MEF element. 30

5.2 Black et al. tests: W8x20 coupon tensile loading test. 33

5.3 Black et al. tests: W8x20 coupon tensile loading test (contd.). 34
5.4 Black et al. tests: Pinned ended W8x20 strut (1) with KL/r=120 – Loading history. 34
5.5 Black et al. tests: Pinned ended W8x20 strut (1) with KL/r=120, axial displacement versus axial force history – (a) Experiment (b) Simulation. 35
5.6 Black et al. tests: Pinned ended W8x20 strut (1) with KL/r=120, lateral displacement versus axial force history – (a) Experiment (b) Simulation. 36
5.7 Fell et al. test 2 on HSS4x4x1/4 (KL/r $\sim$ 80): Compression-dominated near-field loading history 39
5.8 Comparison of simulation against data from Fell et al. test 2 on HSS4x4x1/4 (KL/r $\sim$ 80): (a) Axial displacement versus axial force history; (b) Minor direction lateral displacement versus axial force history. 40
5.9 Fell et al. test 16 on W12x16 (KL/r $\sim$ 159): Tension-dominated near-field loading history . . 41
5.10 Comparison of simulation against data from Fell et al. test 16 on W12x16 (KL/r $\sim$ 159): (a) Axial displacement versus axial force history; (b) Minor direction lateral displacement versus axial force history. 42
5.11 FRAME3D model of the Tremblay et al. experimental setup, data from which is used to validate the MEF element. 44
5.12 Tremblay et al. test S2A/S2B on RHS102x76x4.8: Displacement history "H1" 47
5.13 Comparison of simulation against data from Tremblay et al. tests: (a) Specimen S2A and (b) Specimen S2B with RHS102x76x4.8 diagonal – frame sway versus applied lateral force history. 48
5.14 Tremblay et al. test S1QA/S1QB on RHS127x76x4.8: Displacement history "H2" 49
5.15 Comparison of simulation against data from Tremblay et al. tests: (a) Specimen S1QA and (b) Specimen S1QB with RHS127x76x4.8 diagonal – frame sway versus applied lateral force history. 50
5.16 Histogram of the ratio of (a) model yield stress to measured (or nominal if unmeasured) yield stress, and (b) model ultimate stress to measured (or nominal if unmeasured) ultimate stress for all the brace specimen considered in this study (including the Black et al., Fell et al., and Tremblay et al. specimen). 51
5.17 Histogram of the fiber ultimate strain used in the MEF element modeling of all the brace specimen considered in this study (including the Black et al., Fell et al., and Tremblay et al. specimen). 51

6.1 6-story steel braced structure tested under the US/Japan cooperative research program: (a) FRAME3D model. (b) Plan and elevations. Primary lateral-force resistance in the loading direction came from a single bay braced frame (BF), although beams in the other bays (MF) were moment-connected to the columns, providing supplementary lateral resistance. 56
6.2 Comparison of analytical and experimental inter-story drift ratio time-series of the 6-story test structure – **Base model**. 57

6.3 Comparison of analytical and experimental story shears of the 6-story test structure – **Tuned model**. . . . 58
6.4 Comparison of analytical and experimental inter-story drift ratio time-series of the 6-story test structure – **Tuned model**. . . . 59
6.5 Comparison of analytical and experimental inter-story drift ratio versus story shear of the 6-story test structure – **Tuned model**. . . . 60
6.6 Simulated brace out-of-plane lateral displacement versus axial force histories in stories 4–6 of the tuned model. Buckling is not seen in any cases. . . . 61
6.7 Simulated brace out-of-plane lateral displacement versus axial force histories in stories 1–3 of the tuned model. Buckling is not seen in any cases. . . . 62
6.8 Simulated brace in-plane lateral displacement versus axial force histories in stories 4–6 of the tuned model. In-plane buckling occurs in the north braces of stories 4 and 5. . . . 63
6.9 Simulated brace in-plane lateral displacement versus axial force histories in stories 1–3 of the tuned model. In-plane buckling is seen in the north and south braces of stories 2 and 3, and the north brace of the first story. . . . 64
6.10 Snapshot of the deformed shape of the FRAME3D model of the 6-story test structure at time 10.85s from the start of the Miyagi-Ken-Oki shaking (deformations exaggerated by a factor of 5). Note the in-plane buckling of the north brace of stories 1–5, and the south brace of stories 2 and 3 on the elevation views. Out-of-plane buckling is not seen in any of the braces. The ground motion velocity and acceleration waveforms, and the roof North and East displacement histories are also shown. A movie of the shaking of the model can be downloaded from http://krishnan.caltech.edu . . . 65

7.1 Structural plan, section, elevation, and member sizes of the proposed benchmark water-tank problem. Note that the X-braces are assumed not to be connected at the intersecting point. . . . 68
7.2 Undeformed shape of the collapsing benchmark steel braced water-tank subjected to the 1995 Kobe earthquake Takatori record scaled down by a factor of 0.32. . . . 69
7.3 5.5s snapshot of the collapsing benchmark steel braced water-tank subjected to the 1995 Kobe earthquake Takatori record scaled down by a factor of 0.32. Deformations are exaggerated by a factor of 5. . . . 70
7.4 7s snapshot of the collapsing benchmark steel braced water-tank subjected to the 1995 Kobe earthquake Takatori record scaled down by a factor of 0.32. Deformations are exaggerated by a factor of 5. . . . 71
7.5 9s snapshot of the collapsing benchmark steel braced water-tank subjected to the 1995 Kobe earthquake Takatori record scaled down by a factor of 0.32. Deformations are exaggerated by a factor of 5. . . . 72
7.6 11s snapshot of the collapsing benchmark steel braced water-tank subjected to the 1995 Kobe earthquake Takatori record scaled down by a factor of 0.32. Deformations are exaggerated by a factor of 5. . . . 73

7.7 13s snapshot of the collapsing benchmark steel braced water-tank subjected to the 1995 Kobe earthquake Takatori record scaled down by a factor of 0.32. Deformations are exaggerated by a factor of 5. 74
7.8 15s snapshot of the collapsing benchmark steel braced water-tank subjected to the 1995 Kobe earthquake Takatori record scaled down by a factor of 0.32. Deformations are exaggerated by a factor of 5. 75
7.9 16s snapshot of the collapsing benchmark steel braced water-tank subjected to the 1995 Kobe earthquake Takatori record scaled down by a factor of 0.32. Deformations are exaggerated by a factor of 5. 76

A.1 Comparison of the numerical solution using MEF elements (dashed lines) against a second-order analytical solution (solid lines) for the L-shaped Koiter-Roorda frame with a downward force (P) acting at the corner (black), or at eccentricities of e/L=0.001 (red), 0.01 (green), and 0.05 (blue): Case 1: TS8x8x3/16, L/R=80) – (a) Corner rotation versus P/P_{CR}; (b) Corner in-plane lateral displacement versus P/P_{CR}. 79
A.2 Comparison of the numerical solution using MEF elements (dashed lines) against a second-order analytical solution (solid lines) for the L-shaped Koiter-Roorda frame with a downward force (P) acting at the corner (black), or at eccentricities of e/L=0.001 (red), 0.01 (green), and 0.05 (blue): Case 1: TS8x8x3/16, L/R=120) – (a) Corner rotation versus P/P_{CR}; (b) Corner in-plane lateral displacement versus P/P_{CR}. 80
A.3 Comparison of the numerical solution using MEF elements (dashed lines) against a second-order analytical solution (solid lines) for the L-shaped Koiter-Roorda frame with a downward force (P) acting at the corner (black), or at eccentricities of e/L=0.001 (red), 0.01 (green), and 0.05 (blue): Case 1: TS8x8x3/16, L/R=160) – (a) Corner rotation versus P/P_{CR}; (b) Corner in-plane lateral displacement versus P/P_{CR}. 81
A.4 Comparison of the numerical solution using MEF elements (dashed lines) against a second-order analytical solution (solid lines) for the L-shaped Koiter-Roorda frame with a downward force (P) acting at the corner (black), or at eccentricities of e/L=0.001 (red), 0.01 (green), and 0.05 (blue): Case 1: TS8x8x3/16, L/R=200) – (a) Corner rotation versus P/P_{CR}; (b) Corner in-plane lateral displacement versus P/P_{CR}. 82
A.5 Comparison of the numerical solution using MEF elements (dashed lines) against a second-order analytical solution (solid lines) for the L-shaped Koiter-Roorda frame with a downward force (P) acting at the corner (black), or at eccentricities of e/L=0.001 (red), 0.01 (green), and 0.05 (blue): Case 1: TS12x12x7/16, L/R=40) – (a) Corner rotation versus P/P_{CR}; (b) Corner in-plane lateral displacement versus P/P_{CR}. 83
A.6 Comparison of the numerical solution using MEF elements (dashed lines) against a second-order analytical solution (solid lines) for the L-shaped Koiter-Roorda frame with a downward force (P) acting at the corner (black), or at eccentricities of e/L=0.001 (red), 0.01 (green), and 0.05 (blue): Case 1: TS12x12x7/16, L/R=80) – (a) Corner rotation versus P/P_{CR}; (b) Corner in-plane lateral displacement versus P/P_{CR}. 84

A.7 Comparison of the numerical solution using MEF elements (dashed lines) against a second-order analytical solution (solid lines) for the L-shaped Koiter-Roorda frame with a downward force (P) acting at the corner (black), or at eccentricities of e/L=0.001 (red), 0.01 (green), and 0.05 (blue): Case 1: TS12x12x7/16, L/R=120) – (a) Corner rotation versus P/P_{CR}; (b) Corner in-plane lateral displacement versus P/P_{CR}. 85
A.8 Comparison of the numerical solution using MEF elements (dashed lines) against a second-order analytical solution (solid lines) for the L-shaped Koiter-Roorda frame with a downward force (P) acting at the corner (black), or at eccentricities of e/L=0.001 (red), 0.01 (green), and 0.05 (blue): Case 1: TS12x12x7/16, L/R=160) – (a) Corner rotation versus P/P_{CR}; (b) Corner in-plane lateral displacement versus P/P_{CR}. 86
A.9 Comparison of the numerical solution using MEF elements (dashed lines) against a second-order analytical solution (solid lines) for the L-shaped Koiter-Roorda frame with a downward force (P) acting at the corner (black), or at eccentricities of e/L=0.001 (red), 0.01 (green), and 0.05 (blue): Case 1: TS12x12x7/16, L/R=200) – (a) Corner rotation versus P/P_{CR}; (b) Corner in-plane lateral displacement versus P/P_{CR}. 87
A.10 Comparison of the numerical solution using MEF elements (dashed lines) against a second-order analytical solution (solid lines) for the L-shaped Koiter-Roorda frame with a downward force (P) acting at the corner (black), or at eccentricities of e/L=0.001 (red), 0.01 (green), and 0.05 (blue): Case 1: W10x39, L/R=40) – (a) Corner rotation versus P/P_{CR}; (b) Corner in-plane lateral displacement versus P/P_{CR}. 88
A.11 Comparison of the numerical solution using MEF elements (dashed lines) against a second-order analytical solution (solid lines) for the L-shaped Koiter-Roorda frame with a downward force (P) acting at the corner (black), or at eccentricities of e/L=0.001 (red), 0.01 (green), and 0.05 (blue): Case 1: W10x39, L/R=80) – (a) Corner rotation versus P/P_{CR}; (b) Corner in-plane lateral displacement versus P/P_{CR}. 89
A.12 Comparison of the numerical solution using MEF elements (dashed lines) against a second-order analytical solution (solid lines) for the L-shaped Koiter-Roorda frame with a downward force (P) acting at the corner (black), or at eccentricities of e/L=0.001 (red), 0.01 (green), and 0.05 (blue): Case 1: W10x39, L/R=120) – (a) Corner rotation versus P/P_{CR}; (b) Corner in-plane lateral displacement versus P/P_{CR}. 90
A.13 Comparison of the numerical solution using MEF elements (dashed lines) against a second-order analytical solution (solid lines) for the L-shaped Koiter-Roorda frame with a downward force (P) acting at the corner (black), or at eccentricities of e/L=0.001 (red), 0.01 (green), and 0.05 (blue): Case 1: W10x39, L/R=160) – (a) Corner rotation versus P/P_{CR}; (b) Corner in-plane lateral displacement versus P/P_{CR}. 91

A.14 Comparison of the numerical solution using MEF elements (dashed lines) against a second-order analytical solution (solid lines) for the L-shaped Koiter-Roorda frame with a downward force (P) acting at the corner (black), or at eccentricities of e/L=0.001 (red), 0.01 (green), and 0.05 (blue): Case 1: W10x39, L/R=200) – (a) Corner rotation versus P/P_{CR}; (b) Corner in-plane lateral displacement versus P/P_{CR}. 92
A.15 Comparison of the numerical solution using MEF elements (dashed lines) against a second-order analytical solution (solid lines) for the L-shaped Koiter-Roorda frame with a downward force (P) acting at the corner (black), or at eccentricities of e/L=0.001 (red), 0.01 (green), and 0.05 (blue): Case 1: W14x90, L/R=40) – (a) Corner rotation versus P/P_{CR}; (b) Corner in-plane lateral displacement versus P/P_{CR}. 93
A.16 Comparison of the numerical solution using MEF elements (dashed lines) against a second-order analytical solution (solid lines) for the L-shaped Koiter-Roorda frame with a downward force (P) acting at the corner (black), or at eccentricities of e/L=0.001 (red), 0.01 (green), and 0.05 (blue): Case 1: W14x90, L/R=80) – (a) Corner rotation versus P/P_{CR}; (b) Corner in-plane lateral displacement versus P/P_{CR}. 94
A.17 Comparison of the numerical solution using MEF elements (dashed lines) against a second-order analytical solution (solid lines) for the L-shaped Koiter-Roorda frame with a downward force (P) acting at the corner (black), or at eccentricities of e/L=0.001 (red), 0.01 (green), and 0.05 (blue): Case 1: W14x90, L/R=120) – (a) Corner rotation versus P/P_{CR}; (b) Corner in-plane lateral displacement versus P/P_{CR}. 95
A.18 Comparison of the numerical solution using MEF elements (dashed lines) against a second-order analytical solution (solid lines) for the L-shaped Koiter-Roorda frame with a downward force (P) acting at the corner (black), or at eccentricities of e/L=0.001 (red), 0.01 (green), and 0.05 (blue): Case 1: W14x90, L/R=160) – (a) Corner rotation versus P/P_{CR}; (b) Corner in-plane lateral displacement versus P/P_{CR}. 96
A.19 Comparison of the numerical solution using MEF elements (dashed lines) against a second-order analytical solution (solid lines) for the L-shaped Koiter-Roorda frame with a downward force (P) acting at the corner (black), or at eccentricities of e/L=0.001 (red), 0.01 (green), and 0.05 (blue): Case 1: W14x90, L/R=200) – (a) Corner rotation versus P/P_{CR}; (b) Corner in-plane lateral displacement versus P/P_{CR}. 97

B.1 Black et al. tests: W6x20 coupon tensile loading test. 98
B.2 Black et al. tests: W6x20 coupon tensile loading test (contd.). 99
B.3 Black et al. tests: Pinned ended W6x20 strut (3) with KL/r=80 – Loading history. 99
B.4 Black et al. tests: Pinned ended W6x20 strut (1) with KL/r=80, axial displacement versus axial force history – (a) Experiment (b) Simulation. 100
B.5 Black et al. tests: Pinned ended W6x20 strut (1) with KL/r=80, lateral displacement versus axial force history – (a) Experiment (b) Simulation. 101
B.6 Black et al. tests: TS4x4x1/4 coupon tensile loading test. 102
B.7 Black et al. tests: Pinned ended TS4x4x1/4 strut (17) with KL/r=80 – Loading history. . . . 103

B.8 Black et al. tests: Pinned ended TS4x4x1/4 strut (17) with KL/r=80, axial displacement versus axial force history – (a) Experiment (b) Simulation. 104
B.9 Black et al. tests: Pinned ended TS4x4x1/4 strut (17) with KL/r=80, lateral displacement versus axial force history – (a) Experiment (b) Simulation. 105
B.10 Black et al. tests: TS4x4x1/2 coupon tensile loading test. 106
B.11 Black et al. tests: Pinned ended TS4x4x1/2 strut (18) with KL/r=80 – Loading history. . . . 107
B.12 Black et al. tests: Pinned ended TS4x4x1/2 strut (18) with KL/r=80, axial displacement versus axial force history – (a) Experiment (b) Simulation. 108
B.13 Black et al. tests: Pinned ended TS4x4x1/2 strut (18) with KL/r=80, lateral displacement versus axial force history – (a) Experiment (b) Simulation. 109
B.14 Black et al. tests: W6x20 strut (19) with KL/r=40 pinned at one end and fixed at the other – Loading history. 110
B.15 Black et al. tests: W6x20 strut (19) with KL/r=40 pinned at one end and fixed at the other, axial displacement versus axial force history – (a) Experiment (b) Simulation. 111
B.16 Black et al. tests: W6x20 strut (19) with KL/r=40 pinned at one end and fixed at the other, lateral displacement versus axial force history – (a) Experiment (b) Simulation. 112
B.17 Black et al. tests: Pinned ended TS4x4x1/2 strut (22) with KL/r=80 – Loading history. . . . 113
B.18 Black et al. tests: TS4x4x1/2 strut (22) with KL/r=80 pinned at one end and fixed at the other, axial displacement versus axial force history – (a) Experiment (b) Simulation. 114
B.19 Black et al. tests: TS4x4x1/2 strut (22) with KL/r=80 pinned at one end and fixed at the other, lateral displacement versus axial force history – (a) Experiment (b) Simulation. 115
B.20 Black et al. tests: W5x16 coupon tensile loading test. 116
B.21 Black et al. tests: W5x16 coupon tensile loading test (contd.). 117
B.22 Black et al. tests: W5x16 strut (23) with KL/r=80 pinned at one end and fixed at the other – Loading history. 118
B.23 Black et al. tests: W5x16 strut (23) with KL/r=80 pinned at one end and fixed at the other, axial displacement versus axial force history – (a) Experiment (b) Simulation. 119
B.24 Black et al. tests: W5x16 strut (23) with KL/r=80 pinned at one end and fixed at the other, lateral displacement versus axial force history – (a) Experiment (b) Simulation. 120

C.1 NEESR project by Fell et al.: HSS4x4x1/4 coupon tensile loading test. 121
C.2 Fell et al. test 1 on HSS4x4x1/4 (KL/r $\sim$ 80): Loading History 122
C.3 Comparison of simulation against data from Fell et al. test 1 on HSS4x4x1/4 (KL/r $\sim$ 80): (a) Axial displacement versus axial force history; (b) Minor direction lateral displacement versus axial force history. 123
C.4 Fell et al. test 3 on HSS4x4x1/4 (KL/r $\sim$ 80): Loading History 124
C.5 Comparison of simulation against data from Fell et al. test 3 on HSS4x4x1/4 (KL/r $\sim$ 80): (a) Axial displacement versus axial force history; (b) Minor direction lateral displacement versus axial force history. 125
C.6 NEESR project by Fell et al.: HSS4x4x3/8 coupon tensile loading test. 126

C.7 Fell et al. test 4 on HSS4x4x3/8 (KL/r $\sim$ 82): Loading History 127
C.8 Comparison of simulation against data from Fell et al. test 4 on HSS4x4x3/8 (KL/r $\sim$ 82): (a) Axial displacement versus axial force history; (b) Minor direction lateral displacement versus axial force history. 128
C.9 Fell et al. test 5 on HSS4x4x3/8 (KL/r $\sim$ 82): Loading History 129
C.10 Comparison of simulation against data from Fell et al. test 5 on HSS4x4x3/8 (KL/r$\sim$82): (a) Axial displacement versus axial force history; (b) Minor direction lateral displacement versus axial force history. 130
C.11 NEESR project by Fell et al.: W12x16 coupon tensile loading test. 131
C.12 Fell et al. test 14 on W12x16 (KL/r $\sim$ 159): Loading History 131
C.13 Comparison of simulation against data from Fell et al. test 14 on W12x16 (KL/r $\sim$ 159): (a) Axial displacement versus axial force history; (b) Minor direction lateral displacement versus axial force history. 132
C.14 Fell et al. test 15 on W12x16 (KL/r $\sim$ 159): Loading History 133
C.15 Comparison of simulation against data from Fell et al. test 15 on W12x16 (KL/r $\sim$ 159): (a) Axial displacement versus axial force history; (b) Minor direction lateral displacement versus axial force history. 134

D.1 Comparison of simulation against data from Tremblay et al. tests: (a) Specimen S1A and (b) Specimen S1B with RHS127x76x4.8 diagonal – frame sway versus applied lateral force history. 136
D.2 Comparison of simulation against data from Tremblay et al. tests: (a) Specimen S3A and (b) Specimen S3B with RHS76x76x4.8 diagonal – frame sway versus applied lateral force history. 137
D.3 Comparison of simulation against data from Tremblay et al. tests: (a) Specimen S4A and (b) Specimen S4B with RHS127x64x4.8 diagonal – frame sway versus applied lateral force history. 138
D.4 Comparison of simulation against data from Tremblay et al. tests: (a) Specimen S5A and (b) Specimen S5B with RHS102x76x6.4 diagonal – frame sway versus applied lateral force history. 139
D.5 Comparison of simulation against data from Tremblay et al. tests: (a) Specimen S4QA and (b) Specimen S4QB with RHS127x64x4.8 diagonal – frame sway versus applied lateral force history. 140

E.1 Time histories of displacement at the (a) south-west and (b) north-east corners of the roof of the water-tank under the Takatori ground excitation scaled down by a factor of 0.32. 142
E.2 Time histories of lateral deformation (a,b) and axial forces (c,d) in the base mega-columns at the south-west and south-east corners of the water-tank under the Takatori ground excitation scaled down by a factor of 0.32. 143

E.3 Time histories of lateral deformation (a,b) and axial forces (c,d) in the base mega-columns at the north-west and north-east corners of the water-tank under the Takatori ground excitation scaled down by a factor of 0.32. 144
E.4 Time histories of lateral deformation (a,b) and axial forces (c,d) in the bottom braces on the south face of the water-tank under the Takatori ground excitation scaled down by a factor of 0.32. 145
E.5 Time histories of lateral deformation (a,b) and axial forces (c,d) in the bottom braces on the north face of the water-tank under the Takatori ground excitation scaled down by a factor of 0.32. 146
E.6 Time histories of lateral deformation (a,b) and axial forces (c,d) in the bottom braces on the east face of the water-tank under the Takatori ground excitation scaled down by a factor of 0.32. 147
E.7 Time histories of lateral deformation (a,b) and axial forces (c,d) in the bottom braces on the west face of the water-tank under the Takatori ground excitation scaled down by a factor of 0.32. 148

List of Tables

5.1 Strut properties (section, boundary conditions, area, moment of inertia about the minor axis, effective slenderness ratio, observed elastic critical buckling load, and the smaller of the theoretical Euler buckling load and the axial yield capacity) in Black et al. experiments . . . 31

5.2 Black et al. coupon test data (yield stress, ultimate stress, and strain at ultimate stress) and MEF element model parameters (yield stress, ultimate stress, strain at ultimate stress, strain at the onset of strain-hardening, and minor direction eccentricity/geometric imperfection as a percentage of the span). An elastic modulus of 29000ksi, and a tangent modulus at the initiation of strain hardening E_{sh} of 580ksi is used for all models is used for all models. . . . 31

5.3 Strut properties (section, load-history, area, moment of inertia about the minor axis, effective slenderness ratio (with K=1.0), observed elastic critical buckling load, and the smaller of the theoretical Euler buckling load (with K=1.0) and the axial yield capacity) in Fell et al. experiments. The length of each specimen was 123 inches. 37

5.4 Fell et al. coupon test data (yield stress, ultimate stress, and strain at ultimate stress) and MEF element model parameters (yield stress, ultimate stress, strain at ultimate stress, strain at the onset of strain-hardening, minor direction eccentricity/geometric imperfection as a percentage of the span, and end fixity factor (FF) – fiber strains due to element end rotations are scaled by the fixity factor resulting in depleted moment transfer). Coupons from the W12x16 section were not tested. An elastic modulus E of 29000ksi, and a tangent modulus at the initiation of strain hardening E_{sh} of 580ksi is used for all models. 39

5.5 Tremblay et al. experiments: Strut properties (section, load-history, area, moment of inertia about the minor axis, and slenderness ratio. 43

5.6 Tremblay et al. coupon test data (yield stress, ultimate stress, and strain at ultimate stress) and MEF element model parameters (yield stress, ultimate stress, strain at ultimate stress, strain at the onset of strain-hardening, and fixity factors for the two ends (FF_1 and FF_2) – fiber strains due to element end rotations are scaled by the fixity factor resulting in depleted moment transfer). An infinitesimally small geometric imperfection, and fracture strains larger than rupture strain are assumed for all models. 45

5.7 Comparison of minimum and maximum lateral force applied to the frame in the Tremblay et al. experiments, against the corresponding story shears in the FRAME3D models under the imposed lateral displacement history. Also shown is a comparison of the brace peak out-of-plane (o-of-p) deformations observed in the experiments against that computed from the models. Note that braces in S3A and S3B models have significant in-plane deformations too, as apparent in the square root of the sum of the squares (SRSS) of their in-plane and out-of-plane deformations, listed in the table. 46

6.1 MEF element model parameters used for the braces in the BASE and TUNED models. Listed parameters are fiber yield stress (σ_y), fiber ultimate stress (σ_u), fiber ultimate strain (ϵ_u), fiber strain-hardening initiation strain, ϵ_{sh}, brace out-of-plane eccentricity (e_{min}), brace in-plane eccentricity (e_{maj}), and fixity factors at the bottom (FFB) and top (FFT) of the brace. An elastic modulus E of 29000ksi, and a tangent modulus at the initiation of strain hardening E_{sh} of 580ksi is used for all elements in both models. 54

Chapter 1 Introduction and Motivation

A cyclically, axially loaded slender element has a tendency to buckle laterally under compression, and straighten out and possibly yield in the ensuing tensile excursion. Subsequent loading cycles may result in localization of the buckled region at the mid-length of the member followed possibly by cracking and/or rupturing, ultimately severing the element completely. The buckling instability is greatly sensitive to end-fixity conditions and initial geometric imperfection. While the initial buckling may be a purely elastic phenomenon, subsequent compression excursions may result in significant inelastic buckling accompanied with a gradual reduction in the buckling load. Thus, what starts out as a purely geometric nonlinearity evolves into a complex interplay between material and geometric nonlinearities, with the ductility of the material playing an important role in determining the low-cycle fatigue degradation and ultimate failure of the member. Accurately modeling such a multi-faceted phenomenon using a single element to represent the entire member is highly challenging, given the uncertainties associated with the member geometry including boundary conditions and the sensitivity of buckling response to the geometry. In addition, the ill-conditioning of the element stiffness matrix close to buckling and/or the stiffening of an imperfect or a buckled member due to a tensile excursion might make the solution difficult to converge numerically when using the tangent stiffness matrix for Newton-Raphson iterations. The objective of this study is to develop a beam-column element that can overcome these challenges and incorporate it into a previously developed 3-D analysis framework, FRAME3D (Krishnan 2003a; Krishnan and Hall 2006a; Krishnan and Hall 2006b; Krishnan 2009). The end goal is to be able to perform efficient and accurate 3-D collapse analysis of tall braced steel structures under strong earthquake ground motion.

Early studies on braced structures (e.g., (Jain and Goel 1978; Ikeda and Mahin 1984; Tang and Goel 1989; Hassan and Goel 1991; Tremblay 2002; Tremblay and Poncet 2005; Han et al. 2007) were exclusively conducted using phenomenological models implemented on the DRAIN2D analysis framework (Kanaan and Powell 1973; Allahabadi and Powell 1988; Prakash et al. 1993). Recent brace modeling efforts have concentrated on multi-element or multi-segment approaches to model a single brace. These include an inelastic beam-column element model by Uriz et al. (2008), incorporated into the OpenSees computational framework (McKenna 1997; Mazzoni et al. 2005), that accounts for distributed inelasticity through integration of material response over the cross-section, and subsequent integration of section response along the element, a flexibility based element with exact interpolation of forces evaluated at a number of integration points along the length of the element and interpolation of displacements using compatibility equations by Schachter and Reinhorn (2007), a distributed inelasticity element, with a bounding plasticity model of force resultants for the interaction between bending moment and axial force, by Jin and El-Tawil (2003), a 2-D 8-segment fiber element model, with geometric updating of the interior nodes enabling the modeling of large deformations, by Hall and Challa (1995), and a 2-D plastic hinge element model with geometric updating, that requires at least two elements to model each member, also by Hall and Challa (1995), and a 56-segment version of the Hall-Challa fiber element model by Gan and Hall (1998) with mass of the brace

included. While the early phenomenological models were too closely dependent on the data (and specimen) used for calibration and could not be easily generalized, the modern formulations result in a large number of degrees of freedom for each brace and using these for the analysis of large scale braced structures would be an expensive proposition.

What is required is a physical modeling approach (with physically measurable parameters whose calibration is not specimen or loading-history dependent) that retains the attractive feature of few degrees of freedom in phenomenological models, yet can accurately capture nonlinear geometric and material effects. The work presented here is an effort in this direction. The modified elastofiber element developed here is a 3-D hybrid extension of the 2-D Hall-Challa fiber element and plastic hinge models (Hall and Challa 1995), that facilitates the modeling of large three-dimensional braced steel structures in a computationally efficient manner.

Chapter 2 The Modified Elastofiber Element and its Integration into the FRAME3D Analysis Framework

The structural model in the FRAME3D analysis framework consists of beam/column/brace elements connected to 3-D panel zone elements at panel mid-points (attachment points) or panel corners (Figure 2.1). The panel zone element models nonlinear shear deformation in the region of the joint where the beams and columns intersect. One column, the associated column of the joint, runs continuously through the height of the joint, and the panel zone element models the joint consisting of the length of the associated column that lies within the depth of the connecting beams. Each panel zone element consolidates the flanges, webs, and doubler plates of the associated column into two orthogonal panels ① and ② which always remain planar and orthogonal [Figure 2.2(a)]. Edges of these panels contain attachment points a, b, c, and d, where beams attach, and e and f on the top and bottom, where columns attach. Braces attach to one of the eight panel corners. Eight global degrees of freedom (DOF) are associated with each node (J, K, etc.) located at the center of the panel zone elements. They include three translational DOF, U_{JX}, U_{JY}, U_{JZ}, with respect to the global coordinate system, XYZ, and five rotational degrees of freedom, $\theta_{J\bar{X}}$, $\theta^B_{J\bar{Y}}$, $\theta^C_{J\bar{Y}}$, $\theta^B_{J\bar{Z}}$, and $\theta^C_{J\bar{Z}}$, with respect to the panel zone coordinate system, $\bar{X}\bar{Y}\bar{Z}$. $\theta_{J\bar{X}}$ is the rotation of the panel zone element as a rigid body about the $\bar{X}$ axis, while the rotations $\theta^B_{J\bar{Y}}$ and $\theta^C_{J\bar{Y}}$ together accommodate a rigid rotation of panel ① about $\bar{Y}$ plus its shear deformation, and the rotations $\theta^B_{J\bar{Z}}$ and $\theta^C_{J\bar{Z}}$ together accommodate a rigid rotation of panel ② about $\bar{Z}$ plus its shear deformation [Figures 2.2(c)–2.2(f)]. Material nonlinearity in each panel is included by assuming a linear-quadratic shear stress-strain backbone behavior until ultimate shear stress is reached, and perfectly plastic behavior thereafter, as first proposed by Hall and Challa (1995). Hysteresis loops, defined by linear segments and cubic ellipses, and hysteresis rules, based on an extended Masing's hypothesis, are used to model the cyclic response of each panel [Figure 2.2(b)].

Beams, columns, and braces can be modeled using either plastic hinge elements or 3-segment elastofiber elements (Krishnan 2003a; Krishnan and Hall 2006a; Krishnan and Hall 2006b; Krishnan 2009) or 5-segment modified elastofiber elements, described later in this chapter. The element arrangement in the structural model with explicit modeling of the joint enables the clear length of these elements to be accurately captured. The clear span plays a particularly important role in the buckling phenomenon. Four-noded elastic plane-stress elements, connecting directly to the joint nodes at the center of the panel zone elements, are used to model the in-plane stiffness of floor slabs. Following the structure to collapse requires satisfying the dynamic equations of equilibrium in the deformed configuration at each instant of time. The analysis framework includes geometric updating of the joint nodes, the attachment points and the interior nodes, and orientations of the plastic hinge, elastofiber and modified elastofiber elements, to accommodate large translations and rotations, automatically accounting for $P-\Delta$ effects and allowing the analysis to follow a structure's response well into collapse.

The matrix equation of motion of the structure (Cook et al. 1989; Chopra 1995) as a function of time, t,

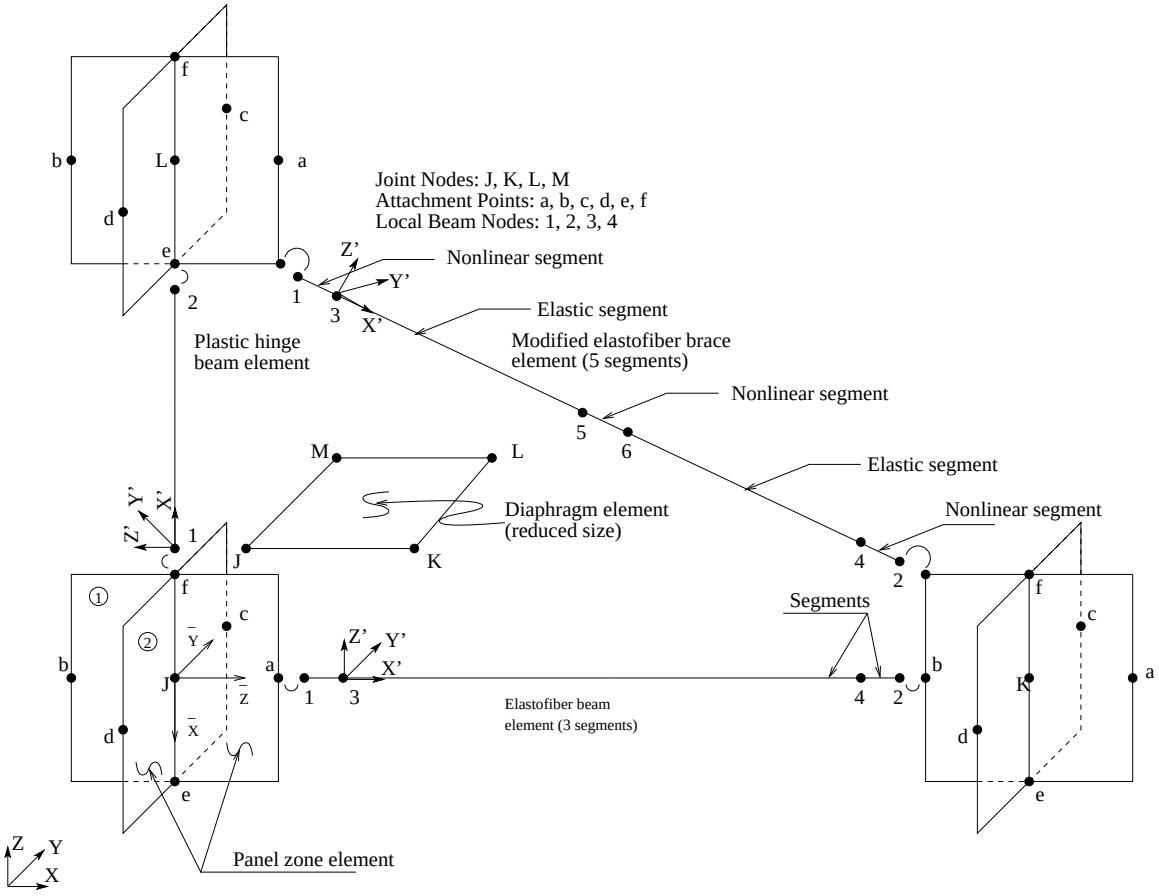

Figure 2.1: Element arrangement in the FRAME3D modeling framework, showing joint nodes, attachment points, beam internal nodes, and the three coordinate systems, XYZ (global), $X'Y'Z'$ (element/segment local), $\bar{X}\bar{Y}\bar{Z}$ (panel zone local). Also shown are the plastic hinge and elastofiber elements for beam/column modeling, the 5-segment modified elastofiber element for brace/slender-column modeling, the panel zone element for joint modeling, and the diaphragm element for floor slab modeling.

is

$$[M]\left\{\ddot{U}(t)\right\} + [C]\left\{\dot{U}(t)\right\} + \{R(t)\} = \{f_g\} - [M]\,[r]\left\{\ddot{U}_g(t)\right\}. \tag{2.1}$$

where $\{U(t)\}$ is the vector of global displacements at time, t, comprising the 8 global translations and rotations at each node, J, K, etc, not including the fixed support DOF; $\left\{\dot{U}(t)\right\}$, $\left\{\ddot{U}(t)\right\}$ are the corresponding nodal velocity and acceleration vectors, respectively; $[M]$ is the structure mass matrix, which is diagonal with non-zero terms only at the translational degrees of freedom as a consequence of lumping the masses at the joint nodes and neglecting the associated rotary inertia; $[C]$ is the structure damping matrix, assumed to be of the Rayleigh type (proportional to the initial stiffness and mass matrices); $\{R(t)\}$ is the vector of stiffness forces corresponding to the configuration $\{U(t)\}$, computed considering all material and geometric nonlinear effects; $\{f_g\}$ is the vector of static gravity loads for which a static analysis is performed first; $\left\{\ddot{U}_g(t)\right\}$ is the vector consisting of two horizontal components (X and Y) and one vertical component

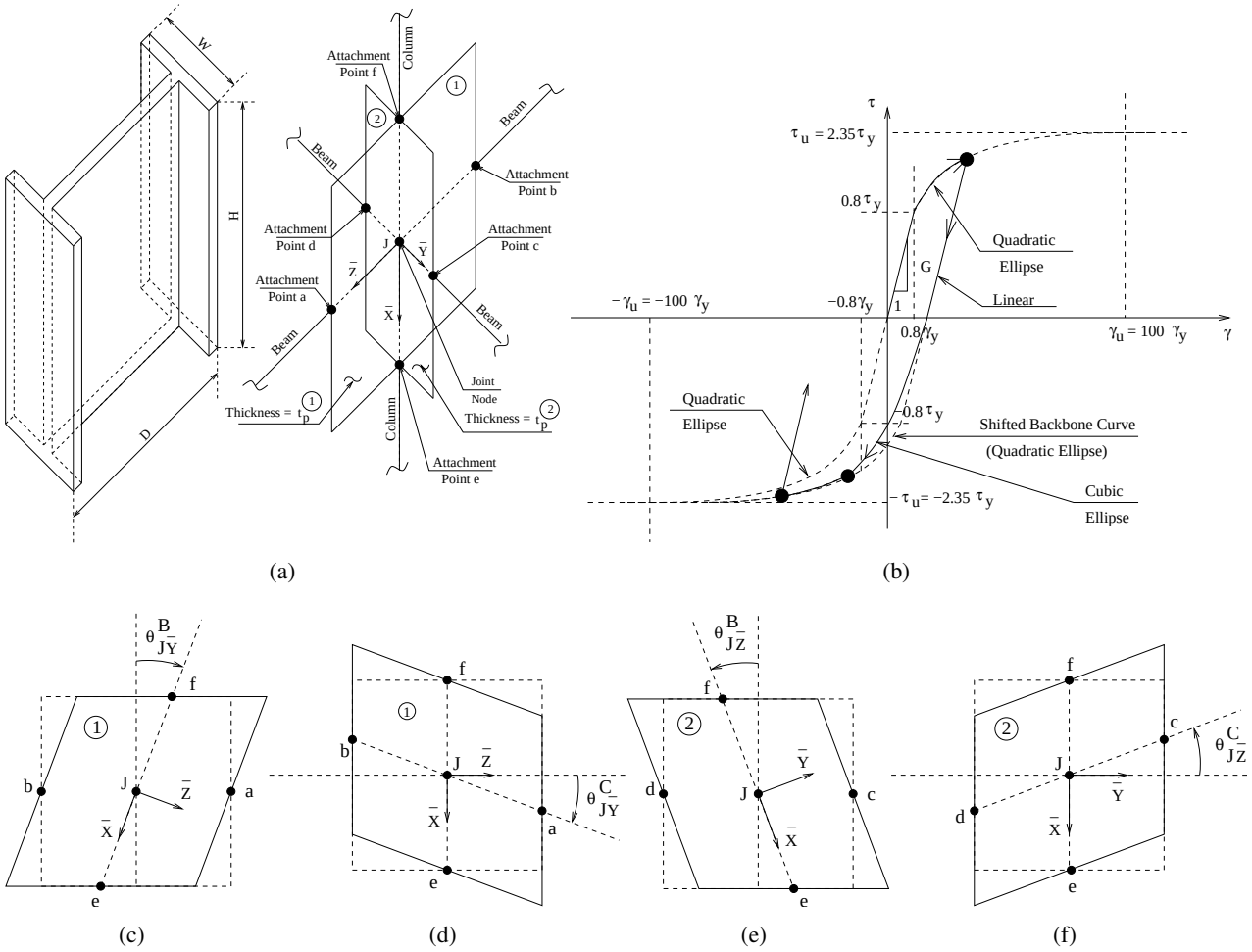

Figure 2.2: Four rotational degrees of freedom of a panel zone element: Joints, comprising of a length of column within the depth of the connecting beams, are modeled using panel zone elements consisting of two rectangular panels which are perpendicular to each other, panel ① in the $\bar{X} - \bar{Z}$ plane and panel ② in the $\bar{X} - \bar{Y}$ plane, forming a cruciform section. The thicknesses of all web plates and web doubler plates of the associated column are combined to form the thickness of panel ①, $t_p^{①}$, while the thicknesses of all flange plates of the associated column are combined to form the thickness of panel ②, $t_p^{②}$. Each panel has two DOF which are also global DOF: $\theta^B_{J\bar{Y}}$ and $\theta^C_{J\bar{Y}}$ for panel ① and $\theta^B_{J\bar{Z}}$ and $\theta^C_{J\bar{Z}}$ for panel ②, where J is the global node at the center of the joint. These rotations deform the two panels into parallelograms. The B and C indicate that the rotating panel edges are connected to columns and beams, respectively. Strain or rotation in one of the panels causes a rigid body rotation but no strain in the orthogonal panel.

(Z) of the free-field ground acceleration at time t, which is assumed to be spatially uniform; and $[r]$ is a 3-column matrix of zeroes except for ones in the first, second, and third columns in the positions corresponding to the X, Y, and Z translational DOF, respectively.

Linearizing the nonlinear stiffness force vector, $\{R(t)\}$ over the time interval between t and $t+\Delta t$ using the tangent stiffness matrix, $[K_T]$, the increment in the global displacements can be computed using eq. 2.1 and constant average acceleration approximations to the velocity and acceleration vectors at time $t + \Delta t$. However, this linearization will not hold through the entire time step, and hence iterations are used within

each time step. The equation that is solved in iteration l is:

$$\left[\frac{4}{(\Delta t)^2}M + \frac{2}{\Delta t}C + K_T^l\right]\{\Delta U\} = \{f_g\} - \left\{R^l\right\} - [M][r]\left\{\ddot{U}_g(t)\right\} + [M]\left\{\frac{4}{(\Delta t)^2}U(t) + \frac{4}{\Delta t}\dot{U}(t) + \ddot{U}(t)\right\} + [C]\left\{\frac{2}{\Delta t}U(t) + \dot{U}(t)\right\} - \left[\frac{4}{(\Delta t)^2}M + \frac{2}{\Delta t}C\right]\left\{U^l\right\}. \tag{2.2}$$

where $\left[K_T^l\right]$ and $\left\{R^l\right\}$ correspond to the displacement configuration at the beginning of iteration l, $\left\{U^l\right\}$. Solution of this equation leads to $\{\Delta U\}$ which adds to $\left\{U^l\right\}$ to give $\left\{U^{l+1}\right\}$. $\{\Delta U\}$ is also used to update the coordinates of the nodes and the attachment points, and the orientations of plastic hinge, elastofiber, and modified elastofiber elements. For each time step, iterations continue until convergence, with the next iteration using the updated values of $\left[K_T^{l+1}\right]$ and $\left\{R^{l+1}\right\}$ corresponding to configuration $\left\{U^{l+1}\right\}$. This updating is done at the element level and then assembly is used to construct $\left[K_T^{l+1}\right]$ and $\left\{R^{l+1}\right\}$, i.e., contributions to $\left[K_T^{l+1}\right]$ are the element matrices $\left[K_{pz}^{l+1}\right]$, $\left[K_{ph}^{l+1}\right]$, $\left[K_{ef}^{l+1}\right]$, $\left[K_{mef}^{l+1}\right]$, and $\left[K_d^{l+1}\right]$, and contributions to $\left\{R^{l+1}\right\}$ are the element vectors $\left\{R_{pz}^{l+1}\right\}$, $\left\{R_{ph}^{l+1}\right\}$, $\left\{R_{ef}^{l+1}\right\}$, $\left\{R_{mef}^{l+1}\right\}$, and $\left\{R_d^{l+1}\right\}$. The subscripts stand for panel zone element, plastic hinge element, elastofiber element, modified elastofiber element, and diaphragm element, respectively.

2.1 3-D Modified Elastofiber (MEF) Element to Model Slender Columns and Braces

Fiber elements have been successfully implemented to more accurately account for nonlinear material behavior under combined bending and axial load, including PMM interaction, strain hardening, cracking, and spread of nonlinearity along the member. Each element is divided into a number of segments and each segment is discretized into a number of fibers in the cross-section, with each fiber running the full length of the segment. Fully discretized fiber elements are computationally expensive, especially when implemented in a three-dimensional framework. Fortunately, in a series of cyclic load analyses conducted on isolated braces modeled using fully discretized 2-D Hall-Challa fiber elements (Hall and Challa 1995), Gan and Hall observed that strain is concentrated in a short segment at mid-span of braces with pinned ends, and in short segments at the two ends as well as at mid-span of braces with clamped ends (Gan 1996; Gan and Hall 1998). This observation suggests the possibility of efficiently, yet accurately, modeling braces by concentrating nonlinearity in short segments at the ends and at mid-span of the element.

The modified elastofiber (MEF) beam element is designed to take advantage of this observed behavior. It is divided into five segments delineated by six nodes [Figure 2.3(a)]. The two exterior nodes, 1 and 2, coincide with one of the six attachment points or one of the eight panel corners of the adjacent panel zone elements at the left and the right. The four interior nodes, 3-6, separate the two end fiber segments and the central fiber segment from the two elastic segments. Each elastic segment is thus sandwiched

between an end fiber segment and the central fiber segment. The elastic segments are elastic versions of the plastic hinge element (Krishnan and Hall 2006a), i.e., no axial yielding and no plastic hinging. The fiber segment is based on the finite element method, wherein the beam translations and rotations are interpolated linearly and independently from their nodal values, requiring a one-point integration on the shear terms to prevent locking. Each fiber segment is discretized into 20 fibers that run the entire length of the segment. Associated with each fiber is a nonlinear hysteretic stress-strain law, proposed by Hall and Challa (1995), for axial stress, σ_n, and axial strain, ϵ_n, where n denotes the n^{th} fiber. This hysteresis model defines a backbone curve [Figure 2.3(b)] consisting of a linear portion, a yield plateau, a strain-hardening region which is described by a cubic ellipse, and a strain softening region described by a continuation of the same cubic ellipse culminating in fiber rupture. The backbone curve is characterized by seven parameters: yield stress σ_y, ultimate stress σ_u, Young's modulus E, strain at initiation of strain hardening ϵ_{sh}, strain at ultimate stress ϵ_u, rupture strain ϵ_r, and the tangent modulus at initiation of strain hardening E_{sh}. Hysteresis loops [Figure 2.3(b)] consist of linear segments and cubic ellipses, and the hysteretic rules to define the cyclic response of each panel are given by (Challa 1992).

Local buckling and fracture have been observed and reported in many cyclic axial load tests on braces (Black et al. 1980; Zayas et al. 1980; Uang and Bertero 1986; Yamanouchi et al. 1989; Tremblay et al. 2003). More recently, Fell et al. tested 19 brace specimen (8 HSS sections, 8 pipe sections, and 3 wide-flange sections) subjected to near-fault and far-field cyclic loading, under the auspices of the Network for Earthquake Engineering Simulation (NEES) program (Fell et al. 2006; Fell 2008; Fell et al. 2009). They observed buckling with kinking in the gusset plates at the ends and at the brace mid-span, with increased yield localization under larger load amplitudes. This was followed by local buckling at the mid-span hinge, subsequently triggering ductile fracture. Upon further cycling, the cracks propagated across the section in a ductile manner, leading to sudden severing of the brace in a subsequent tensile excursion. In a different set of experiments on cold-formed HSS bracing members subjected to cyclic loading, Han et al. (2007) observed local buckling followed by fracture at the mid-span of specimen with low width-to-thickness ratios, and fracture at the end slotted connection in specimen with high width-thickness ratios. After local buckling, large jumps occurred in the strain-rates once the strain reached 0.015–0.030, possibly indicative of initiation of fracture. Strain measurements at and beyond local buckling cannot necessarily be relied upon due to the uncertainties in the integrity of the strain gauges at large strains. Even if the strain measurements can be made accurately, the fracture strains are likely to vary from specimen to specimen. While the MEF element formulation is not amenable to the inclusion of local buckling, a fiber fracture capability, in the form of a user-specified probabilistic description of the fracture strain, is included to approximately represent brace fracturing. At the beginning of the analysis, the fracture strains for the fibers in all the MEF elements of the model are determined as independent realizations using the corresponding user-defined probability distributions. These initial fracture strains are held constant for the entire duration of the dynamic analysis. This method was first proposed by Hall (1995, 1998) to simulate fracture of welded beam-to-column connections in moment frames, accounting for variability and uncertainty in fracture initiation strains. It should be noted that this strain is an average fiber strain over the length of the entire segment, and does not correspond to the true strain in the continuum that can get much larger locally. When the fiber strain reaches the fracture strain,

it fractures and can no longer take tension, but upon reversal of loading the fractured and separated parts can come in contact, and the fiber is able to resist compression again. This is, by design, unlike fiber rupture upon which the fiber can take no compression. Successive fracturing or rupturing of fibers can ultimately lead to complete severing of the brace. The phenomenological models of past studies incorporated fracture either by specifying the plastic rotation at fracture as a function of brace slenderness and plate width-to-thickness ratios (Tremblay 2002; Tremblay et al. 2003; Tremblay and Poncet 2005) or by transforming the axial deformation history of brace into standard cycles and assuming that the brace is fractured when the number of standard cycles exceeds a value that is dependent on the slenderness ratio, width-to-thickness ratio of the compression flange, width-to-depth ratio of the section, and the mechanical properties of steel (Tang and Goel 1989; Hassan and Goel 1991).

Assumptions in the MEF element formulation include prismatic doubly-symmetric sections, plane sections remain plane, small strains, no warping restraint, and no along-span loads. Lateral deflections relative to the chord in the two elastic segments are assumed small. Each of the six nodes of the MEF element have 6 degrees of freedom, three translational and three rotational. The interior nodes are assumed massless, and this allows for static condensation to be performed on the associated DOF, labeled 1–24 in Figure 2.3. As a result, for each MEF element, updating the $\left[K_{mef}^{l+1}\right]$ matrix and the $\left\{R_{mef}^{l+1}\right\}$ vector requires an iterative nonlinear local structural analysis, within each global iteration. The updating process is as follows. From the $\{\Delta U\}$ vector computed in global iteration l, the 12 displacement increments at the exterior nodes (1 and 2) of the MEF element are found as:

$$\{\Delta U_{mef}\}_L = \left[T_{mef}^{l}\right] \{\Delta U_{mef}\} \tag{2.3}$$

where $\{\Delta U_{ef}\}$ contains the 16 terms extracted from $\{\Delta U\}$ corresponding to the nodes J and K connected to element nodes 1 and 2, and $\left[T_{mef}^{l}\right]$ is the transformation matrix between these 16 global DOF and the 12 local DOF at nodes 1 and 2 (terms of the $\{\Delta U_{mef}\}_L$ vector) of the MEF element, calculated using the joint configuration at iteration l. The computations for the MEF element are done in the global coordinate system, XYZ, and the terms in $\{\Delta U_{mef}\}_L$ are with respect to XYZ. This transformation is carried out in three steps:

$$\{\Delta U_{mef}\} \xrightarrow{1} \{\Delta \bar{U}_{mef}\} \xrightarrow{2} \{\Delta \bar{U}_{mef}\}_L \xrightarrow{3} \{\Delta U_{mef}\}_L \,. \tag{2.4}$$

where the translational DOF in $\{\Delta U_{mef}\}$ are with respect to the global coordinate system XYZ, and the rotational DOF are with respect to the panel zone local coordinate system $\bar{X}\bar{Y}\bar{Z}$ at the nodes J and K. $\bar{Y}$ is perpendicular to panel ① of a panel zone element, $\bar{Z}$ is perpendicular to panel ② and $\bar{X}$ is along the panel intersection line $e-f$. As the panels deform, the orientation of these axes continue to change. In the first step, the translational DOF in $\{\Delta U_{mef}\}$ are transformed to the $\bar{X}\bar{Y}\bar{Z}$ coordinate system. In the second step, the eight DOF at node J are transformed to the six local beam DOF at node 1 (still in the J's $\bar{X}\bar{Y}\bar{Z}$ coordinate system), and the eight DOF at node K are transformed to the six local beam DOF at node 2 (still in the K's $\bar{X}\bar{Y}\bar{Z}$ coordinate system). The subscript L denotes the presence of the terms for the 12 DOF at MEF element local nodes 1 and 2. The third transformation converts the MEF element end displacement

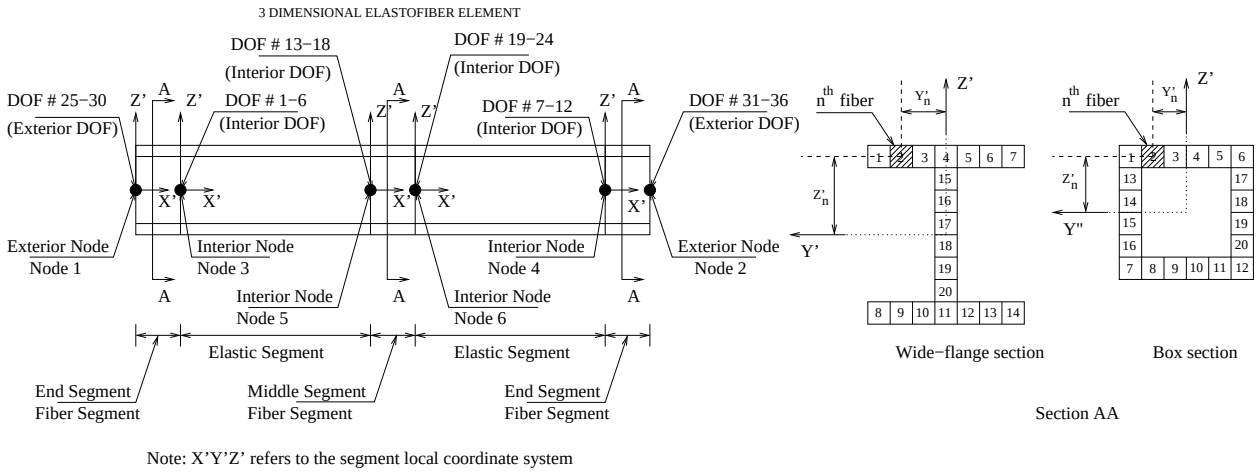

(a)

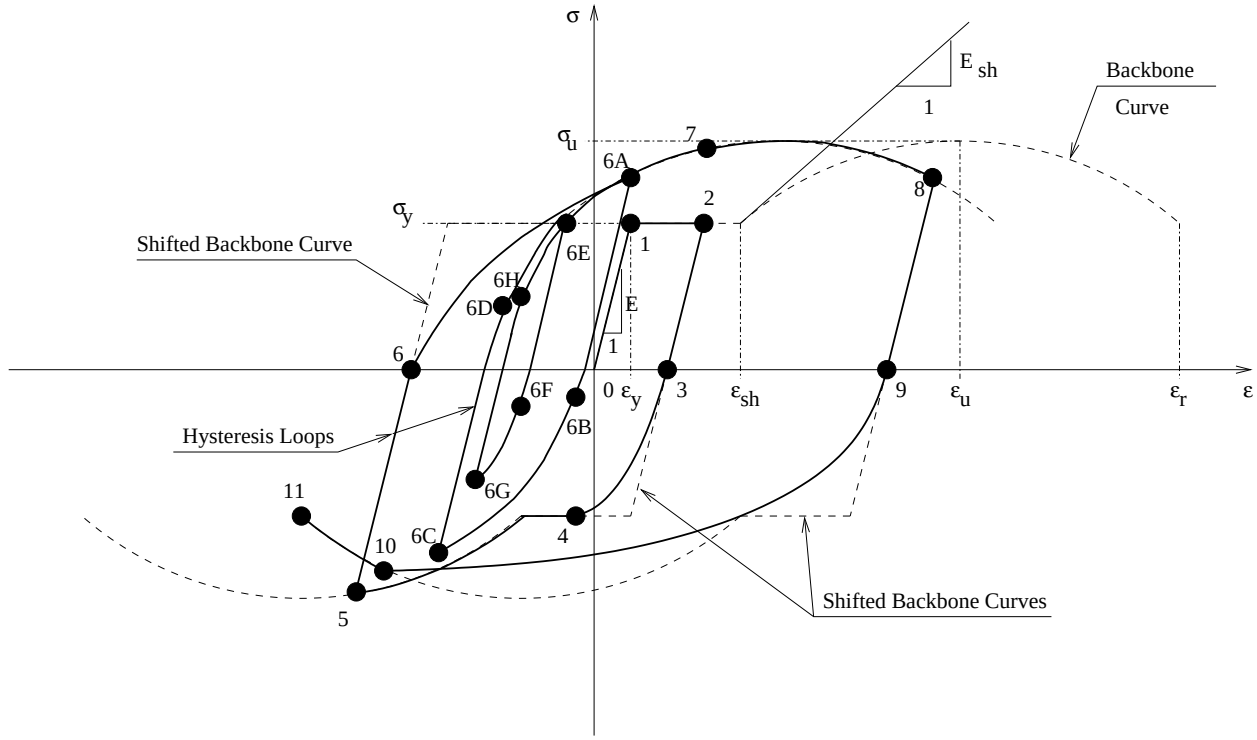

(b)

Figure 2.3: (a) Layout of the five-segment modified elastofiber element (fiber arrangement is shown for an I-section and a box section. (b) Axial stress-strain hysteresis model for each fiber.

increments from the two panel zone coordinate systems ($\bar{X}\bar{Y}\bar{Z}$) to the global coordinate system, XYZ.

Thus, the transformation matrix $\left[T^l_{mef}\right]$ can be written as the product of three transformations, $[T_1]$, $[T_2]$, and $[T_3]$:

$$[T_{mef}] = [T_3]\,[T_2]\,[T_1]\,. \tag{2.5}$$

The matrices $[T_1]$ and $[T_3]$, consisting of the direction cosines of the panel zone coordinate systems $(\bar{X}\bar{Y}\bar{Z})$ at joint nodes, are given in Krishnan and Hall (2006a). The matrix $[T_2]$ depends on the panel zone attachment/corner points to which the element local nodes 1 and 2 are connected at nodes J and K of the joint. Columns connect to attachment points e or f, beams connect to points a, b, c, or d, while braces connect to the panel corners $a-e$, $a-f$, $b-e$, $b-f$, $c-e$, $c-f$, $d-e$, or $d-f$. Thus, $[T_2]$ will be different for beams, columns, and braces. Examples of $[T_2]$ for beams and columns are given in Krishnan and Hall (2006a) and Krishnan (2003b). Constructing the $[T_2]$ matrix for braces requires determining the incremental translations of the panel corners and the incremental rotations of the lines connecting the joint nodes and the panel corners, given the incremental translations of the joint nodes, the incremental beam and column rotations associated with each panel, and the incremental twisting of the joint. The incremental translations of the corners can be deduced from the incremental translations of the attachment points a through f, given in Krishnan and Hall (2006a). The incremental rotations of the line connecting the panel corners with the joint nodes due to the beam rotations, $\Delta\theta^B_{J\bar{Y}}$ and $\Delta\theta^B_{J\bar{Z}}$, and column rotations, $\Delta\theta^C_{J\bar{Y}}$ and $\Delta\theta^C_{J\bar{Z}}$, are derived in Figures 2.4, 2.5, 2.6, and 2.7, respectively.

For a brace that is attached to node J at the panel corner $a-f$ and node K at the panel corner $b-e$, $[T_2]$ can be written as

$$[T]_2^{br(a-f):(b-e)(12\times16)} = \begin{bmatrix} \left[T^J_{a-f}\right]^{(6\times8)} & [0]^{(6\times8)} \\ [0]^{(6\times8)} & \left[T^K_{b-e}\right]^{(6\times8)} \end{bmatrix} \tag{2.6}$$

where

$$\left[T^J_{a-f}\right]^{(6\times8)} = \begin{bmatrix} 1.0 & 0.0 & 0.0 & 0.0 & 0.0 & 0.5D_J\cos\xi^{①}_J & 0.0 & 0.0 \\ 0.0 & 1.0 & 0.0 & -0.5D_J\cos\xi^{①}_J & 0.0 & 0.0 & -0.5H_J & 0.0 \\ 0.0 & 0.0 & 1.0 & 0.0 & 0.5H_J & -0.5D_J\sin\xi^{①}_J & 0.0 & 0.0 \\ 0.0 & 0.0 & 0.0 & 1.0 & 0.0 & 0.0 & 0.0 & 0.0 \\ 0.0 & 0.0 & 0.0 & 0.0 & \frac{\left(H_J+D_J\sin\eta^{①}_J\right)H_J}{{H_J}^2+{D_J}^2+2H_JD_J\sin\eta^{①}_J} & \frac{\left(D_J+H_J\sin\xi^{①}_J\right)D_J}{{H_J}^2+{D_J}^2+2H_JD_J\sin\xi^{①}_J} & 0.0 & 0.0 \\ 0.0 & 0.0 & 0.0 & 0.0 & 0.0 & 0.0 & 0.5 & 0.5 \end{bmatrix}$$

$$\left[T^K_{b-e}\right]^{(6\times8)} = \begin{bmatrix} 1.0 & 0.0 & 0.0 & 0.0 & 0.0 & -0.5D_K\cos\xi^{①}_K & 0.0 & 0.0 \\ 0.0 & 1.0 & 0.0 & 0.5D_K\cos\xi^{①}_K & 0.0 & 0.0 & 0.5H_K & 0.0 \\ 0.0 & 0.0 & 1.0 & 0.0 & -0.5H_K & 0.5D_K\sin\xi^{①}_K & 0.0 & 0.0 \\ 0.0 & 0.0 & 0.0 & 1.0 & 0.0 & 0.0 & 0.0 & 0.0 \\ 0.0 & 0.0 & 0.0 & 0.0 & \frac{\left(H_K+D_K\sin\eta^{①}_K\right)H_K}{{H_K}^2+{D_K}^2+2H_KD_K\sin\eta^{①}_K} & \frac{\left(D_K+H_K\sin\xi^{①}_K\right)D_K}{{H_K}^2+{D_K}^2+2H_KD_K\sin\xi^{①}_K} & 0.0 & 0.0 \\ 0.0 & 0.0 & 0.0 & 0.0 & 0.0 & 0.0 & 0.5 & 0.5 \end{bmatrix}$$

An incremental twist in the joint at node J leads to a translation of all the brace attachment points (panel corners) of the joint. Hence term [2,4] of the $\left[T^J_{a-f}\right]$ matrix is $-0.5D_J\cos\xi^{①}_J$. Likewise, an incremental beam rotation, $\Delta\theta^B_{K\bar{Y}}$, of panel ① at node K leads to an incremental brace rotation, $\Delta\theta^{Br}_{K\bar{Y}}$, as shown in Figure 2.4. Hence term [5,4] of the $\left[T^K_{a-f}\right]$ matrix is $\frac{\left(H_K+D_K\sin\eta^{①}_K\right)H_K}{{H_K}^2+{D_K}^2+2H_KD_K\sin\eta^{①}_K}$.

Similarly, for a brace that is attached to node J at the panel corner $a-e$ and node K at the panel corner

$b-f$, $[T_2]$ can be written as

$$[T]_2^{br(a-e):(b-f)(12\times16)} = \begin{bmatrix} \left[T^J_{a-e}\right]^{(6\times8)} & [0]^{(6\times8)} \\ [0]^{(6\times8)} & \left[T^K_{b-f}\right]^{(6\times8)} \end{bmatrix} \tag{2.7}$$

where

$$\left[T^J_{a-e}\right]^{(6\times8)} = \begin{bmatrix} 1.0 & 0.0 & 0.0 & 0.0 & 0.0 & 0.5D_J\cos\xi_J^{①} & 0.0 & 0.0 \\ 0.0 & 1.0 & 0.0 & -0.5D_J\cos\xi_J^{①} & 0.0 & 0.0 & 0.5H_J & 0.0 \\ 0.0 & 0.0 & 1.0 & 0.0 & -0.5H_J & -0.5D_J\sin\xi_J^{①} & 0.0 & 0.0 \\ 0.0 & 0.0 & 0.0 & 1.0 & 0.0 & 0.0 & 0.0 & 0.0 \\ 0.0 & 0.0 & 0.0 & 0.0 & \frac{\left(H_J-D_J\sin\eta_J^{①}\right)H_J}{{H_J}^2+{D_J}^2-2H_JD_J\sin\eta_J^{①}} & \frac{\left(D_J-H_J\sin\xi_J^{①}\right)D_J}{{H_J}^2+{D_J}^2-2H_JD_J\sin\xi_J^{①}} & 0.0 & 0.0 \\ 0.0 & 0.0 & 0.0 & 0.0 & 0.0 & 0.0 & 0.5 & 0.5 \end{bmatrix}$$

$$\left[T^K_{b-f}\right]^{(6\times8)} = \begin{bmatrix} 1.0 & 0.0 & 0.0 & 0.0 & 0.0 & -0.5D_K\cos\xi_K^{①} & 0.0 & 0.0 \\ 0.0 & 1.0 & 0.0 & 0.5D_K\cos\xi_K^{①} & 0.0 & 0.0 & -0.5H_K & 0.0 \\ 0.0 & 0.0 & 1.0 & 0.0 & 0.5H_K & 0.5D_K\sin\xi_K^{①} & 0.0 & 0.0 \\ 0.0 & 0.0 & 0.0 & 1.0 & 0.0 & 0.0 & 0.0 & 0.0 \\ 0.0 & 0.0 & 0.0 & 0.0 & \frac{\left(H_K-D_K\sin\eta_K^{①}\right)H_K}{{H_K}^2+{D_K}^2-2H_KD_K\sin\eta_K^{①}} & \frac{\left(D_K-H_K\sin\xi_K^{①}\right)D_K}{{H_K}^2+{D_K}^2-2H_KD_K\sin\xi_K^{①}} & 0.0 & 0.0 \\ 0.0 & 0.0 & 0.0 & 0.0 & 0.0 & 0.0 & 0.5 & 0.5 \end{bmatrix}$$

For a brace that is connected to panel ② of node J at corner $c-f$, and to panel ② of node K at corner $d-e$, $[T_2]$ can be written as,

$$[T]_2^{br(c-f):(d-e)(12\times16)} = \begin{bmatrix} \left[T^J_{c-f}\right]^{(6\times8)} & [0]^{(6\times8)} \\ [0]^{(6\times8)} & \left[T^K_{d-e}\right]^{(6\times8)} \end{bmatrix} \tag{2.8}$$

where

$$\left[T^J_{c-f}\right]^{(6\times8)} = \begin{bmatrix} 1.0 & 0.0 & 0.0 & 0.0 & 0.0 & 0.0 & 0.0 & -0.5W_J\cos\xi_J^{②} \\ 0.0 & 1.0 & 0.0 & 0.0 & 0.0 & 0.0 & -0.5H_J & -0.5W_J\sin\xi_J^{②} \\ 0.0 & 0.0 & 1.0 & 0.5W_J\cos\xi_J^{②} & 0.5H_J & 0.0 & 0.0 & 0.0 \\ 0.0 & 0.0 & 0.0 & 1.0 & 0.0 & 0.0 & 0.0 & 0.0 \\ 0.0 & 0.0 & 0.0 & 0.0 & 0.5 & 0.5 & 0.0 & 0.0 \\ 0.0 & 0.0 & 0.0 & 0.0 & 0.0 & 0.0 & \frac{\left(H_J-W_J\sin\eta_J^{②}\right)H_J}{{H_J}^2+{W_J}^2-2H_JW_J\sin\eta_J^{②}} & \frac{\left(W_J-H_J\sin\xi_J^{②}\right)W_J}{{H_J}^2+{W_J}^2-2H_JW_J\sin\xi_J^{②}} \end{bmatrix}$$

$$\left[T^K_{d-e}\right]^{(6\times8)} = \begin{bmatrix} 1.0 & 0.0 & 0.0 & 0.0 & 0.0 & 0.0 & 0.0 & 0.5W_K\cos\xi_K^{②} \\ 0.0 & 1.0 & 0.0 & 0.0 & 0.0 & 0.0 & 0.5H_K & 0.5W_K\sin\xi_K^{②} \\ 0.0 & 0.0 & 1.0 & -0.5W_K\cos\xi_K^{②} & -0.5H_K & 0.0 & 0.0 & 0.0 \\ 0.0 & 0.0 & 0.0 & 1.0 & 0.0 & 0.0 & 0.0 & 0.0 \\ 0.0 & 0.0 & 0.0 & 0.0 & 0.5 & 0.5 & 0.0 & 0.0 \\ 0.0 & 0.0 & 0.0 & 0.0 & 0.0 & 0.0 & \frac{\left(H_K-W_K\sin\eta_K^{②}\right)H_K}{{H_K}^2+{W_K}^2-2H_KW_K\sin\eta_K^{②}} & \frac{\left(W_K-H_K\sin\xi_K^{②}\right)W_K}{{H_K}^2+{W_K}^2-2H_KW_K\sin\xi_K^{②}} \end{bmatrix}$$

Similarly, for a brace that is connected to panel ② of node J at corner $c-e$, and to panel ② of node K

at corner $d-f$, $[T_2]$ can be written as,

$$[T]_2^{br(c-f):(d-e)(12\times16)} = \begin{bmatrix} \left[T^J_{c-e}\right]^{(6\times8)} & [0]^{(6\times8)} \\ [0]^{(6\times8)} & \left[T^K_{d-f}\right]^{(6\times8)} \end{bmatrix} \tag{2.9}$$

where

$$\left[T^J_{c-e}\right]^{(6\times8)} = \begin{bmatrix} 1.0 & 0.0 & 0.0 & 0.0 & 0.0 & 0.0 & 0.0 & -0.5W_J\cos\xi_J^{②} \\ 0.0 & 1.0 & 0.0 & 0.0 & 0.0 & 0.0 & 0.5H_J & -0.5W_J\sin\xi_J^{②} \\ 0.0 & 0.0 & 1.0 & 0.5W_J\cos\xi_J^{②} & -0.5H_J & 0.0 & 0.0 & 0.0 \\ 0.0 & 0.0 & 0.0 & 1.0 & 0.0 & 0.0 & 0.0 & 0.0 \\ 0.0 & 0.0 & 0.0 & 0.0 & 0.5 & 0.5 & 0.0 & 0.0 \\ 0.0 & 0.0 & 0.0 & 0.0 & 0.0 & 0.0 & \frac{\left(H_J+W_J\sin\eta_J^{②}\right)H_J}{{H_J}^2+{W_J}^2+2H_JW_J\sin\eta_J^{②}} & \frac{\left(W_J+H_J\sin\xi_J^{②}\right)W_J}{{H_J}^2+{W_J}^2+2H_JW_J\sin\xi_J^{②}} \end{bmatrix}$$

$$\left[T^K_{d-f}\right]^{(6\times8)} = \begin{bmatrix} 1.0 & 0.0 & 0.0 & 0.0 & 0.0 & 0.0 & 0.0 & 0.5W_K\cos\xi_K^{②} \\ 0.0 & 1.0 & 0.0 & 0.0 & 0.0 & 0.0 & -0.5H_K & 0.5W_K\sin\xi_K^{②} \\ 0.0 & 0.0 & 1.0 & -0.5W_K\cos\xi_K^{②} & 0.5H_K & 0.0 & 0.0 & 0.0 \\ 0.0 & 0.0 & 0.0 & 1.0 & 0.0 & 0.0 & 0.0 & 0.0 \\ 0.0 & 0.0 & 0.0 & 0.0 & 0.5 & 0.5 & 0.0 & 0.0 \\ 0.0 & 0.0 & 0.0 & 0.0 & 0.0 & 0.0 & \frac{\left(H_K+W_K\sin\eta_K^{②}\right)H_K}{{H_K}^2+{W_K}^2+2H_KW_K\sin\eta_K^{②}} & \frac{\left(W_K+H_K\sin\xi_K^{②}\right)W_K}{{H_K}^2+{W_K}^2+2H_KW_K\sin\xi_K^{②}} \end{bmatrix}$$

The $[T_2]$ matrix for other brace attachment combinations can be easily deduced taking appropriate combinations of the $[T_{a-e}]$, $[T_{a-f}]$, $[T_{b-e}]$, $[T_{b-f}]$, $[T_{c-e}]$, $[T_{c-f}]$, $[T_{d-e}]$, and $[T_{d-f}]$ matrices.

At the end of global iteration l, the panel zone element geometries are updated as described in reference (Krishnan and Hall 2006a), the updated matrices, $\left[T_1^{l+1}\right]$, $\left[T_2^{l+1}\right]$, and $\left[T_3^{l+1}\right]$, are computed, and the modified elastofiber element transformation matrix is updated as

$$\left[T_{mef}^{l+1}\right] = \left[T_3^{l+1}\right]\left[T_2^{l+1}\right]\left[T_1^{l+1}\right]. \tag{2.10}$$

Next, the displacement increments $\{\Delta U_{mef}\}_L$ are applied to nodes 1 and 2 of the MEF element, and the resulting displacements of the interior nodes, 3–6, are computed by an iterative structural analysis. In the k^{th} iteration of this process (iteration (k) where the $()$ denotes element iterations within global iteration l), the equation to be solved is

$$\begin{bmatrix} K_{T,II}^{(k)} & K_{T,IE}^{(k)} \\ K_{T,EI}^{(k)} & K_{T,EE}^{(k)} \end{bmatrix} \begin{Bmatrix} \Delta U_I \\ \Delta U_E \end{Bmatrix} = \begin{Bmatrix} 0 \\ F_E \end{Bmatrix} - \begin{Bmatrix} R_I^{(k)} \\ R_E^{(k)} \end{Bmatrix} \tag{2.11}$$

which has been partitioned into the 24 DOF group I at the interior nodes 3–6, and the 12 DOF group E at the end nodes 1 and 2, where

$$\begin{bmatrix} K_{T,II}^{(k)} & K_{T,IE}^{(k)} \\ K_{T,EI}^{(k)} & K_{T,EE}^{(k)} \end{bmatrix} \text{ and } \begin{Bmatrix} R_I^{(k)} \\ R_E^{(k)} \end{Bmatrix}$$

are the tangent stiffness matrix and stiffness force vector for configuration (k) respectively; $\{F_E\}$ is a vector of unknown loads applied to the element through nodes 1 and 2 by the surrounding structure; and $\{\Delta U_E\}$

is set to $\{\Delta U_{mef}\}_L$ for iteration $(k) = 1$ and to 0 for iteration $(k) > 1$. Eq. 2.11 is solved for $\{\Delta U_I\}$ by substituting in the known vector $\{\Delta U_E\}$ and then solving the upper partitioned equation, which does not involve $\{F_E\}$. The $\{\Delta U_I\}$ so computed is used to update the locations of the four element interior nodes. This geometric updating is critical for simulating large-deformation processes such as buckling. Using the updated configuration (and the updated segment local coordinate systems), the $\left[K'_{T,s}\right]$ and $\{R'_s\}$ are computed for each of the five segments as described in Krishnan and Hall (2006b), and assembled into the MEF element matrix $\begin{bmatrix} K_{T,II} & K_{T,IE} \\ K_{T,EI} & K_{T,EE} \end{bmatrix}$ and vector $\begin{Bmatrix} R_I \\ R_E \end{Bmatrix}$, respectively. For the three fiber segments, the incremental fiber strains are calculated from the incremental segment node displacements and rotations. If the beam ends are pinned ended, the contribution from the rotations is not included. For partially continuous connections, this contribution is scaled by two user-specified fixity factors (one for each end) ranging from zero to one, with zero corresponding to a perfectly pinned condition and one corresponding to full continuity. Using the fiber material model, and its axial stress-strain history, the fiber axial stress is updated, and the new axial forces and bending moments at mid-length of the segments are computed. Shear forces, which are assumed constant along the beam at their values at segment mid-length to prevent shear locking, and twisting moments are also updated at this time. Using the values of internal forces at mid-length, the segment nodal forces are computed and assembled into $\{R'_s\}$. For the middle segment, $\left\{R_s^{'(k+1)}\right\}$ and $\left[K_{T,s}^{'(k+1)}\right]$ are found by the procedure used for the plastic hinge element except that no plastic hinges are allowed to form (Krishnan and Hall 2006a).

MEF element local iterations continue to convergence to the global $l+1$ state at which point the tangent stiffness matrix and stiffness force vector are denoted by

$$\begin{bmatrix} K_{T,II}^{l+1} & K_{T,IE}^{l+1} \\ K_{T,EI}^{l+1} & K_{T,EE}^{l+1} \end{bmatrix} \text{and} \begin{Bmatrix} R_I^{l+1} \\ R_E^{l+1} \end{Bmatrix}.$$

These are used to start the MEF element analysis at $(k) = 1$ after global iteration $l+1$.

The contributions to the global $\left[K_T^{l+1}\right]$ and $\left\{R^{l+1}\right\}$ are obtained from the $l+1$ tangent stiffness matrix and stiffness force vector by condensing out the I degrees of freedom:

$$\left[K_{T,mef}^{l+1}\right]_L = \left[K_{T,EE}^{l+1}\right] - \left[K_{T,EI}^{l+1}\right]\left[K_{T,II}^{l+1}\right]^{-1}\left[K_{T,IE}^{l+1}\right] \tag{2.12}$$

$$\left\{R_{mef}^{l+1}\right\}_L = \left\{R_E^{l+1}\right\} - \left[K_{T,EI}^{l+1}\right]\left[K_{T,II}^{l+1}\right]^{-1}\left\{R_I^{l+1}\right\} \tag{2.13}$$

and then transformation to

$$\left[K_{T,mef}^{l+1}\right] = \left[T_{mef}^{l+1}\right]^T\left[K_{T,mef}^{l+1}\right]_L\left[T_{mef}^{l+1}\right] \tag{2.14a}$$

$$\left\{R_{mef}^{l+1}\right\} = \left[T_{mef}^{l+1}\right]^T\left\{R_{mef}^{l+1}\right\}_L. \tag{2.14b}$$

These are assembled into $\left[K_T^{l+1}\right]$ and $\left\{R^{l+1}\right\}$.

2.2 Modeling Considerations

1. **Gusset Plate Yielding:** In cyclic loading tests on braces connected to supports through gusset plates, it has been observed that the gusset plates yield due to out-of-plane bending after just a few cycles. This causes the brace support condition to transition from a fixed end condition to a pinned end condition. The bending of gusset plates can be approximately modeled by matching the moment capacity of the gusset with a portion of the flange fibers of the end segments of the MEF element and zeroing the areas of the remaining fibers in the flanges. Another alternative is to use end-fixity factors smaller than unity.

2. **Initial Geometric Imperfection:** The interior nodes of the middle fiber segment of the MEF element are initially displaced laterally based upon a user-specified major and/or minor direction eccentricity. This initial geometric imperfection can be input as a percentage of the length of the member. During the member iterations, the coordinates of the interior nodes are constantly updated starting from this imperfect initial configuration.

3. **Residual Stresses:** Differential cooling results in nonuniform residual stresses in steel sections. Residual stresses can be easily incorporated into the MEF element by shifting the fiber stress-strain curve along the strain axis until the residual stress level is located at zero strain. Various levels of residual stresses can be assigned to various fibers of a fiber segment. However, this feature has not been incorporated in the current version of FRAME3D.

4. **Loading history:** In a series of cyclic axial loading experiments on 24 structural steel struts, Black et al. (1980) observed significantly different buckling loads for two identical specimen, one initially loaded and caused to yield in tension, and the other initially loaded in compression. They attributed this behavior to the Bauschinger effect, that caused the stress-strain diagram in compression to be significantly rounded, reducing the elastic range of response. The MEF element will be able to approximately capture this effect since the hysteresis loops [Figure 2.3(b)] of the fiber axial stress-strain behavior consist of linear segments upon unloading to zero stress and cubic ellipses for further continuation of loading in the reverse direction.

2.3 Calibration and Validation

The fiber segment length of the MEF element needs calibration, and a general criterion that is applicable to different types of cross-sections, slenderness ratios, and support conditions is to be established. There are various aspects to the axial cyclic behavior of struts that can be impacted by the fiber segment length which limits the extent of the buckled region of the strut, including elastic critical buckling load, buckling loads in subsequent compressive cycles (elastic post-buckling degradation of the member), post-buckling inelastic behavior of strut (axial and lateral deformation, peak tension, tension capacity degradation, and cycles to local buckling and fracture/rupture/severing of the strut). Of these, except for the elastic critical buckling load, all other aspects are affected by mechanical properties of steel distinct from modulus of elasticity

(yield strain, ultimate/rupture strain, fracture strain, yield stress, ultimate stress, and the evolution of strain hardening). Elastic critical buckling load depends on the simulated buckling mode shape which is sampled by the interior nodes, hence the sole dependence on the location of the interior nodes (i.e., dependence on the fiber segment length). Thus, the generalized criterion for the selection of the fiber segment length in MEF elements is derived solely from its ability to predict the elastic critical buckling load for various cross-sections, slenderness ratios, and support conditions. This is described in the next chapter.

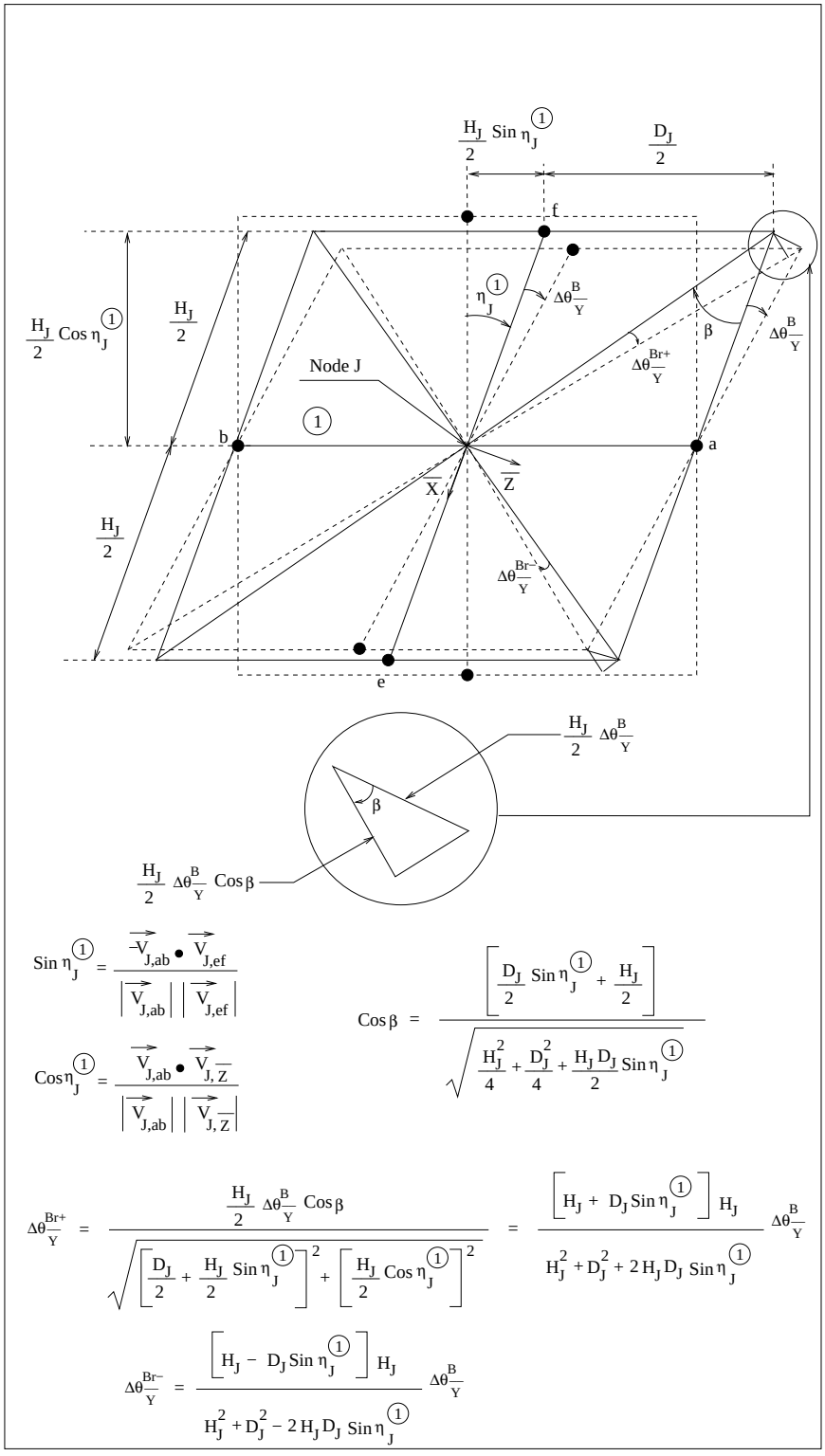

Figure 2.4: The incremental beam rotation, $\Delta\theta^B_{J\bar{Y}}$, lead to incremental rotations of the lines connecting the node J to the brace attachment points, corners $a-e$, $a-f$, $b-e$, and $b-f$ of panel ①, in addition to incremental translation of these corners. Shown here is the deformed geometry of the panel, and the derivation of the resulting incremental brace rotations, needed for the construction of the $[T_2]$ transformation for a brace.

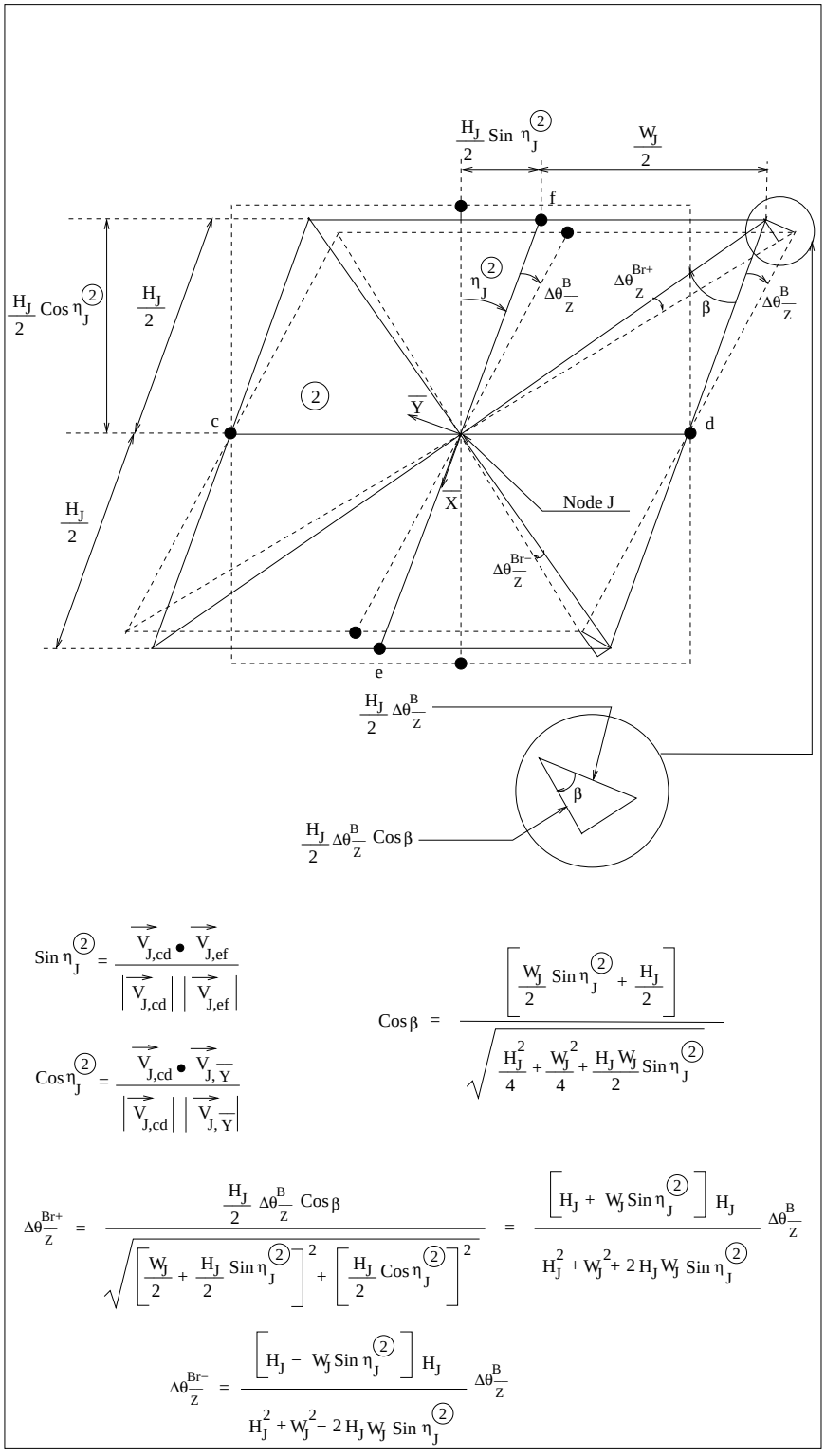

Figure 2.5: The incremental beam rotation, $\Delta\theta^B_{J\bar{Z}}$, lead to incremental rotations of the lines connecting the node J to the brace attachment points, corners $c-e$, $c-f$, $d-e$, and $d-f$ of panel ②, respectively, in addition to incremental translation of these corners. Shown here is the deformed geometry of the panel, and the derivation of the resulting incremental brace rotations, needed for the construction of the $[T_2]$ transformation for a brace.

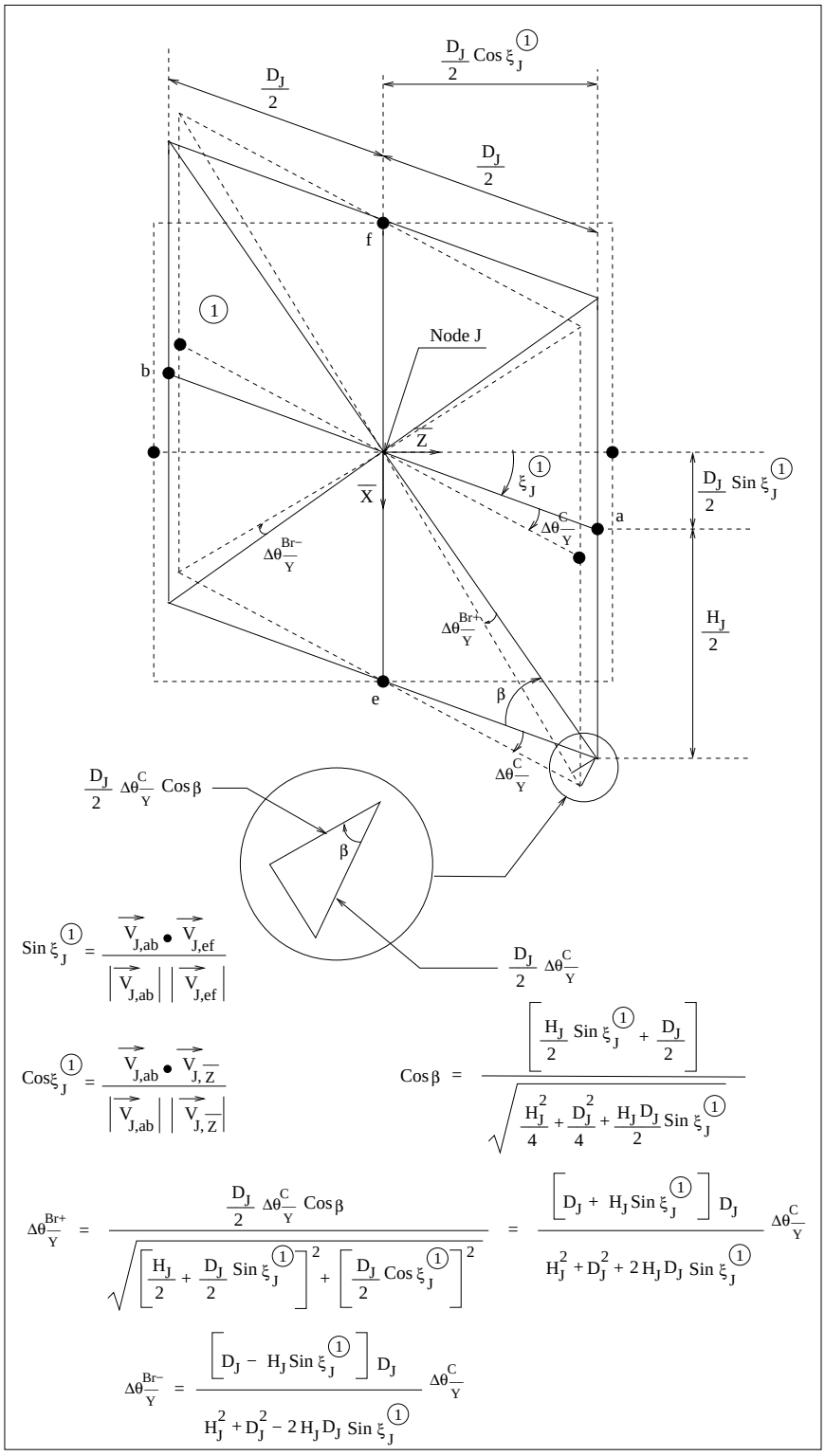

Figure 2.6: The column rotation, $\Delta\theta^{C}_{J\bar{Y}}$, leads to incremental rotations of the lines connecting the node J to the brace attachment points, corners $a-e$, $a-f$, $b-e$, and $b-f$ of panel ①, in addition to incremental translation of these corners. This figure illustrates the deformed geometry of the panel, and the resulting incremental brace rotations, needed for the construction of the $[T_2]$ transformation for a brace.

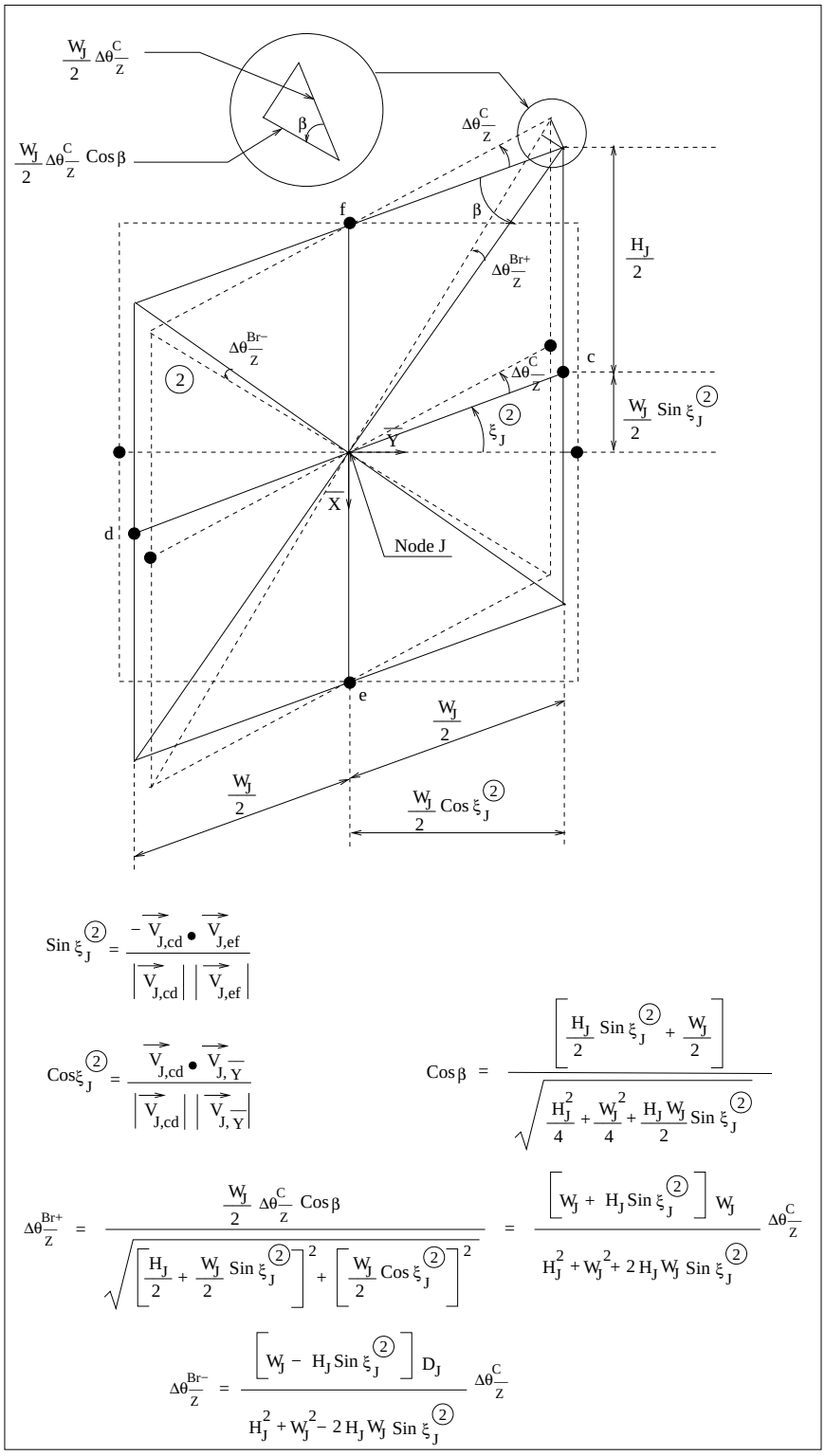

Figure 2.7: The column rotation, $\Delta\theta^C_{J\bar{Z}}$, leads to incremental rotations of the lines connecting the node J to the brace attachment points, corners $c-e$, $c-f$, $d-e$, and $d-f$ of panel ②, in addition to incremental translation of these corners. This figure illustrates the deformed geometry of the panel, and the resulting incremental brace rotations, needed for the construction of the $[T_2]$ transformation for a brace.

Chapter 3 Elastic Buckling of Struts and the Selection of Middle Segment Length

The Euler elastic critical buckling load for pinned ended members, fixed ended members, and members with one end pinned and one end fixed is $\pi^2 EI/L^2$, $4\pi^2 EI/L^2$, and $2.0466\pi^2 EI/L^2$, respectively. A single MEF element is used to model idealized struts with varying geometry, axially loaded in monotonically increasing compression. The struts are made of box (B8x8x3/16, B10x10x5/16, B12x12x7/16, and B14x14x1/2) and wide-flange (W8x20, W10x39, W12x72, and W14x90) sections, with varying slenderness ratios (L/r = 40, 80, 120, 160 and 200), and support conditions (pinned-pinned, pinned-fixed, and fixed-fixed). All the members are specified with large yield stresses such that they remain elastic until buckling. A fiber segment length of 2% of the element length gives the best predictions for the elastic critical buckling load, with over-prediction in roughly half the cases and under-prediction in the remaining cases. The ratio of the computed elastic critical buckling load, P_{cr}, to the theoretical Euler buckling load for various KL/r ratios is shown on Figure 3.1 (note that K is 1.0 for pinned-pinned condition, 0.5 for fixed-fixed condition, and 0.699 for fixed-pinned condition). Prediction errors are under 3% in most cases with errors up to -11.5% in cases with the low KL/r of 20.

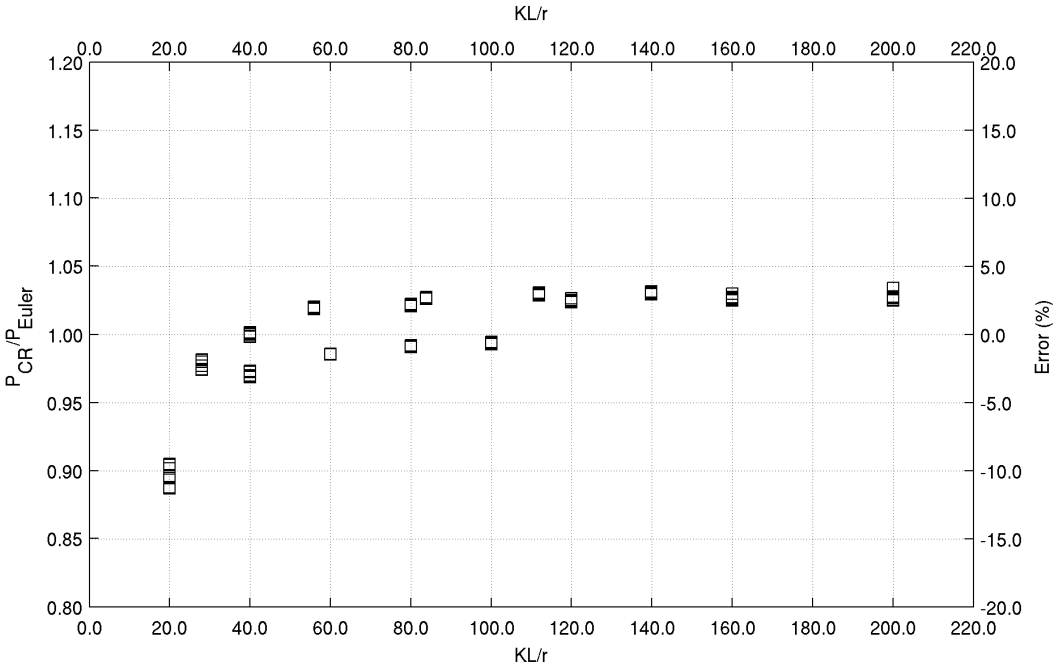

(a)

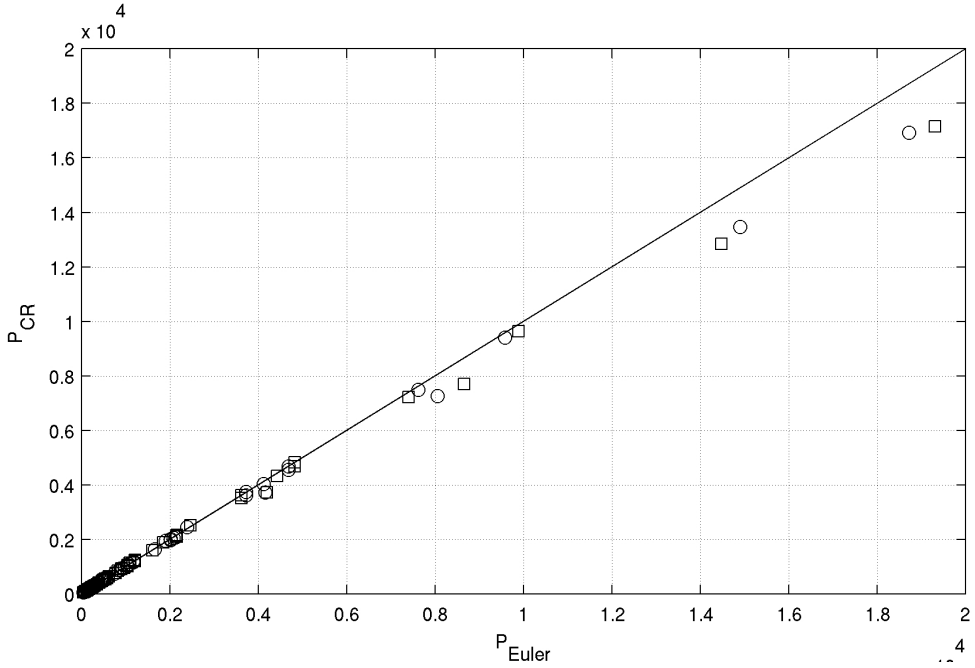

(b)

Figure 3.1: Calibration of fiber segment length for MEF elements: (a) Ratio of elastic critical buckling load, predicted using MEF elements with fiber segment length of 2% of the element length, to the theoretical Euler buckling load plotted as a function of KL/r (four box sections, four wide-flange sections, five slenderness ratios and three support conditions give rise to 120 possible combinations; plotted here are 120 points corresponding to each of these 120 cases). Prediction errors are roughly equally distributed about zero. Except for cases with very small effective slenderness ratios, errors are below 3%. (b) Predicted elastic critical buckling loads plotted against the theoretical Euler buckling load for each of the 120 cases. The diagonal line represents zero prediction error.

Chapter 4 Modeling the Elastic Post-Buckling Behavior of the Koiter-Roorda Frame

The ability of the MEF element to accurately simulate elastic post-buckling behavior is investigated by modeling the L-shaped Koiter-Roorda frame, that severely distorts due to column buckling under persistently growing corner loading, using a single MEF element to model either leg of the frame. Approximate analytical solutions are available in the literature for convenient performance assessment.

4.1 The Koiter-Roorda Frame

The L-shaped frame shown in Figure 4.1 is loaded by a vertical force P at a small horizontal eccentricity e relative to the corner. The bars of the frame are of equal length and have equal uniform bending rigidities EI. Two buckling modes exist for the frame as shown in the figure. Simple free-body diagrams of the joint suggest three clear reasons for the inward buckling mode (shown in (c)) to be favored: (i) larger column axial force in this mode; (ii) beam is in compression in this mode reducing the flexural stiffness; (iii) curvature of the beam is smaller in this mode selectively facilitating this mode over the outward buckling mode. The asymmetric elastic buckling of this frame was first illustrated by Koiter (1967), who provided solution for the evolution of the corner rotation as a function of the applied axial load. Roorda (1965) experimentally confirmed this result. Since then numerous approximate analytical solutions have been proposed (Kounadis 1985; Bazant and Cedolin 1989; Bazant and Cedolin 2003). Numerical solutions using multiple elements to represent each bar (Bazant and El Nimeiri 1973), as well as semi-analytical solutions (Rizzi et al. 1980; Poulsen and Damkilde 1998; Silvestre and Camotim 2005) have been investigated. Here, this frame is modeled using a single MEF element for each of the two bars. Multiple cases have been studied (box sections, B8x8x3/16 and B12x12x7/16; wide-flange sections, W10x39 and W14x90; bar slenderness ratios L/r=40, 80, 120, 160 and 200; applied load eccentricity e=0.001L, 0.01L and 0.05L). Shown in Figure 4.2(a) is the comparison of the numerical solution against the approximate analytical second-order solution proposed by Bazant and Cedolin (1989) for the corner elastic rotation as a function of the axial force normalized by the critical buckling load of the perfect frame ($P_{CR} = 1.407\pi^2 EI/L^2$), for one of the cases. The single-MEF-element solution does quite well for reasonably large corner rotations. The smaller the applied loading eccentricity, the better the MEF element solution. The in-plane horizontal displacement of the corner is shown plotted in Figure 4.2(b) to provide some insight into the extent of frame deformation until which the numerical solution is accurate. The results are excellent for corner displacements up to about 15%L, and they are satisfactory up to corner displacements of about 40%L. Similar results are found for all other cases (Appendix A).

The evolution of the deformed shape of the frame with increasing vertical load is shown in Figures 4.3 through 4.6. The inward buckling mode shape is realized in the numerical solution, as warranted by the

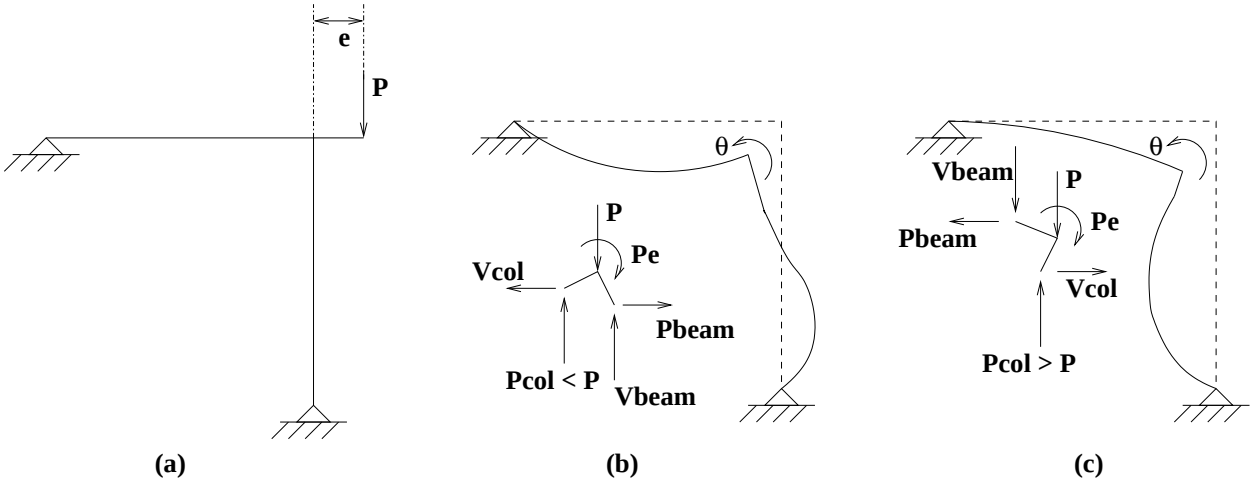

Figure 4.1: (a) Undeformed geometry of the L-shaped Koiter-Roorda frame eccentrically loaded at the corner. Two possible buckling modes, shown in (b) and (c), exist (after Bazant and Cedolin). The force equilibrium at the joint is shown for both cases. Buckling to the left (mode shown in (c)) is favored for the following reasons: the column axial force is smaller than P in (b) whereas it is larger in (c); the beam is in tension in (b) increasing the stiffness whereas it is in compression in (c) lowering its stiffness; and beam curvature in (b) is greater than that in (c).

theory. While the mode shape is not (and indeed cannot be) exact, the approximation is quite satisfactory, especially in light of the numerical efficiency achieved as a result of the use of a single element to model either bar.

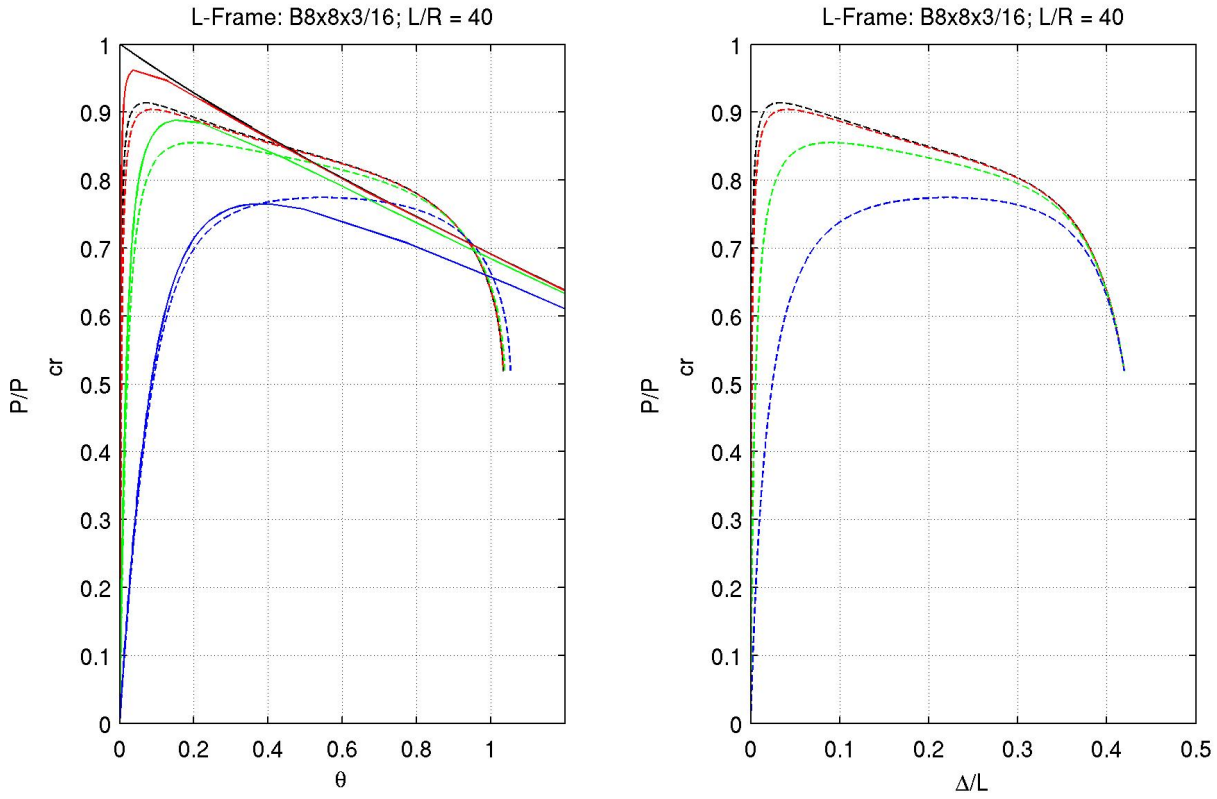

(a) (b)

Figure 4.2: Comparison of the numerical solution using MEF elements (dashed lines) against a second-order analytical solution (solid lines) for the L-shaped Koiter-Roorda frame with a downward force (P) acting at the corner (black), or at eccentricities of e/L=0.001 (red), 0.01 (green), and 0.05 (blue): Case 1: TS8x8x3/16, L/R=40) – (a) Corner rotation versus P/P_{CR}; (b) Corner in-plane lateral displacement versus P/P_{CR}.

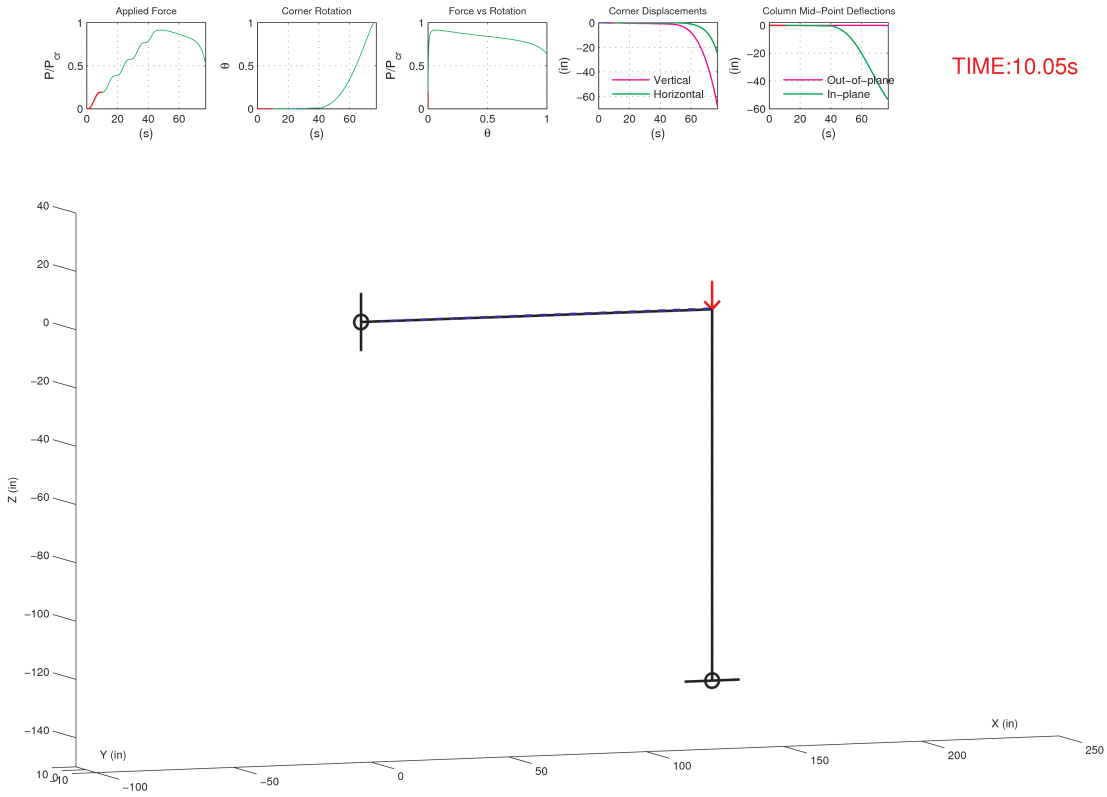

(a)

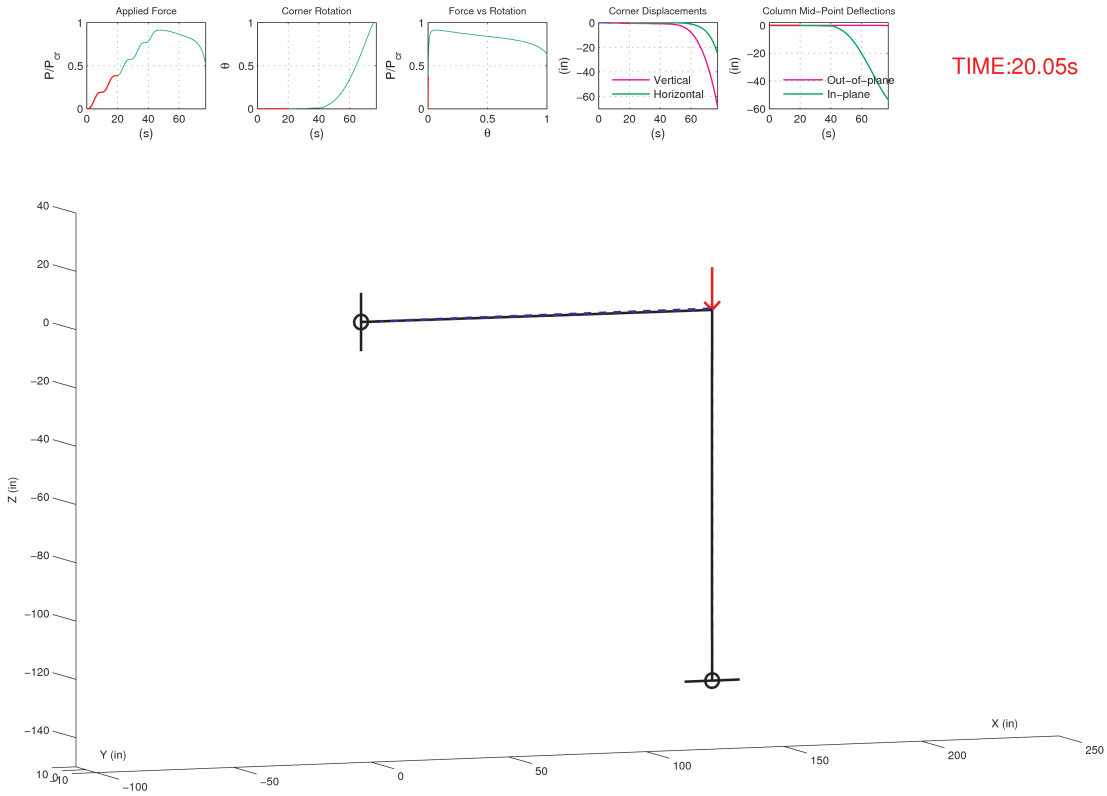

(b)

Figure 4.3: Deformed shape of TS8x8x3/16, L/R=40 frame at various levels of corner loading (zero eccentricity). The applied force history, corner rotation and displacement histories, and column mid-point deflection history for the TS8x8x3/16, L/R=40 case are also shown.

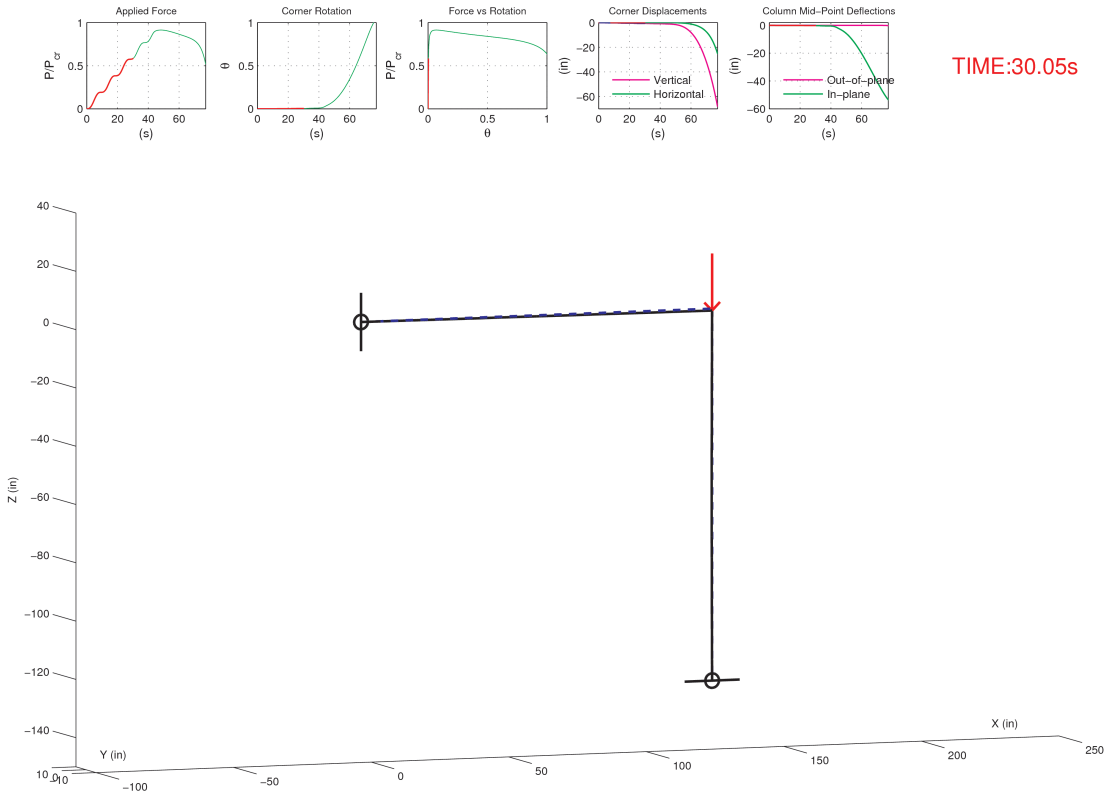

(a)

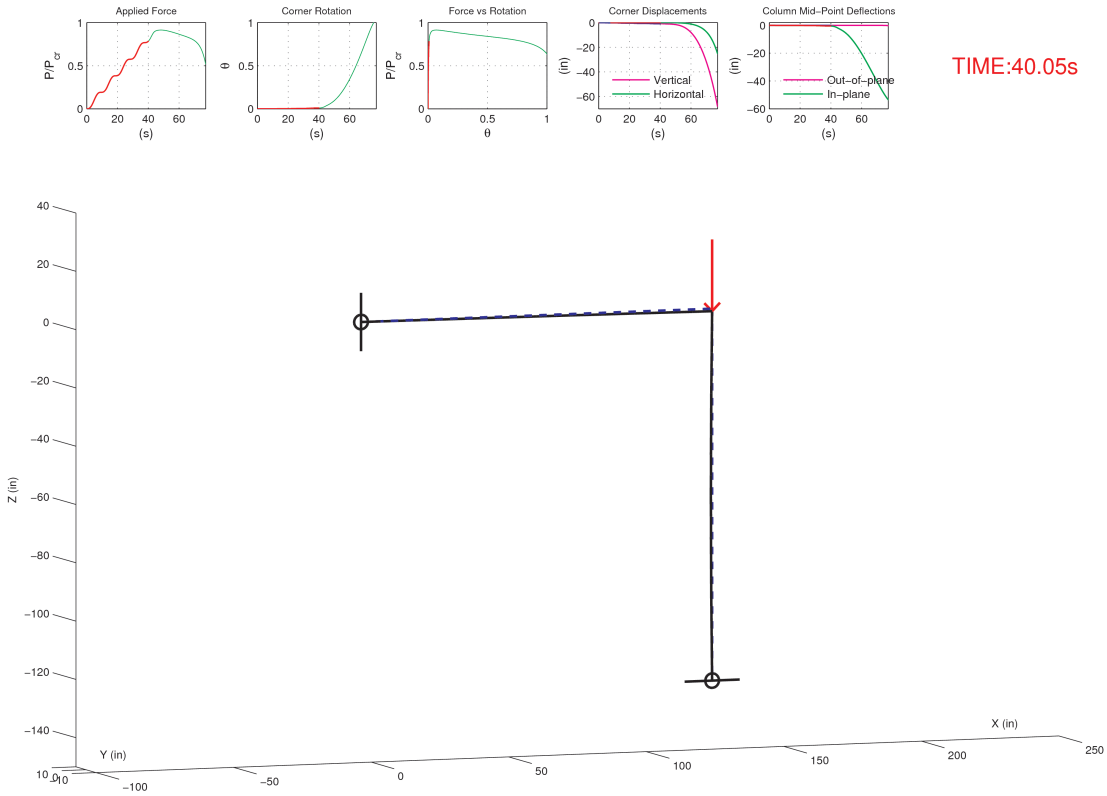

(b)

Figure 4.4: Deformed shape of TS8x8x3/16, L/R=40 frame at various levels of corner loading (zero eccentricity).

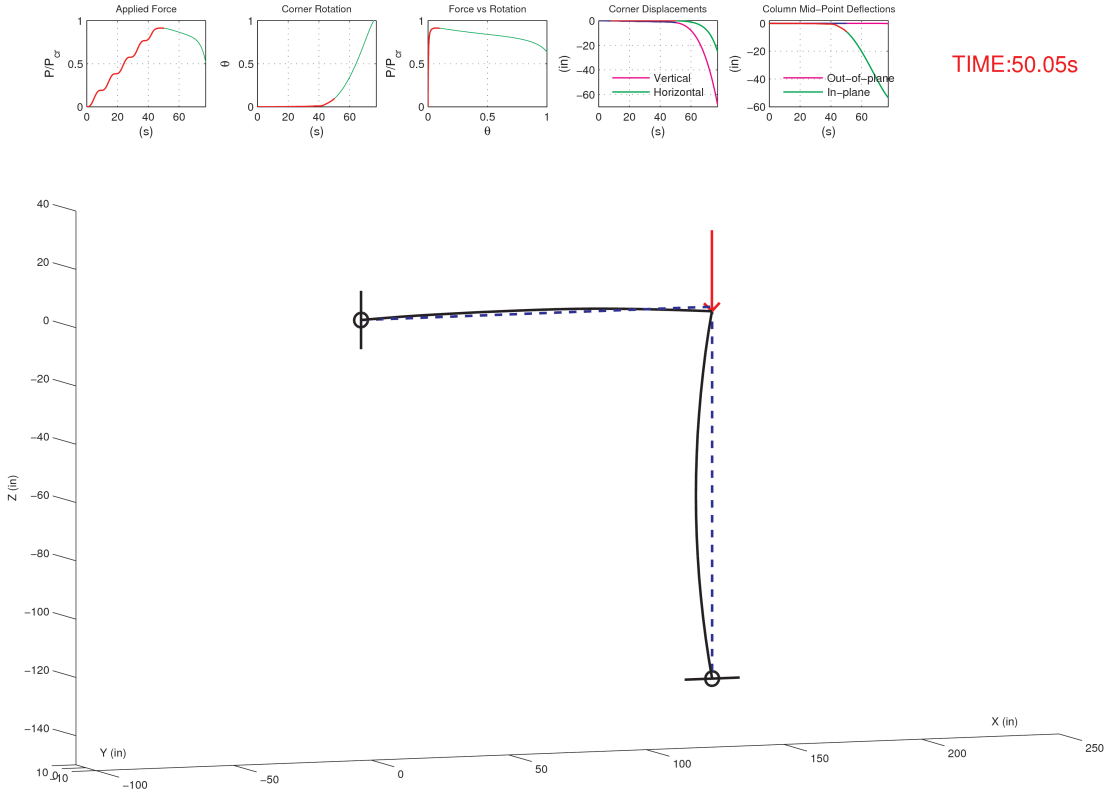

(a)

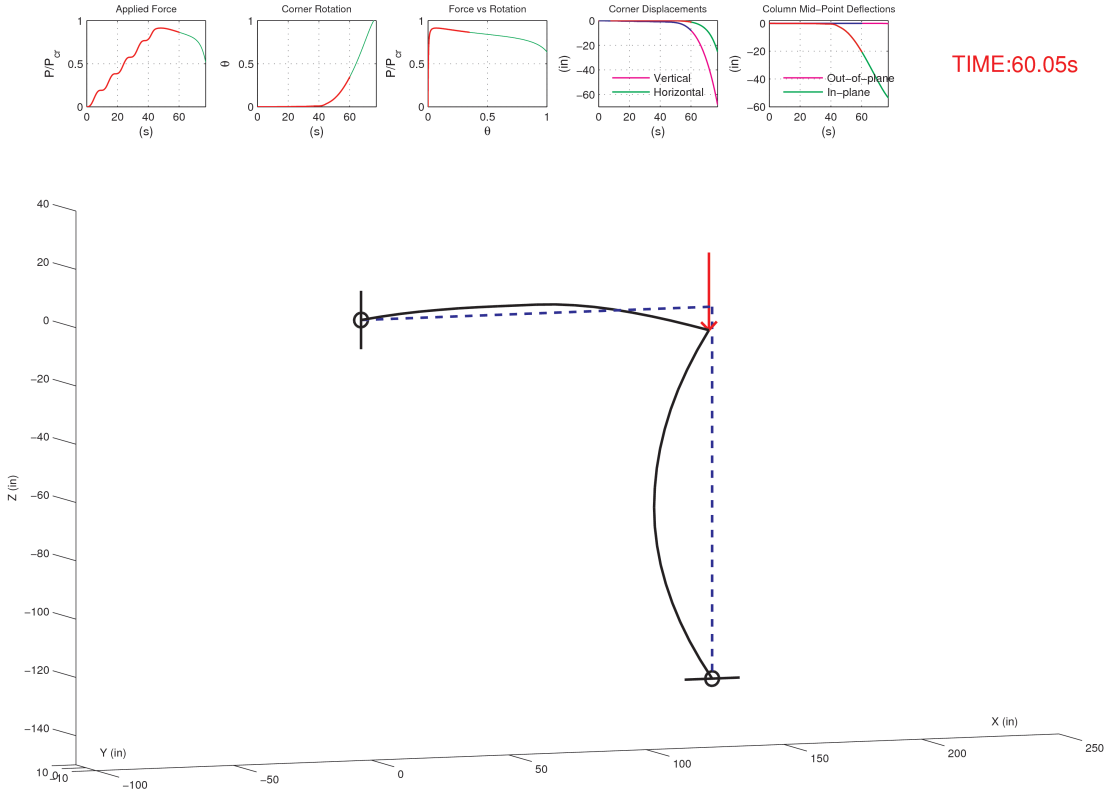

(b)

Figure 4.5: Deformed shape of TS8x8x3/16, L/R=40 frame at various levels of corner loading (zero eccentricity).

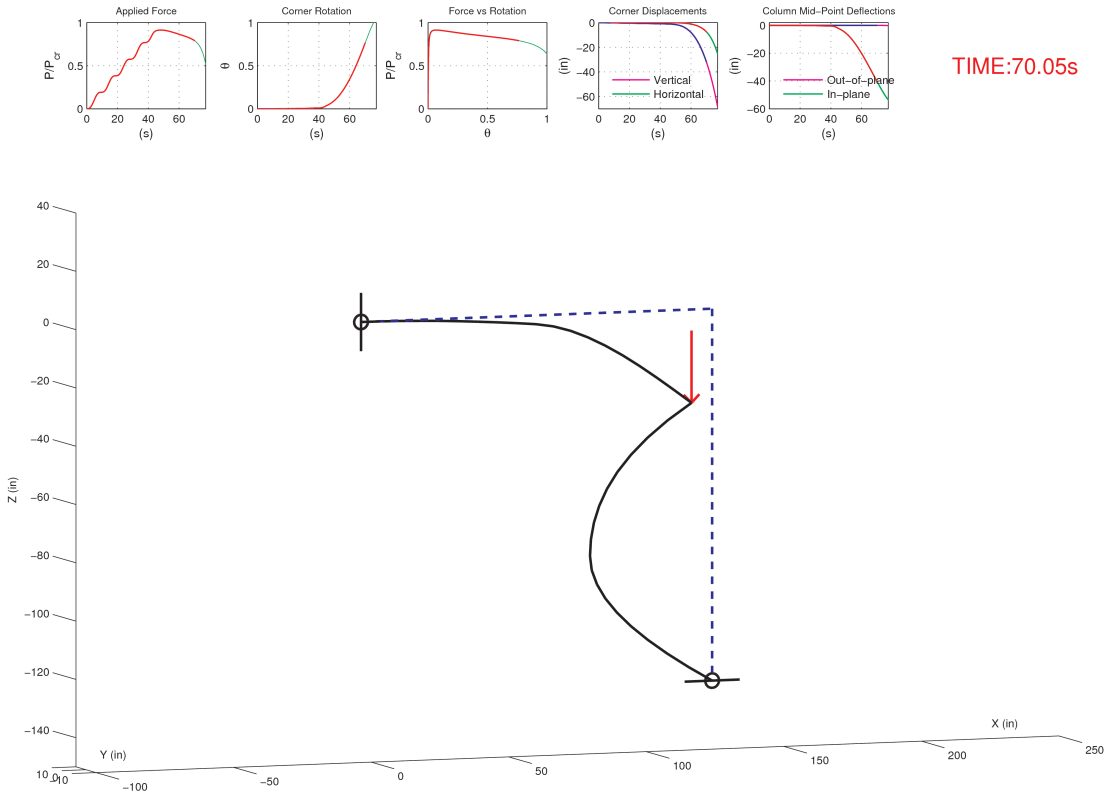

(a)

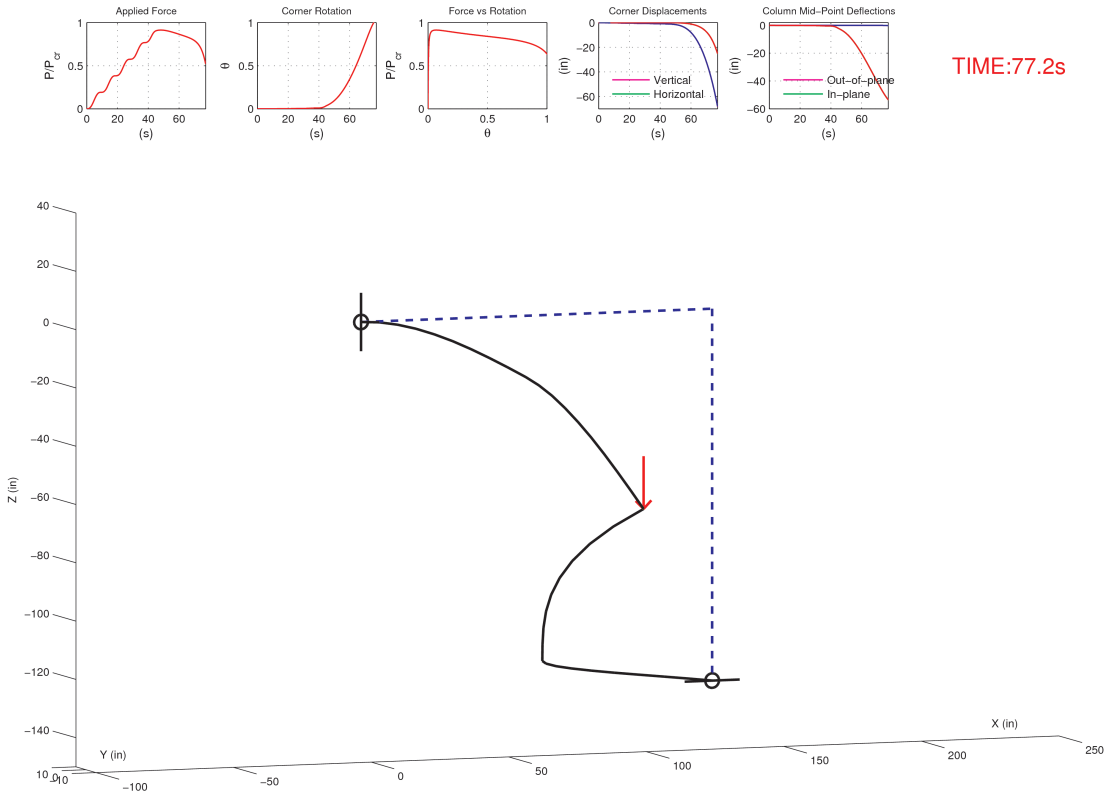

(b)

Figure 4.6: Deformed shape of TS8x8x3/16, L/R=40 frame at various levels of corner loading (zero eccentricity).

Chapter 5 Modeling the Inelastic Buckling of Cyclically Loaded Struts in Pseudodynamic Tests

Numerous tests have been conducted to characterize the inelastic behavior of struts under cyclic axial loading. Of particular interest is the effect of various loading histories (protocols) on the degradation of compression and tension capacities, and the axial and lateral deformations due to successive buckling under compression, and straightening and possibly yielding under tension. For the MEF element to be used effectively in predicting inelastic buckling behavior, it must be able to reproduce the experimental results. This is a challenging task. The sensitivity of response to boundary conditions and geometric imperfections is well documented in the literature. Experimental conditions can vary significantly and the absolute control on these variables cannot be guaranteed. For example, typical brace connections are neither perfectly hinged nor completely fixed, some moment is always transferred. However, the degree of fixity cannot be reliably quantified. Likewise, perfectly straight members cannot be rolled in the steel mill or cold-formed in the shop. As a result, a certain degree of tuning is typically needed to match the experimental results. Because trade-offs exist between say end-fixity conditions and geometric imperfection in as far as the elastic critical buckling load is concerned, there is no unique way to tune the model parameters. The approach taken here is to choose an initial set of model parameters based on the available experimental data, and tune these parameters to realize the best possible match for the elastic buckling load, the peak tension, and the time to rupture or severing of the strut. The hysteretic behavior of this tuned model is then compared against data from the experiment. Three distinct data-sets (Black et al. 1980; Fell et al. 2006; Tremblay et al. 2003) are considered to ensure that the MEF element is able to capture inelastic buckling behavior satisfactorily under a variety of experimental conditions.

5.1 Black et al. test data

The Black et al. (1980) testing program comprised 24 steel struts with cross-sectional shapes and slenderness ratios commonly encountered in practice. A36 steel was used for wide-flange and other rolled shapes, and A501 steel was used for square tubes. 18 specimen were pinned at both ends, and had slenderness ratios of 40, 80, and 120, while 6 specimen, with slenderness ratios of 40 and 80, were pinned at one end and fixed at the other. All specimen were subjected to a series of quasi-static, axially applied, displacement and load reversal cycles. Most specimen received a compressive load first, while some were given an initial tensile load.

Since the data from this set of experiments is not readily available, those struts for which the published axial force–strut end displacement plots could be used to visually trace the loading history are the only ones simulated here. These include two wide-flange sections, struts 1 (W8x20) and 3 (W6x20), with pinned-end conditions and slenderness ratios of 120 and 80, respectively, two wide-flange sections, struts 19 (W6x20)

and 23 (W5x16), with one end pinned and the other fixed and slenderness ratios of 40 and 80, respectively, two tube sections, struts 17 (TS4x4x0.25) and 18 (TS4x4x0.5), with pinned-end conditions and a slenderness ratio of 80, and a tube section, strut 22 (TS4x4x0.5), with one end pinned and the other fixed and a slenderness ratio of 80. True pinned end conditions were realized in these tests by employing clevis-pins and clevises to allow free rotation in the buckling plane at the ends. Each strut is modeled using a single MEF element (Figure 5.1). Ideal pinned-end and fixed-end conditions are assumed in the analysis, however, the initial geometric imperfection is adjusted in each case such that the initial buckling load matches the observed value. The fiber yield stress and ultimate stress are adjusted to realize a good match between the observed and simulated peak tension. The fiber strain at peak fiber stress is adjusted to ensure that the simulated fracture/rupture/severing of the brace occurs at about the same time as in the experiment. With this initial tuning of the model, the hysteresis behavior of the struts is compared against the observed behavior.

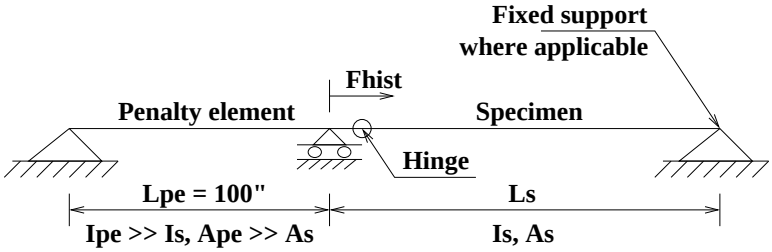

Legend:

Lpe Length of penalty element
Ape Area of penalty element
Ipe Moment of inertia of penalty element
Ls Length of specimen
As Area of specimen
Is Moment of inertia of specimen
Fhist Applied force history in the model

$$\text{Fhist} = \frac{E\ A_{pe}\ \delta_{exp}}{L_{pe}}$$

δ_{exp} **Axial displacement history applied to the specimen during the experiment**

Figure 5.1: FRAME3D model of the Black et al. and Fell et al. experimental setup, data from which is used to validate the MEF element.

The properties of the seven struts are summarized in Table 5.1. The observed mechanical properties and the model parameters are listed in Table 5.2. It is clear that the fiber ultimate stress, used in the model to realize a good match with the peak tension recorded in the experiment, is substantially lower than that observed in the coupon tests in many cases. This may be because the coupon tests are monotonic tests whereas peak tension is achieved after a few cycles of compression buckling and tension yielding. Perhaps what is needed is the peak stress from a cyclically loaded coupon, which is usually hard to generate in practice. Coupon test results for the W8x20 section are shown in Figures 5.2 and 5.3.

The loading history for strut 1 (W8x20) is shown in Figure 5.4. It should be noted that this loading history is visually determined from the recorded axial displacement versus axial load history for strut 1, shown

Strut	**Section**	**BCs**	L **(in)**	A **(in**^{2}**)**	I_{min} **(in**^{4}**)**	KL/r	P_{cr} **(exp)**	**min(**P_{cr}**,** P_y**)**
1	W8x20	Pin-Pin	150.00	5.8138	9.2198	119	95	117.3
3	W6x20	Pin-Pin	120.84	5.8168	13.2799	80	202	233.0
17	TS4x4x0.25	Pin-Pin	120.00	3.7500	8.8275	78	123	175.5
18	TS4x4x0.5	Pin-Pin	108.84	7.0000	14.5825	75	272	352.3
19	W6x20	Pin-Fix	86.28	5.8168	13.2799	40	240	233.0
22	TS4x4x0.5	Pin-Fix	155.40	7.0000	14.5825	75	239	353.7
23	W5x16	Pin-Fix	144.00	4.6296	7.5049	79	165	189.6

Table 5.1: Strut properties (section, boundary conditions, area, moment of inertia about the minor axis, effective slenderness ratio, observed elastic critical buckling load, and the smaller of the theoretical Euler buckling load and the axial yield capacity) in Black et al. experiments

		Coupon Tests			**Model Parameters**				
Strut	**Section**	σ_y **(ksi)**	σ_u **(ksi)**	ϵ_u	σ_y **(ksi)**	σ_u **(ksi)**	ϵ_u	ϵ_{sh}	e_{min} **(%L)**
1	W8x20	41.9	69.8	0.16	37.12	43.45	0.16	0.012	0.24300
3	W6x20	40.0	65.7	0.16	41.35	45.92	0.29	0.012	0.05965
17	TS4x4x0.25	57.6	66.4	0.08	55.71	60.03	0.30	0.012	0.28100
18	TS4x4x0.5	80.0	82.0	0.04	50.47	55.00	0.27	0.012	0.06348
19	W6x20	40.0	65.7	0.16	41.30	42.24	0.25	0.002	0.00050
22	TS4x4x0.5	80.0	82.0	0.04	82.00	83.00	0.09	0.012	0.61000
23	W5x16	41.0	60.5	0.10	35.73	36.00	0.20	0.012	0.00050

Table 5.2: Black et al. coupon test data (yield stress, ultimate stress, and strain at ultimate stress) and MEF element model parameters (yield stress, ultimate stress, strain at ultimate stress, strain at the onset of strain-hardening, and minor direction eccentricity/geometric imperfection as a percentage of the span). An elastic modulus of 29000ksi, and a tangent modulus at the initiation of strain hardening E_{sh} of 580ksi is used for all models is used for all models.

in Figure 5.5(a). The corresponding lateral displacement versus axial load history is shown in Figure 5.6(a). It should be noted that these figures are scanned from the Black et al. (1980) report and hence cannot be overlaid on the results from the model, which are illustrated in Figures 5.5(b) and 5.6(b). There is excellent agreement in the shape of the hysteresis loops, the degradation of the axial compression buckling load in successive cycles, the lateral deformation in successive cycles including the degree of alternate kinking and straightening during compression and tension cycles, respectively. Results for the remaining struts are presented in Appendix B. The results are equally accurate for tube sections and wide-flange sections, as well as pinned-pinned and pinned-fixed boundary conditions demonstrating the robustness of the MEF element modeling approach.

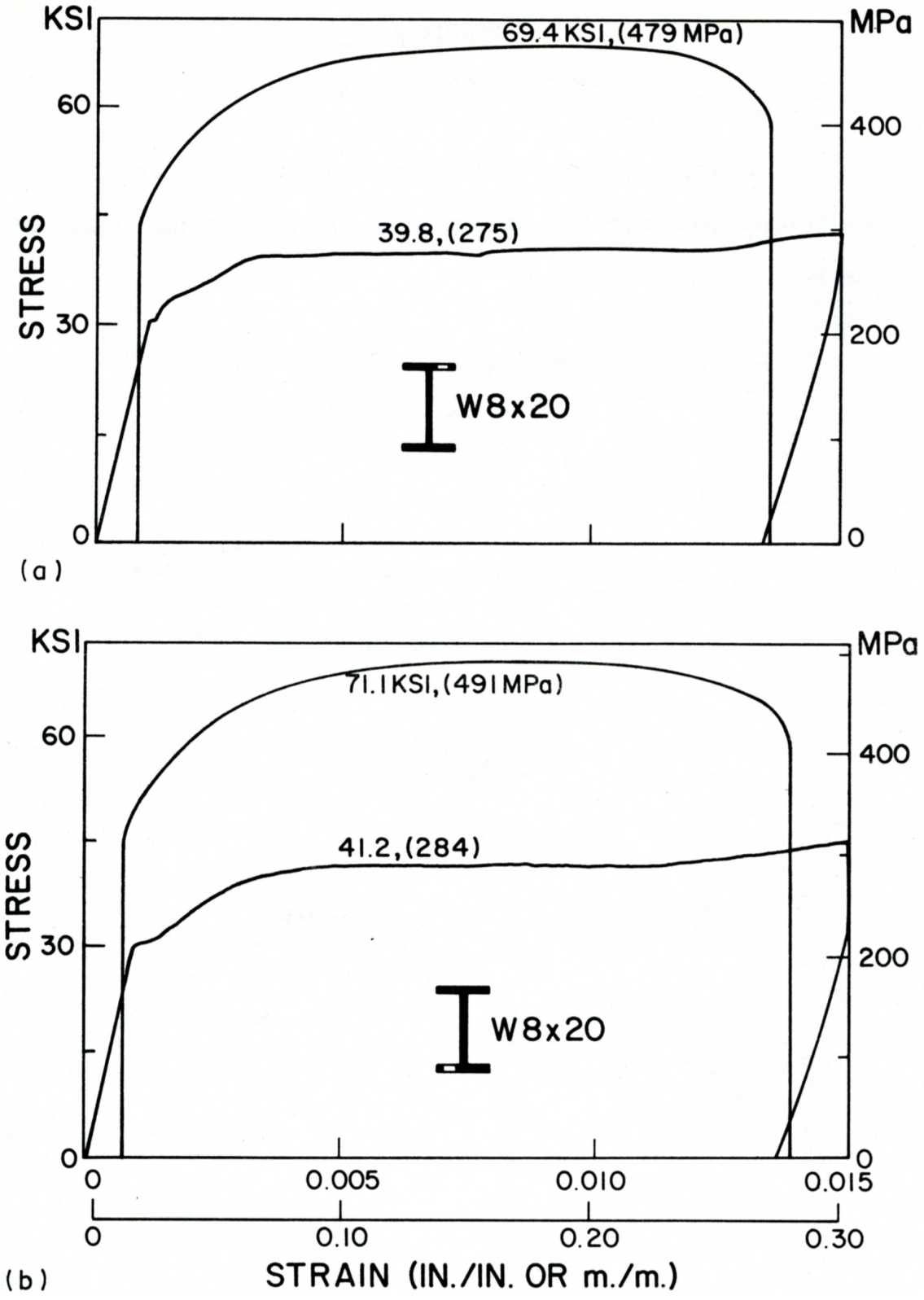

Figure 5.2: Black et al. tests: W8x20 coupon tensile loading test.

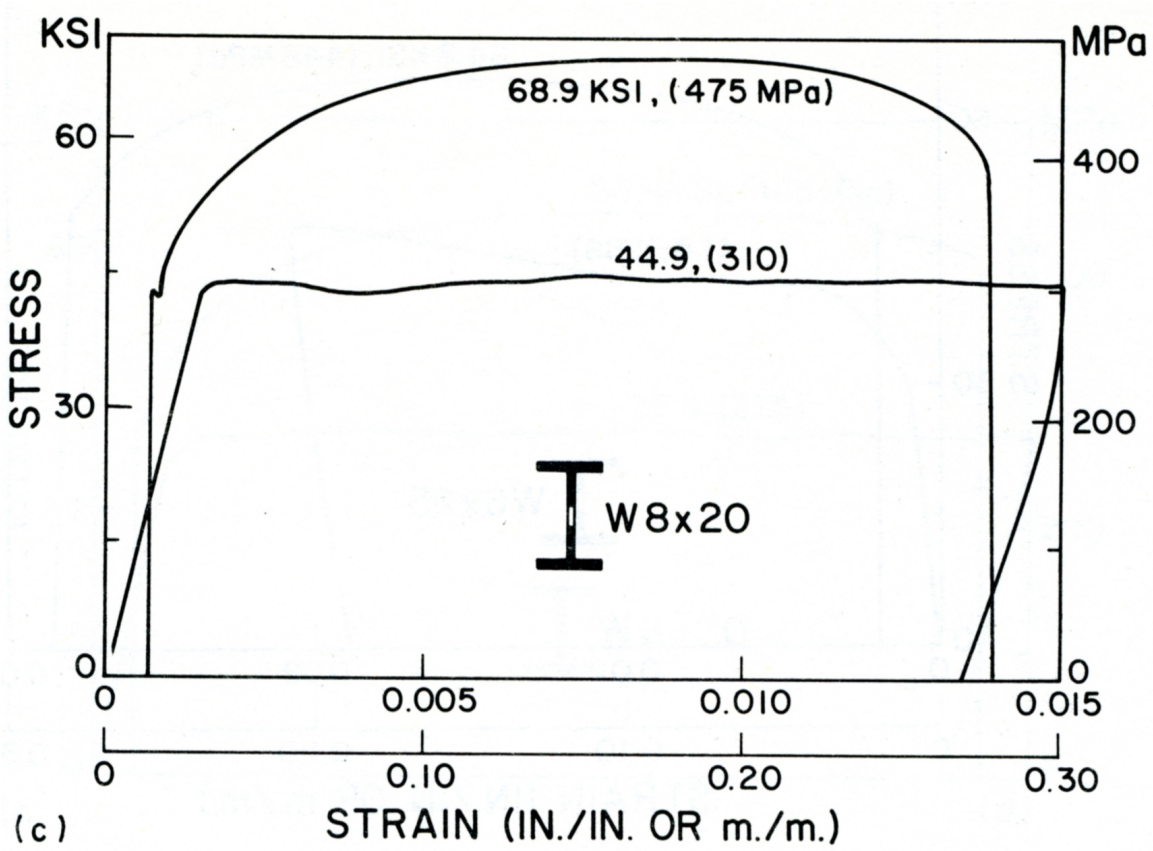

Figure 5.3: Black et al. tests: W8x20 coupon tensile loading test (contd.).

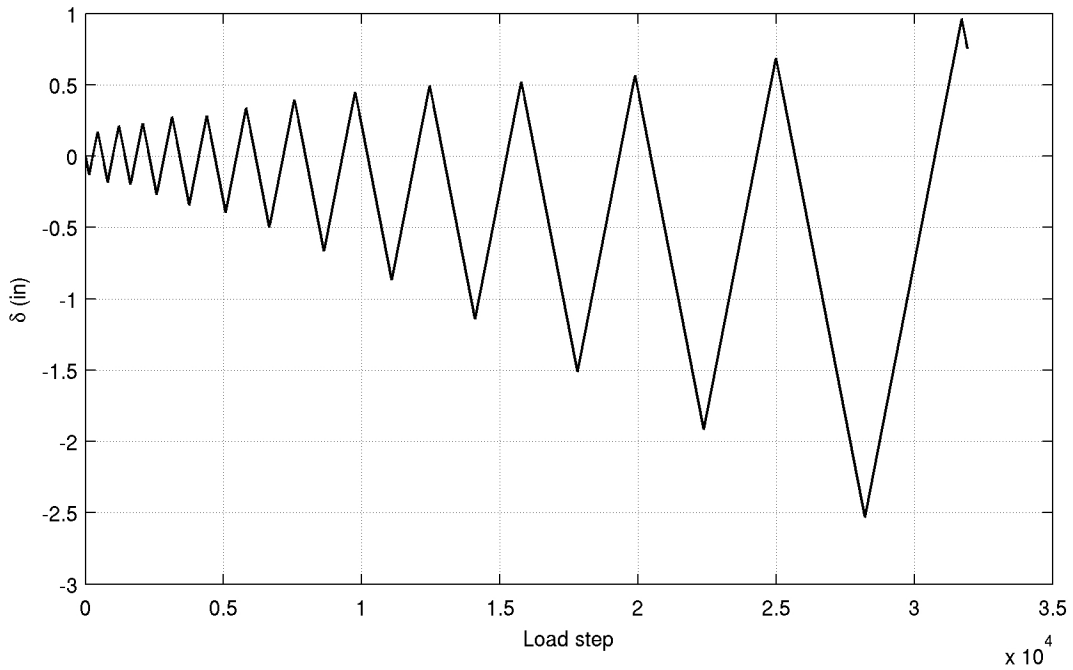

Figure 5.4: Black et al. tests: Pinned ended W8x20 strut (1) with KL/r=120 – Loading history.

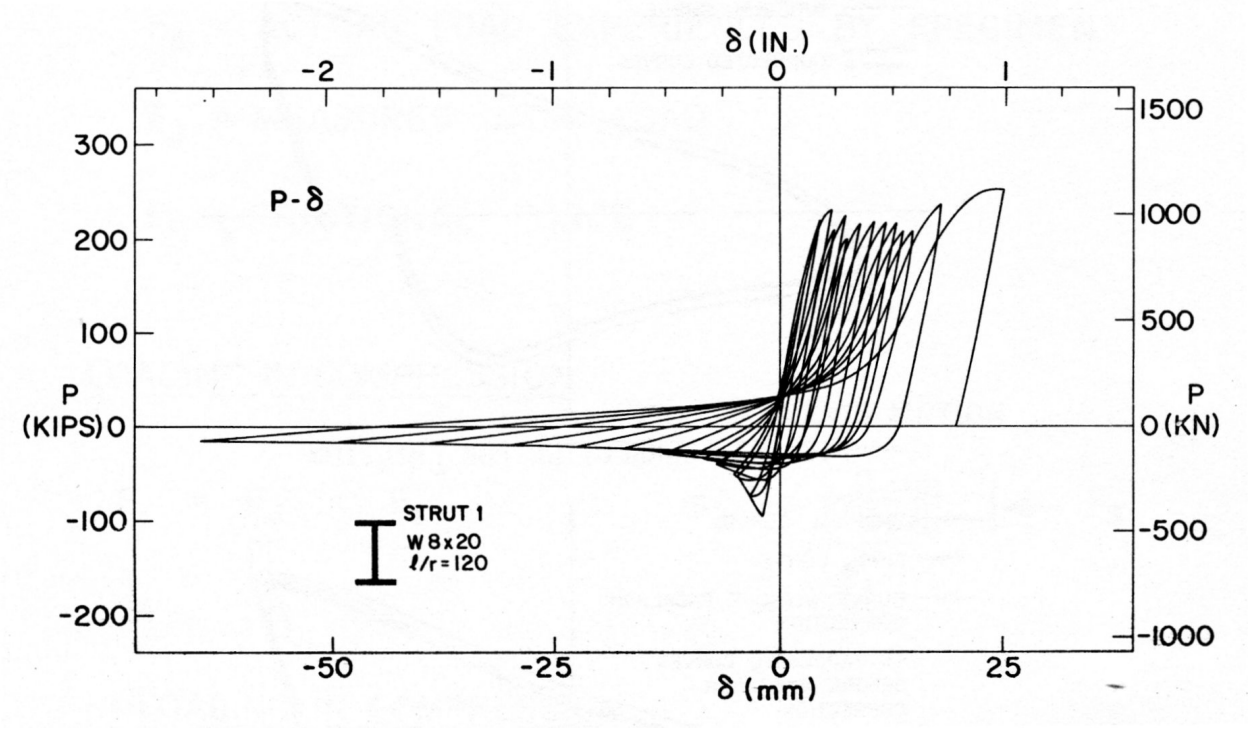

(a)

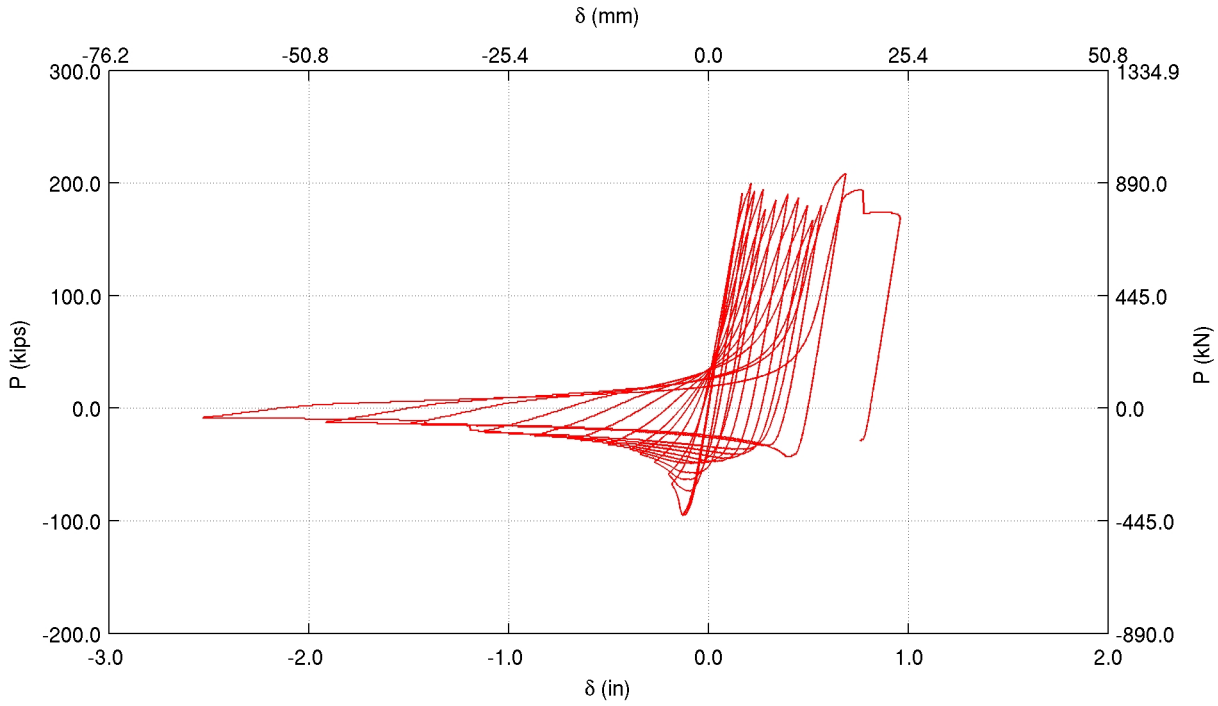

(b)

Figure 5.5: Black et al. tests: Pinned ended W8x20 strut (1) with KL/r=120, axial displacement versus axial force history – (a) Experiment (b) Simulation.

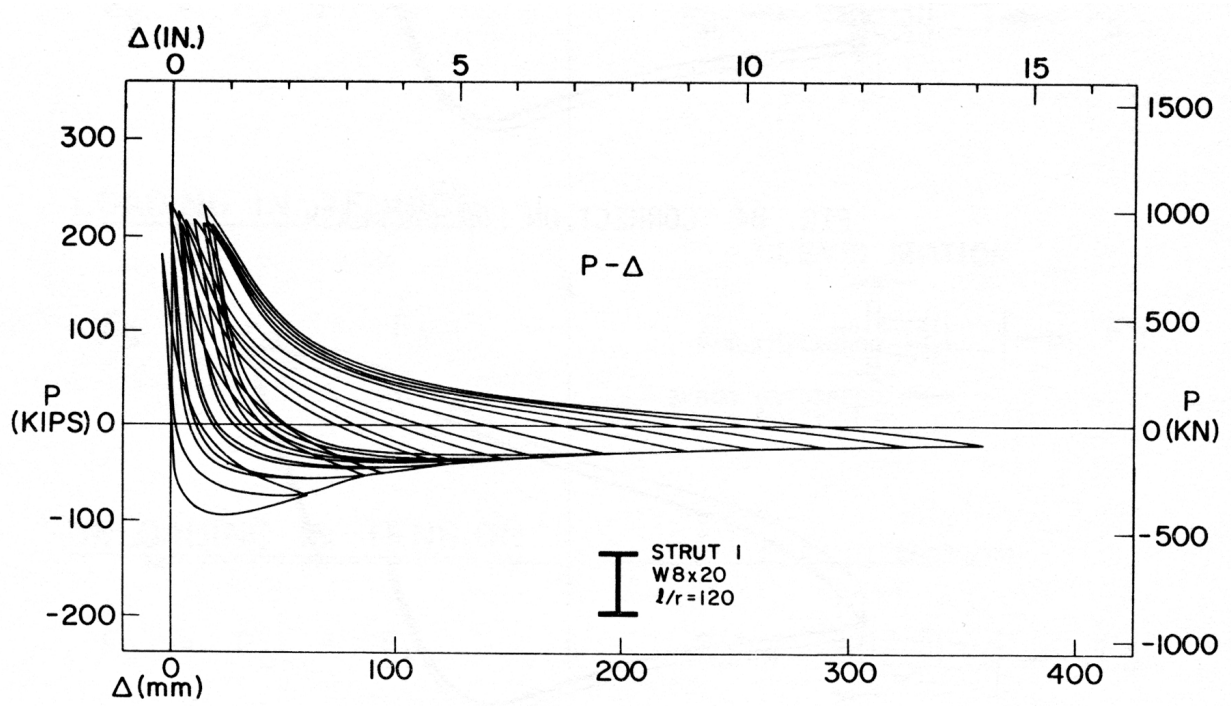

(a)

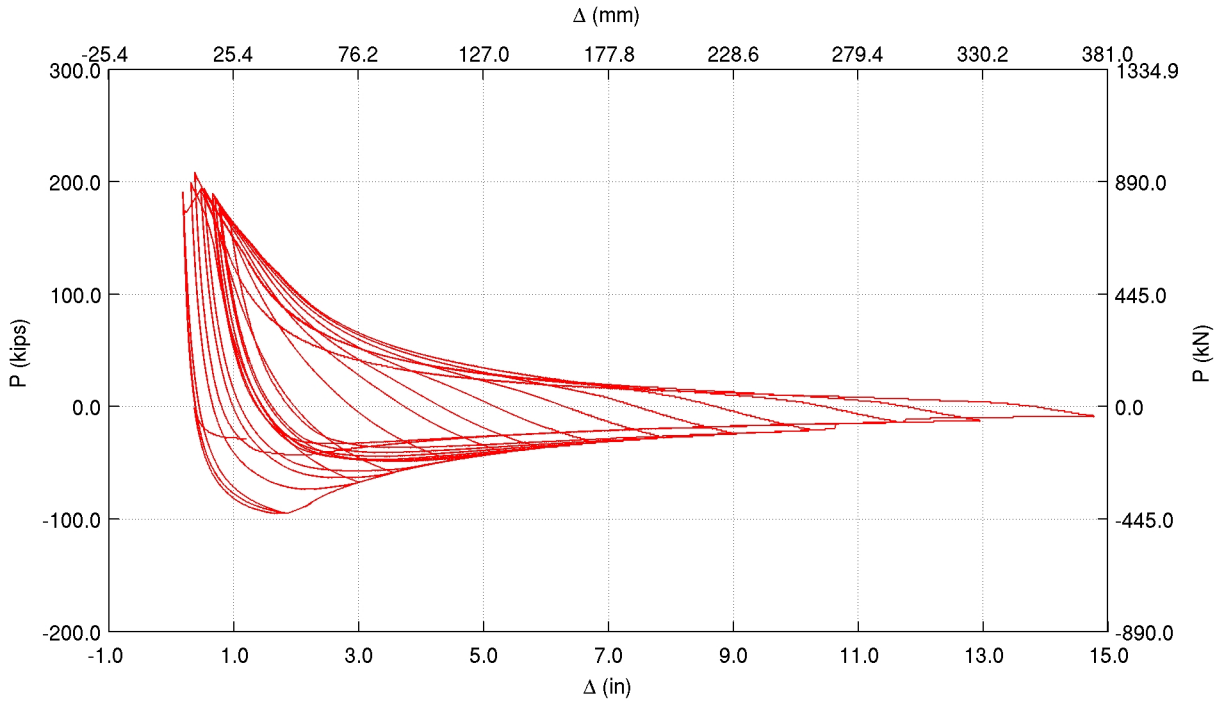

(b)

Figure 5.6: Black et al. tests: Pinned ended W8x20 strut (1) with KL/r=120, lateral displacement versus axial force history – (a) Experiment (b) Simulation.

Strut	**Section**	**Load History**	A **(in^2)**	I_{min} **(in^4)**	KL/r	P_{cr} **(exp)**	**min(P_{cr}, P_y) (comp)**
1	HSS4x4x1/4	Far-Field	3.369	8.038	80	157	155.5
2	HSS4x4x1/4	Near-Field (C)	3.369	8.038	80	119	113.2
3	HSS4x4x1/4	Far-Field (Eqke Rate)	3.369	8.038	80	161	155.5
4	HSS4x4x3/8	Far-Field	4.804	10.888	82	186	186.4
5	HSS4x4x3/8	Far-Field (Eqke Rate)	4.804	10.888	82	184	186.4
14	W12x16	Near-Field (C)	4.710	2.820	159	82	86.9
15	W12x16	Far-Field	4.710	2.820	159	93	86.4
16	W12x16	Near-Field (T)	4.710	2.820	159	75	78.3

Table 5.3: Strut properties (section, load-history, area, moment of inertia about the minor axis, effective slenderness ratio (with K=1.0), observed elastic critical buckling load, and the smaller of the theoretical Euler buckling load (with K=1.0) and the axial yield capacity) in Fell et al. experiments. The length of each specimen was 123 inches.

5.2 Fell et al. test data

A series of cyclic load tests were conducted recently by Fell et al. on 19 tube (HSS, A500 Grade B), pipe (A53, Grade B), and wide-flange (A992) sections under the auspices of the Network for Earthquake Engineering Simulation (NEES) program, with the objective of investigating earthquake-induced buckling and fracture behavior (Fell et al. 2006; Fell 2008; Fell et al. 2009). Three loading protocols were used, a far-field loading protocol that is conceptually similar to the Black et al. study, and two near-fault – compression dominated and tension dominated – loading protocols that reflect demands imposed by near-fault ground motions. Another distinguishing feature of these tests was the use of typical braced frame connections (as opposed to the ideal pins and fixed connections employed in the Black et al. study), with the strut welded to a gusset plate that is bolted to the movable constraint frame and the stationary reaction block. The gusset plates were designed to preclude buckling. In fact, they yielded in out-of-plane plate bending in all the tests. While this resulted in an effectively pinned-end condition for the tube specimen (due to their superior out-of-plane stiffness dwarfing the low out-of-plane stiffness of the yielded gusset), partially fixed end conditions were created for the wide-flanged sections (whose lower out-of-plane stiffness is not enough to render the stiffness of the yielded gusset insignificant). The investigators paid close attention to the onset of local buckling and fracture and cataloged these events for each test. Details of the test program pertaining to HSS and wide-flange sections are summarized in Table 5.3.

In this study, the Fell et al. specimen utilizing HSS and wide-flange sections are modeled using single MEF elements. The fiber yield and ultimate stresses are tuned to achieve the experimentally observed peak tension, the fiber fracture strain is tuned to synchronize the first occurrence of fracture in the model with that in the experiment, the fiber rupture strain is tuned to synchronize the severing of the brace in the model with that in the experiment. As in the Black et al. series of tests, there is significant discrepancy

between the best-fit model fiber yield and ultimate stresses, and the coupon test data. The model values are uniformly lower than the corresponding coupon test values, possibly because the coupons were tested under monotonic tension, whereas peak tension in the brace is reached after a few cycles of successive compression and tension. While pinned-end boundary conditions are assumed for all the HSS braces (since the gusset plates yielded and full plastic hinging occurred), partial fixity conditions are assumed for the wide-flange sections whose out-of-plane stiffnesses do not dwarf that of the partially-yielded gusset plates. The model parameters (and the corresponding coupon test data) are summarized in Table 5.4. The hysteretic response of the tuned model is compared against the observed behavior through axial force – axial deformation and axial force – lateral deformation histories.

Specimen #2 (HSS 4x4x1/4) was subjected to the asymmetric compression loading history shown in Figure 5.7. In the first strong cycle, the brace was loaded to 2% drift angle in tension, followed by 6% drift angle in compression (the axial deformation of the brace was converted to a story drift angle using a chevron-braced frame assumption with brace angle of 45° to the horizontal plane; $\theta = 2\delta/L_b$, where θ is the story drift angle, δ is the axial deformation of the brace, and L_b is the length of the brace). The brace yielded and elongated in the first tensile excursion, significantly lowering the compressive buckling load. Local buckling was observed during the first large compression excursion (at a drift of 2.5%). The brace cycled at a residual drift of 3% for the remainder of the test. The MEF element is able to capture the hysteretic behavior accurately as evidenced by the agreement in the observed and computed axial force – axial deformation and axial force – lateral deformation histories shown in Figure 5.8. The tensile severing of the brace is not adequately captured, however the lateral deformation of the brace agrees quite well with the experiment.

Specimen #16 (W12x16) was subjected to the asymmetric tension loading history shown in Figure 5.9. This tension dominated history consisted of a large monotonic pull (8% drift) followed by subsequent lower amplitude cycles. It is similar to the compression dominated history, except that it does not consist of a large compression excursion prior to the first tension pull to avoid buckling. While the nature of the hysteretic response of the model is remarkably similar to that observed in the experiment, the peak lateral deformation in the model ($\sim$15 inches) falls short of the observed brace lateral displacement ($\sim$22 inches). As in the case of the near-field compression dominated loading history, the severing of the brace is not adequately captured in the simulation. The results of simulations of the remaining specimen, presented in Appendix C, are generally better with synchronized brace severing in the model and the experiment.

Strut	Section	Coupon Tests			Model Parameters						
		σ_y (ksi)	σ_u (ksi)	ϵ_u	σ_y (ksi)	σ_u (ksi)	ϵ_u	ϵ_{sh}	$\frac{\epsilon_{frac}}{\epsilon_y}$	e_{min} (%L)	FF
1	HSS4x4x1/4	71.9	77.6	0.07	69.87	73.47	0.30	0.010	236	0.0005	0.000
2	HSS4x4x1/4	71.9	77.6	0.07	69.87	73.47	0.30	0.010	146	0.0005	0.000
3	HSS4x4x1/4	71.9	77.6	0.07	69.87	73.47	0.25	0.010	210	0.0005	0.000
4	HSS4x4x3/8	76.5	83.9	0.05	65.10	72.86	0.50	0.012	450	0.1000	0.000
5	HSS4x4x3/8	76.5	83.9	0.05	65.10	72.86	0.50	0.012	450	0.1000	0.000
14	W12x16	N/A	N/A	N/A	60.00	62.00	0.25	0.012	275	0.0005	0.200
15	W12x16	N/A	N/A	N/A	60.00	62.00	0.55	0.016	500	0.0005	0.032
16	W12x16	N/A	N/A	N/A	60.00	70.00	0.55	0.016	500	0.0005	0.400

Table 5.4: Fell et al. coupon test data (yield stress, ultimate stress, and strain at ultimate stress) and MEF element model parameters (yield stress, ultimate stress, strain at ultimate stress, strain at the onset of strain-hardening, minor direction eccentricity/geometric imperfection as a percentage of the span, and end fixity factor (FF) – fiber strains due to element end rotations are scaled by the fixity factor resulting in depleted moment transfer). Coupons from the W12x16 section were not tested. An elastic modulus E of 29000ksi, and a tangent modulus at the initiation of strain hardening E_{sh} of 580ksi is used for all models.

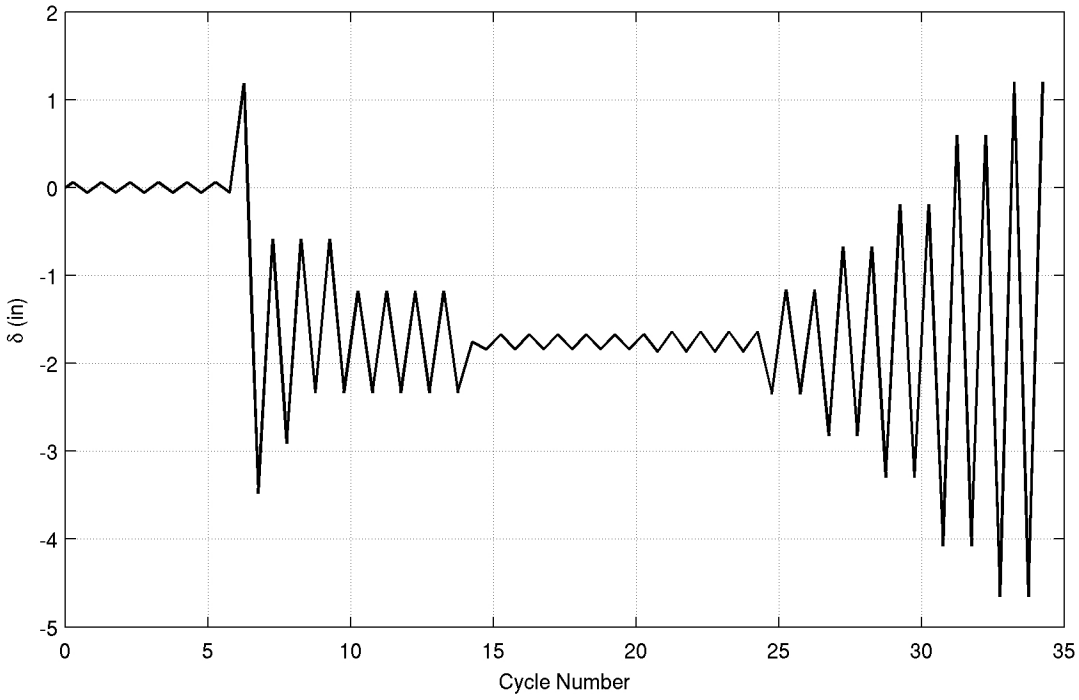

Figure 5.7: Fell et al. test 2 on HSS4x4x1/4 (KL/r $\sim$ 80): Compression-dominated near-field loading history

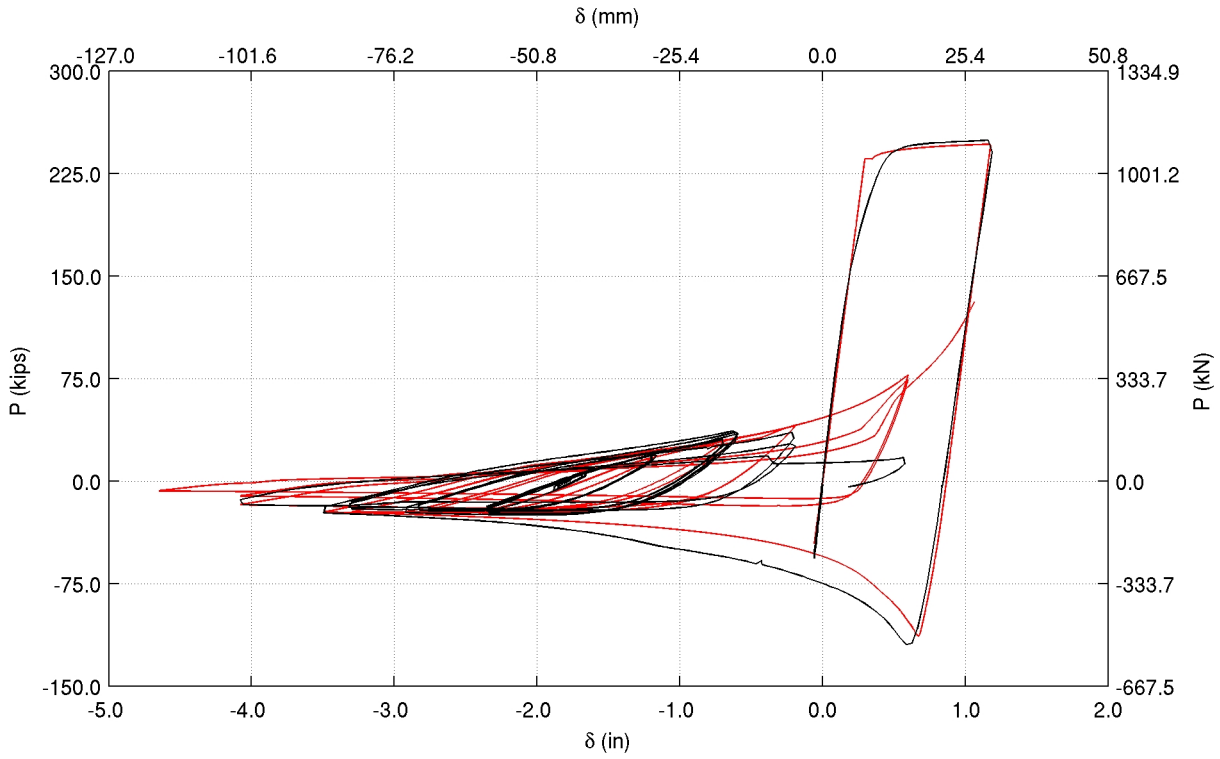

(a)

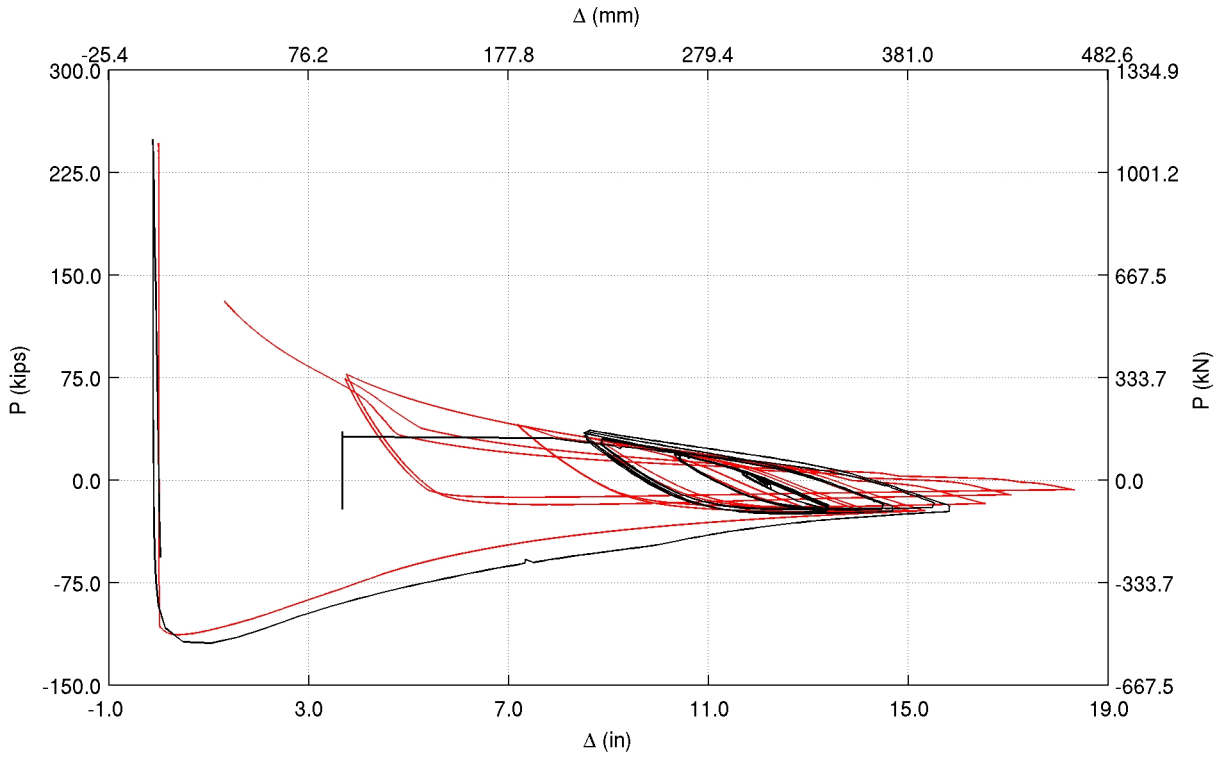

(b)

Figure 5.8: Comparison of simulation against data from Fell et al. test 2 on HSS4x4x1/4 (KL/r $\sim$ 80): (a) Axial displacement versus axial force history; (b) Minor direction lateral displacement versus axial force history.

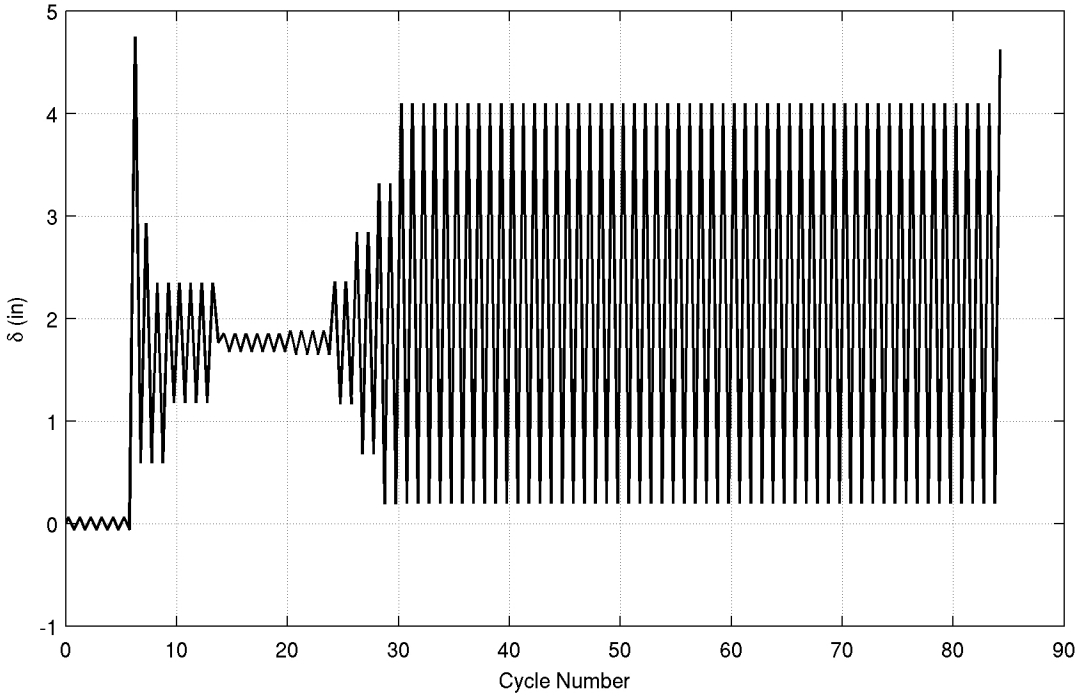

Figure 5.9: Fell et al. test 16 on W12x16 (KL/r $\sim$ 159): Tension-dominated near-field loading history

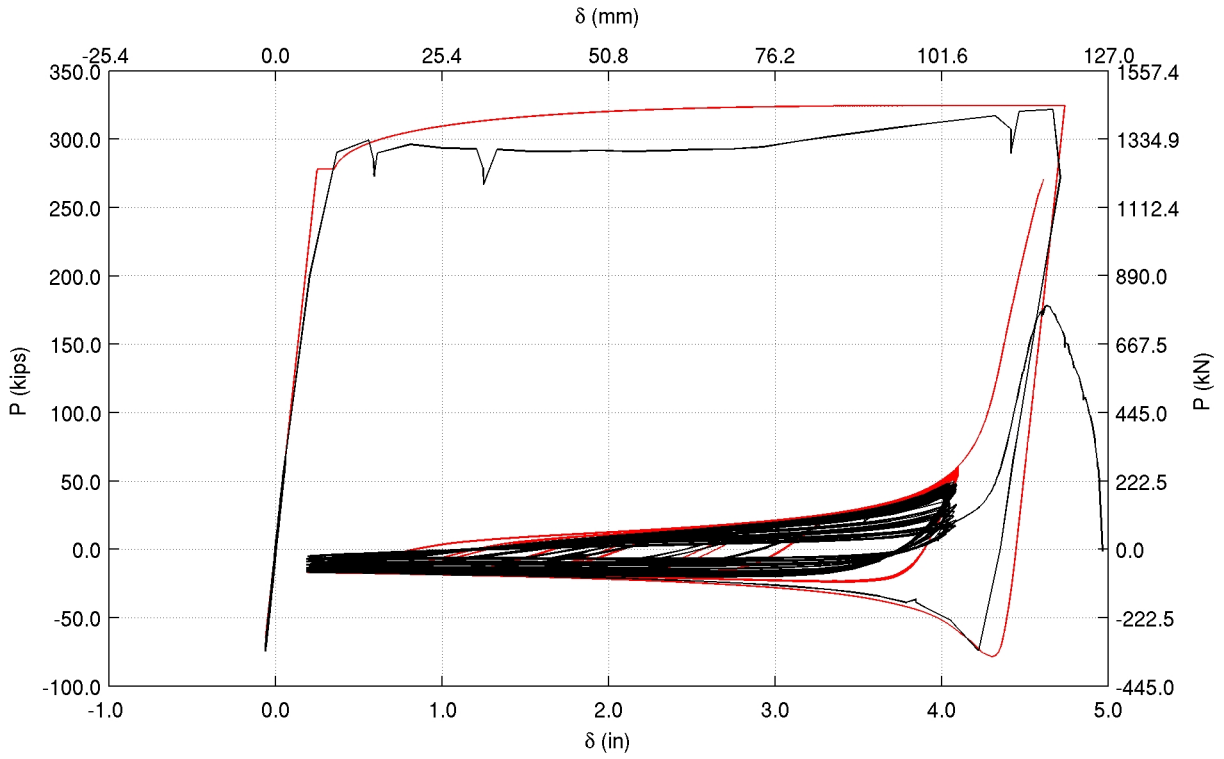

(a)

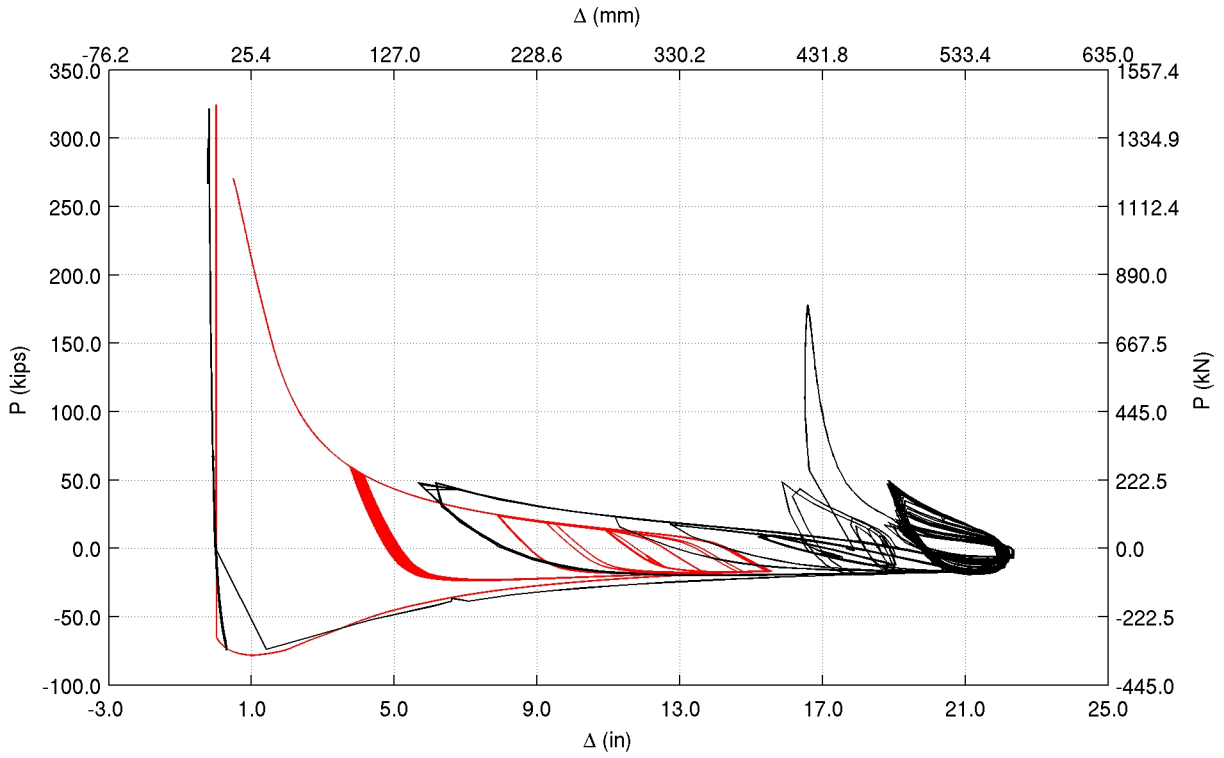

(b)

Figure 5.10: Comparison of simulation against data from Fell et al. test 16 on W12x16 (KL/r $\sim$ 159): (a) Axial displacement versus axial force history; (b) Minor direction lateral displacement versus axial force history.

Strut	Section	Load History	A (in^2)	I_{min} (in^4)	L/r
S1A	RHS127x76x4.8	H1	2.775	4.168	187
S1B	RHS127x76x4.8	H1	2.775	4.168	187
S2A	RHS102x76x4.8	H1	3.369	8.038	191
S2B	RHS102x76x4.8	H1	4.804	10.888	191
S3A	RHS76x76x4.8	H1	4.804	10.888	198
S3B	RHS76x76x4.8	H1	4.710	2.820	198
S4A	RHS127x64x4.8	H1	4.710	2.820	223
S4B	RHS127x64x4.8	H1	4.710	2.820	223
S5A	RHS102x76x6.4	H1	3.369	8.038	195
S5B	RHS102x76x6.4	H1	4.804	10.888	195
S1QA	RHS127x76x4.8	H2	3.369	8.038	187
S1QB	RHS127x76x4.8	H2	3.369	8.038	187
S4QA	RHS127x64x4.8	H2	4.710	2.820	223
S4QB	RHS127x64x4.8	H2	4.710	2.820	223

Table 5.5: Tremblay et al. experiments: Strut properties (section, load-history, area, moment of inertia about the minor axis, and slenderness ratio.

5.3 Tremblay et al. test data

Tremblay et al. (2003) conducted a set of 24 full-scale cyclic quasistatic tests on a one-story, single-bay steel braced frame with single diagonal brace and X-bracing configurations. The braces were made of rectangular hollow sections. The mechanical properties of the brace in each test are summarized in Table 5.5. The frame was hinged at the four corners by means of high-strength steel pins inserted in carefully machined bushings, and mounted horizontally on a strong floor. The hinges at the bottom end of each column were restrained from translation. The frame was allowed to sway laterally at the upper end. Two displacement time histories were employed. The story drift sequence was applied by two alternating single-action actuators. The braces were connected to the frame by means of a gusset plate. For the single brace schemes, two brace configurations are possible – bottom-left to top-right (identified by label "A") or bottom-right to top-left (identified by label "B"). The same displacement history was applied in both configurations so that the brace in Test A was first loaded in tension, whereas the brace in Test B was first loaded in compression. The lateral sway of the frame and the story shear (the applied force history) were recorded until brace failure.

Recently, Aguero et al. (2006) modeled the inelastic cyclic response of two of these braces (S2A and S1QB), with 8 elements per brace, using the OpenSees computational framework (McKenna 1997; Mazzoni et al. 2005). Here, the viability of using a single MEF element to model the same is investigated. A

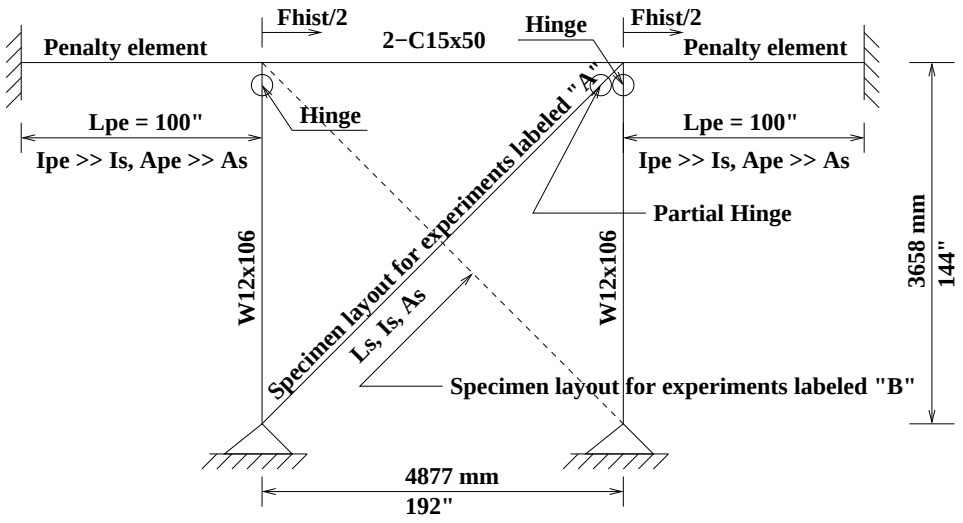

Legend:

Lpe Length of penalty element
Ape Area of penalty element
Ipe Moment of inertia of penalty element
Ls Length of specimen
As Area of specimen
Is Moment of inertia of specimen

Fhist Applied force history in the model

$$\text{Fhist} = \frac{\text{E Ape}\,\delta_{\text{exp}}}{\text{Lpe}}$$

δ_{exp} Axial displacement history applied to the specimen during the experiment

Figure 5.11: FRAME3D model of the Tremblay et al. experimental setup, data from which is used to validate the MEF element.

schematic representation of the FRAME3D models is shown in Figure 5.11. The columns and beam in the frame are modeled using plastic hinge elements. No yielding or other forms of nonlinearity were observed in these members during the experiments, hence using MEF elements to model them will not have a notable impact on the results. Only the single-bracing schemes are considered in this study. The brace-to-column and brace-to-beam connections in the test setup were made through gusset plates, and brace end-fixity is related to the out-of-plane bending stiffness of the connecting plates. Since the column was shorter than the beam, the angle made by the brace to the column was closer to 90° than the angle made by the brace to beam. As a result the effective length of the connecting plates at the brace-to-column connection was shorter (and hence the bending stiffness was greater) than that at the brace-to-beam connection. In the FRAME3D model, it is assumed that there is full fixity at the brace-to-column connection (although the joint itself is assumed simply supported allowing free rotation as in the experiment, and the end moment in the brace must be balanced by the column end moment; this is generally quite small relative to the moment capacity of the brace). The end-fixity at the beam-to-brace connection is adjusted to yield the best possible results for lateral forces at critical buckling and buckling at subsequent cycles. In many instances a compromise is made by choosing a lower end-fixity to achieve a better match for the lateral loads corresponding to buckling of the brace in post-critical compression excursions, while not accurately matching that corresponding to critical buckling. The model parameters corresponding to each experiment are listed in Table 5.6. While yield stress of the material was recorded from stub column tests, no information is available on the ultimate stresses. The fiber ultimate stress in the model is tuned to realize a good match between the lateral force

Strut	Section	Model Parameters							
		E (ksi)	E_{sh} (ksi)	σ_y (ksi)	σ_u (ksi)	ϵ_u	ϵ_{sh}	FF_1	FF_2
S1A-S1B	RHS127x76x4.8	28704.3	1200	57.3	62.0	0.0975	0.012	1.00	0.35
S2A-S2B	RHS102x76x4.8	26817.7	1200	55.3	62.0	0.1600	0.012	1.00	0.20
S3A-S3B	RHS76x76x4.8	27079.4	580	56.4	65.0	0.2300	0.012	1.00	0.00
S4A-S4B	RHS127x64x4.8	28185.5	580	55.9	57.0	0.0700	0.012	1.00	0.90
S5A-S5B	RHS102x76x6.4	26526.6	580	61.1	68.0	0.2000	0.012	1.00	0.20
S1QA-S1QB	RHS127x76x4.8	28704.3	580	57.3	68.0	0.1025	0.012	1.00	1.00
S4QA-S4QB	RHS127x64x4.8	27266.1	580	53.9	57.0	0.1000	0.012	1.00	1.00

Table 5.6: Tremblay et al. coupon test data (yield stress, ultimate stress, and strain at ultimate stress) and MEF element model parameters (yield stress, ultimate stress, strain at ultimate stress, strain at the onset of strain-hardening, and fixity factors for the two ends (FF_1 and FF_2) – fiber strains due to element end rotations are scaled by the fixity factor resulting in depleted moment transfer). An infinitesimally small geometric imperfection, and fracture strains larger than rupture strain are assumed for all models.

recorded in brace tension excursions of the experiment and that from the model. The fiber ultimate strain is adjusted to best capture the timing of the severing of the brace in the experiment.

Compared in Table 5.7 are the maximum and minimum lateral forces applied on the frame in each test against the corresponding story shears from FRAME3D models. The significant discrepancies in observed and modeled peak lateral loads are related to the choice of end-fixity which was made to achieve good agreement in the cyclic degradation of brace capacities, as opposed to matching just the critical buckling load, as discussed previously. Also shown in the table are the observed and computed brace peak lateral deformations. The agreement is quite good and points to the ability of the MEF element to capture large deformations.

The frame lateral displacement (sway) response history plotted against the applied lateral force for the two specimen considered by Aguero et al. (2006), S2A and S1QB, along with their counterparts, S2B and S1QA, from FRAME3D models is shown in Figures 5.13 and 5.15, respectively. Loading history H1 (Figure 5.12) is applied to specimen S2A-S2B, while loading history H2 (Figure 5.14) is applied to specimen S1QA-S1QB. Similar plots for the remaining specimen are given in Appendix D. It is clear that while the overall nature of the hysteretic behavior is accurately captured, there are significant differences between the model and the observation. However, the degree of mismatch is no worse than the simulation by Aguero et al. (2006) using 8 elements to model the brace within the OpenSees computational framework. This points to the inherent uncertainties associated with an assembled structure (i.e., variability in the as-built conditions such as connection fixity, resistance to joint rotation, etc., that ought to be considered when predicting the behavior of any structure using a model), rather than the inability of the MEF element to

Strut	Section	Experiment			Model			
		V_{min} **(ksi)**	V_{max} **(ksi)**	δ_{max}^{o-of-p} **(in)**	V_{min} **(ksi)**	V_{max} **(ksi)**	δ_{max}^{o-of-p} **(in)**	δ_{max}^{SRSS} **(in)**
S1A	RHS127x76x4.8	-150.6	89.0	14.53	-137.7	67.7	16.37	16.54
S1B	RHS127x76x4.8	-73.6	118.3	15.16	-67.6	137.8	15.69	15.83
S2A	RHS102x76x4.8	-108.5	48.3	19.04	-116.8	48.6	20.15	21.01
S2B	RHS102x76x4.8	-59.6	129.3	14.15	-48.6	116.4	19.82	20.74
S3A	RHS76x76x4.8	-104.4	25.7	23.08	-100.4	23.1	15.80	25.25
S3B	RHS76x76x4.8	-28.9	104.2	24.19	-23.1	100.5	20.31	26.44
S4A	RHS127x64x4.8	-107.8	53.0	12.06	-118.9	47.5	15.31	15.39
S4B	RHS127x64x4.8	-58.1	106.6	13.73	-47.5	119.2	14.47	14.54
S5A	RHS102x76x6.4	-172.9	56.2	25.84	-164.2	53.1	22.79	23.69
S5B	RHS102x76x6.4	-66.9	166.4	27.30	-53.0	163.7	22.26	23.10
S1QA	RHS127x76x4.8	-158.7	82.9	12.82	-151.4	59.1	18.73	19.32
S1QB	RHS127x76x4.8	-81.4	162.4	9.61	-73.0	151.6	16.01	16.26
S4QA	RHS127x64x4.8	-115.4	46.4	16.71	-118.7	39.3	19.41	19.63
S4QB	RHS127x64x4.8	-61.5	114.5	10.73	-46.6	119.1	16.61	16.73

Table 5.7: Comparison of minimum and maximum lateral force applied to the frame in the Tremblay et al. experiments, against the corresponding story shears in the FRAME3D models under the imposed lateral displacement history. Also shown is a comparison of the brace peak out-of-plane (o-of-p) deformations observed in the experiments against that computed from the models. Note that braces in S3A and S3B models have significant in-plane deformations too, as apparent in the square root of the sum of the squares (SRSS) of their in-plane and out-of-plane deformations, listed in the table.

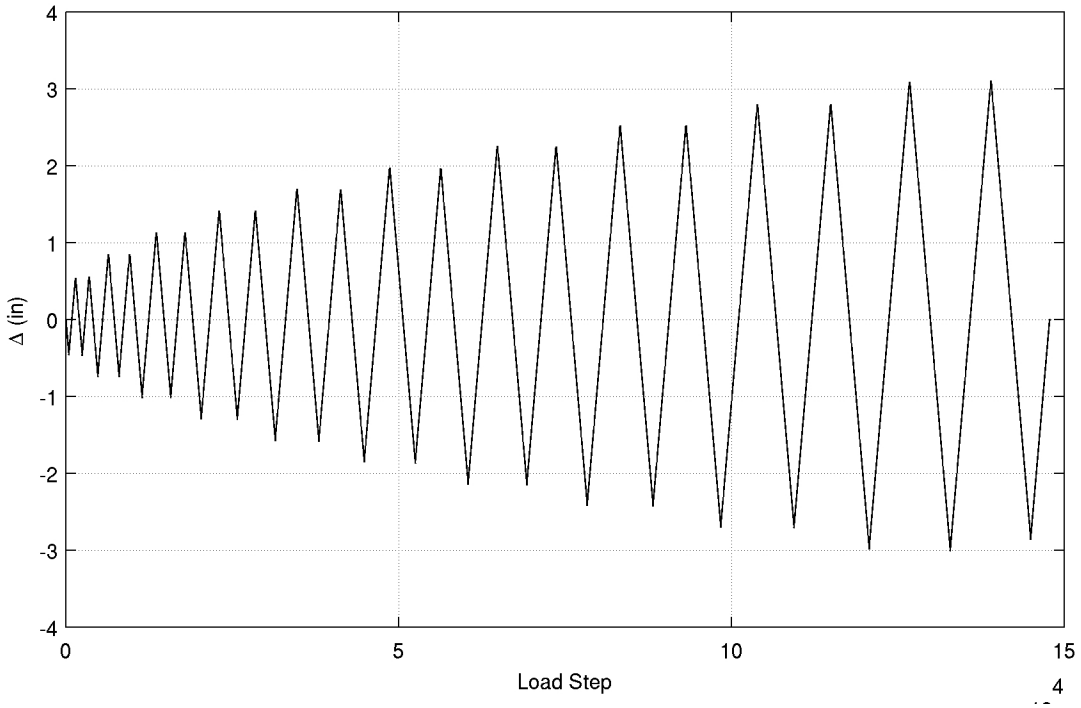

Figure 5.12: Tremblay et al. test S2A/S2B on RHS102x76x4.8: Displacement history "H1"

capture the hysteretic response accurately (the models of the Black et al. and Fell et al. specimen have already established the efficacy of the MEF element). Any model-based prediction of braced structures must duly recognize the significant role played by the field conditions on the response, and the uncertainty in the prediction as a result of the variability in these conditions. Furthermore, yield and ultimate stresses as well as ultimate strains measured in monotonic cyclic tests or stub columns tests applied to fibers within MEF elements undergoing cyclic loading do not yield sufficiently accurate results necessitating tuning of these parameters in the model. This variability is illustrated by histograms of the ratio of the model yield stress to the measured yield stress and the ratio of the model ultimate stress to the measured ultimate stress in Figure 5.16. Parameters from the simulations of all the Black et al. specimen, the Fell et al. specimen, and the Tremblay et al. specimen are included. Where no measurements are available, nominal values from the AISC manual of steel construction are used. Figure 5.17 shows a histogram of the fiber ultimate strain used in the MEF element models to achieve a good match against experimental response. These distributions can be used in making rational choices for MEF element model parameters in future studies.

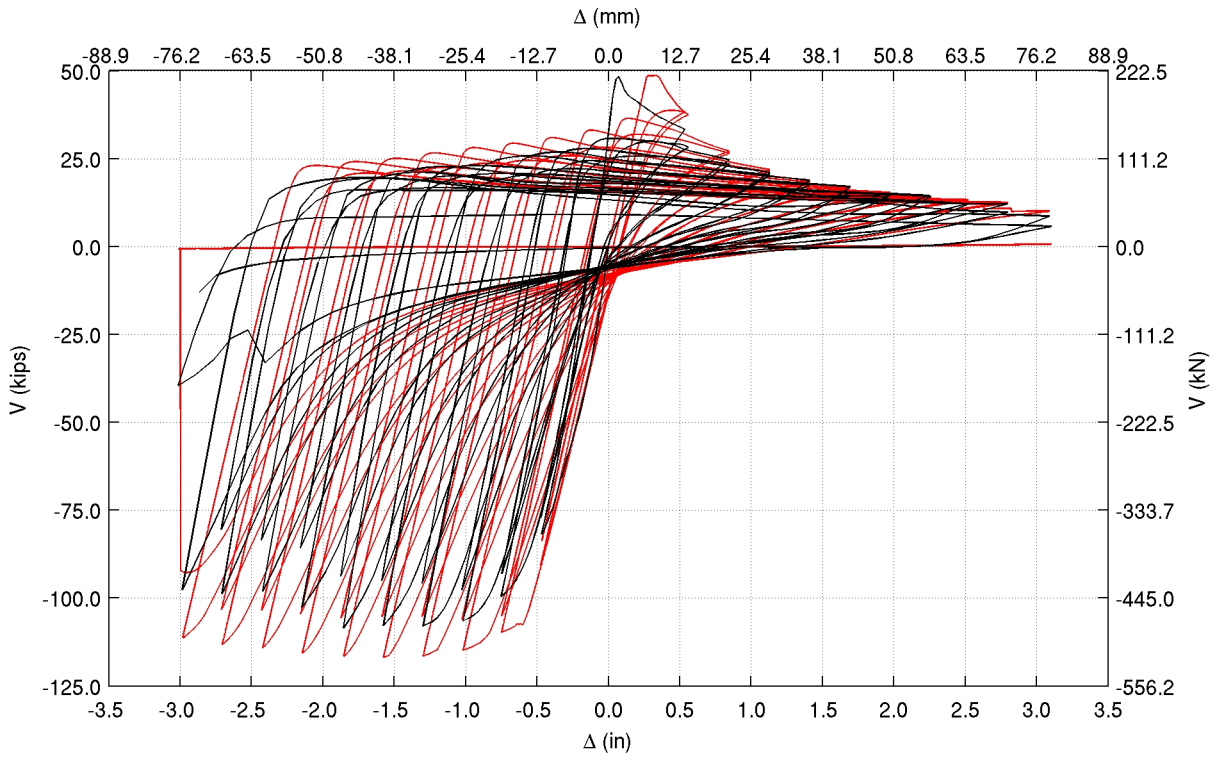

(a)

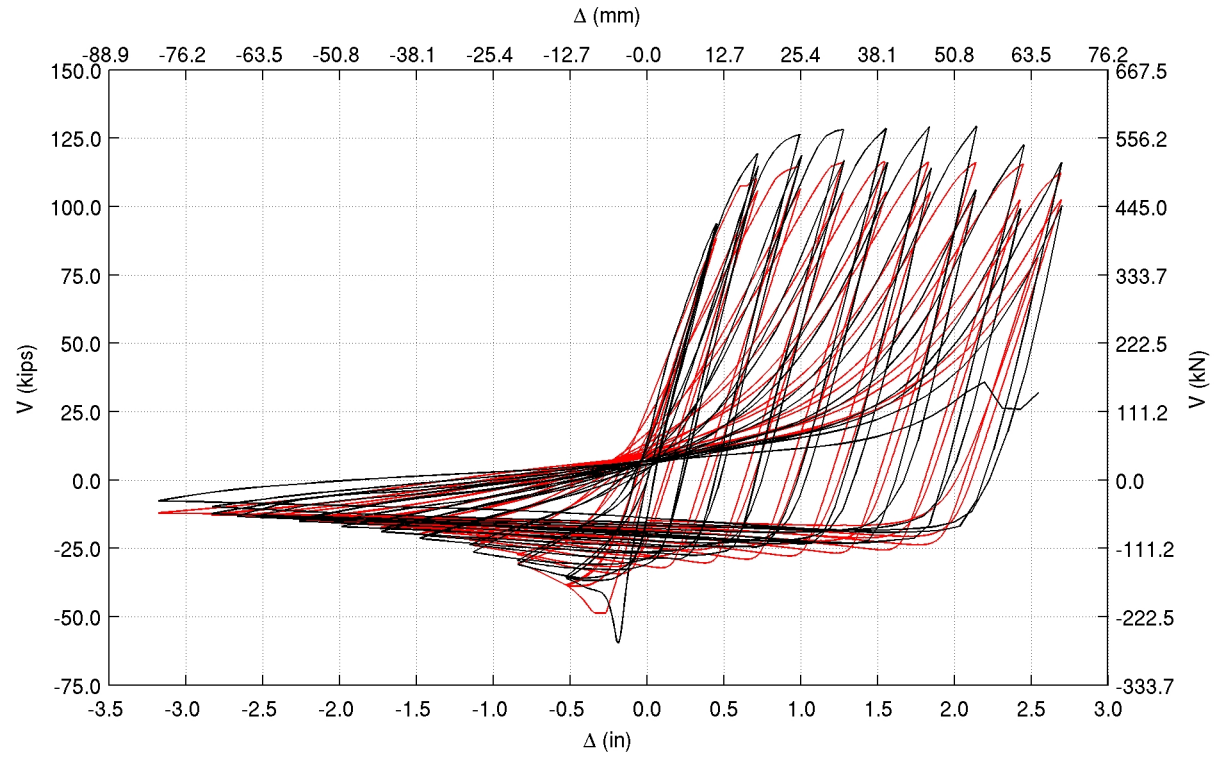

(b)

Figure 5.13: Comparison of simulation against data from Tremblay et al. tests: (a) Specimen S2A and (b) Specimen S2B with RHS102x76x4.8 diagonal – frame sway versus applied lateral force history.

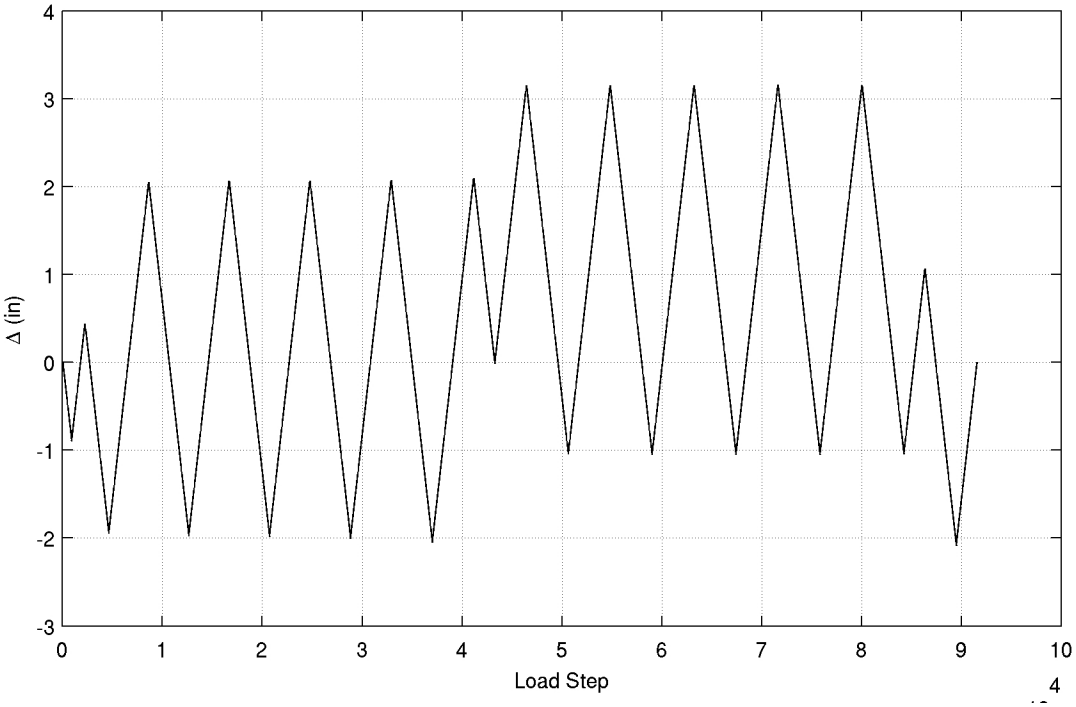

Figure 5.14: Tremblay et al. test S1QA/S1QB on RHS127x76x4.8: Displacement history “H2”

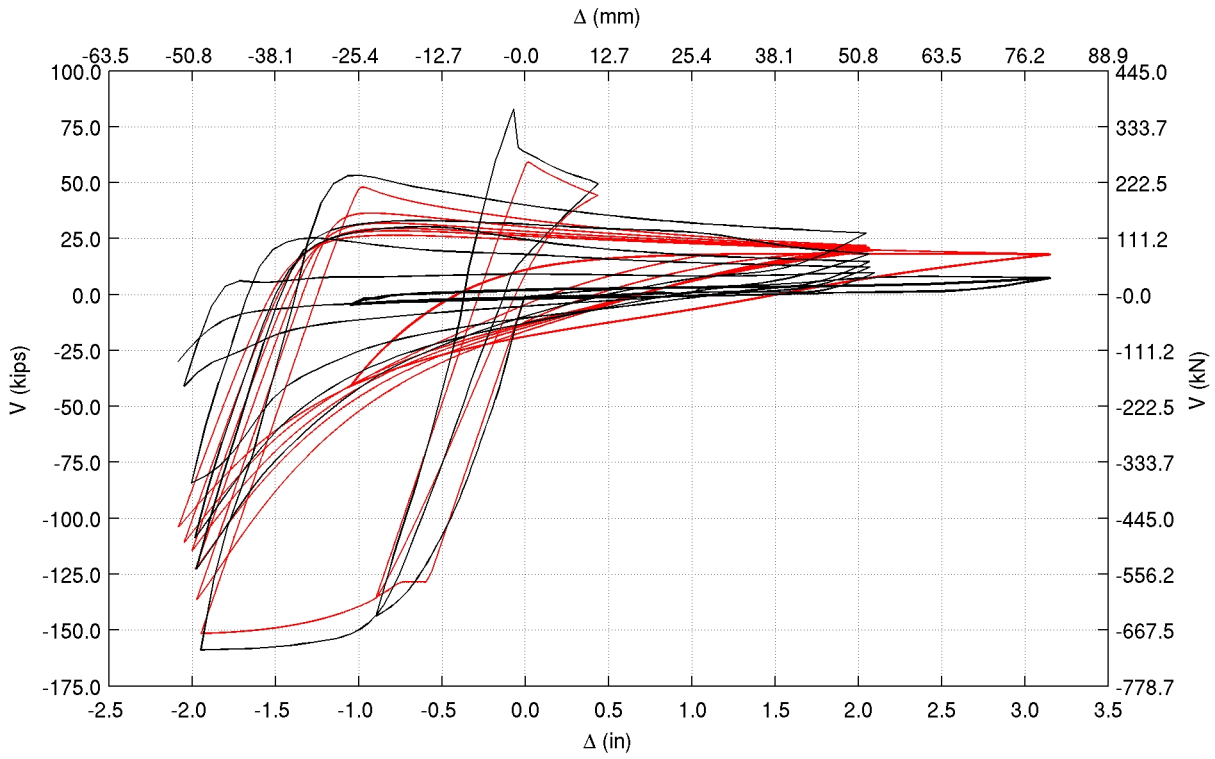

(a)

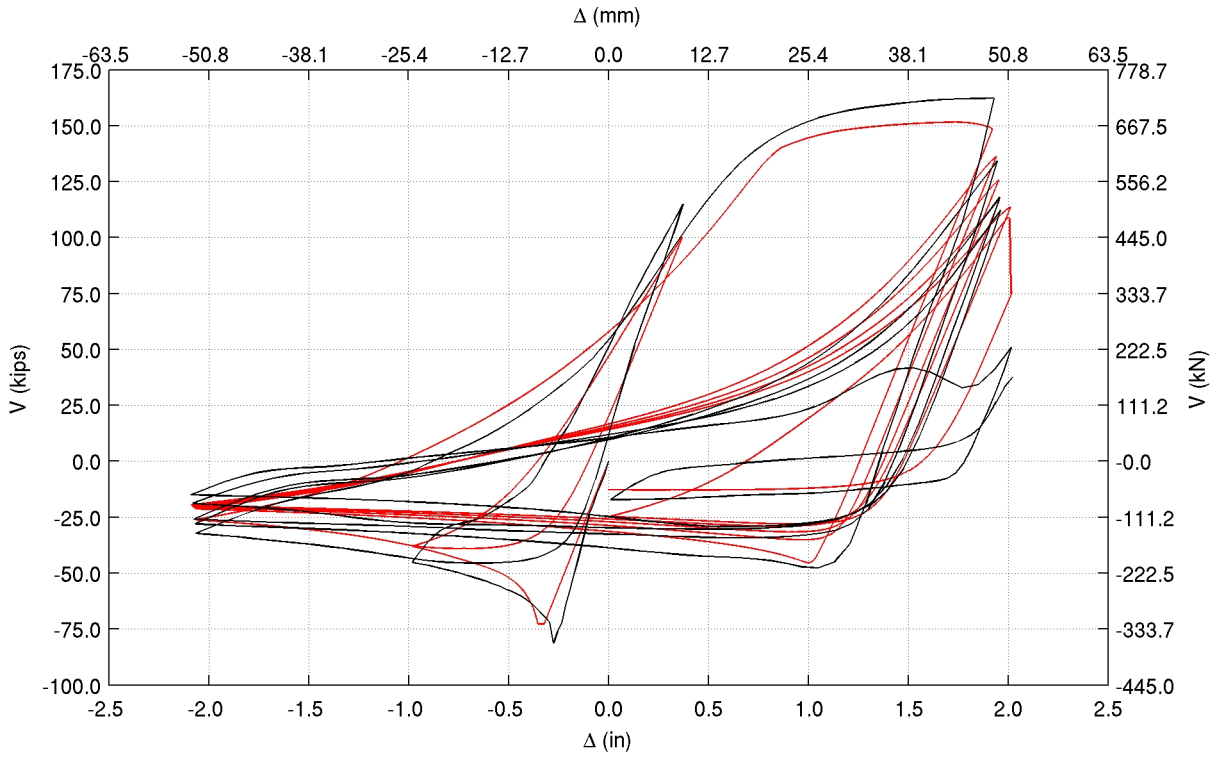

(b)

Figure 5.15: Comparison of simulation against data from Tremblay et al. tests: (a) Specimen S1QA and (b) Specimen S1QB with RHS127x76x4.8 diagonal – frame sway versus applied lateral force history.

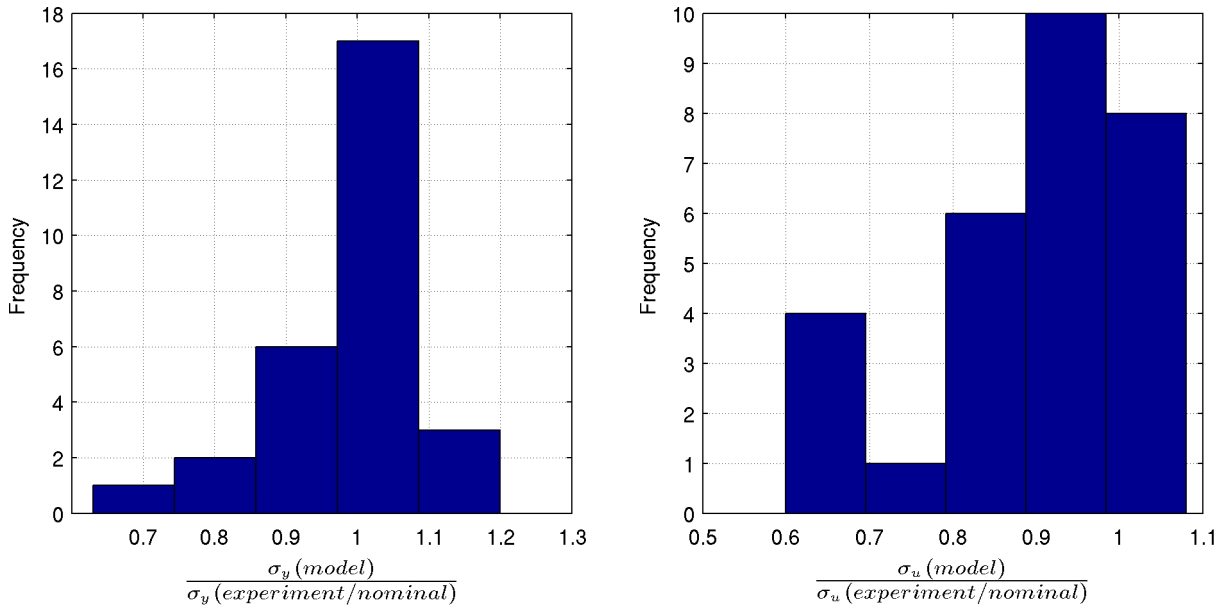

(a) (b)

Figure 5.16: Histogram of the ratio of (a) model yield stress to measured (or nominal if unmeasured) yield stress, and (b) model ultimate stress to measured (or nominal if unmeasured) ultimate stress for all the brace specimen considered in this study (including the Black et al., Fell et al., and Tremblay et al. specimen).

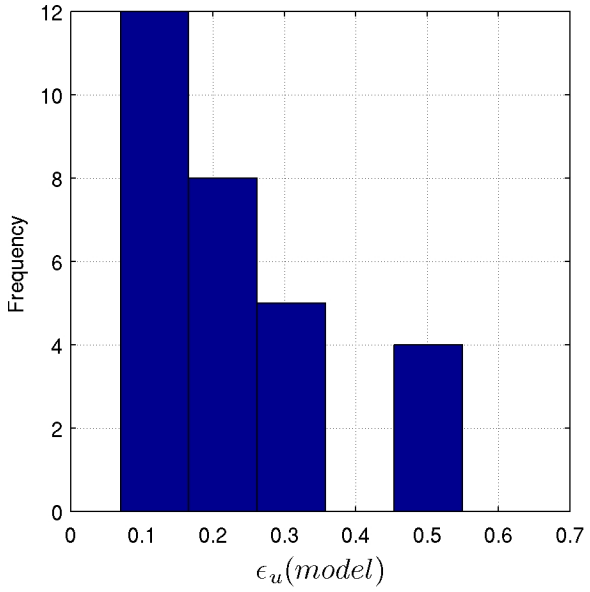

(a)

Figure 5.17: Histogram of the fiber ultimate strain used in the MEF element modeling of all the brace specimen considered in this study (including the Black et al., Fell et al., and Tremblay et al. specimen).

Chapter 6 Analytical simulation of the full-scale pseudodynamic test of a 6-story steel building

In the years 1982–1984, a full-scale six-story braced steel building was designed, constructed, and tested at the Building Research Institute (BRI) in Tsukuba, Japan, under a US-Japan cooperative research program (Foutch et al. 1987; Roeder et al. 1987; Midorikawa et al. 1989b). The building, designed in accordance with both US (UBC 1979) and Japanese design codes, was 15m square in plan (Figure 6.1) with two 7.5m bays in each direction, with a height of 22.38m from the test floor to the top of the roof girders. The test structure consisted of three frames (along grids A, B, and C) parallel to the direction of loading (structure was subjected to single component shaking in the N-S direction). The slab extended beyond grids A and C by 0.5m to the east and west, respectively. A36 steel was used for columns and beams, and A500 Grade B steel was used for the braces. The lateral force-resisting system consisted of concentric K-bracing in the south bay on grid B in each story, in addition to moment-frames in the remaining 5 bays in the loading (N-S) direction. Floor slabs consisted of 165mm concrete poured over a 75mm deep ribbed metal deck. The total weight of the structure including the weight of steel and actuators was 5137kN (913kN in the 2^{nd} floor, 870kN in floors 3–6, and 743kN at the roof). Suitable allowance was made therein for cladding, partitions, and roofing material.

Three pseudodynamic tests were conducted using the N-S component of the Tohoku University accelerogram recorded during the July 12, 1978, Miyagi-Ken-Oki earthquake, which had a peak acceleration of 2.58m/s^2: an "elastic" test with a peak acceleration of 0.65m/s^2, a "moderate" test with a peak acceleration of 2.50m/s^2, and an "inelastic final" test with a peak acceleration of 5.00m/s^2. At the end of the moderate test, limited brace buckling and plastic deformation were noted on the second and third stories, and some cracking was observed in the concrete, but the structure appeared to be in good condition. The structure remained essentially linear-elastic in the fourth, fifth, and sixth stories, although buckling was initiated in the north brace of the fifth story. Due to an unusual connection detail at the K-brace junction on level 1, significant damage was observed in the panel zone region that contained a beam splice. The panel was cut and replaced by a thicker plate that was welded into place using full penetration welds. The final inelastic test was conducted subsequently. Severe brace buckling was noted on the second and third stories during the first few seconds of the acceleration record, with the 2^{nd} story braces buckling out of plane, and the 3^{rd} story braces buckling in plane. Cracking occurred in the braces, which were cold-formed and hence not as ductile. The 3^{rd} story north brace ruptured completely at 11.37s into the seismic record, and both braces in the 2^{nd} story were torn more than 50% at the hinge location, and the test was stopped. Other damage included in-plane buckling of the north braces in the 1^{st} and 4^{th} stories, and minimal out-of-plane buckling of the 5^{th} story north brace. The level 3 and 4 beam splice connection at the K-brace junction experienced the same twisting prying action observed in the level 2 girder during the moderate test, but no fracture occurred.

Two analytical studies were conducted by Midorikawa et al. (1989b, 1989a), and Tang and Goel (1989), using DRAIN-2D (Kanaan and Powell 1973) and DRAIN-2DM (Tang and Goel 1988), respectively, with the brace behavior being modeled by a variant of the Jain et al. (1978, 1978, 1978) brace hysteresis model. Without accounting for fracture both studies under-predicted the 1^{st} story response and over-predicted the 4^{th} and 5^{th} story response. Tang and Goel (1989) do significantly better after accounting for fracture by way of an empirical criterion for the fracture of tubular braces based on axial deformation cycles. They point out the significant impact that fracture sequence has on the ultimate response of the structure. The force carried by a member at the instant of fracture has to be redistributed to other elements and how this redistribution occurs may govern the future state of the structure.

In order to validate the MEF element when used within an assembled structure, a FRAME3D model of the 6-story test structure is developed (Figure 6.1(a)), and subjected to the single component shaking from the N-S component of the Miyagi-Ken-Oki record. The replication of only the final inelastic test is attempted here. The record is scaled to give a peak acceleration of 5.00m/s^2. The first three N-S modes of the model have periods of 0.636s, 0.235s, and 0.137s, respectively (compared to 0.620s, 0.225s, and 0.133s, respectively, for the test structure at the start of the final test). Consistent with the modal damping used in the test setup (Foutch et al. 1987), the Rayleigh damping parameters were chosen to give first and third mode damping of 2%. The observed natural periods of the first and third N-S modes following the final test were 0.84s and 0.16s, respectively, and these values are used to compute the Rayleigh mass and stiffness proportional damping coefficients for the model. In the first analysis pass ("base model"), performed assuming full continuity at brace ends and no geometric imperfection in the braces, the results are quite similar to the results from the Midorikawa study, i.e., under-estimation of the first story response and over-estimation of the fourth and fifth story responses (Figure 6.2).

To get a better match in the model and observed responses, the model parameters of some braces in the base model were tuned to change the buckling sequence. These changes included the introduction of a major direction imperfection (0.4%L) in the 1^{st} story North brace, making the brace-to-beam connections at the 1^{st}, 2^{nd}, and 3^{rd} compliant by reducing the end fixities to 80%, 50%, and 60%, respectively, dropping the fiber strain-hardening initiation strain from 0.012 to 0.002, and reducing the fiber rupturing strain slightly. The MEF element model parameters for braces in the base and tuned models are summarized in Table 6.1. The model parameters for columns and beams in both models are identical to those used to model braces in the base model. The yield stress of the material is an exception in this regard. Coupon test results for column and beam sections are available (Midorikawa et al. 1989b) and used in both models. Ultimate stresses are not available from the experiments, and are assumed to be 80ksi for brace sections, 65ksi for column sections, and 67ksi for beam sections in both models. While cracking was observed during the test in the 2^{nd} story north (at 8.2s) and south braces (at 10.8s), and the 3^{rd} story north brace (at 8.2s), fiber rupture occurs in the simulation in the 2^{nd} story north brace at 8.145s, and in the 3^{rd} story north brace at 11.25s. The story shear comparison (Figure 6.3), the interstory drift ratio comparison (Figure 6.4), and the interstory drift ratio–story shear hysteresis comparisons (Figure 6.5) are quite good, and in general superior to former studies. The fine-tuning of the model that was necessary to achieve this degree of agreement between the observed and computed responses points to the highly sensitive nature of braced frame performance. Subtle

Brace Location	Section	Model Parameters							
		σ_y (ksi)	σ_u (ksi)	ϵ_u	ϵ_{sh}	e_{min} (%L)	e_{maj} (%L)	FFB	FFT
Base Model									
1^{st} Story South	TS6x6x1/2	62.30	80	0.16000	0.012	0.0005	0.0005	1.0	1.0
1^{st} Story North	TS6x6x1/2	61.73	80	0.16000	0.012	0.0005	0.0005	1.0	1.0
2^{nd} Story South	TS6x6x1/4	55.33	80	0.16000	0.012	0.0005	0.0005	1.0	1.0
2^{nd} Story North	TS6x6x1/4	56.32	80	0.16000	0.012	0.0005	0.0005	1.0	1.0
3^{rd} Story South	TS6x6x1/4	55.33	80	0.16000	0.012	0.0005	0.0005	1.0	1.0
3^{rd} Story North	TS6x6x1/4	58.32	80	0.16000	0.012	0.0005	0.0005	1.0	1.0
4^{th} Story South	TS5x5x1/4	56.18	80	0.16000	0.012	0.0005	0.0005	1.0	1.0
4^{th} Story North	TS5x5x1/4	56.18	80	0.16000	0.012	0.0005	0.0005	1.0	1.0
5^{th} Story South	TS5x5x3/16	55.19	80	0.16000	0.012	0.0005	0.0005	1.0	1.0
5^{th} Story North	TS5x5x3/16	55.19	80	0.16000	0.012	0.0005	0.0005	1.0	1.0
6^{th} Story South	TS4x4x3/16	61.59	80	0.16000	0.012	0.0005	0.0005	1.0	1.0
6^{th} Story North	TS4x4x3/16	61.59	80	0.16000	0.012	0.0005	0.0005	1.0	1.0
Tuned Model									
1^{st} Story South	TS6x6x1/2	62.30	80	0.148005	0.002	0.0005	0.0005	1.0	0.8
1^{st} Story North	TS6x6x1/2	61.73	80	0.148005	0.002	0.0005	0.4005	1.0	0.8
2^{nd} Story South	TS6x6x1/4	55.33	80	0.148005	0.002	0.0005	0.0005	1.0	0.5
2^{nd} Story North	TS6x6x1/4	56.32	80	0.148005	0.002	0.0005	0.0005	1.0	0.5
3^{rd} Story South	TS6x6x1/4	55.33	80	0.148005	0.002	0.0005	0.0005	1.0	0.6
3^{rd} Story North	TS6x6x1/4	58.32	80	0.148005	0.002	0.0005	0.0005	1.0	0.6
4^{th} Story South	TS5x5x1/4	56.18	80	0.148005	0.002	0.0005	0.0005	1.0	1.0
4^{th} Story North	TS5x5x1/4	56.18	80	0.148005	0.002	0.0005	0.0005	1.0	1.0
5^{th} Story South	TS5x5x3/16	55.19	80	0.148005	0.002	0.0005	0.0005	1.0	1.0
5^{th} Story North	TS5x5x3/16	55.19	80	0.148005	0.002	0.0005	0.0005	1.0	1.0
6^{th} Story South	TS4x4x3/16	61.59	80	0.148005	0.002	0.0005	0.0005	1.0	1.0
6^{th} Story North	TS4x4x3/16	61.59	80	0.148005	0.002	0.0005	0.0005	1.0	1.0

Table 6.1: MEF element model parameters used for the braces in the BASE and TUNED models. Listed parameters are fiber yield stress (σ_y), fiber ultimate stress (σ_u), fiber ultimate strain (ϵ_u), fiber strain-hardening initiation strain, ϵ_{sh}, brace out-of-plane eccentricity (e_{min}), brace in-plane eccentricity (e_{maj}), and fixity factors at the bottom (FFB) and top (FFT) of the brace. An elastic modulus E of 29000ksi, and a tangent modulus at the initiation of strain hardening E_{sh} of 580ksi is used for all elements in both models.

changes in brace properties could lead to dramatically different dynamic behavior, and blind predictions of braced frame performance will have significant uncertainties. In this respect, the option to probabilistically describe the fiber fracture strain, implemented in FRAME3D, might prove quite useful.

The hysteretic behavior of braces during the analysis is illustrated in axial force versus minor and major direction lateral displacement histories in Figures 6.6–6.9. In-plane buckling occurs in the north brace of stories 1–5, and the south brace of stories 2 and 3. Out-of-plane buckling is not seen in any of the braces. In the test, out-of-plane buckling was observed in both braces of the 2^{nd} story (accompanied by cracking), and the north brace of the 5^{th} story, and in-plane buckling occurred in both braces of the 3^{rd} story (resulting in rupture and complete severing of the north brace), the 1^{st} story north brace, and both braces of the 4^{th} story. Considering that all the brace sections are square tubes, the differences between test and model results (in as far as in-plane versus out-of-plane buckling is concerned) are not of any practical significance. The maximum lateral deflection observed in any brace was 240mm in the test, but as high as 375mm in the simulation. The FRAME3D model can be accessed at http://virtualshaker.caltech.edu.

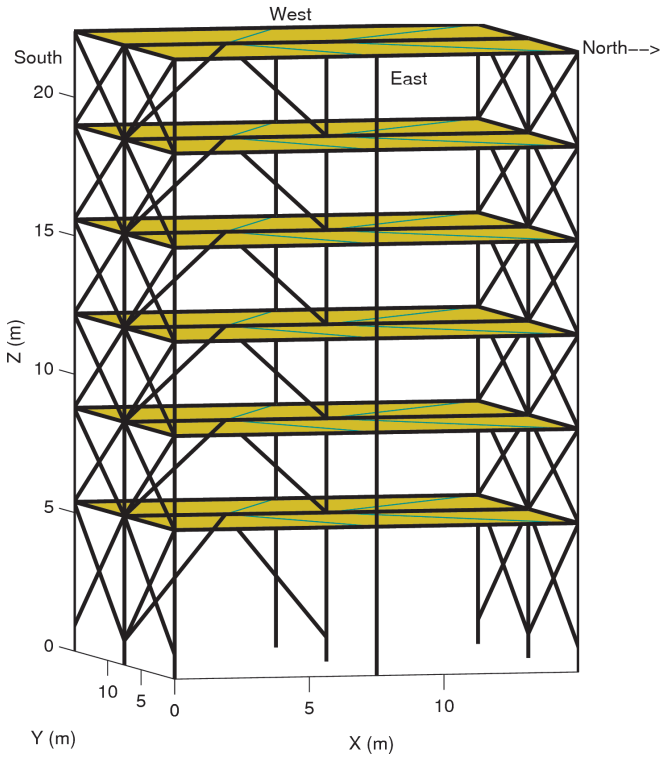

(a)

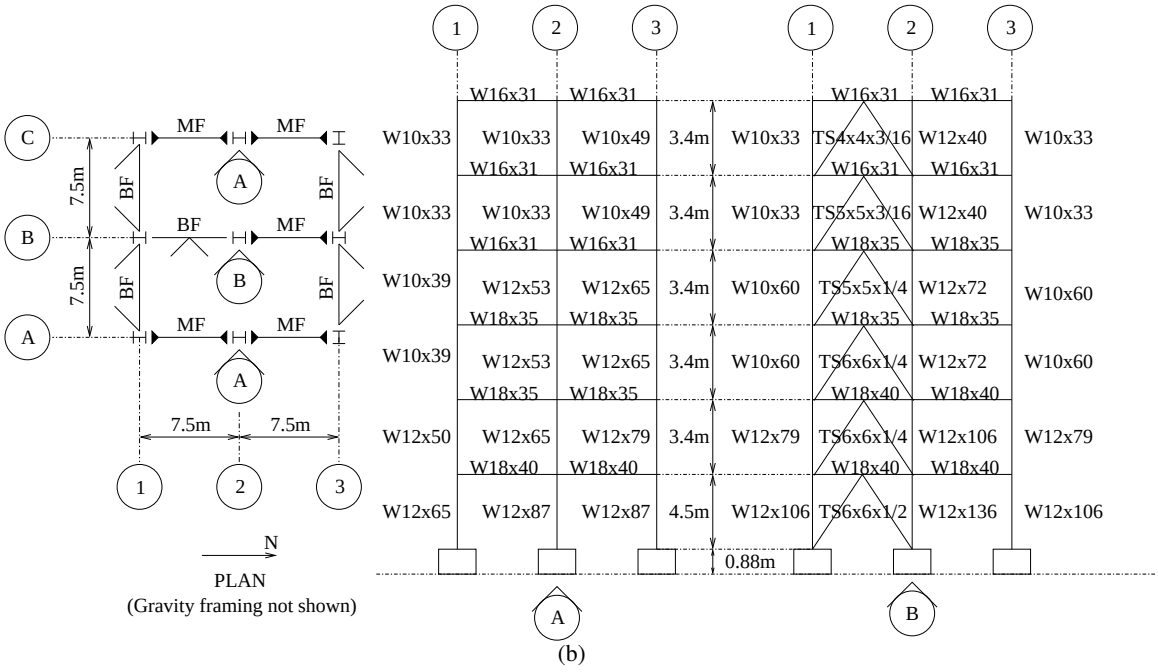

(b)

Figure 6.1: 6-story steel braced structure tested under the US/Japan cooperative research program: (a) FRAME3D model. (b) Plan and elevations. Primary lateral-force resistance in the loading direction came from a single bay braced frame (BF), although beams in the other bays (MF) were moment-connected to the columns, providing supplementary lateral resistance.

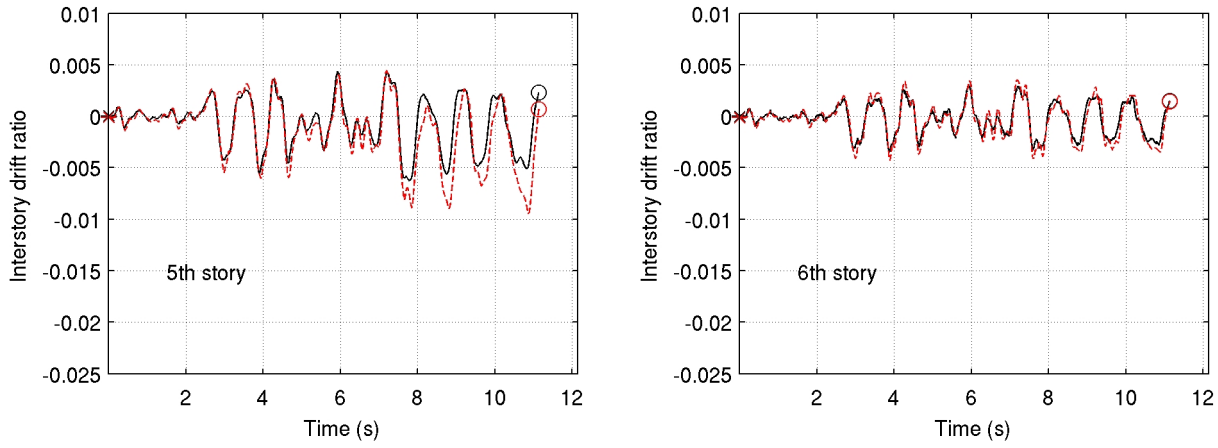

(a)

(b)

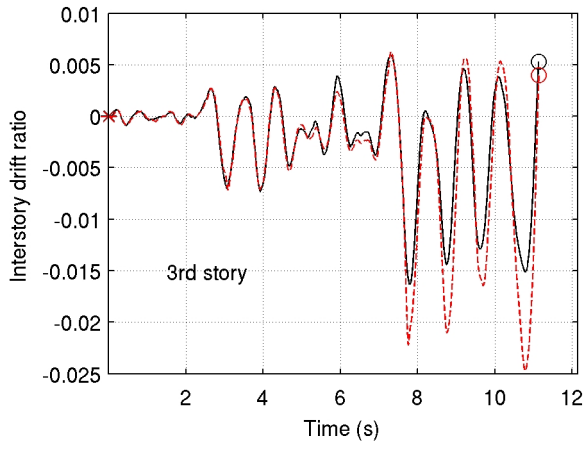

(c)

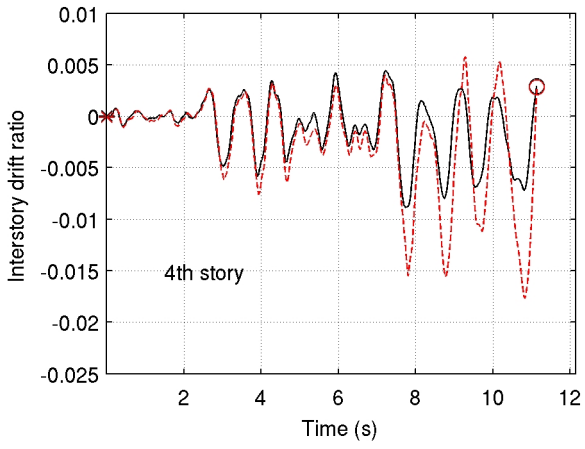

(d)

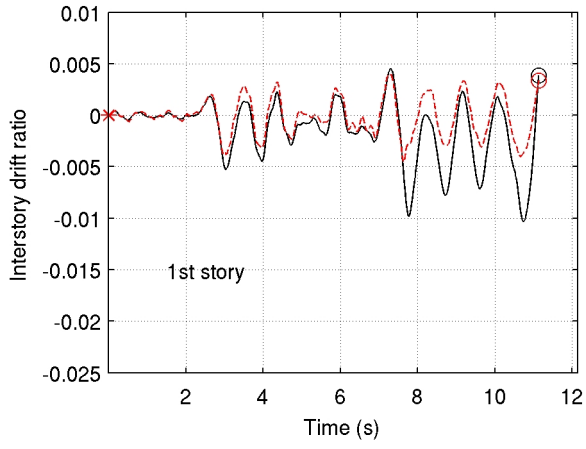

(e)

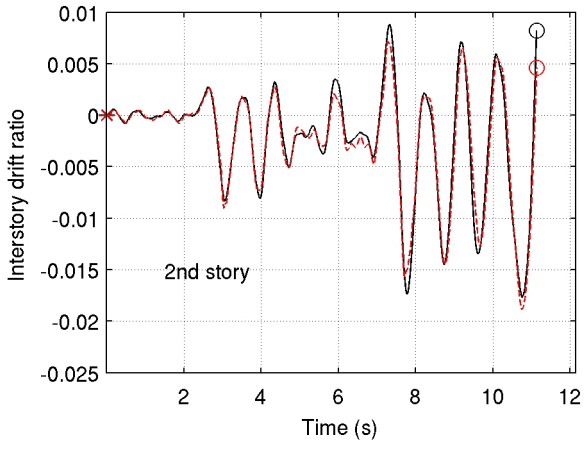

(f)

Figure 6.2: Comparison of analytical and experimental inter-story drift ratio time-series of the 6-story test structure – **Base model**.

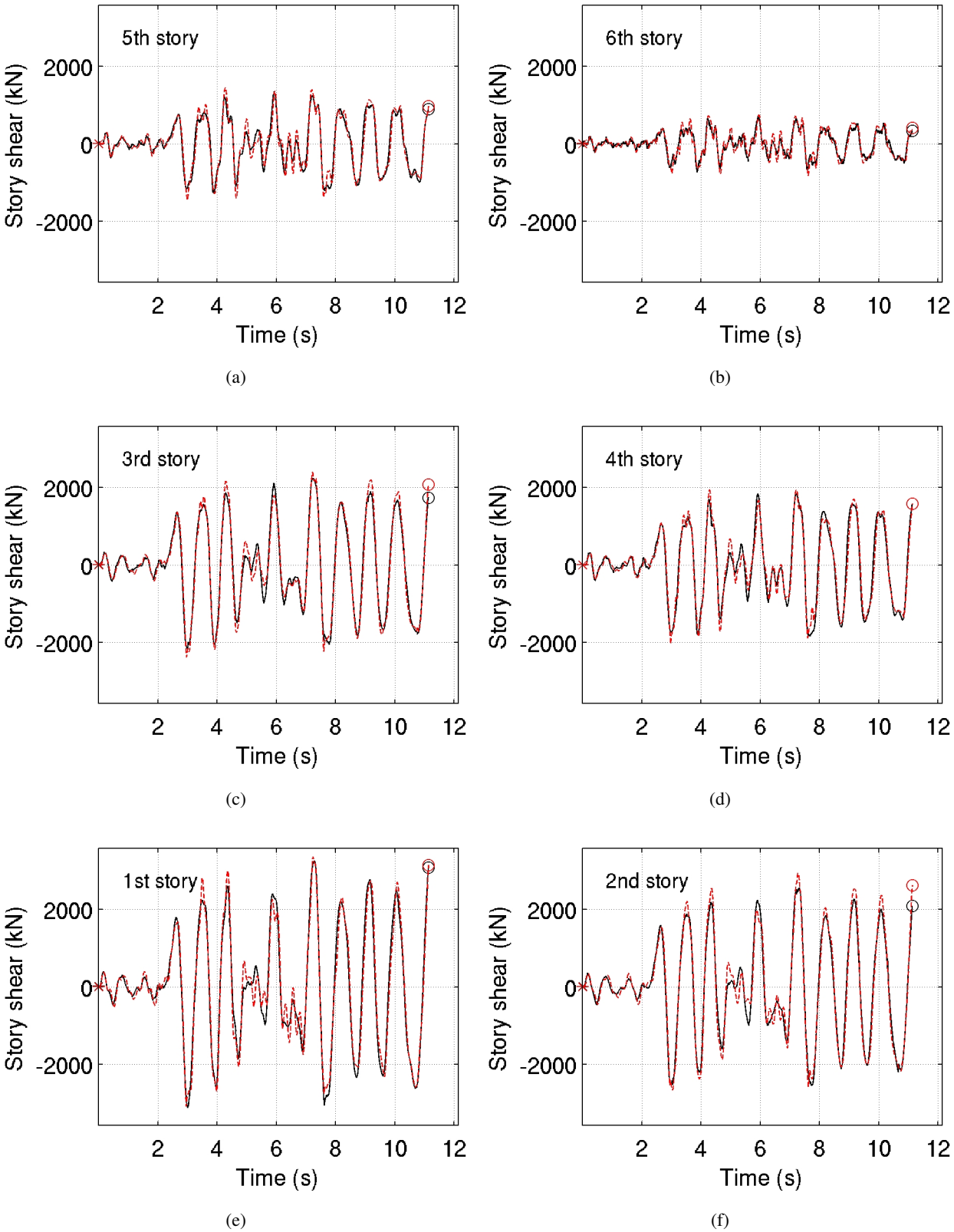

Figure 6.3: Comparison of analytical and experimental story shears of the 6-story test structure – **Tuned model**.

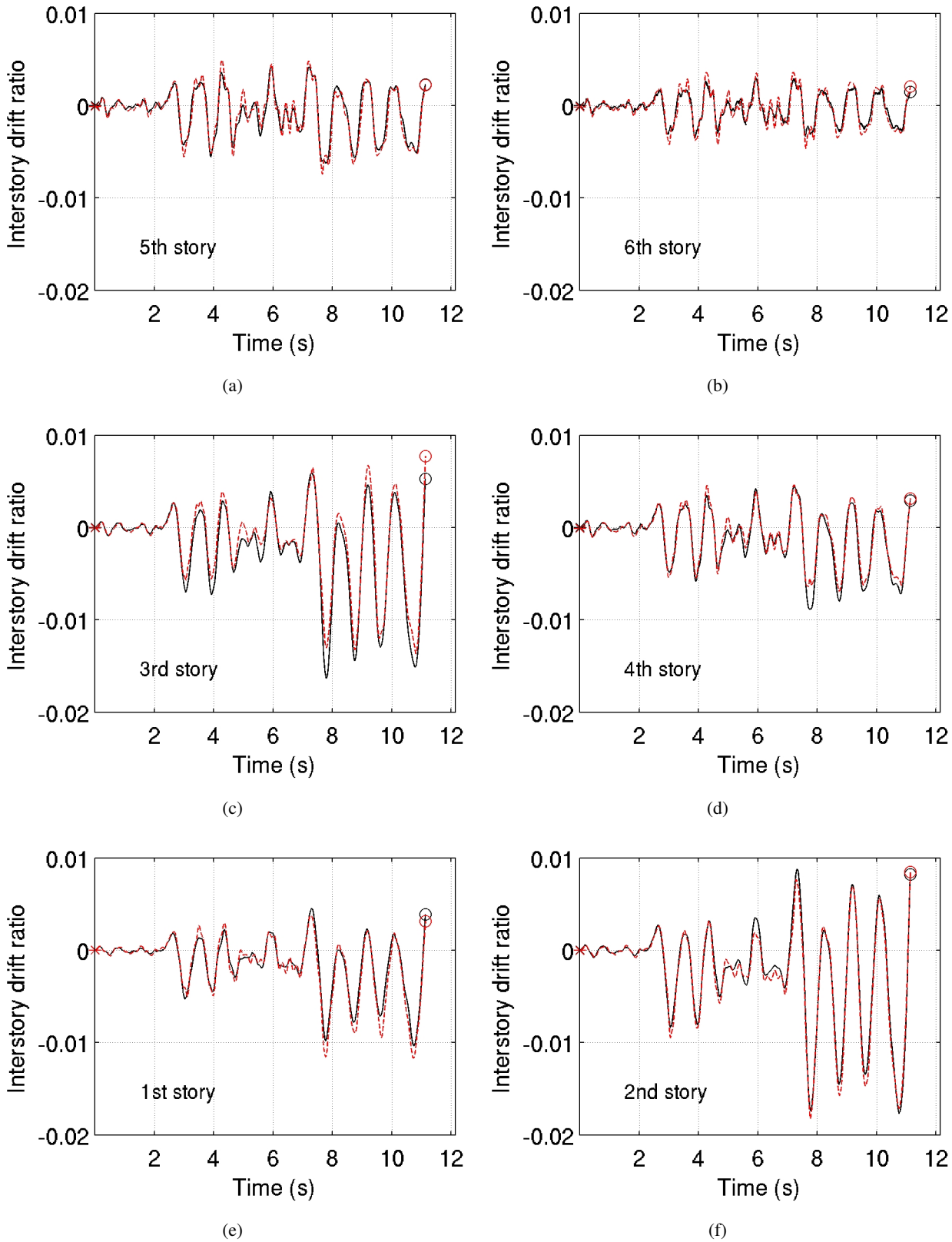

Figure 6.4: Comparison of analytical and experimental inter-story drift ratio time-series of the 6-story test structure – **Tuned model**.

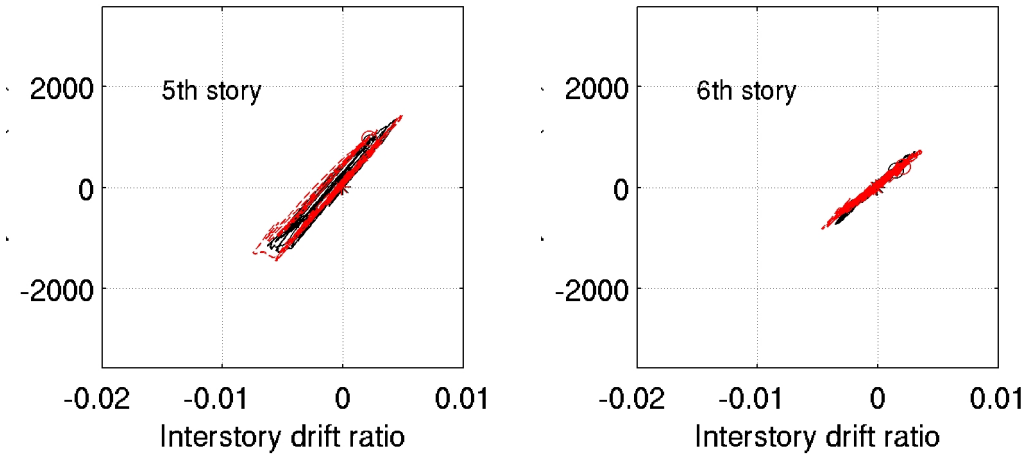

(a)

(b)

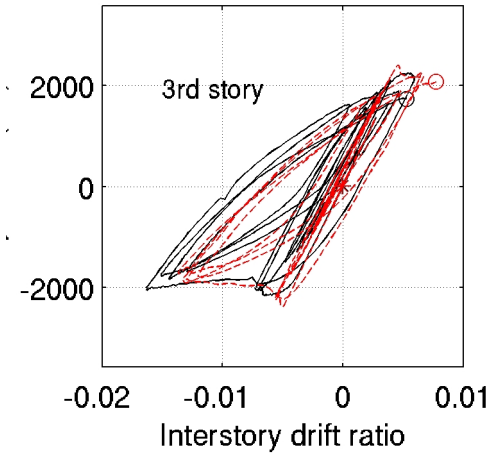

(c)

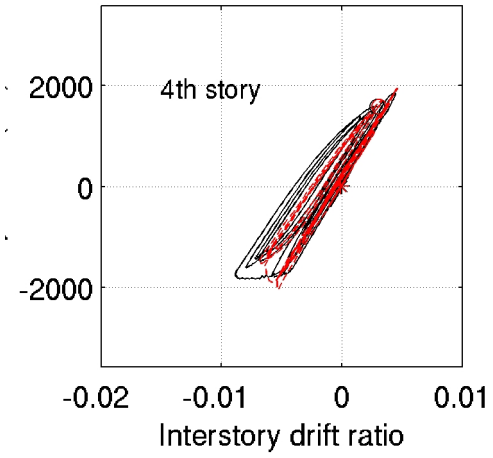

(d)

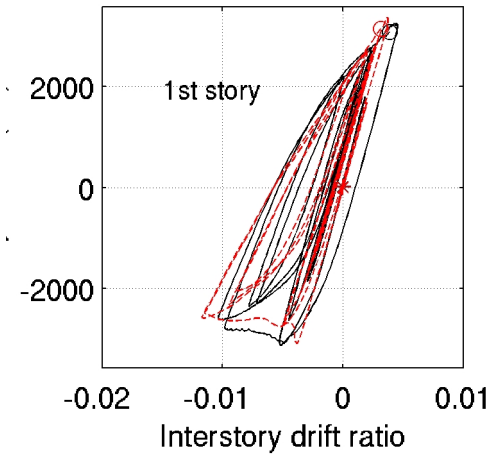

(e)

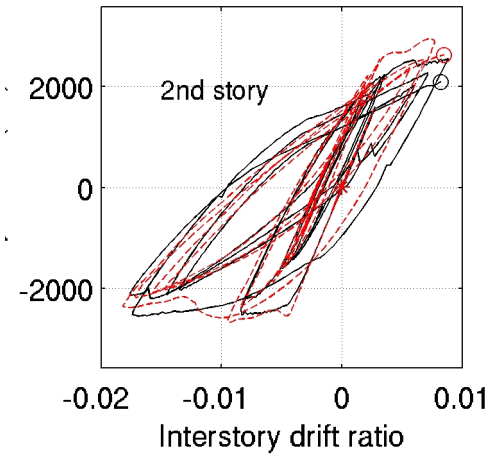

(f)

Figure 6.5: Comparison of analytical and experimental inter-story drift ratio versus story shear of the 6-story test structure – **Tuned model**.

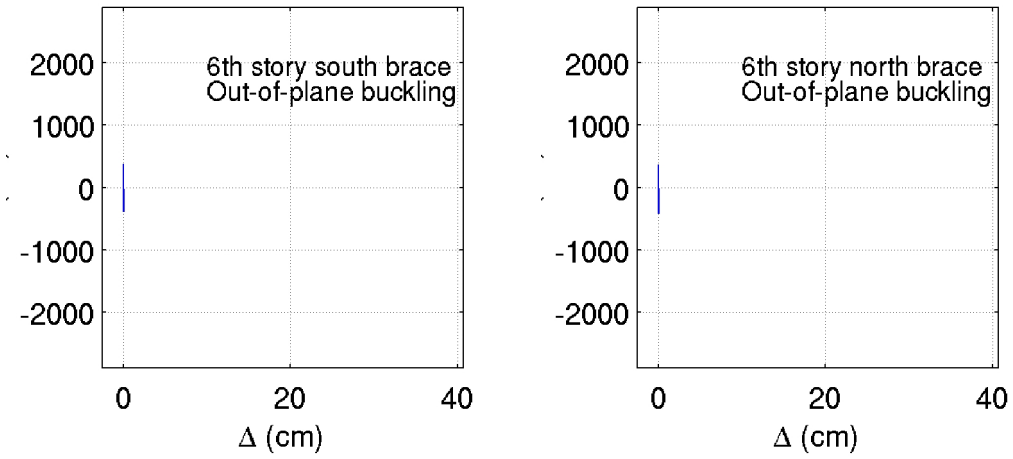

(a)

(b)

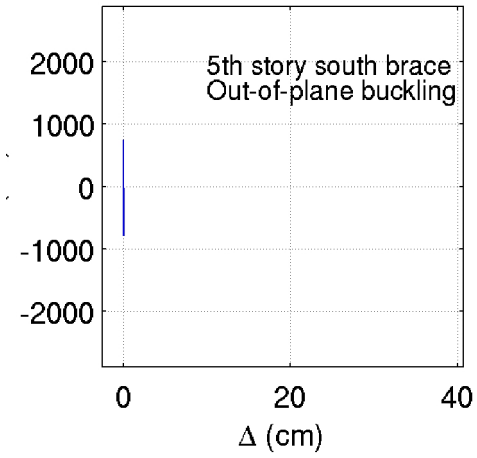

(c)

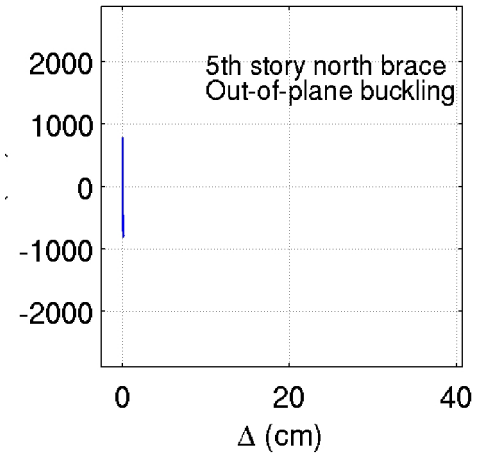

(d)

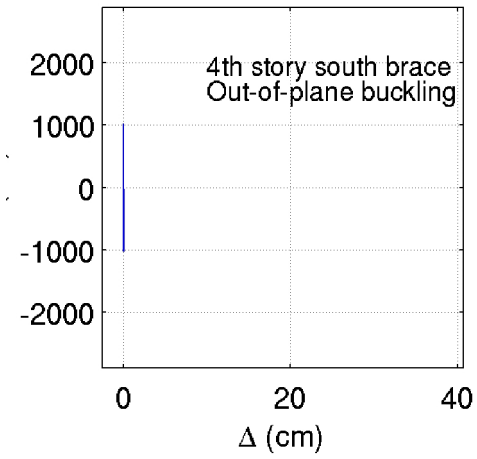

(e)

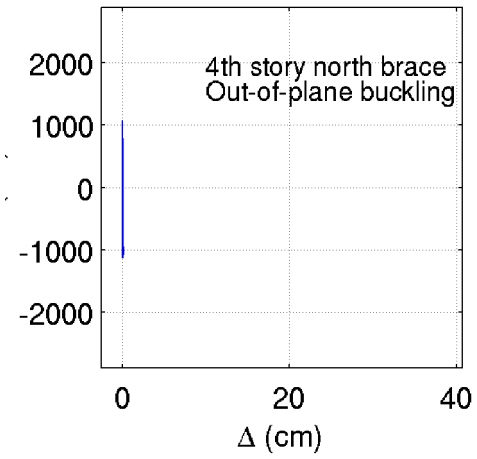

(f)

Figure 6.6: Simulated brace out-of-plane lateral displacement versus axial force histories in stories 4–6 of the tuned model. Buckling is not seen in any cases.

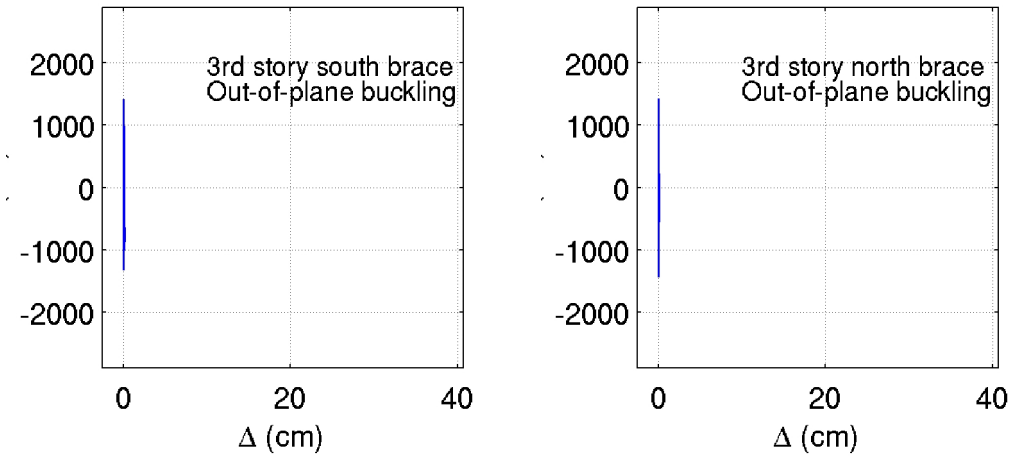

(a)

(b)

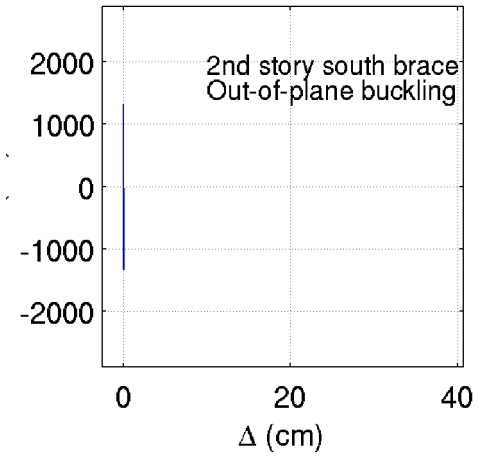

(c)

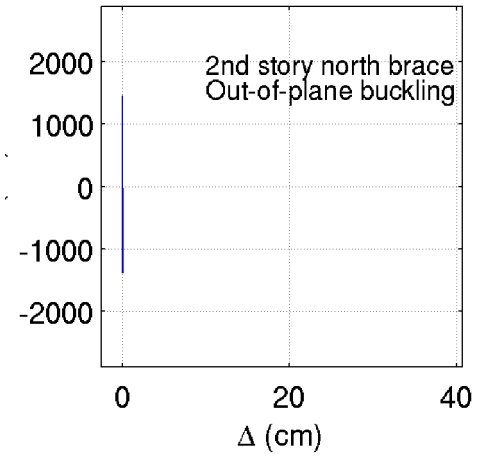

(d)

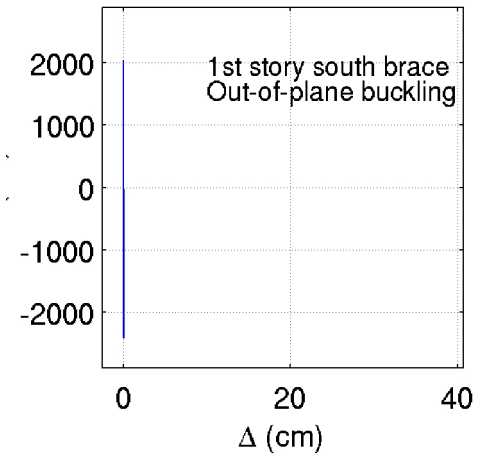

(e)

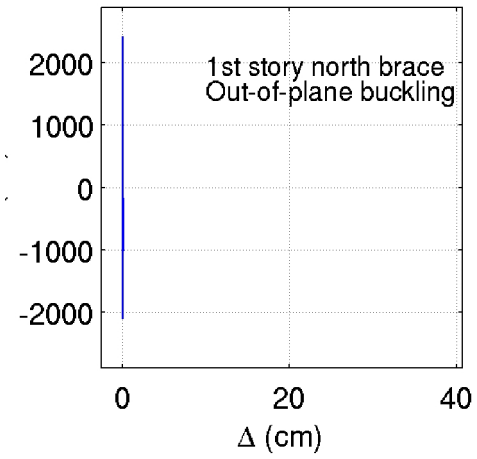

(f)

Figure 6.7: Simulated brace out-of-plane lateral displacement versus axial force histories in stories 1–3 of the tuned model. Buckling is not seen in any cases.

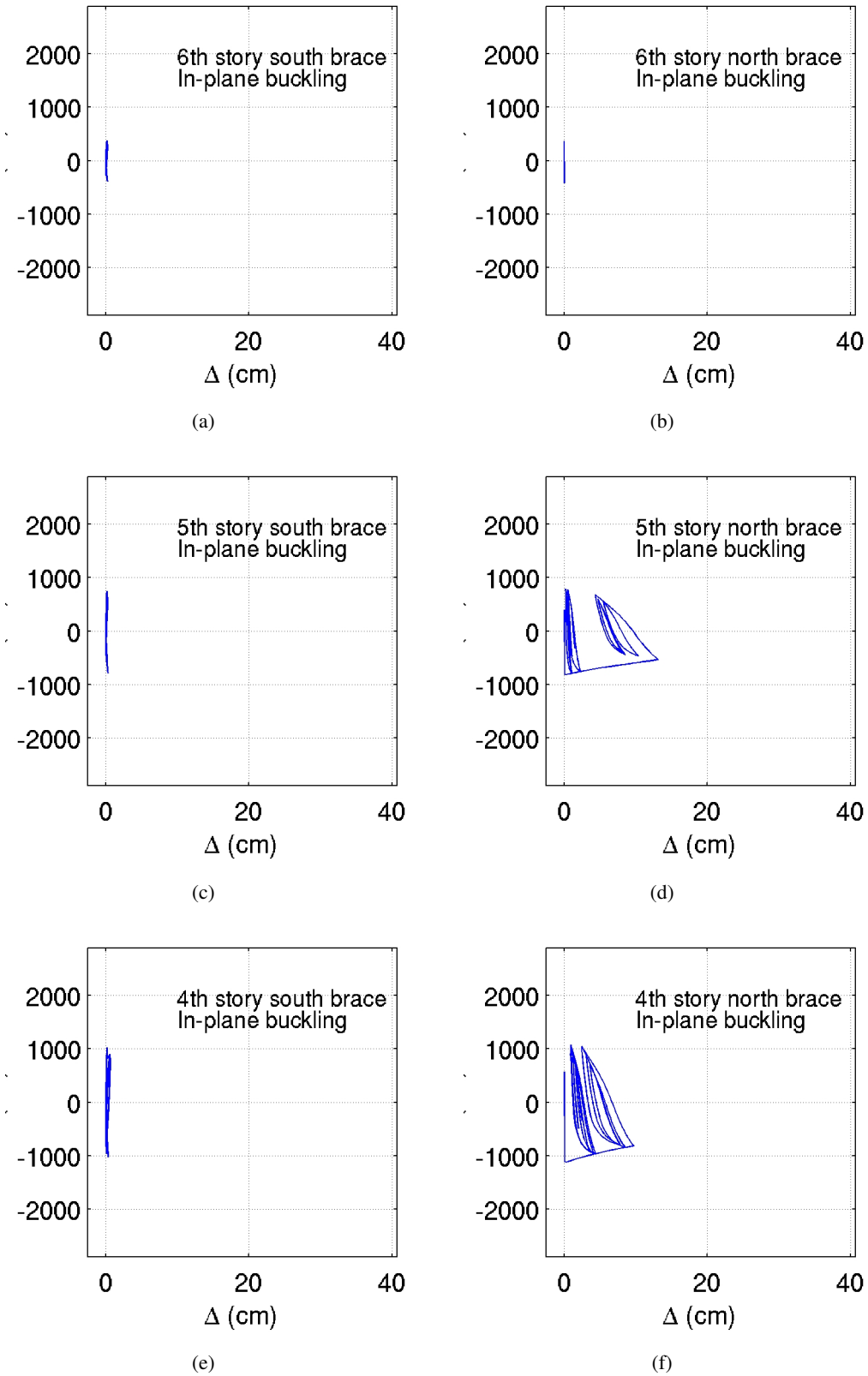

Figure 6.8: Simulated brace in-plane lateral displacement versus axial force histories in stories 4–6 of the tuned model. In-plane buckling occurs in the north braces of stories 4 and 5.

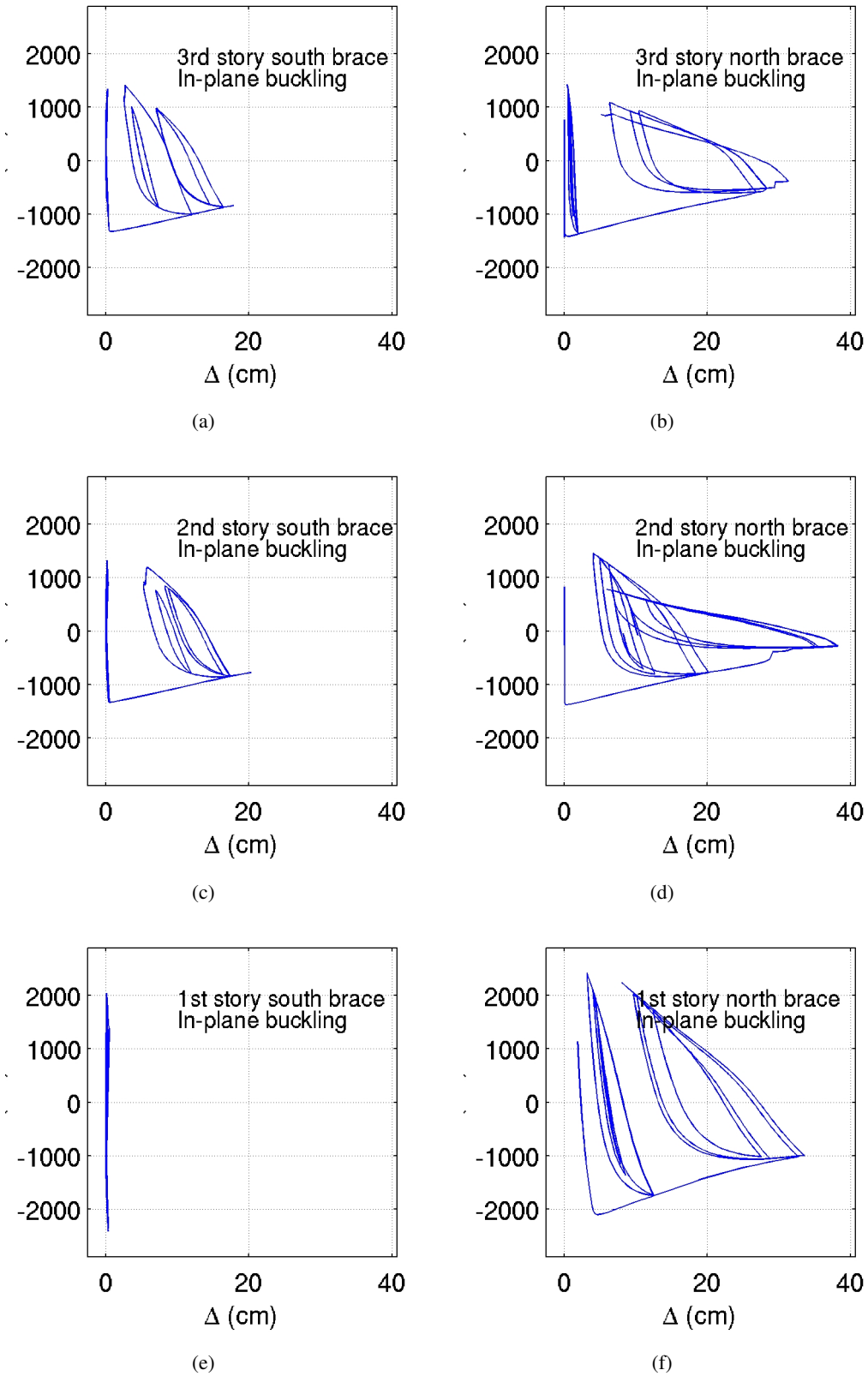

Figure 6.9: Simulated brace in-plane lateral displacement versus axial force histories in stories 1–3 of the tuned model. In-plane buckling is seen in the north and south braces of stories 2 and 3, and the north brace of the first story.

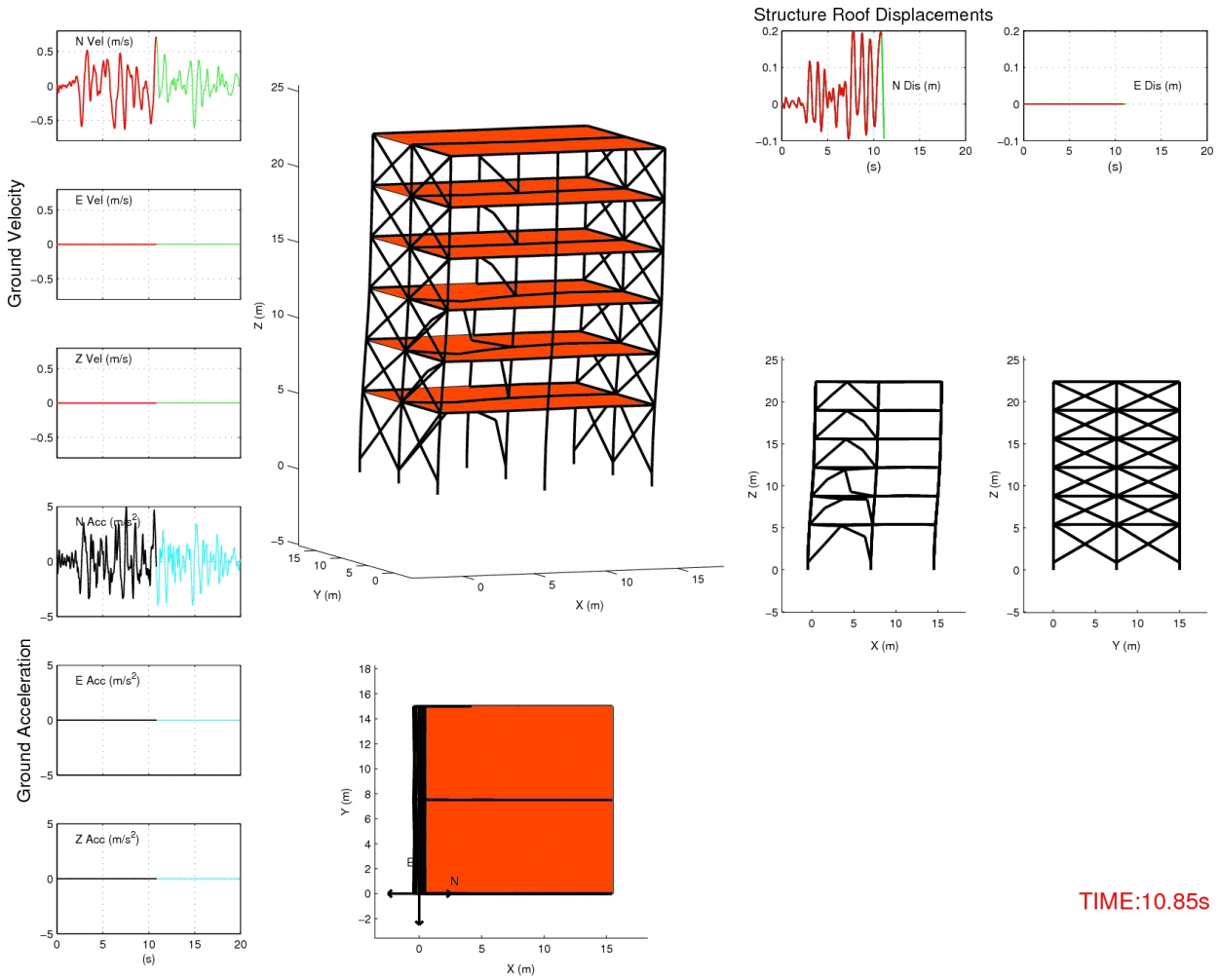

Figure 6.10: Snapshot of the deformed shape of the FRAME3D model of the 6-story test structure at time 10.85s from the start of the Miyagi-Ken-Oki shaking (deformations exaggerated by a factor of 5). Note the in-plane buckling of the north brace of stories 1–5, and the south brace of stories 2 and 3 on the elevation views. Out-of-plane buckling is not seen in any of the braces. The ground motion velocity and acceleration waveforms, and the roof North and East displacement histories are also shown. A movie of the shaking of the model can be downloaded from http://krishnan.caltech.edu

Chapter 7 A Proposed Benchmark Problem to Evaluate the Collapse-Prediction Capability of Competing Methodologies

The water-tank presented here is a fictional structure that has not been designed according to any code, but created to demonstrate the ability of FRAME3D to simulate collapse (Figure 7.1). The tank is configured such that it has a unique collapse mechanism that is independent of the nature of the ground motion, hence it is an ideal candidate for a benchmark problem to evaluate the collapse-prediction capability of competing methodologies. The tank is 160' (48.76m) high and has a capacity of 66390 cu.ft. (1880 cu.m.). The total weight of the structure is 6248 Kips (27802 kN) which includes a full tank of water, a 12" (406mm) thick concrete floor slab with a 4" (100mm) concrete topping for water-proofing, a 12" (305mm) thick concrete roof slab, a 12" (305mm) thick concrete tank wall, and the weight of the steel frame. The four mega-columns are made of B30x30x0.625 tube sections (the non-standard symbol "B" is used to indicate that nominal dimensions and not the true dimensions are used in the model); the beams and braces are made of B14x14x0.625 tube sections; the horizontal diagonals are made of B12x12x0.5 tube sections; and the water-tank perimeter stub columns, vertical braces, and tank floor & roof beams are made of B20x20x0.625 tube sections. The X-braces are assumed to not be connected at the intersection points (and hence there is no restraint to in-plane or out-of-plane buckling at these points). All sections are assumed to be of ASTM-A501 steel with a yield stress of 46ksi and an ultimate stress of 58ksi. Full continuity is assumed at all the connections and a fixed boundary condition is assumed for the base of the water-tank. Due to the structural symmetry, the periods corresponding to the two orthogonal fundamental translational modes is 1.31s, whereas the period of the first torsional mode is 0.72s. If the mass of the members is neglected and all the mass is assumed to be concentrated in the tank portion of the structure, then the structure can be idealized as a 3 degree-of-freedom system (mass translation in X, Y and Z directions). The motion of the mass would lead to overturning moments that are greatest at the base of the tank. So the mega-columns at the bottom are the most stressed; even though the outward flare in the columns increases the lever arm to resist the overturning moment, it is not sufficiently large to make up for the increase in the overturning moment over the height of the tower. At the same time, the bottom columns have slightly longer clear spans when compared to the upper columns. This is because the upper columns have finite-sized joints at both their ends, whereas the bottom columns have finite-sized joints only at the top, with the bottom end being connected to a base plate at elevation zero (see Figure 7.1). The sloping columns also result in longer spans for the bottom braces. Maintaining the size of all columns and braces constant would then necessarily ensure that the collapse of the tank always occurs due to column and brace buckling at the bottom and subsequent overturning due to $P-\Delta$ effects. For benchmarking purposes, a FRAME3D model of the tank, using MEF elements to model all the members (σ_y = 46ksi, σ_u = 58ksi, E_{sh} = 580ksi, ϵ_{sh} = 0.012, ϵ_u = 0.16, minor and major direction eccentricity of 5x10^{-6}L), is subjected to 3-component shaking from the 1995 Kobe earthquake Takatori record, scaled down by a factor of 0.32. Response time-histories are given in Appendix E. 5.6s or so into

the record, the forward phase of the largest near-source pulse initiates buckling, though just barely, in the bottom mega-column at the north-east corner [Figures E.3(b) and E.3(d)]. Before buckling can progress, ground velocity changes direction and the structure is stabilized. However, the reverse phase of the same ground motion pulse induces severe buckling on both bottom mega-columns on the west face of the tower [Figures E.2(a), E.2(c), E.3(a), and E.3(c)], followed almost instantaneously by bottom brace buckling on one of the braces of the west face [Figures E.7(b), and E.7(d)]. Multiple fibers rupture in the two buckled mega-columns starting at 6.34s. Fibers in the middle segment rupture first, followed by fibers in the end segments. The asymmetric buckling of columns on the west face results in a tilt in the structure. Subsequent shaking causes the braces on the south and the north faces of the tower to buckle sequentially at 9.6s, 12.5s, and 14.35s [Figures E.4(a), E.4(c), E.5(a), E.5(c), E.5(b), and E.5(d)]. The loss of lateral force-resisting capacity due to buckling of the braces results in excessive $P - \Delta$ effects and causes the water-tank to collapse. Snapshots of the collapsing water-tank are shown in Figures 7.2 - 7.9. At time 16s, the stiffness matrix becomes so ill-conditioned that the program is unable to follow the collapse of the structure any further. An animation of the tank response can be found online at http://krishnan.caltech.edu, while the FRAME3D model can be accessed at http://virtualshaker.caltech.edu. Nonlinear time-history analysis can be performed remotely on the model through this gateway.

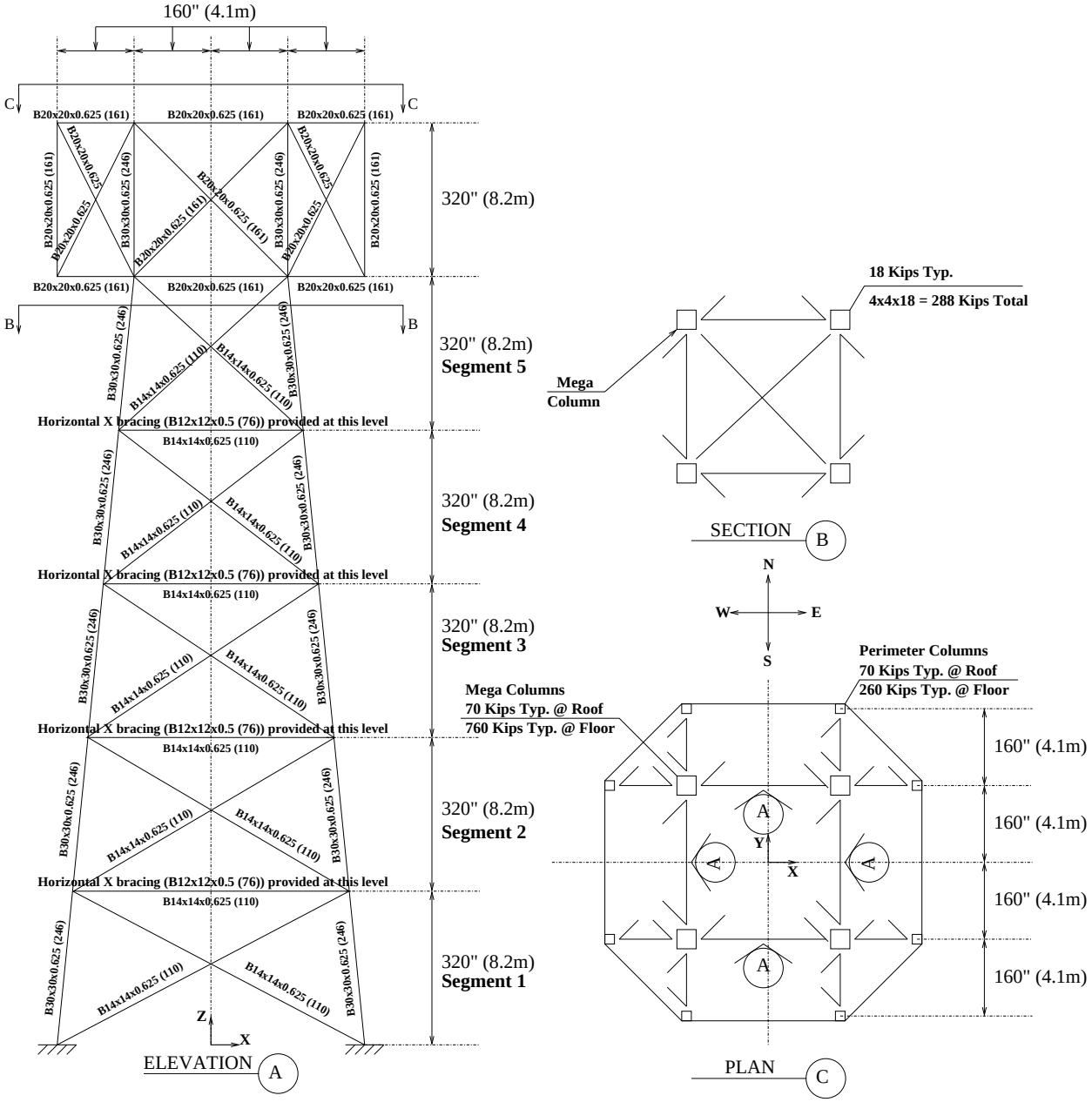

Figure 7.1: Structural plan, section, elevation, and member sizes of the proposed benchmark water-tank problem. Note that the X-braces are assumed not to be connected at the intersecting point.

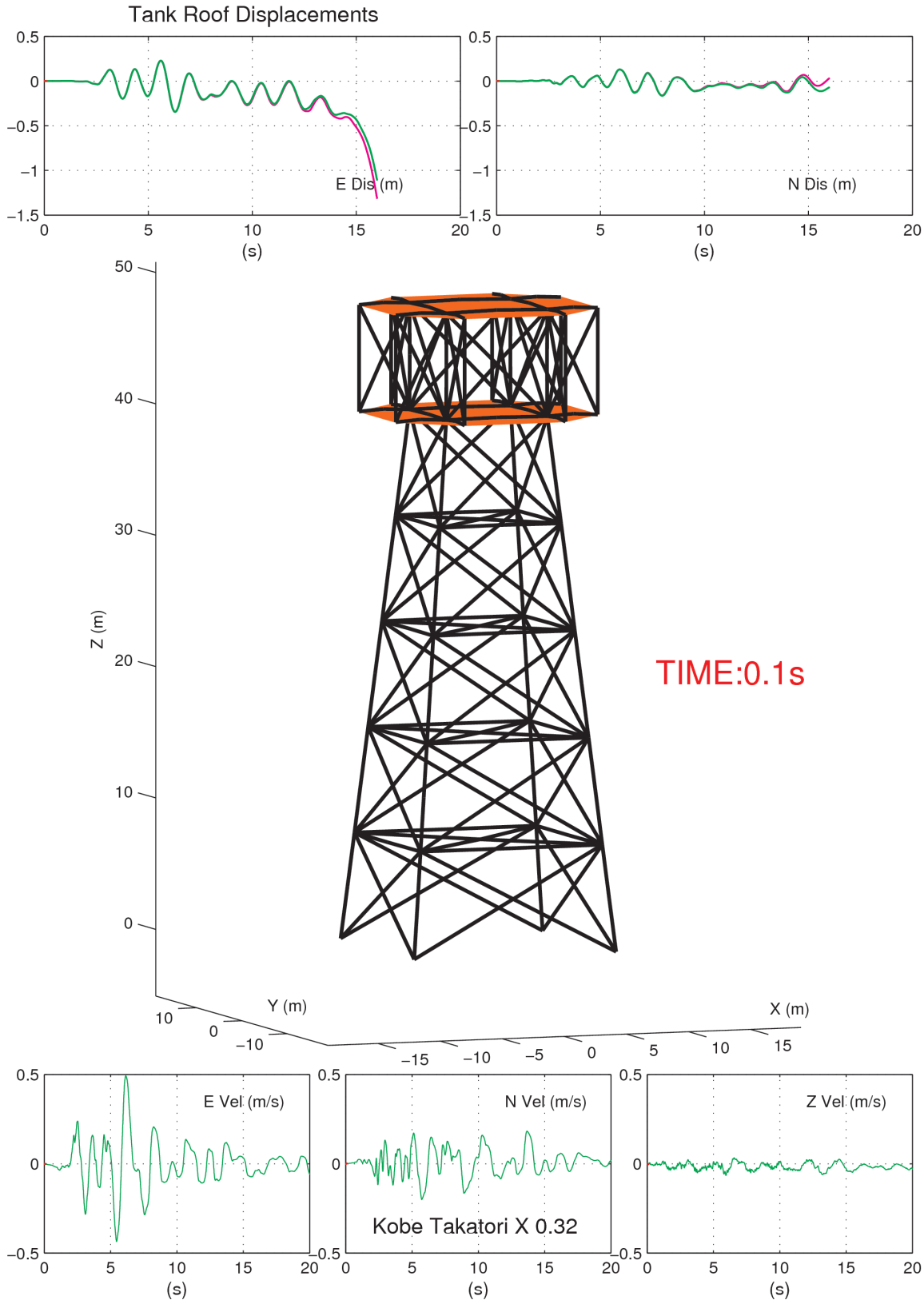

Figure 7.2: Undeformed shape of the collapsing benchmark steel braced water-tank subjected to the 1995 Kobe earthquake Takatori record scaled down by a factor of 0.32.

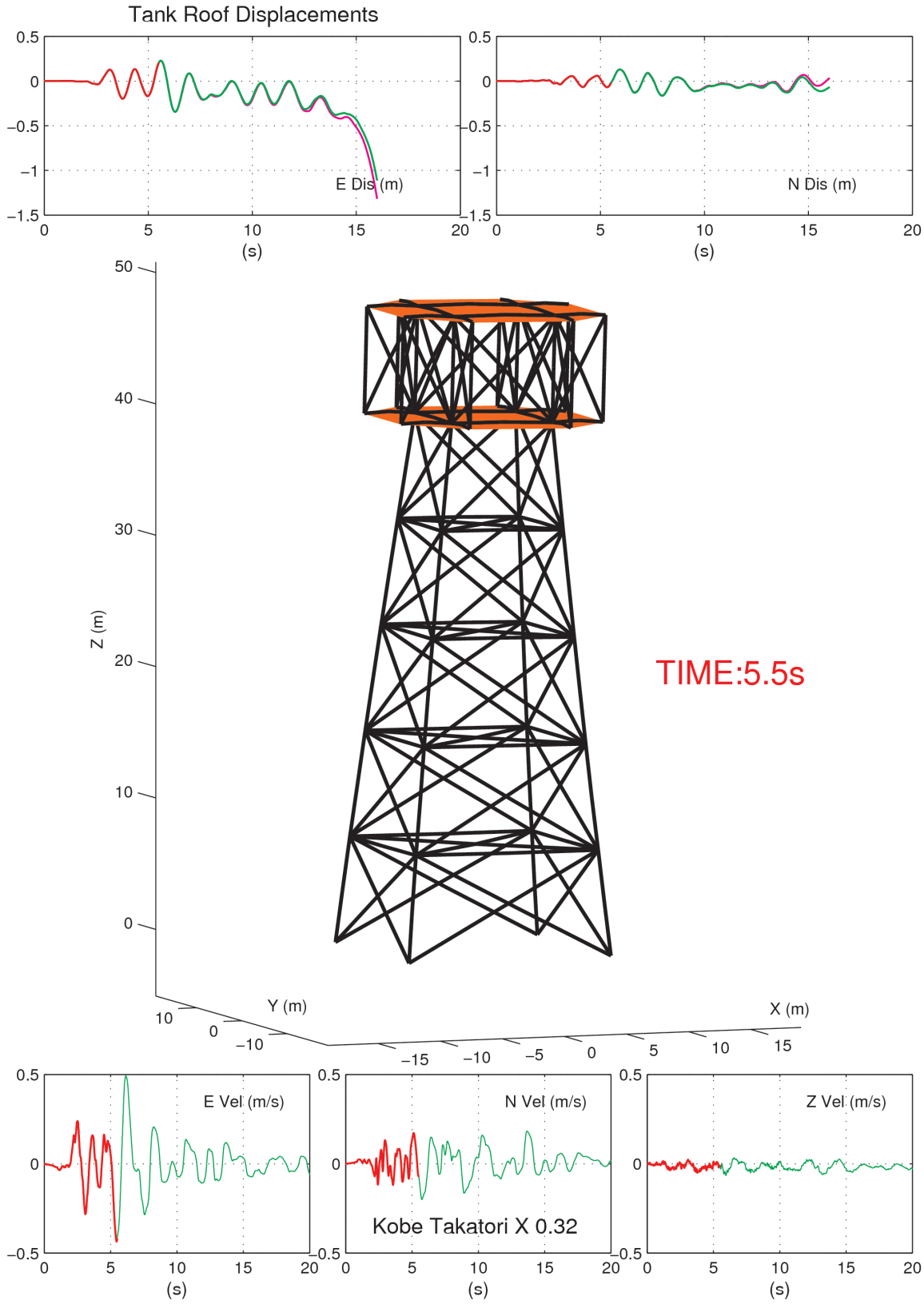

Figure 7.3: 5.5s snapshot of the collapsing benchmark steel braced water-tank subjected to the 1995 Kobe earthquake Takatori record scaled down by a factor of 0.32. Deformations are exaggerated by a factor of 5.

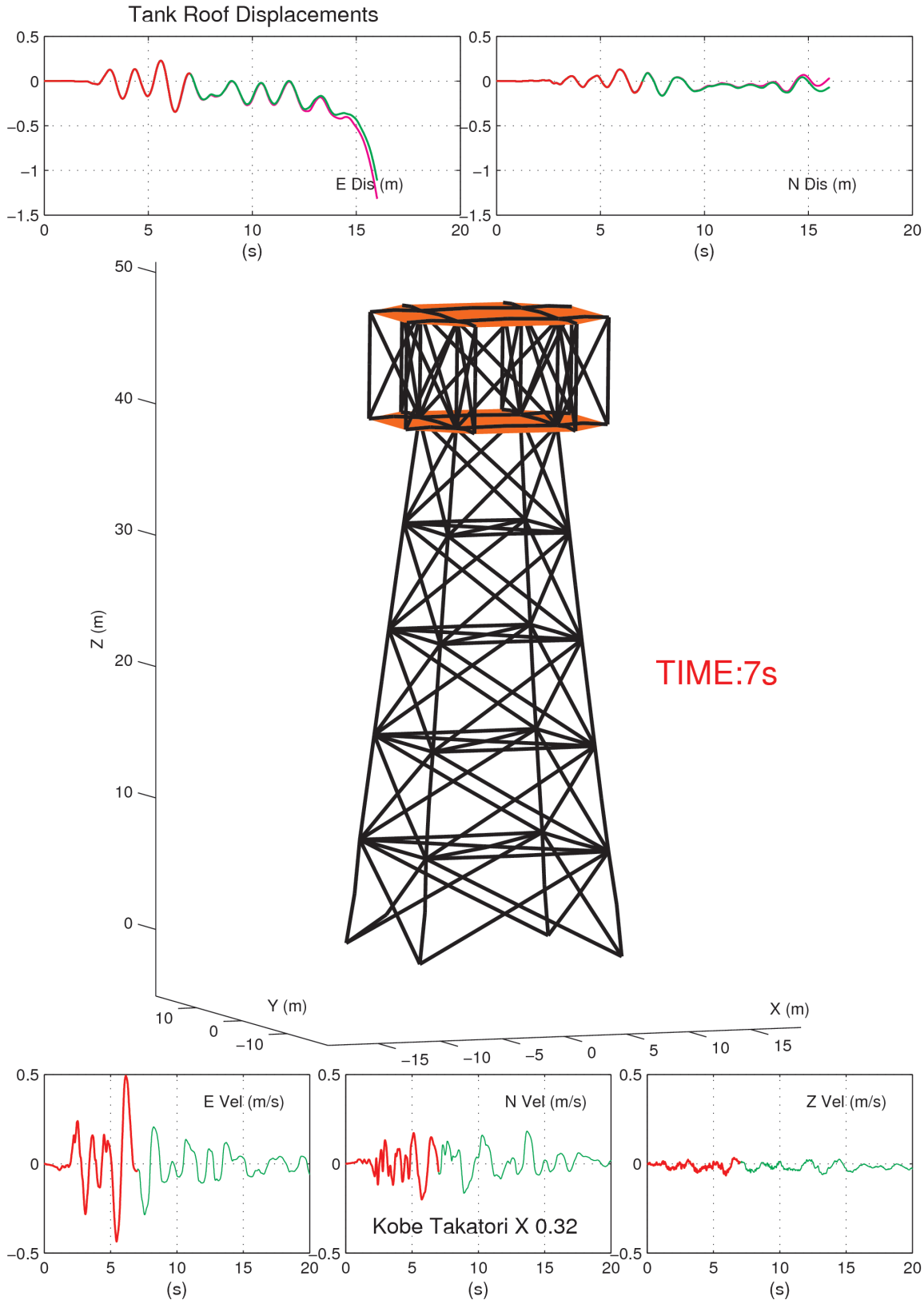

Figure 7.4: 7s snapshot of the collapsing benchmark steel braced water-tank subjected to the 1995 Kobe earthquake Takatori record scaled down by a factor of 0.32. Deformations are exaggerated by a factor of 5.

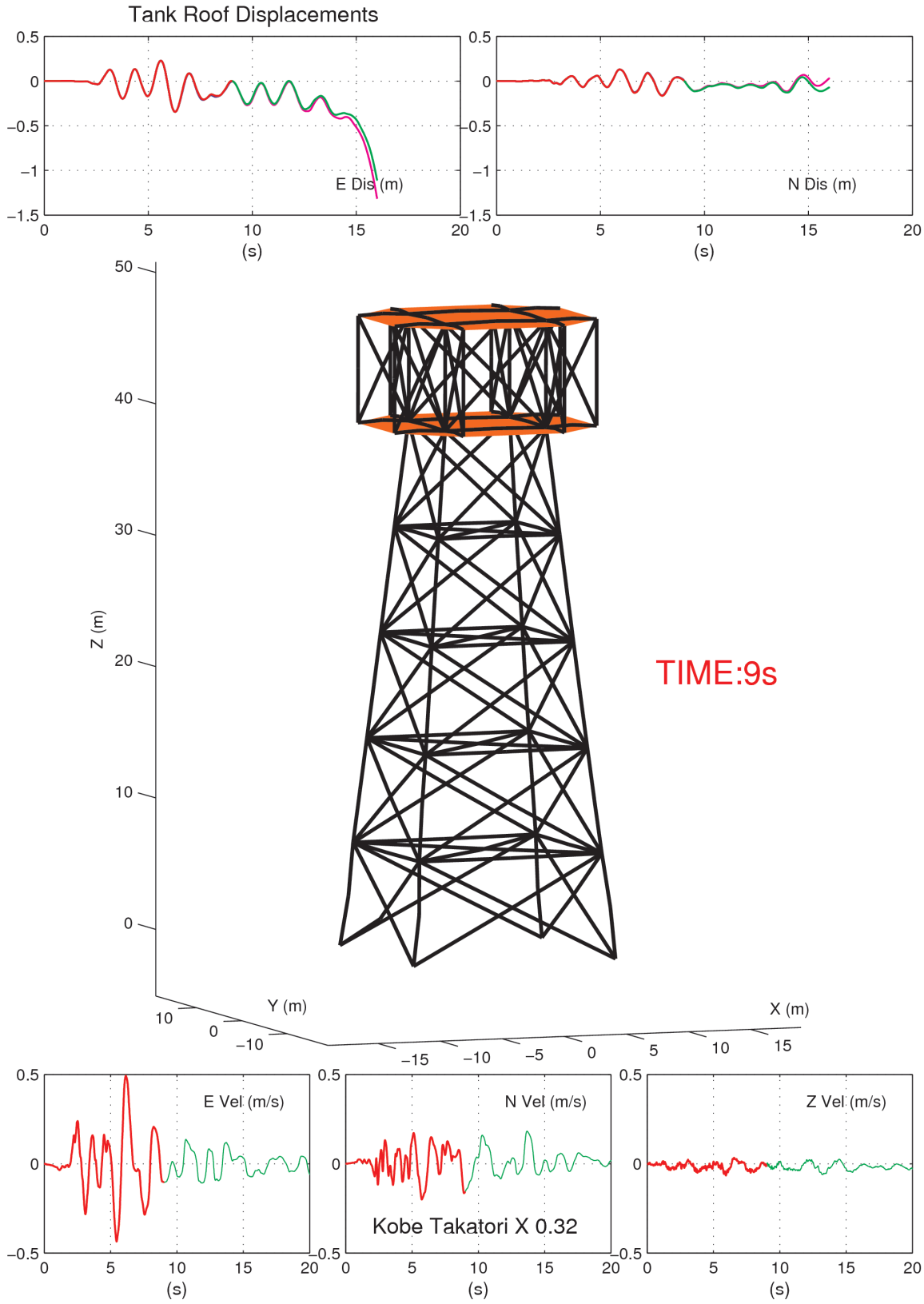

Figure 7.5: 9s snapshot of the collapsing benchmark steel braced water-tank subjected to the 1995 Kobe earthquake Takatori record scaled down by a factor of 0.32. Deformations are exaggerated by a factor of 5.

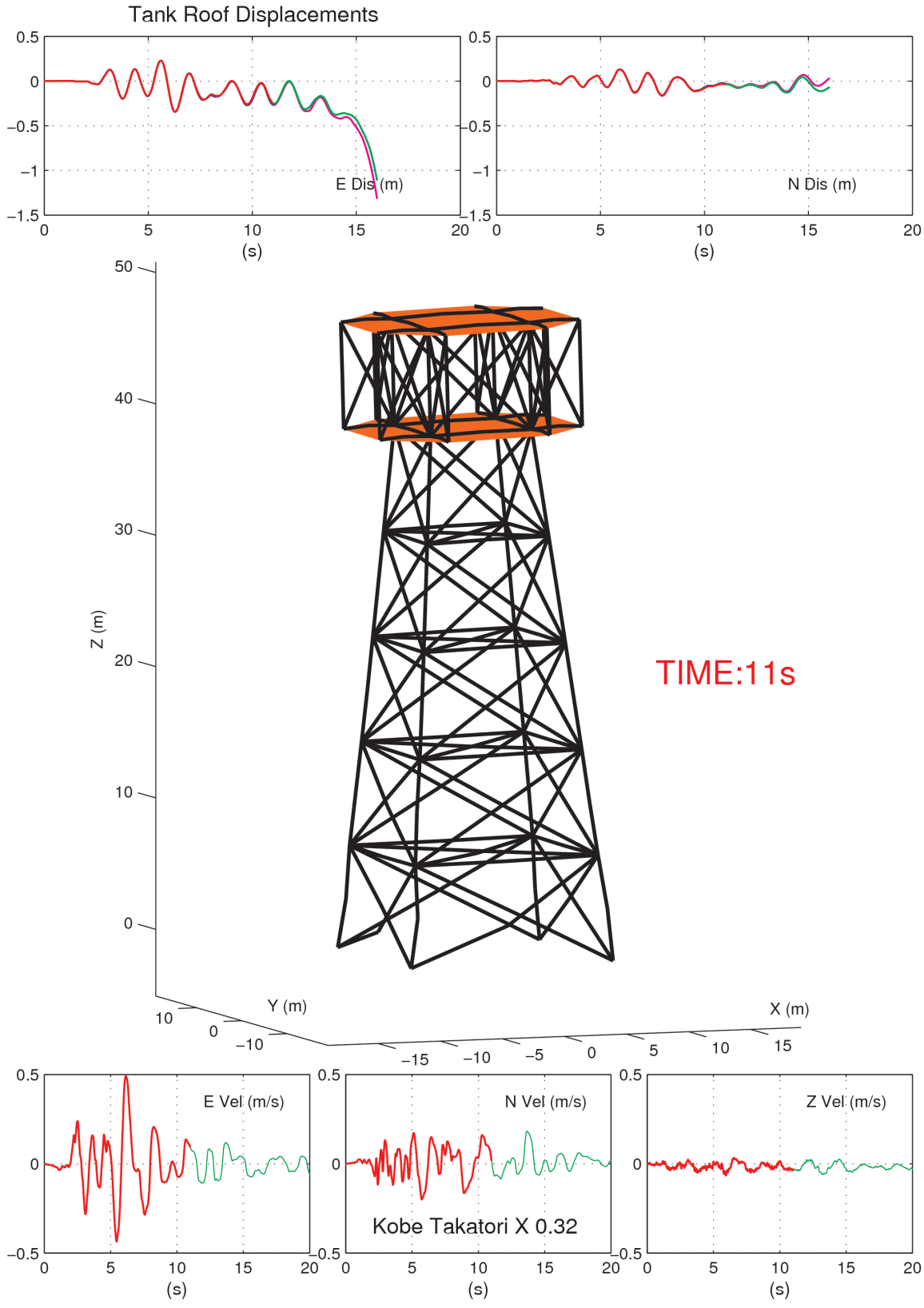

Figure 7.6: 11s snapshot of the collapsing benchmark steel braced water-tank subjected to the 1995 Kobe earthquake Takatori record scaled down by a factor of 0.32. Deformations are exaggerated by a factor of 5.

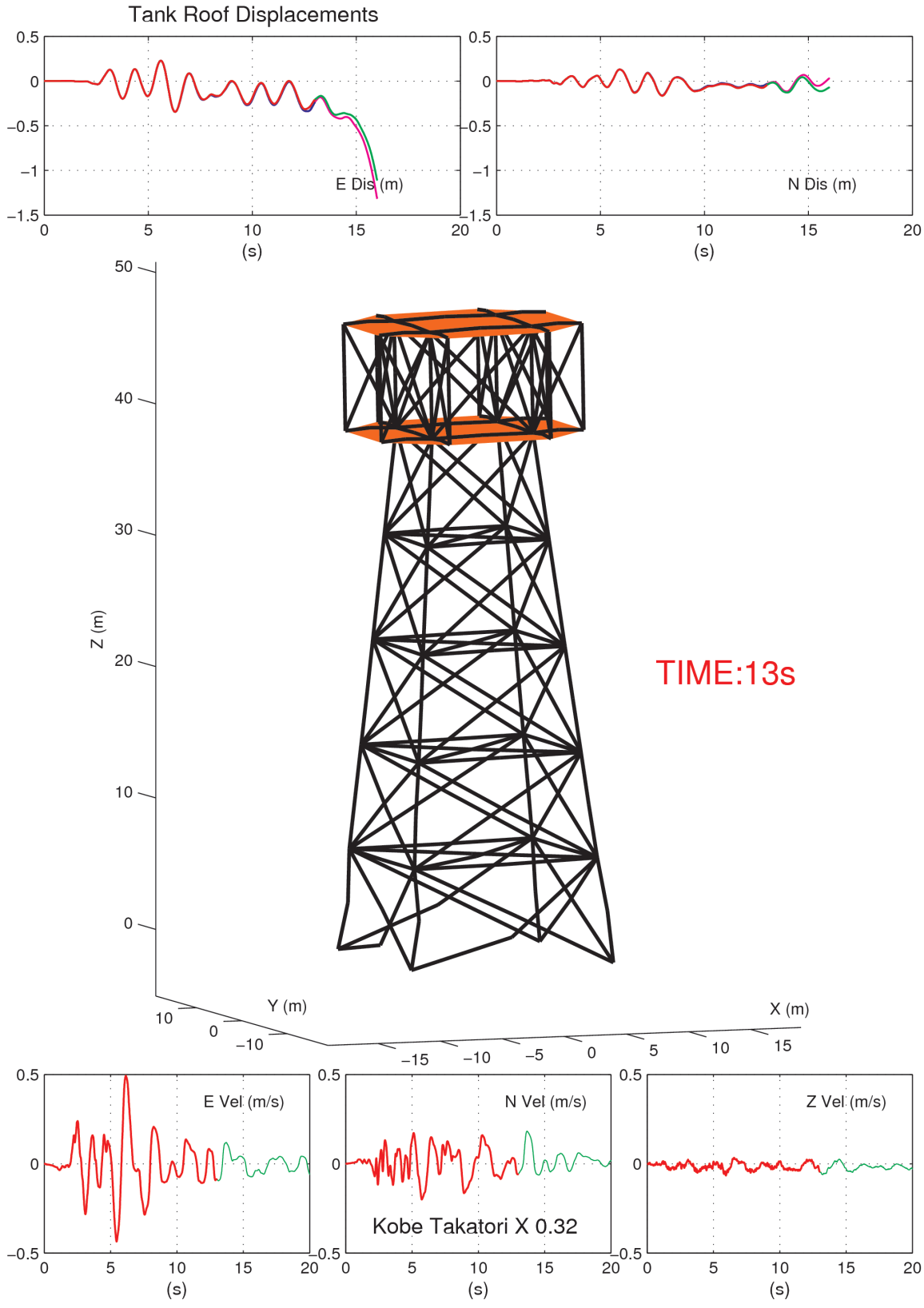

Figure 7.7: 13s snapshot of the collapsing benchmark steel braced water-tank subjected to the 1995 Kobe earthquake Takatori record scaled down by a factor of 0.32. Deformations are exaggerated by a factor of 5.

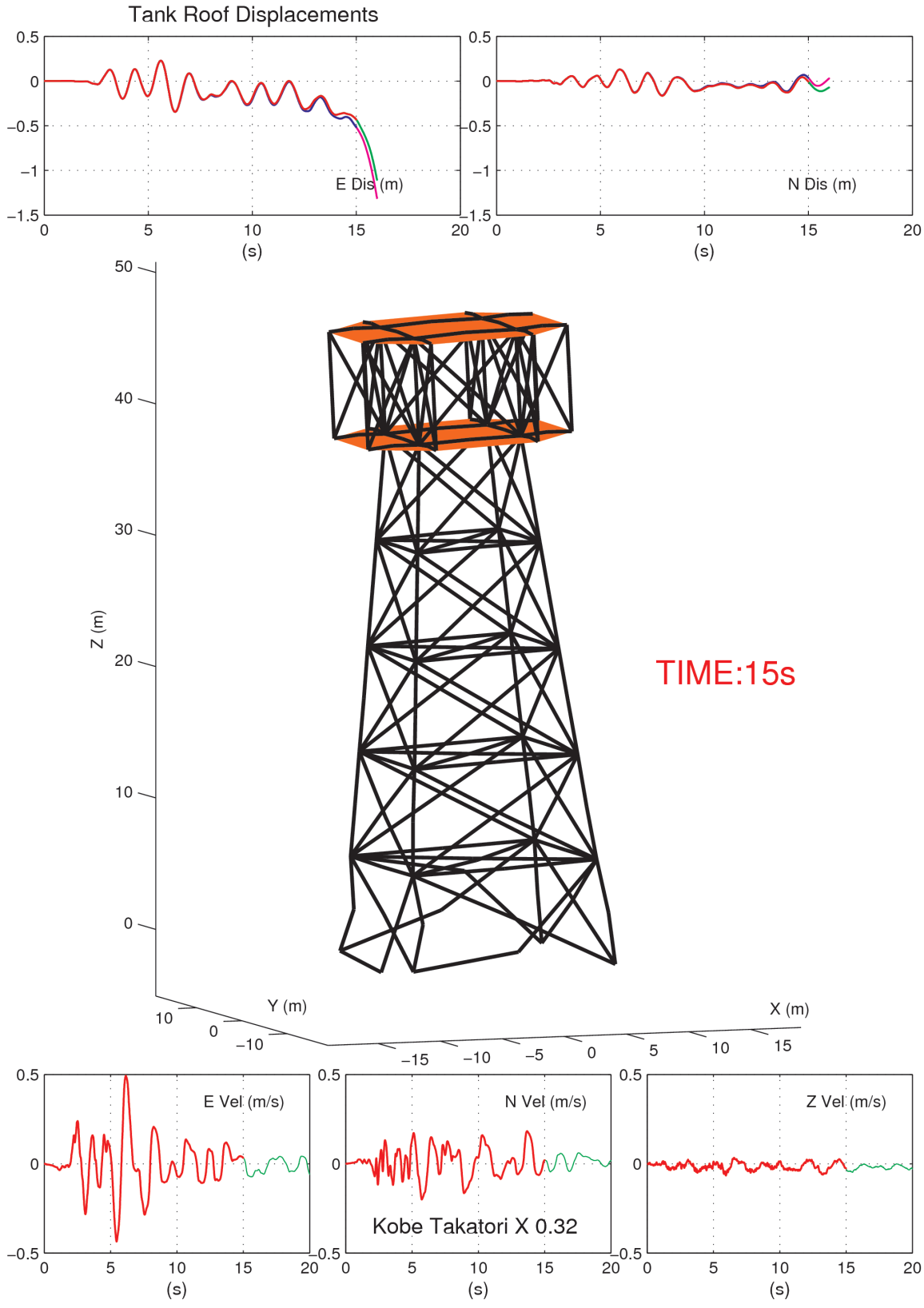

Figure 7.8: 15s snapshot of the collapsing benchmark steel braced water-tank subjected to the 1995 Kobe earthquake Takatori record scaled down by a factor of 0.32. Deformations are exaggerated by a factor of 5.

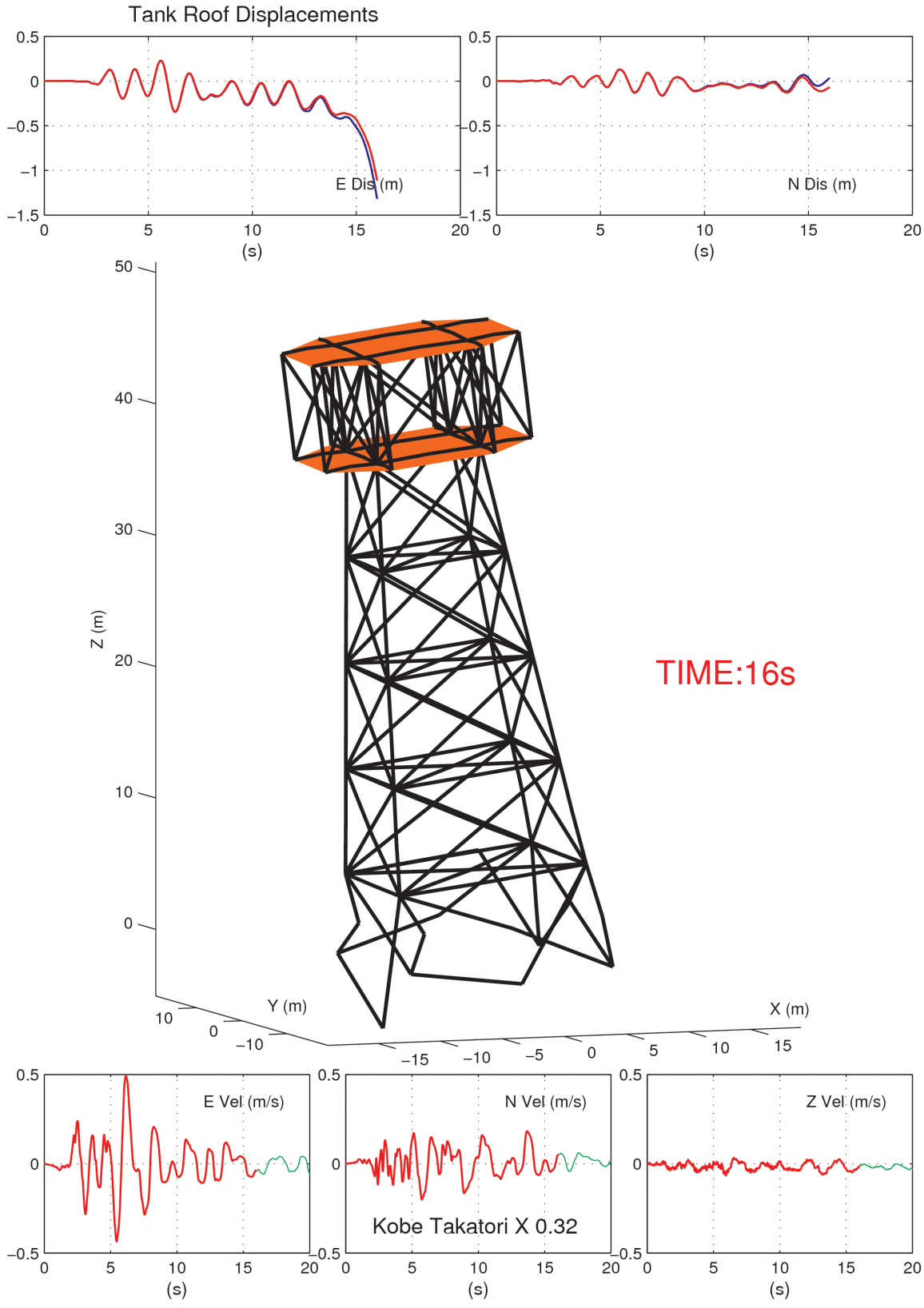

Figure 7.9: 16s snapshot of the collapsing benchmark steel braced water-tank subjected to the 1995 Kobe earthquake Takatori record scaled down by a factor of 0.32. Deformations are exaggerated by a factor of 5.

Chapter 8 Conclusions

1. A beam-column element termed the modified elastofiber (MEF) element has been developed to efficiently model buckling-sensitive slender columns and braces in steel structures. The element consists of 5 segments, 3 nonlinear fiber segments - two at the ends and one at mid-span, and 2 elastic segments sandwiched between the nonlinear segments. It is designed to simulate yielding at the element ends and first mode buckling. A local geometry-updating feature is used to track interior node displacements as the element buckles. A unique feature of the element is the capability to model fracture and rupture of fibers in the plastic-hinging region of the brace, leading to its complete severing.

2. The MEF element is incorporated into the FRAME3D analysis framework which includes global geometry updating in the solution process, with equilibrium being satisfied in the updated configuration at each time step (automatically accounting for $P - \Delta$ effects), enabling the analysis to follow a structure's response well into collapse by accommodating large translations and rotations.

3. The segment length for the MEF element is calibrated to yield satisfactory results for the critical elastic (Euler) buckling load of a suite of slender columns with varying boundary conditions (fixed-fixed, fixed-pinned, pinned-pinned), cross-sections (tubes and wide-flange sections), and slenderness ratios (L/R=40,80,120,160 and 200). A value of 2% of the clear-span results in reasonable predictions with errors limited to under 3% in most cases, the exceptions being the cases with the low KL/r of 20 (errors up to -11.5%).

4. The evolution of the elastic post-buckling deformation of the Koiter-Roorda L-shaped frame, subjected to a monotonically increasing vertical load applied at an eccentricity to the corner, is simulated using a single MEF element for each leg of the frame. Simulations are performed for two tube cross-sections and two wide-flange sections, with bar slenderness ratios L/r=40, 80, 120, 160, and 200, and load eccentricities of e=0.001L, 0.01L, and 0.05L. The numerical solution for each case is compared against an approximate second-order analytical solution proposed by Bazant and Cedolin. The single MEF-element solution is within 5% of the analytical solution for a broad range of corner plastic rotations in almost all cases. The inward buckling mode shape, supported by theory, is realized in the numerical solution.

5. The ability of the MEF element to simulate inelastic buckling of cyclically loaded struts is validated by comparing numerical solutions against data from three sets of experiments – (a) wide-flange and tube sections, with L/R=40, 80, and 120, and ideal pinned-pinned as well as pinned-fixed boundary conditions, axially cycled through a symmetric loading protocol by Black et al.; (b) similar sections, but with gusset-plate connections, axially cycled through near-field and far-field loading protocols by Fell et al.; and (c) one-bay frame, with a diagonal strut, laterally cycled through a symmetric and an asymmetric loading protocol by Tremblay et al. The MEF element is able to uniformly capture the

essence of the inelastic buckling behavior of all the struts. The ability to simulate the response of such a wide range of specimen illustrates the robustness of the designed element.

6. The performance of the MEF element within an assembled structure is judged by simulating the response of a 6-story steel braced structure subjected to the N-S component of the Tohoku University record collected during the 1978 Miyagi-Ken-Oki earthquake, and comparing it against full-scale test results from the US-Japan cooperative research program. While assumptions of ideal (continuous) boundary condition and no geometric imperfection yield poor results, slight tuning of the model to account for geometric imperfection and partial fixity end conditions for the braces yields an excellent match for interstory drift and shear, brace buckling, and fiber rupture timing.

7. A benchmark problem is proposed to evaluate the collapse-prediction capability of competing methodologies. The problem is that of the collapse of a water-tank that is so configured as to have a unique collapse mechanism under any form of ground motion. The tank is biaxially symmetric and is supported by a tower that consists of four sloping mega-columns that are tied together by five levels of vertical and horizontal bracing. The braces, columns, and beams have uniform sizing for the entire height of the tower. This configuration forces the collapse of the tank to occur due to buckling of the mega-columns and braces at the bottom, and overturning due to the ensuing $P - \Delta$ instability. A FRAME3D model of this tank is subjected to the Takatori near-source record from the 1995 Kobe earthquake, scaled down by a factor of 0.32. MEF elements are used to model all the members including braces. Severe buckling occurs in the bottom mega-columns and one of the two braces on the west face of the tower when the structure is hit by the Takatori near-source pulse, resulting a tilt in the structure. This is followed by sequential compression buckling of braces on the south and north faces leading to $P - \Delta$ instability and complete collapse of the tank.

8. The FRAME3D models of the 6-story structure and the benchmark water-tank can be accessed at http://virtualshaker.caltech.edu. Time-history analysis of these models can be performed remotely through this gateway.

Appendix A Koiter-Roorda Frame

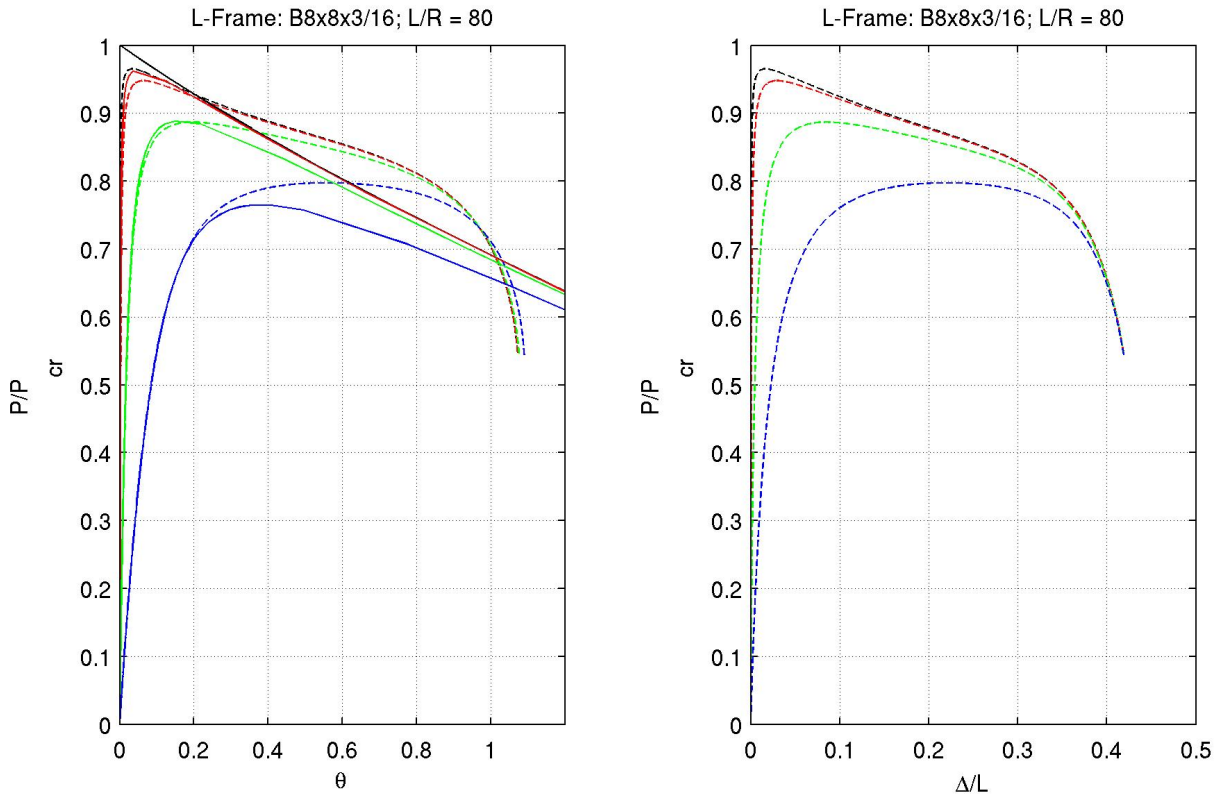

(a) (b)

Figure A.1: Comparison of the numerical solution using MEF elements (dashed lines) against a second-order analytical solution (solid lines) for the L-shaped Koiter-Roorda frame with a downward force (P) acting at the corner (black), or at eccentricities of e/L=0.001 (red), 0.01 (green), and 0.05 (blue): Case 1: TS8x8x3/16, L/R=80) – (a) Corner rotation versus P/P_{CR}; (b) Corner in-plane lateral displacement versus P/P_{CR}.

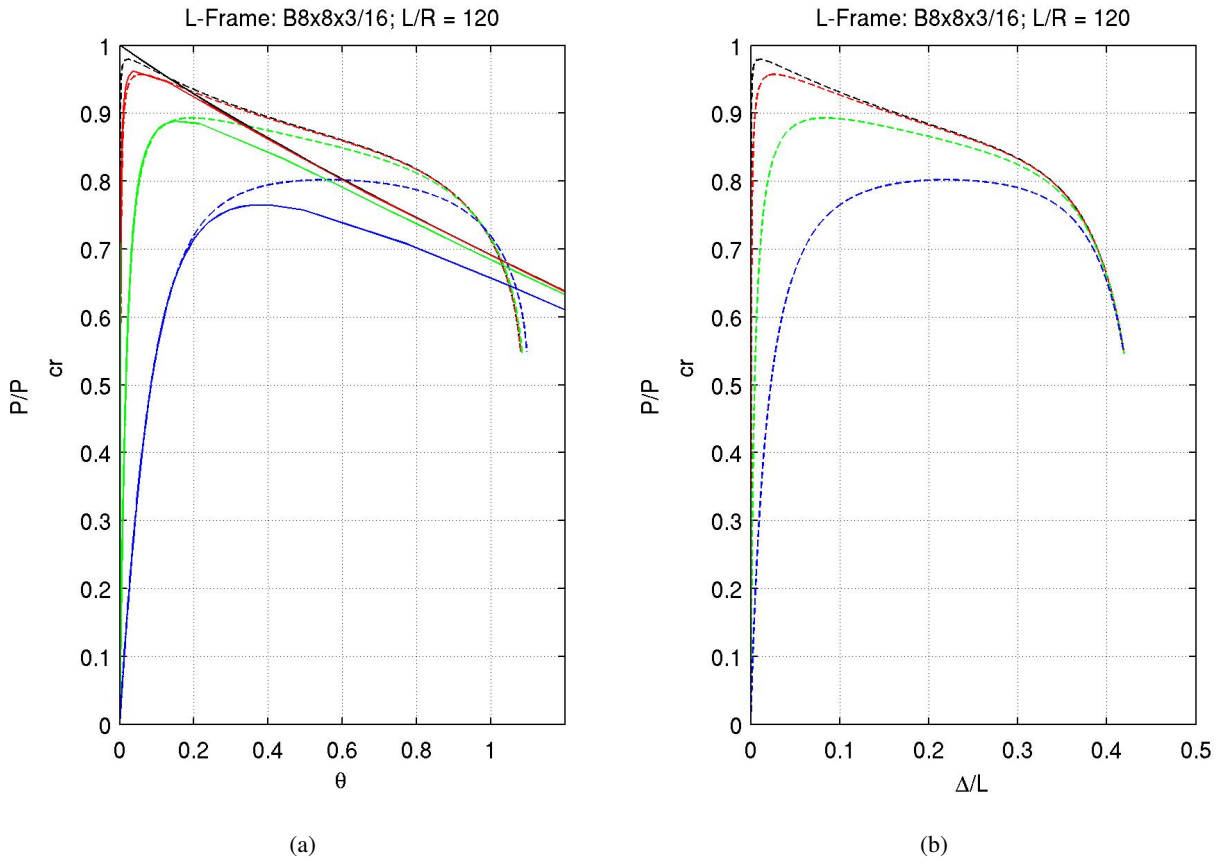

(a) (b)

Figure A.2: Comparison of the numerical solution using MEF elements (dashed lines) against a second-order analytical solution (solid lines) for the L-shaped Koiter-Roorda frame with a downward force (P) acting at the corner (black), or at eccentricities of e/L=0.001 (red), 0.01 (green), and 0.05 (blue): Case 1: TS8x8x3/16, L/R=120) – (a) Corner rotation versus P/P_{CR}; (b) Corner in-plane lateral displacement versus P/P_{CR}.

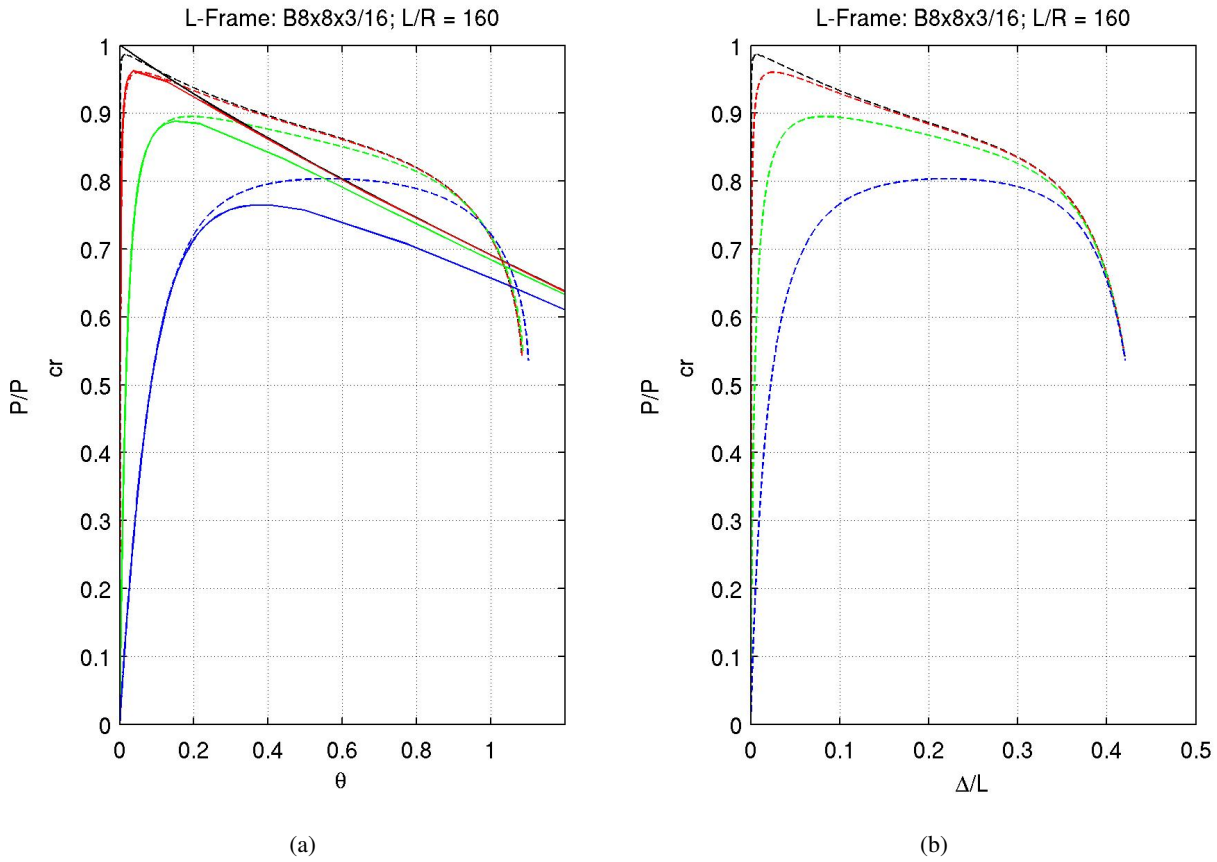

(a) (b)

Figure A.3: Comparison of the numerical solution using MEF elements (dashed lines) against a second-order analytical solution (solid lines) for the L-shaped Koiter-Roorda frame with a downward force (P) acting at the corner (black), or at eccentricities of e/L=0.001 (red), 0.01 (green), and 0.05 (blue): Case 1: TS8x8x3/16, L/R=160) – (a) Corner rotation versus P/P_{CR}; (b) Corner in-plane lateral displacement versus P/P_{CR}.

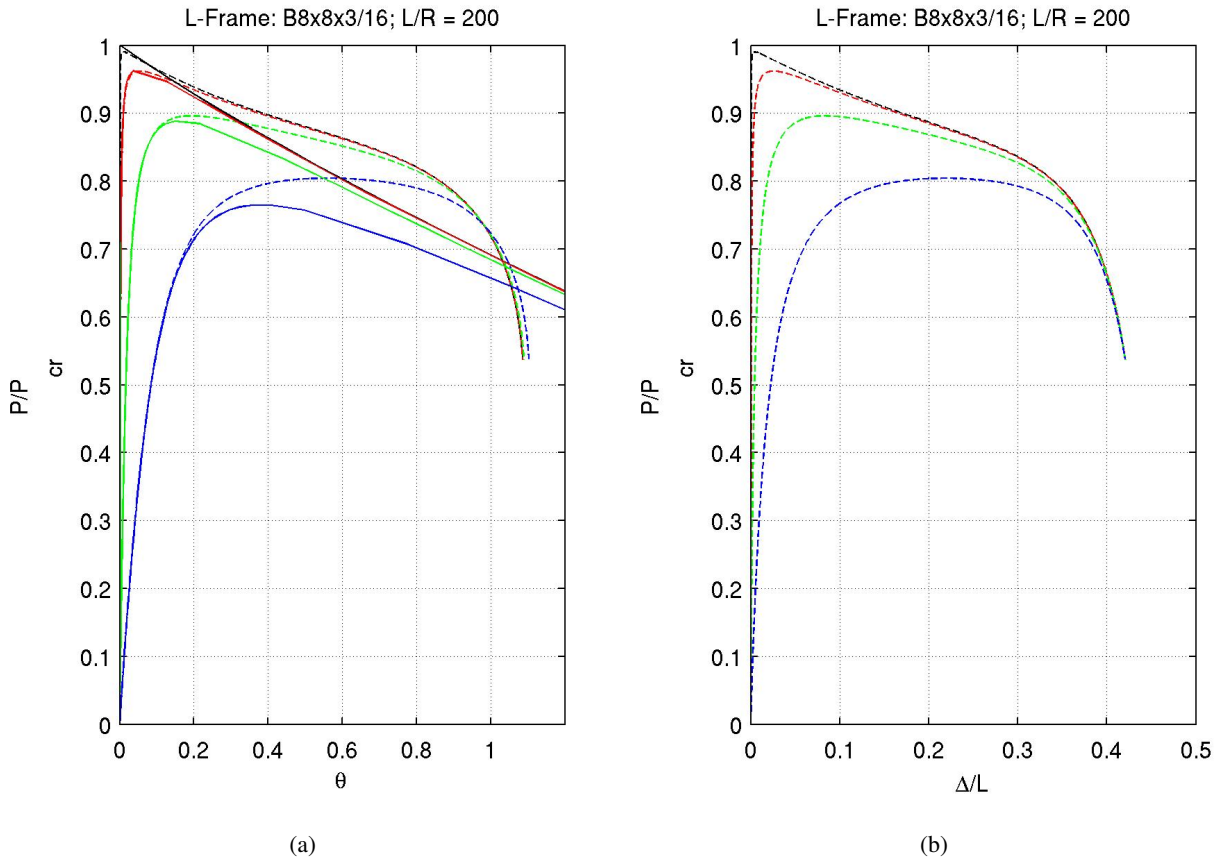

(a) (b)

Figure A.4: Comparison of the numerical solution using MEF elements (dashed lines) against a second-order analytical solution (solid lines) for the L-shaped Koiter-Roorda frame with a downward force (P) acting at the corner (black), or at eccentricities of e/L=0.001 (red), 0.01 (green), and 0.05 (blue): Case 1: TS8x8x3/16, L/R=200) – (a) Corner rotation versus P/P_{CR}; (b) Corner in-plane lateral displacement versus P/P_{CR}.

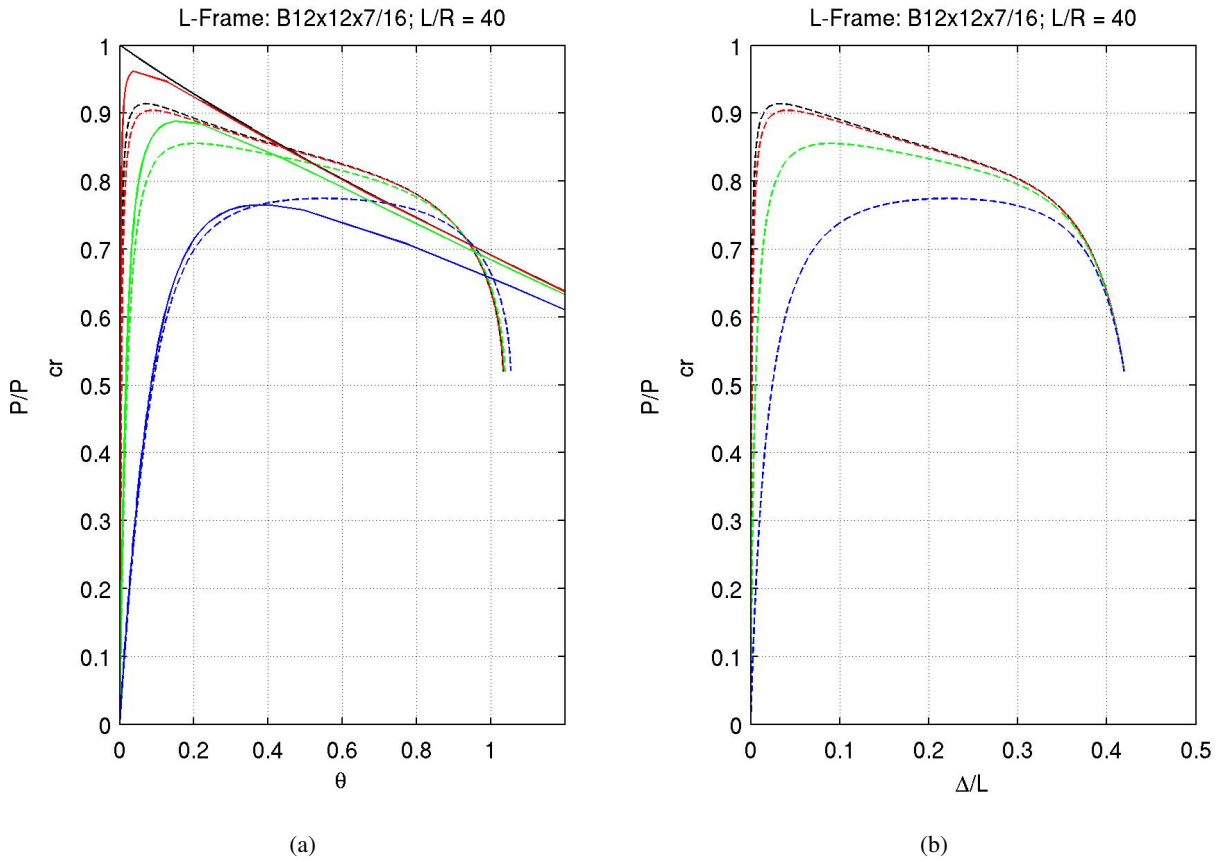

(a) (b)

Figure A.5: Comparison of the numerical solution using MEF elements (dashed lines) against a second-order analytical solution (solid lines) for the L-shaped Koiter-Roorda frame with a downward force (P) acting at the corner (black), or at eccentricities of e/L=0.001 (red), 0.01 (green), and 0.05 (blue): Case 1: TS12x12x7/16, L/R=40) – (a) Corner rotation versus P/P_{CR}; (b) Corner in-plane lateral displacement versus P/P_{CR}.

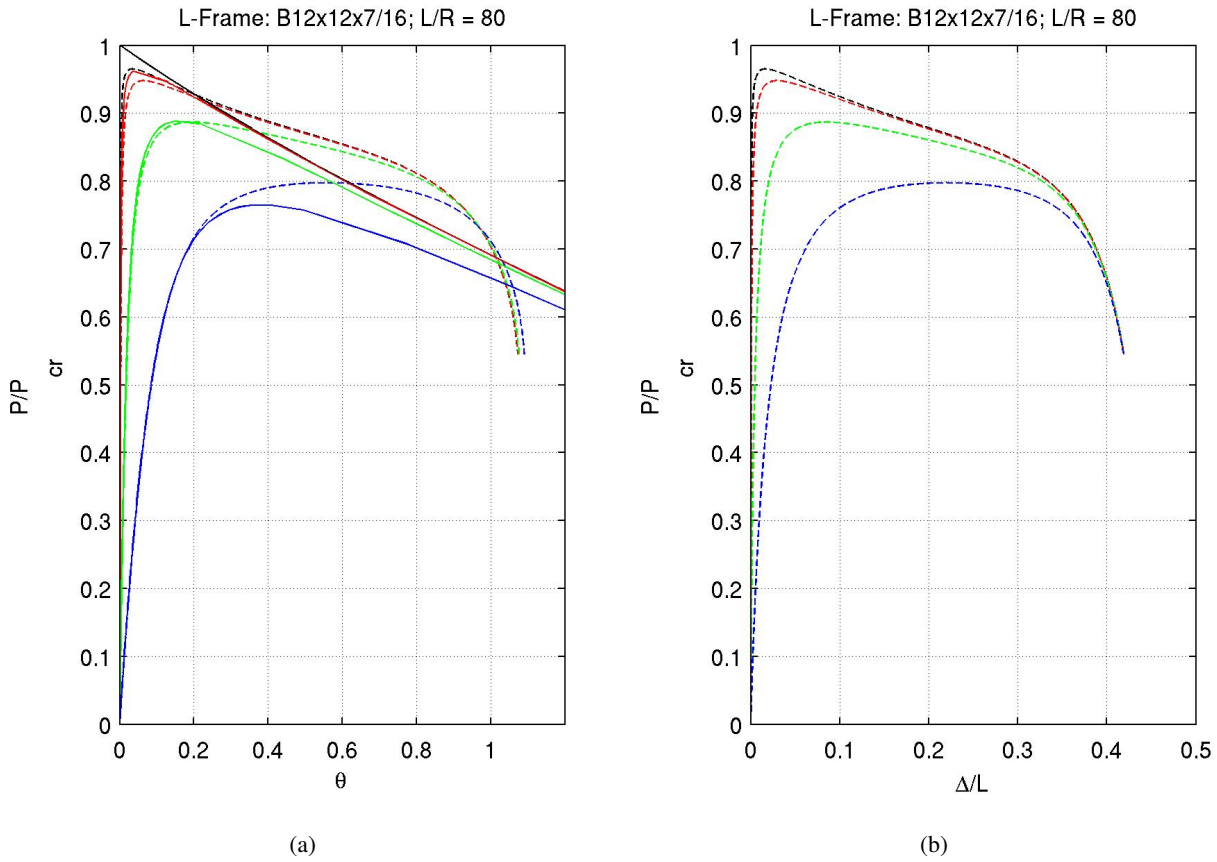

(a) (b)

Figure A.6: Comparison of the numerical solution using MEF elements (dashed lines) against a second-order analytical solution (solid lines) for the L-shaped Koiter-Roorda frame with a downward force (P) acting at the corner (black), or at eccentricities of e/L=0.001 (red), 0.01 (green), and 0.05 (blue): Case 1: TS12x12x7/16, L/R=80) – (a) Corner rotation versus P/P_{CR}; (b) Corner in-plane lateral displacement versus P/P_{CR}.

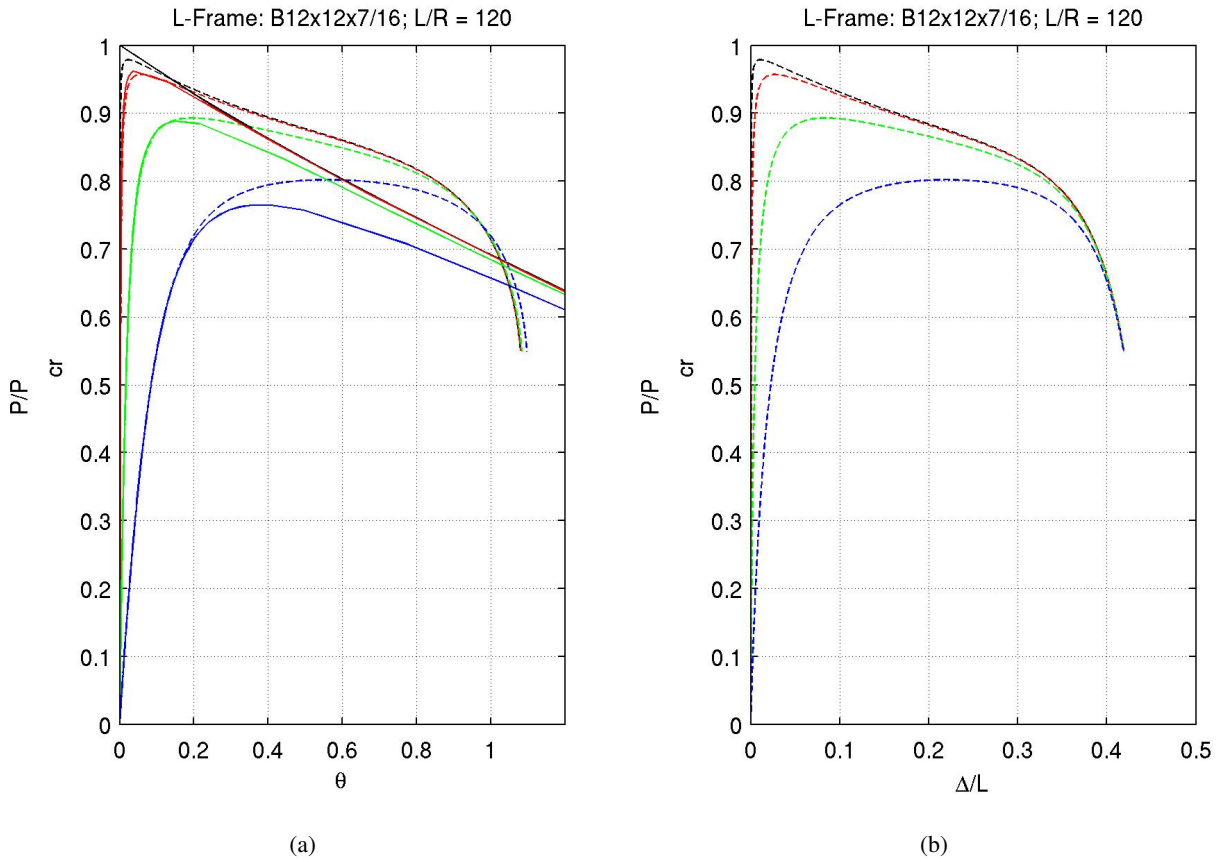

(a) (b)

Figure A.7: Comparison of the numerical solution using MEF elements (dashed lines) against a second-order analytical solution (solid lines) for the L-shaped Koiter-Roorda frame with a downward force (P) acting at the corner (black), or at eccentricities of e/L=0.001 (red), 0.01 (green), and 0.05 (blue): Case 1: TS12x12x7/16, L/R=120) – (a) Corner rotation versus P/P_{CR}; (b) Corner in-plane lateral displacement versus P/P_{CR}.

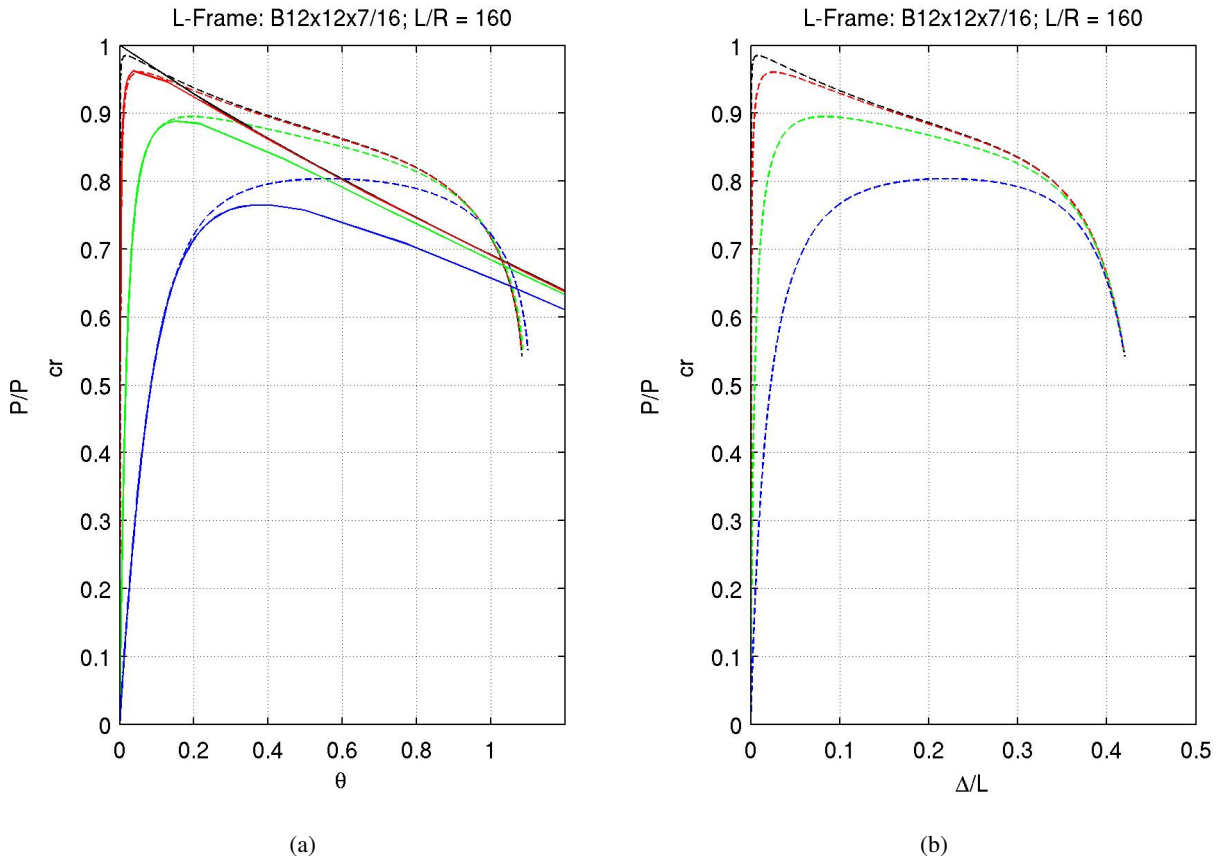

(a) (b)

Figure A.8: Comparison of the numerical solution using MEF elements (dashed lines) against a second-order analytical solution (solid lines) for the L-shaped Koiter-Roorda frame with a downward force (P) acting at the corner (black), or at eccentricities of e/L=0.001 (red), 0.01 (green), and 0.05 (blue): Case 1: TS12x12x7/16, L/R=160) – (a) Corner rotation versus P/P_{CR}; (b) Corner in-plane lateral displacement versus P/P_{CR}.

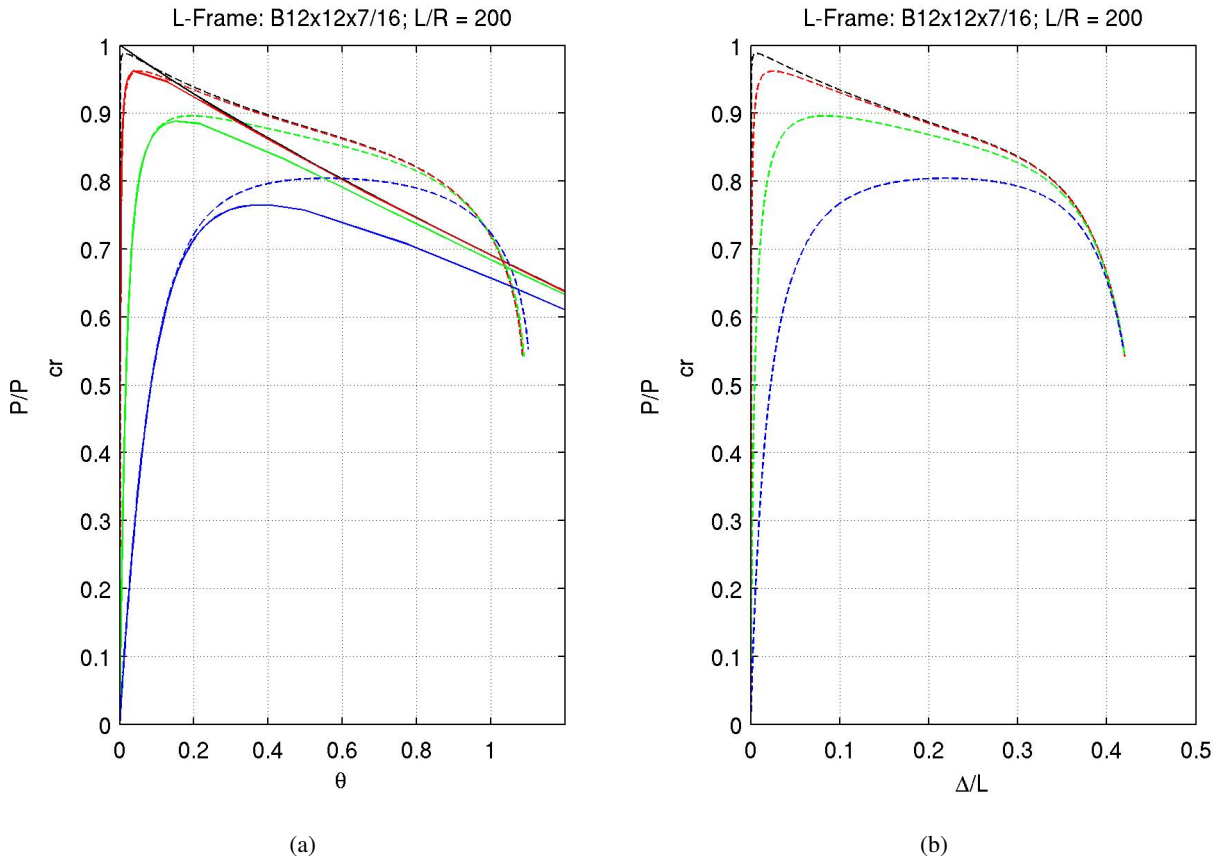

(a) (b)

Figure A.9: Comparison of the numerical solution using MEF elements (dashed lines) against a second-order analytical solution (solid lines) for the L-shaped Koiter-Roorda frame with a downward force (P) acting at the corner (black), or at eccentricities of e/L=0.001 (red), 0.01 (green), and 0.05 (blue): Case 1: TS12x12x7/16, L/R=200) – (a) Corner rotation versus P/P_{CR}; (b) Corner in-plane lateral displacement versus P/P_{CR}.

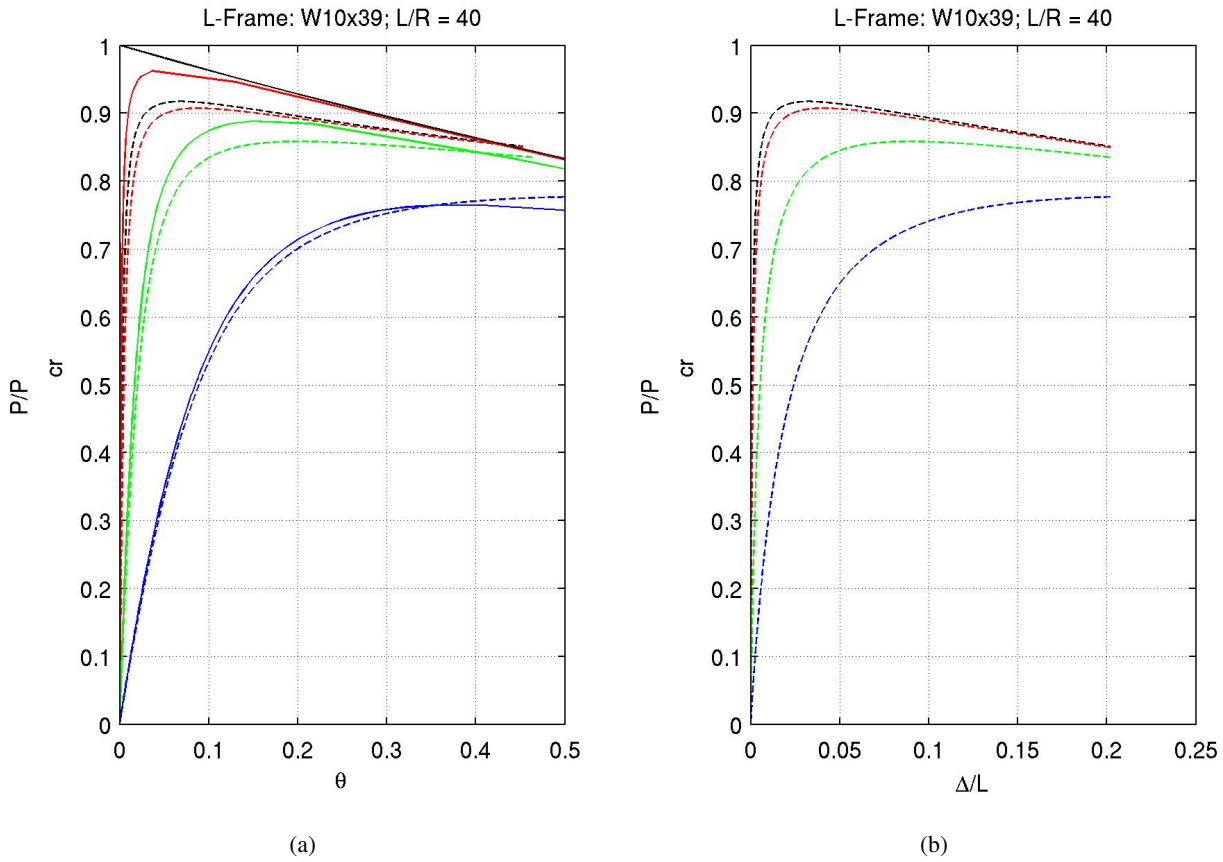

(a) (b)

Figure A.10: Comparison of the numerical solution using MEF elements (dashed lines) against a second-order analytical solution (solid lines) for the L-shaped Koiter-Roorda frame with a downward force (P) acting at the corner (black), or at eccentricities of e/L=0.001 (red), 0.01 (green), and 0.05 (blue): Case 1: W10x39, L/R=40) – (a) Corner rotation versus P/P_{CR}; (b) Corner in-plane lateral displacement versus P/P_{CR}.

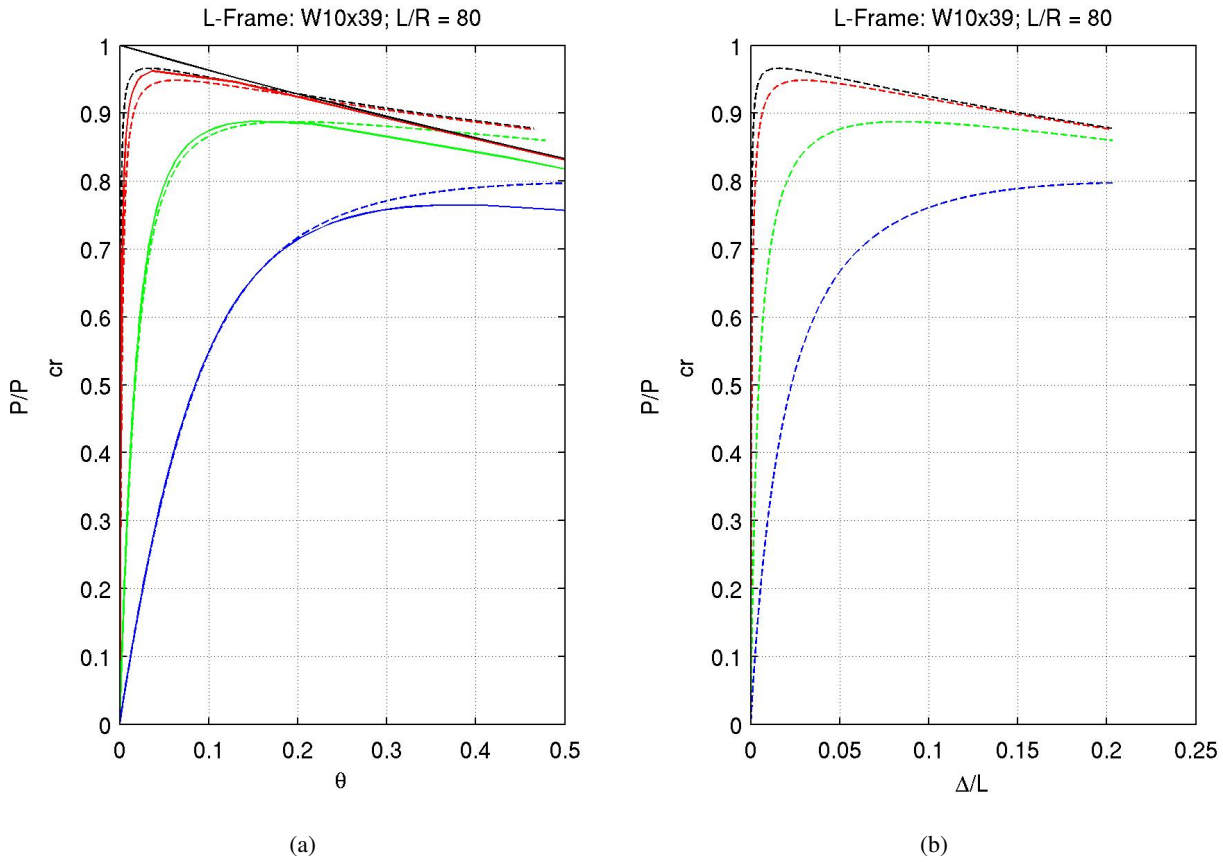

(a) (b)

Figure A.11: Comparison of the numerical solution using MEF elements (dashed lines) against a second-order analytical solution (solid lines) for the L-shaped Koiter-Roorda frame with a downward force (P) acting at the corner (black), or at eccentricities of e/L=0.001 (red), 0.01 (green), and 0.05 (blue): Case 1: W10x39, L/R=80) – (a) Corner rotation versus P/P_{CR}; (b) Corner in-plane lateral displacement versus P/P_{CR}.

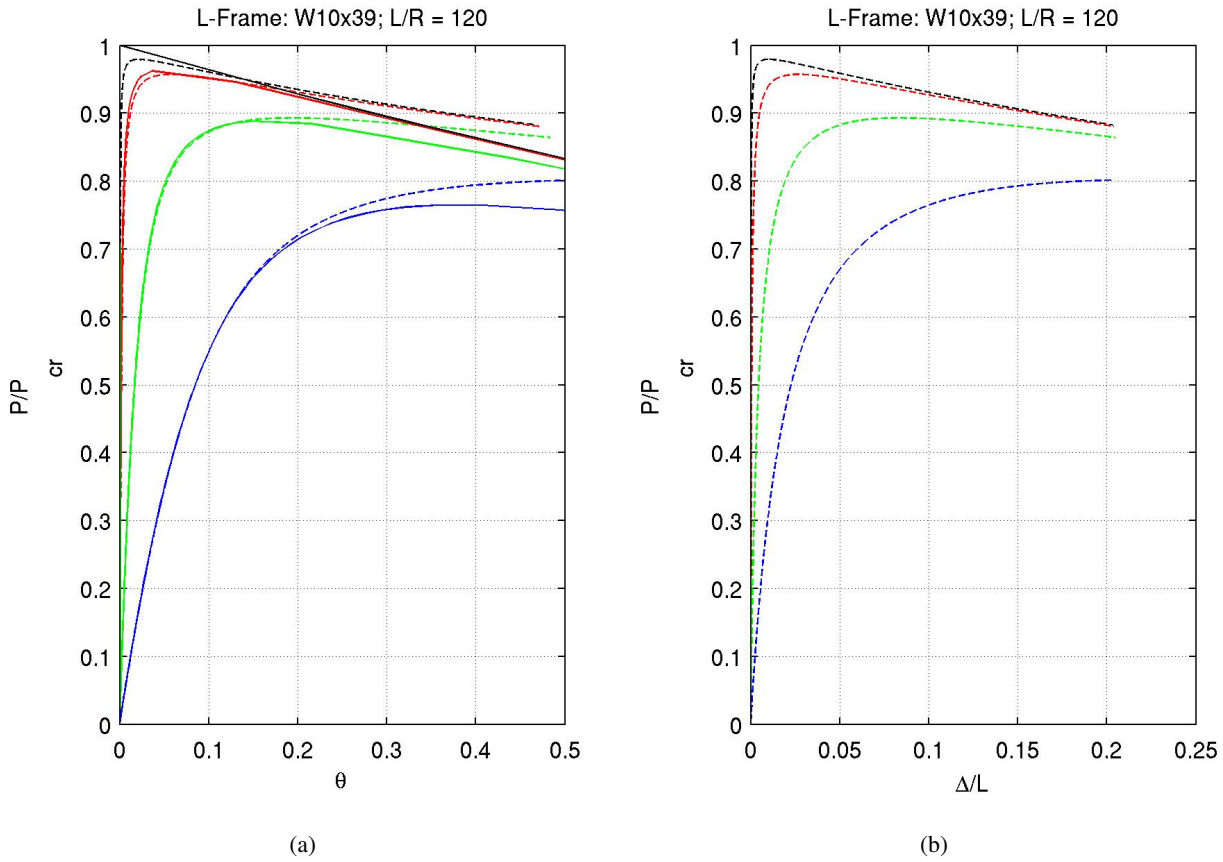

(a) (b)

Figure A.12: Comparison of the numerical solution using MEF elements (dashed lines) against a second-order analytical solution (solid lines) for the L-shaped Koiter-Roorda frame with a downward force (P) acting at the corner (black), or at eccentricities of e/L=0.001 (red), 0.01 (green), and 0.05 (blue): Case 1: W10x39, L/R=120) – (a) Corner rotation versus P/P_{CR}; (b) Corner in-plane lateral displacement versus P/P_{CR}.

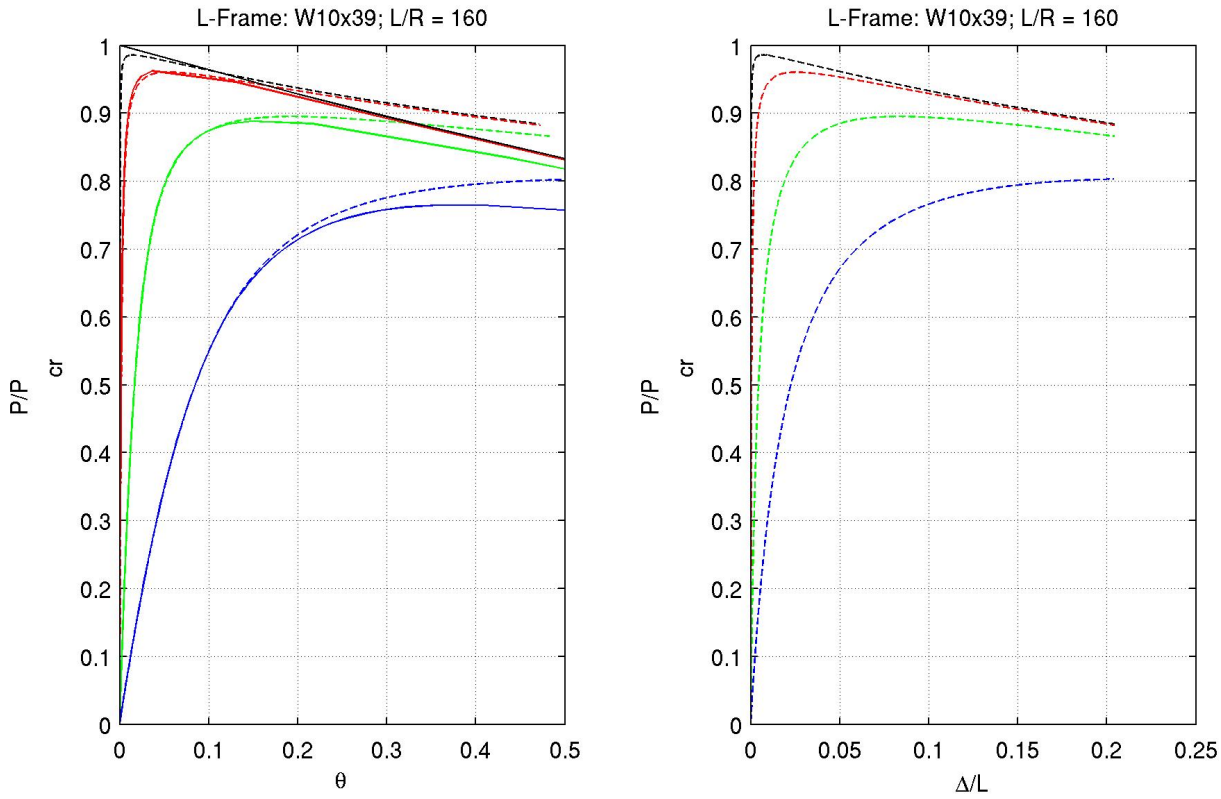

(a) (b)

Figure A.13: Comparison of the numerical solution using MEF elements (dashed lines) against a second-order analytical solution (solid lines) for the L-shaped Koiter-Roorda frame with a downward force (P) acting at the corner (black), or at eccentricities of e/L=0.001 (red), 0.01 (green), and 0.05 (blue): Case 1: W10x39, L/R=160) – (a) Corner rotation versus P/P_{CR}; (b) Corner in-plane lateral displacement versus P/P_{CR}.

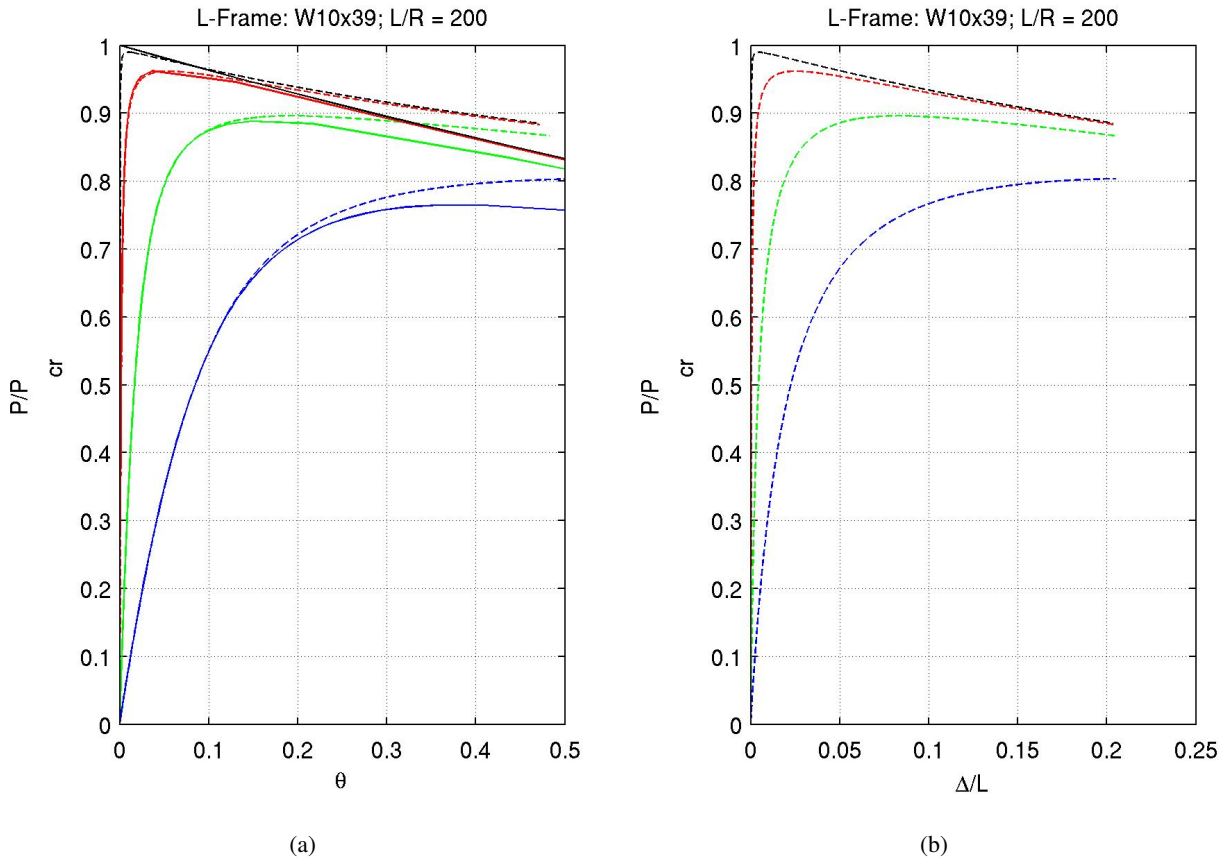

(a) (b)

Figure A.14: Comparison of the numerical solution using MEF elements (dashed lines) against a second-order analytical solution (solid lines) for the L-shaped Koiter-Roorda frame with a downward force (P) acting at the corner (black), or at eccentricities of e/L=0.001 (red), 0.01 (green), and 0.05 (blue): Case 1: W10x39, L/R=200) – (a) Corner rotation versus P/P_{CR}; (b) Corner in-plane lateral displacement versus P/P_{CR}.

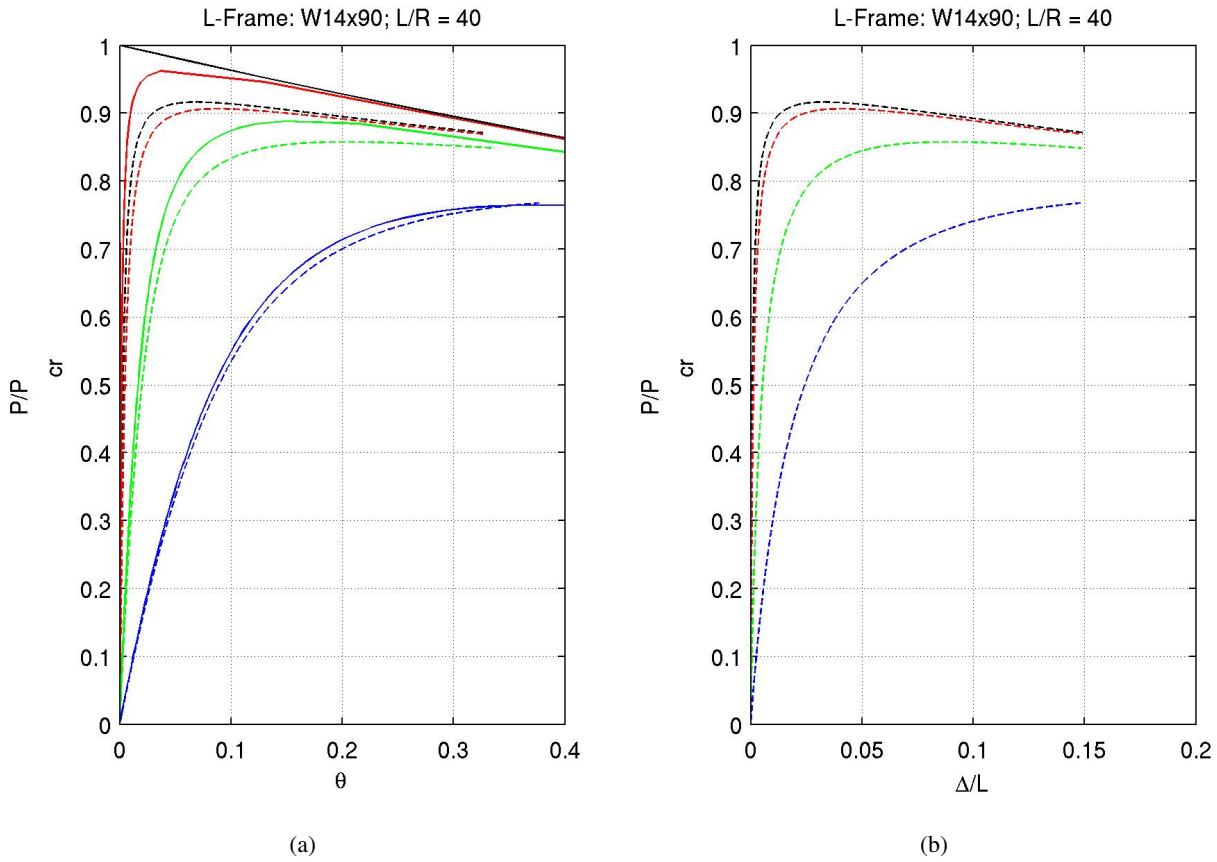

(a) (b)

Figure A.15: Comparison of the numerical solution using MEF elements (dashed lines) against a second-order analytical solution (solid lines) for the L-shaped Koiter-Roorda frame with a downward force (P) acting at the corner (black), or at eccentricities of e/L=0.001 (red), 0.01 (green), and 0.05 (blue): Case 1: W14x90, L/R=40) – (a) Corner rotation versus P/P_{CR}; (b) Corner in-plane lateral displacement versus P/P_{CR}.

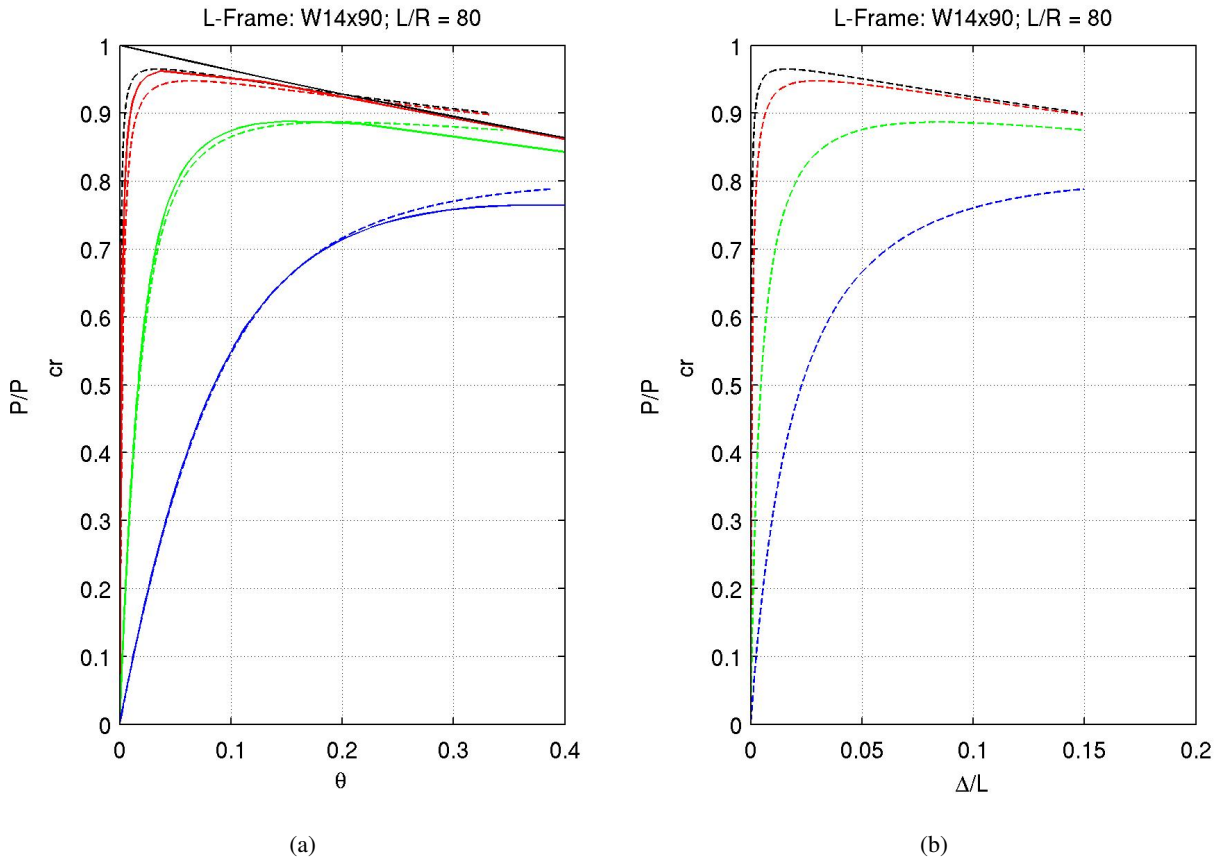

(a) (b)

Figure A.16: Comparison of the numerical solution using MEF elements (dashed lines) against a second-order analytical solution (solid lines) for the L-shaped Koiter-Roorda frame with a downward force (P) acting at the corner (black), or at eccentricities of e/L=0.001 (red), 0.01 (green), and 0.05 (blue): Case 1: W14x90, L/R=80) – (a) Corner rotation versus P/P_{CR}; (b) Corner in-plane lateral displacement versus P/P_{CR}.

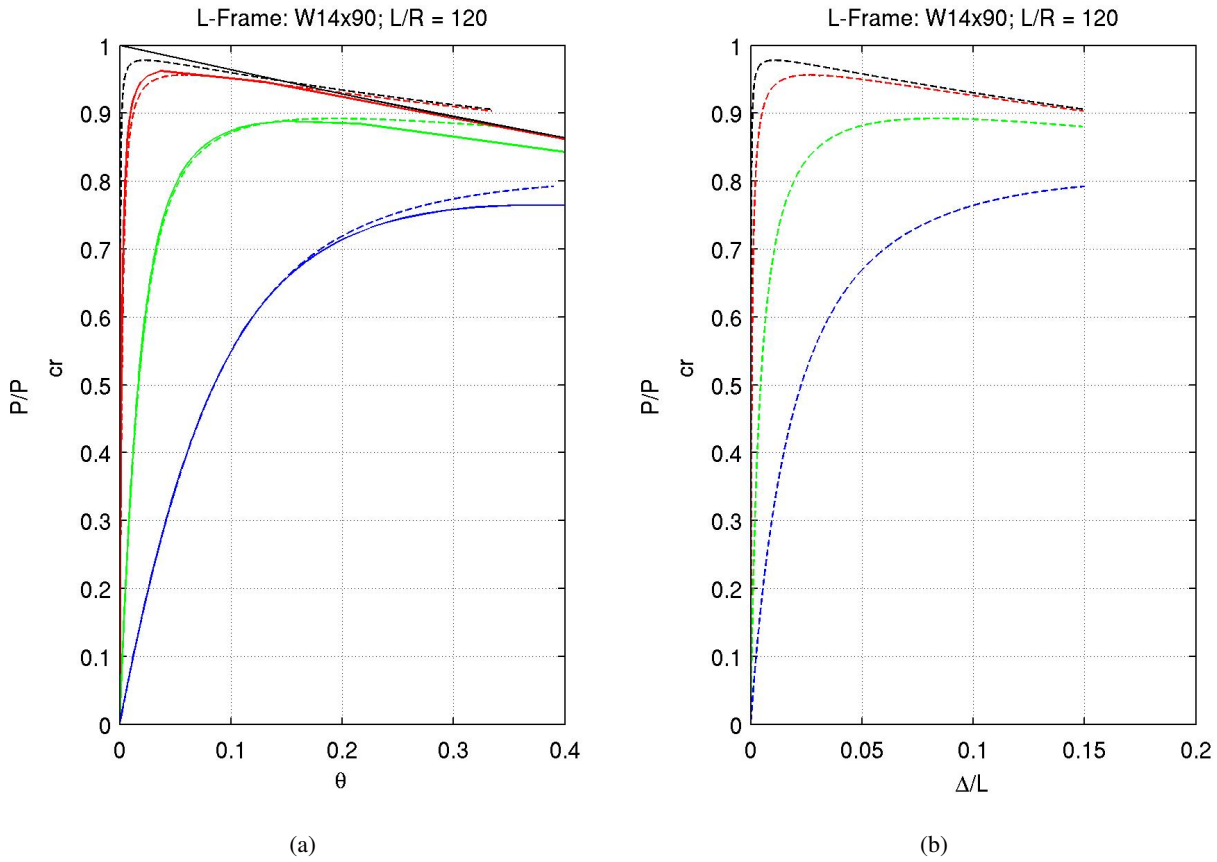

(a) (b)

Figure A.17: Comparison of the numerical solution using MEF elements (dashed lines) against a second-order analytical solution (solid lines) for the L-shaped Koiter-Roorda frame with a downward force (P) acting at the corner (black), or at eccentricities of e/L=0.001 (red), 0.01 (green), and 0.05 (blue): Case 1: W14x90, L/R=120) – (a) Corner rotation versus P/P_{CR}; (b) Corner in-plane lateral displacement versus P/P_{CR}.

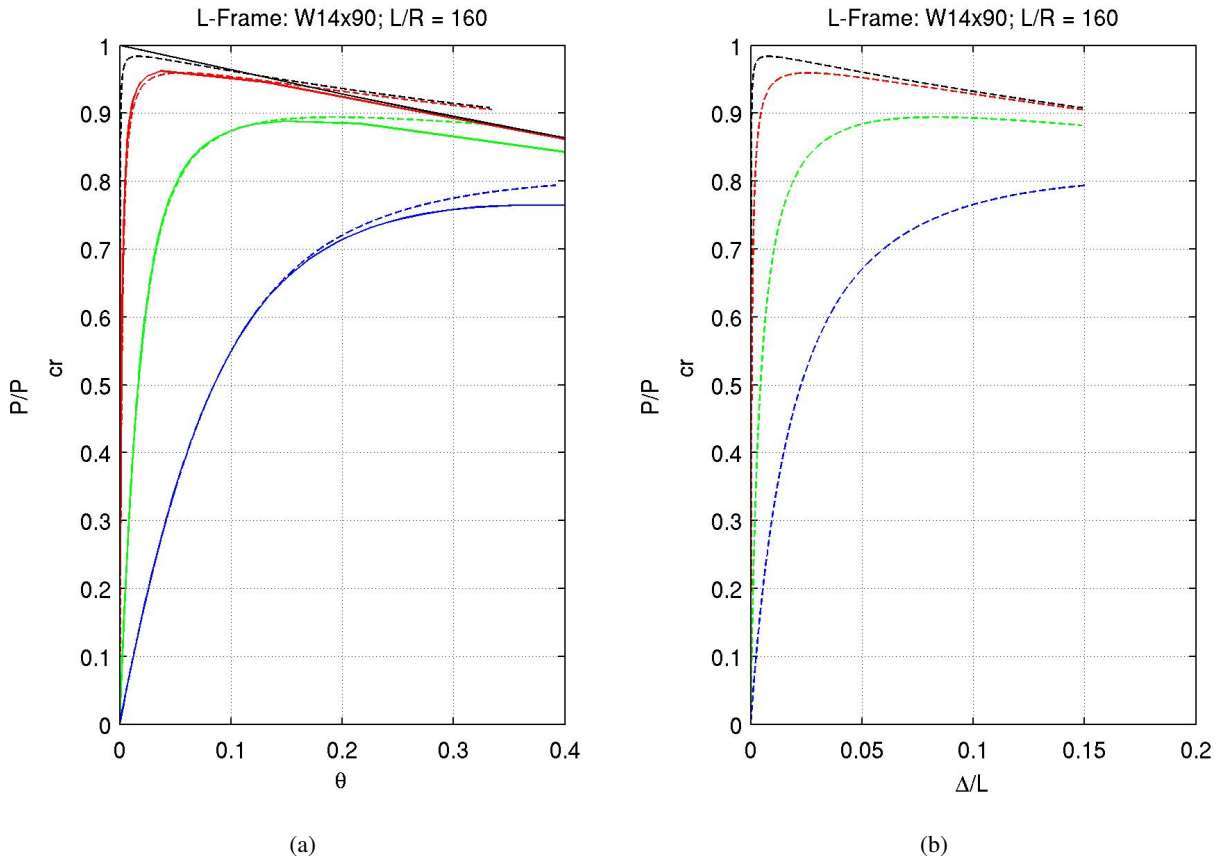

(a) (b)

Figure A.18: Comparison of the numerical solution using MEF elements (dashed lines) against a second-order analytical solution (solid lines) for the L-shaped Koiter-Roorda frame with a downward force (P) acting at the corner (black), or at eccentricities of e/L=0.001 (red), 0.01 (green), and 0.05 (blue): Case 1: W14x90, L/R=160) – (a) Corner rotation versus P/P_{CR}; (b) Corner in-plane lateral displacement versus P/P_{CR}.

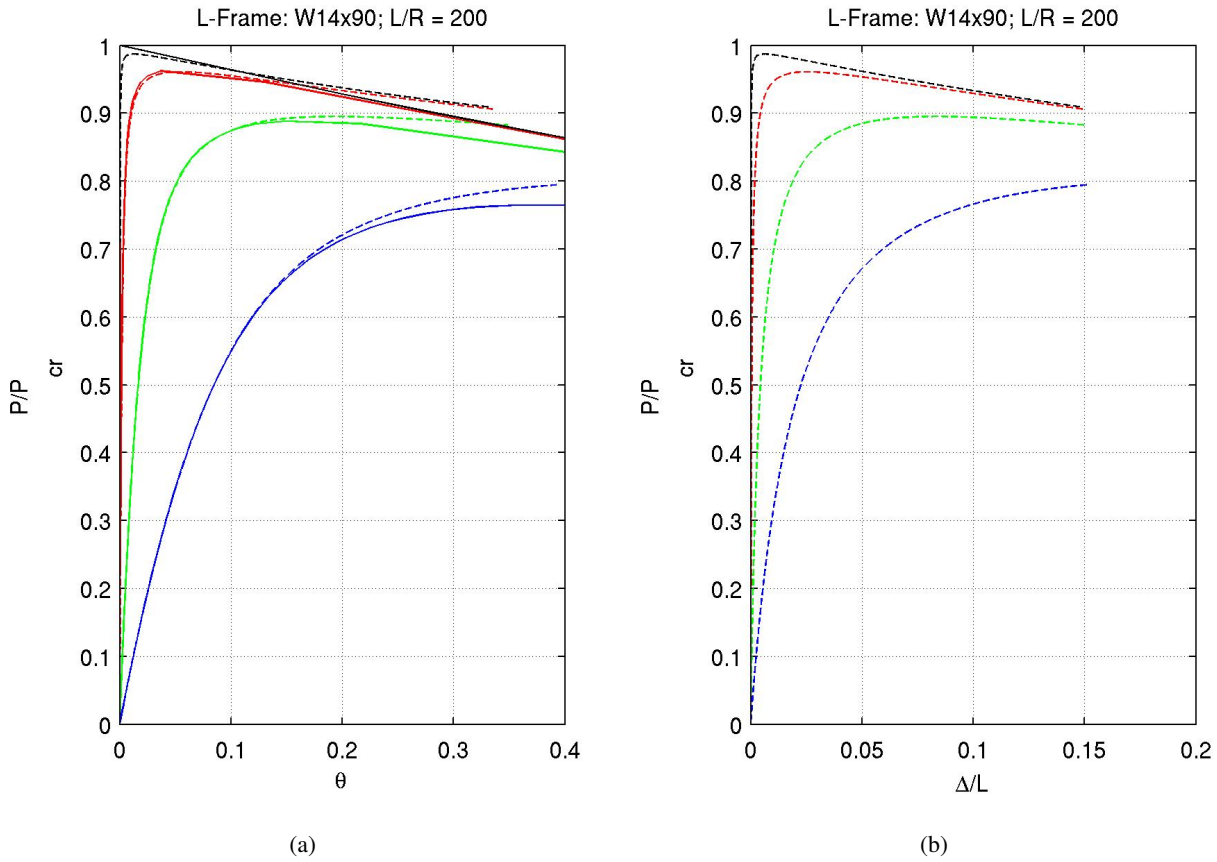

(a) (b)

Figure A.19: Comparison of the numerical solution using MEF elements (dashed lines) against a second-order analytical solution (solid lines) for the L-shaped Koiter-Roorda frame with a downward force (P) acting at the corner (black), or at eccentricities of e/L=0.001 (red), 0.01 (green), and 0.05 (blue): Case 1: W14x90, L/R=200) – (a) Corner rotation versus P/P_{CR}; (b) Corner in-plane lateral displacement versus P/P_{CR}.

Appendix B Black et al. Tests

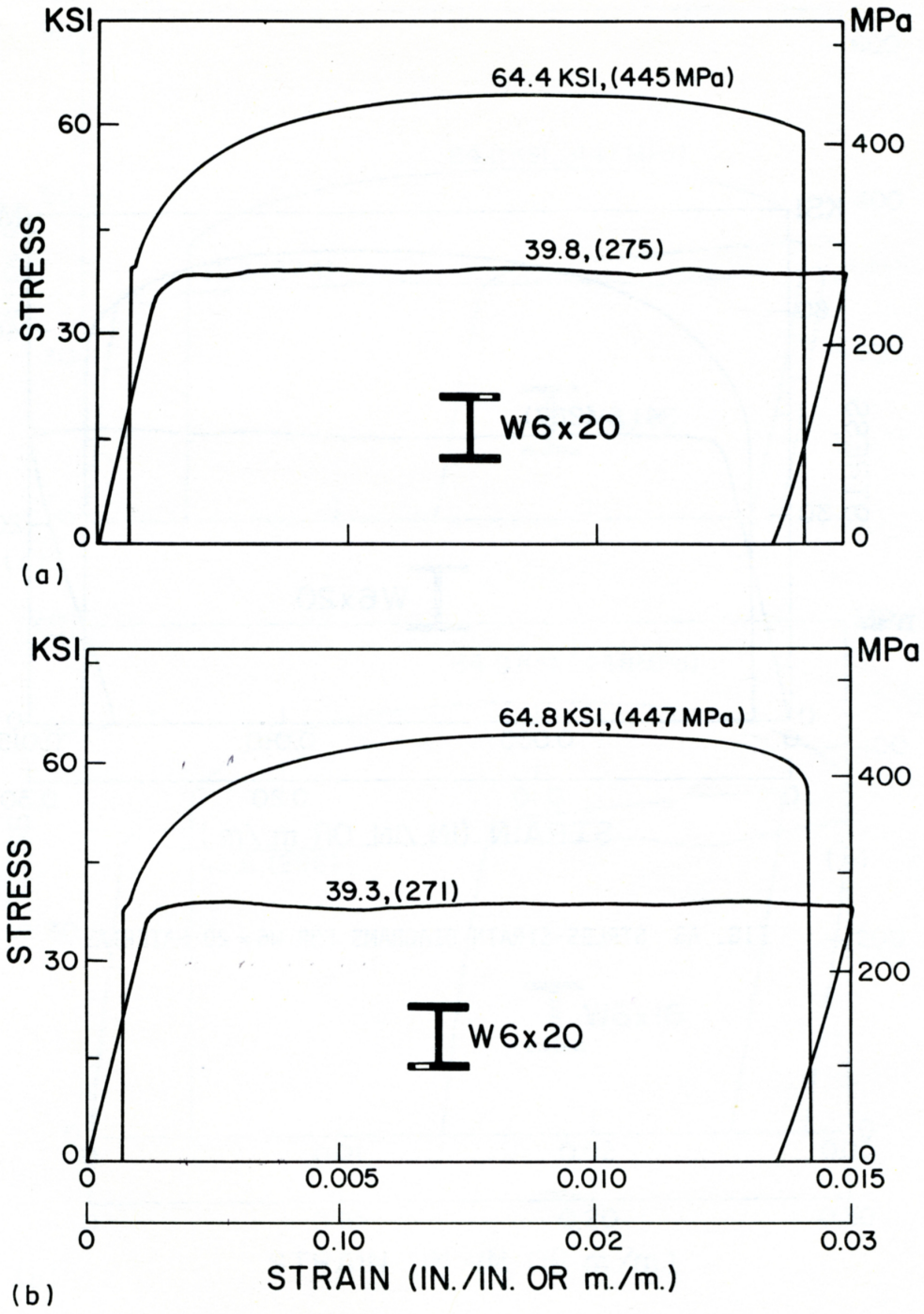

Figure B.1: Black et al. tests: W6x20 coupon tensile loading test.

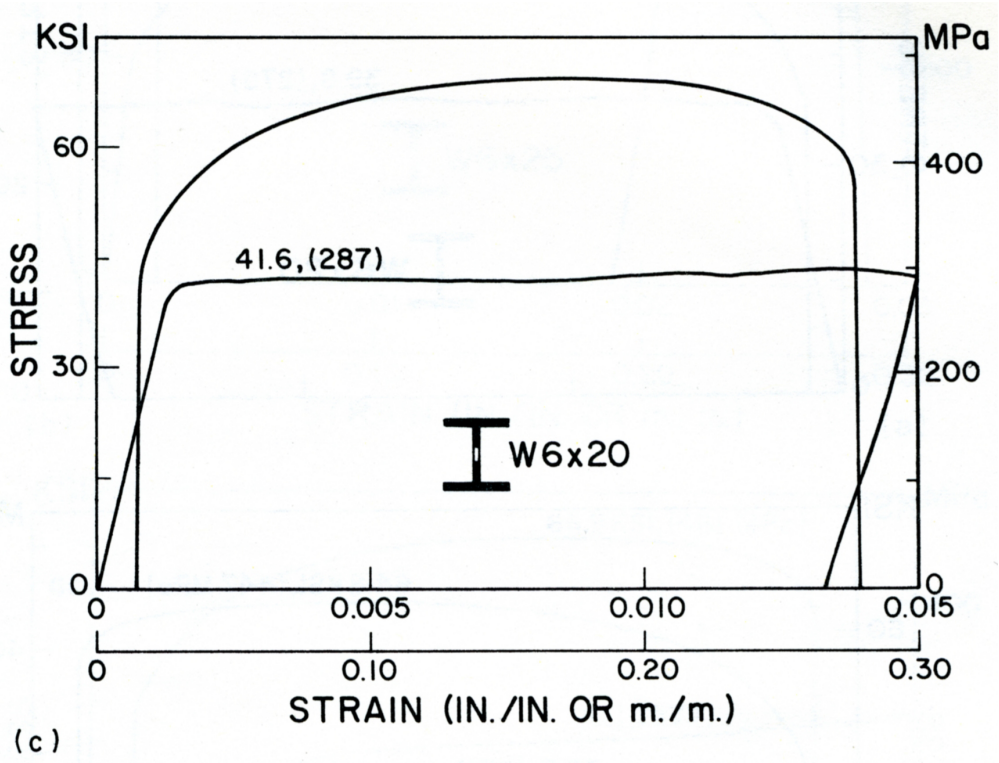

Figure B.2: Black et al. tests: W6x20 coupon tensile loading test (contd.).

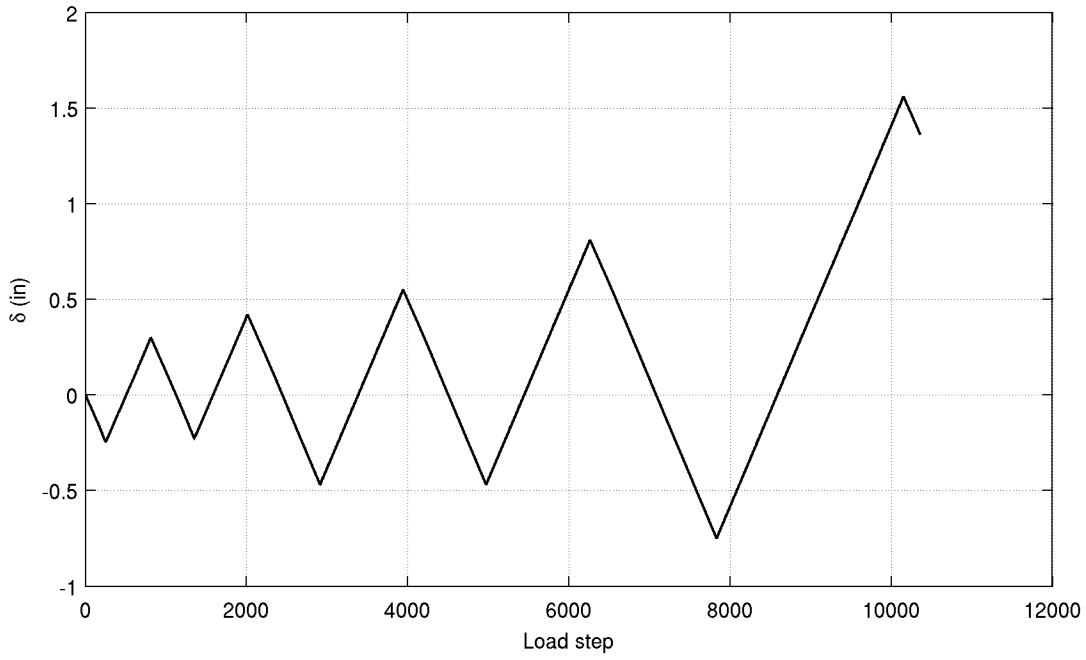

Figure B.3: Black et al. tests: Pinned ended W6x20 strut (3) with KL/r=80 – Loading history.

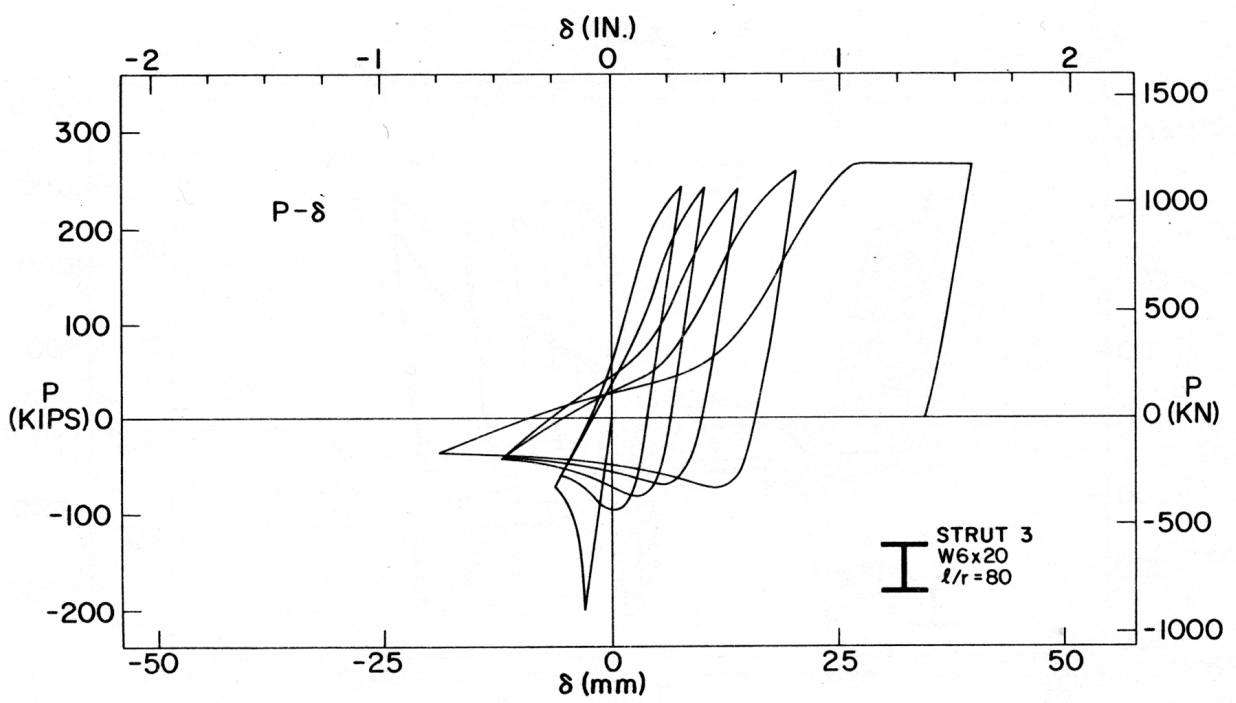

(a)

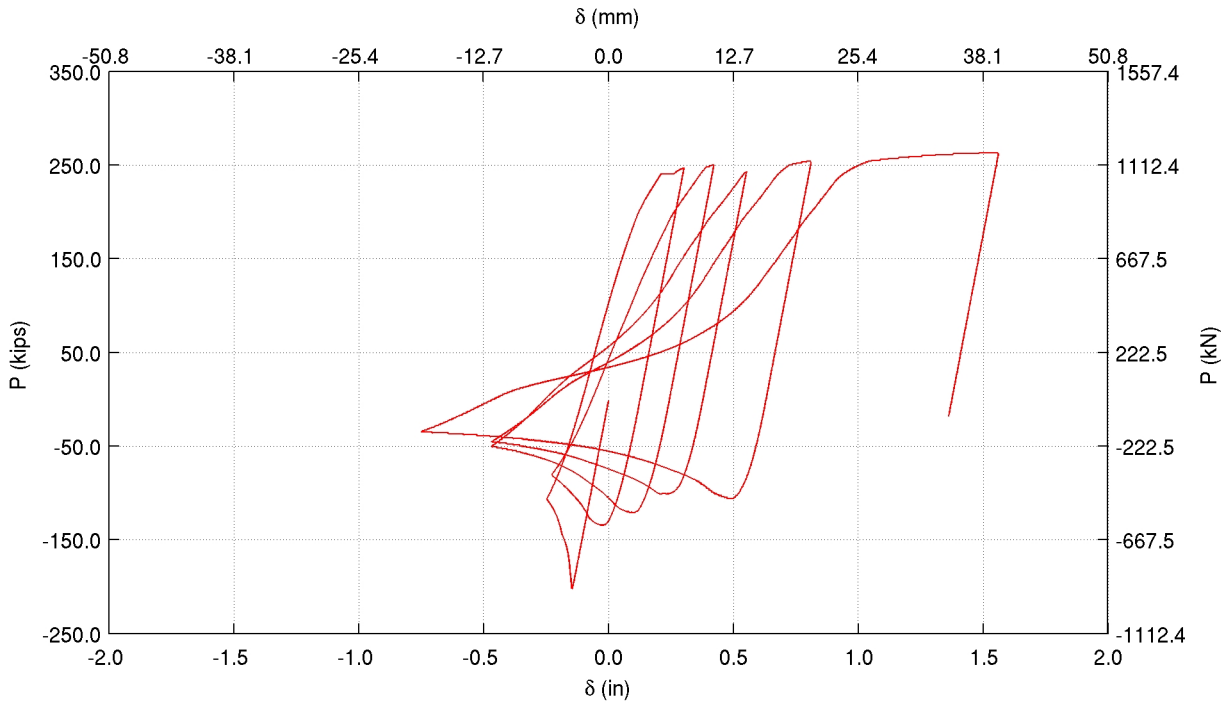

(b)

Figure B.4: Black et al. tests: Pinned ended W6x20 strut (1) with KL/r=80, axial displacement versus axial force history – (a) Experiment (b) Simulation.

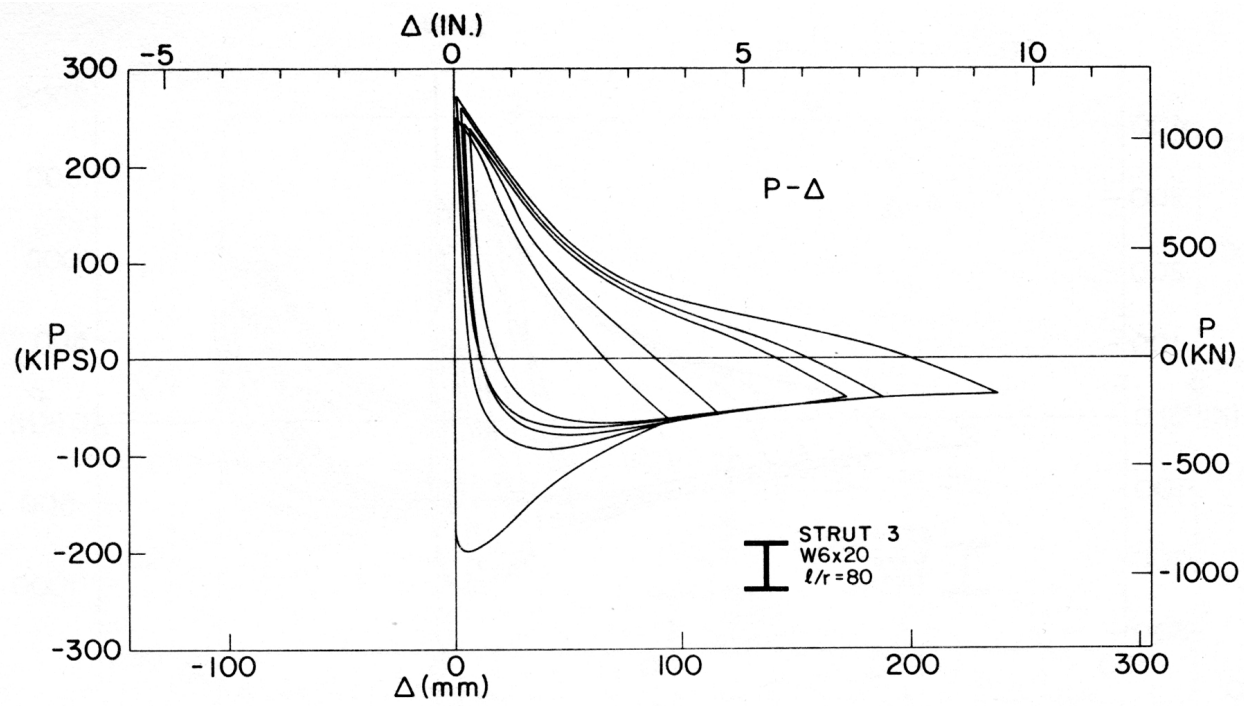

(a)

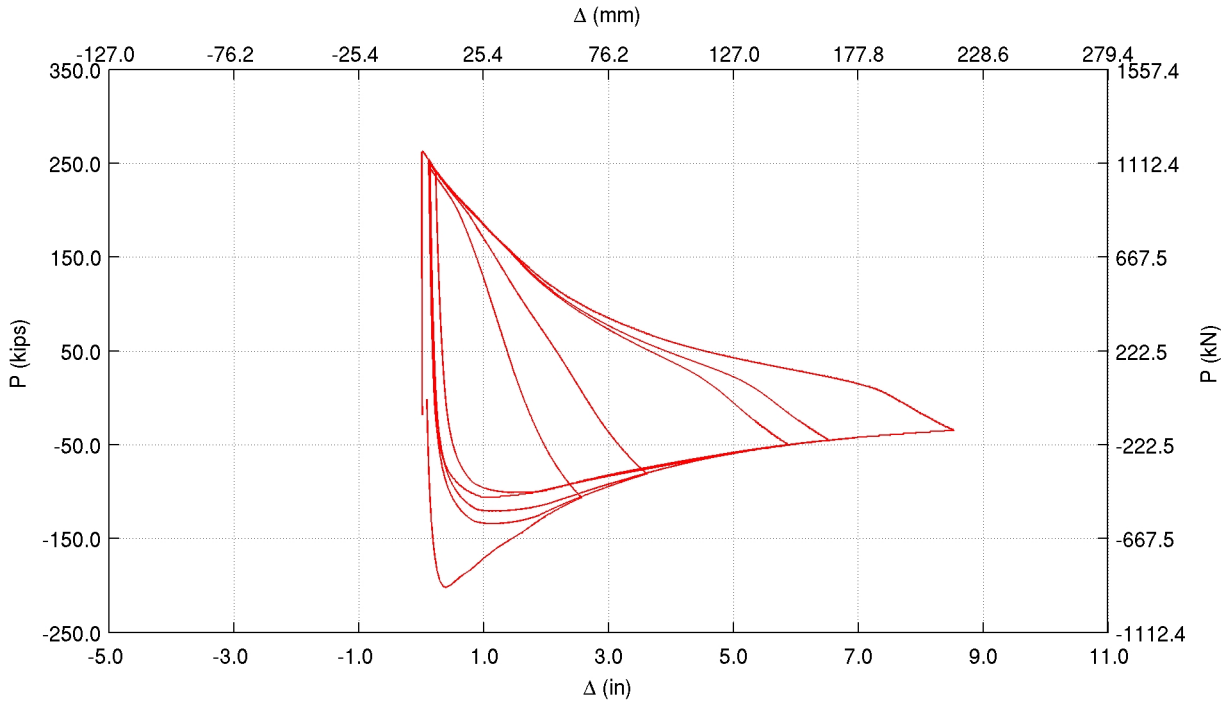

(b)

Figure B.5: Black et al. tests: Pinned ended W6x20 strut (1) with KL/r=80, lateral displacement versus axial force history – (a) Experiment (b) Simulation.

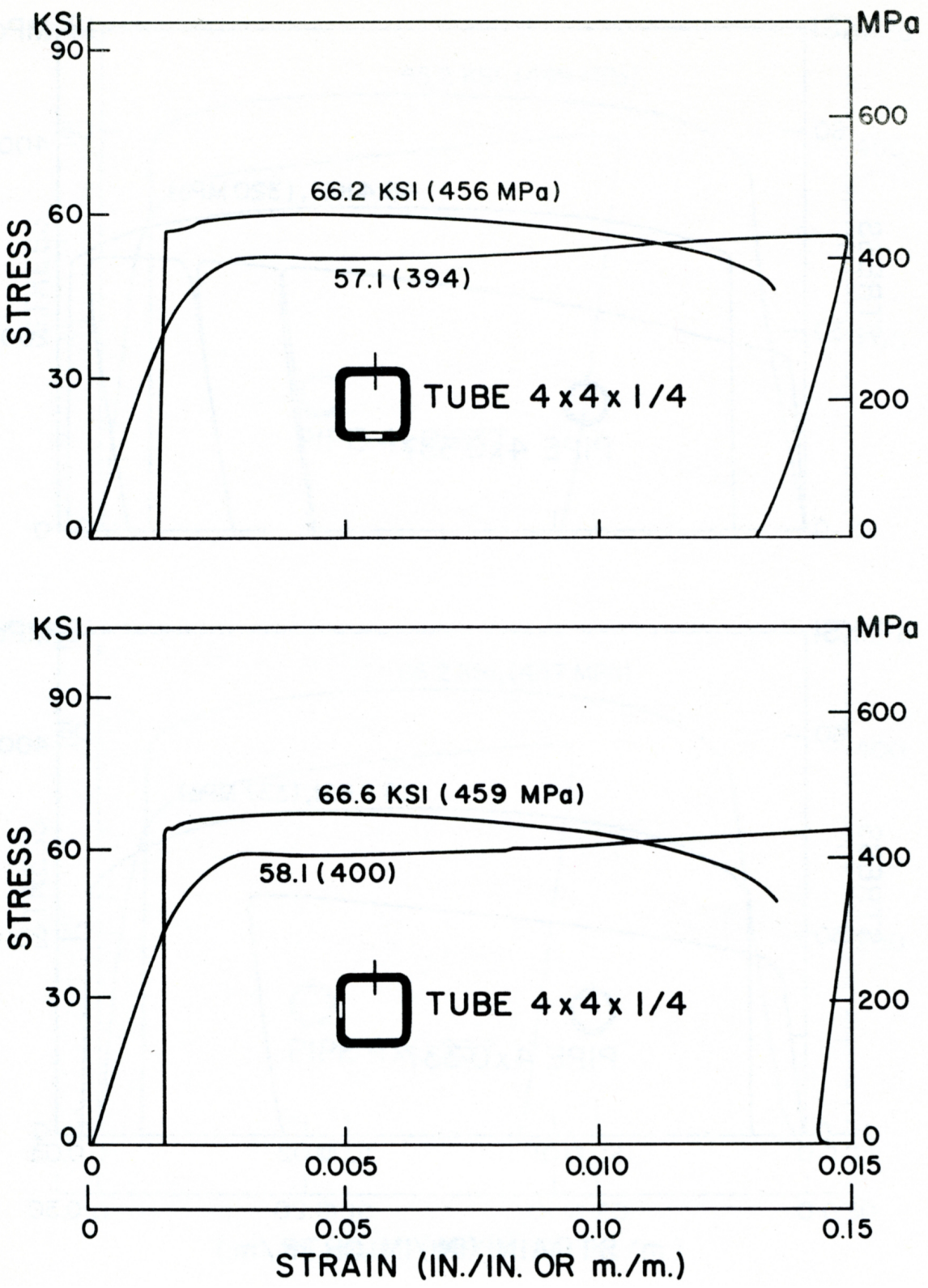

Figure B.6: Black et al. tests: TS4x4x1/4 coupon tensile loading test.

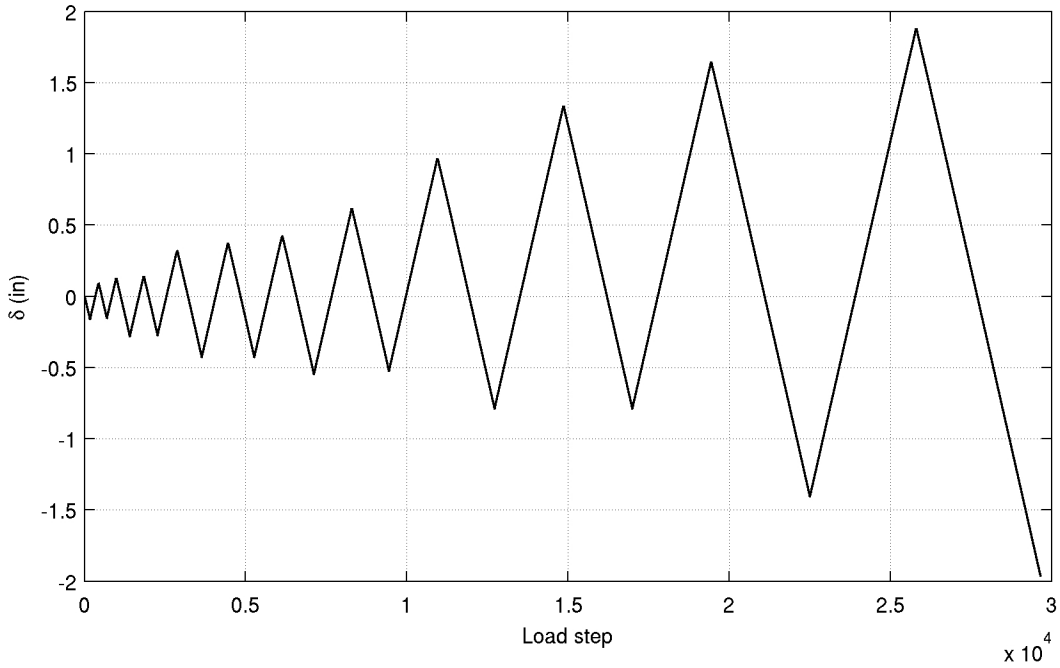

Figure B.7: Black et al. tests: Pinned ended TS4x4x1/4 strut (17) with KL/r=80 – Loading history.

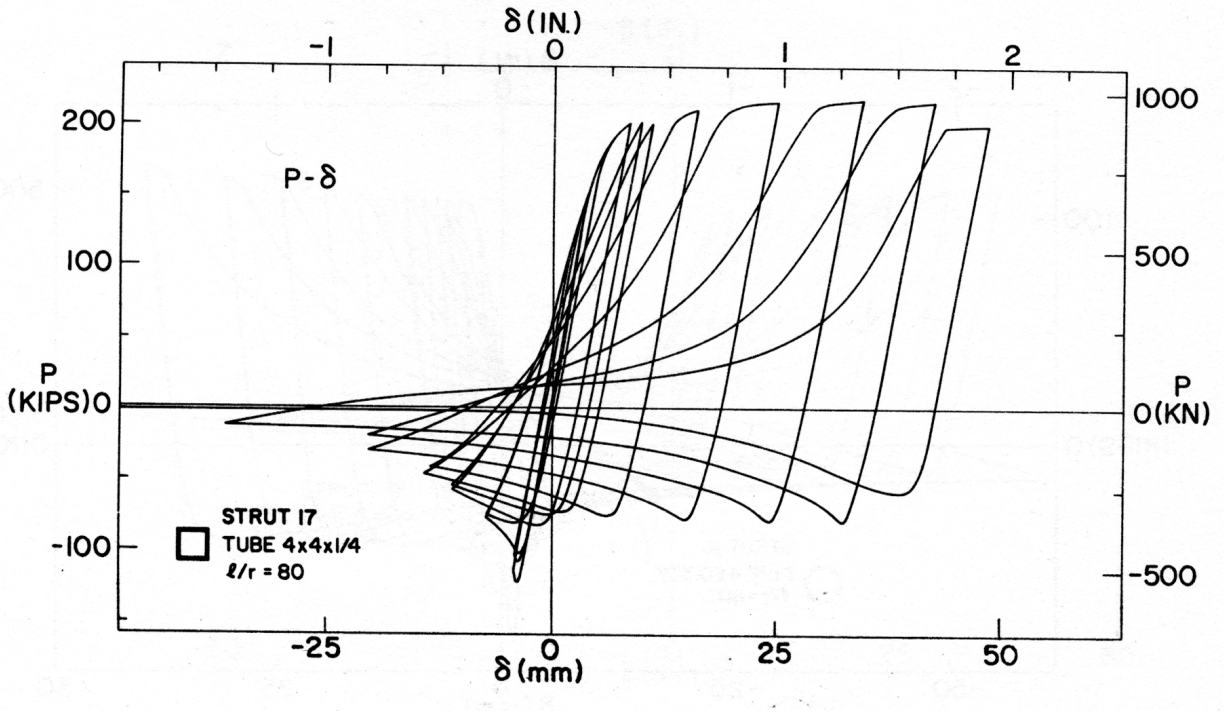

(a)

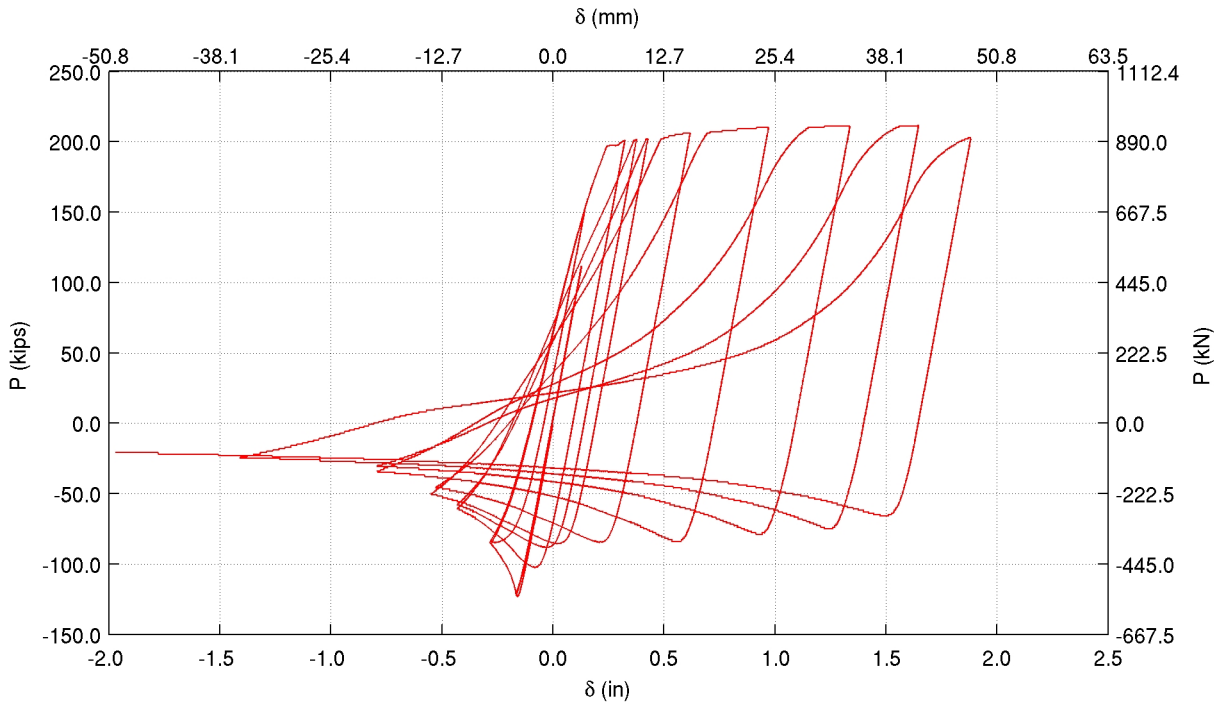

(b)

Figure B.8: Black et al. tests: Pinned ended TS4x4x1/4 strut (17) with KL/r=80, axial displacement versus axial force history – (a) Experiment (b) Simulation.

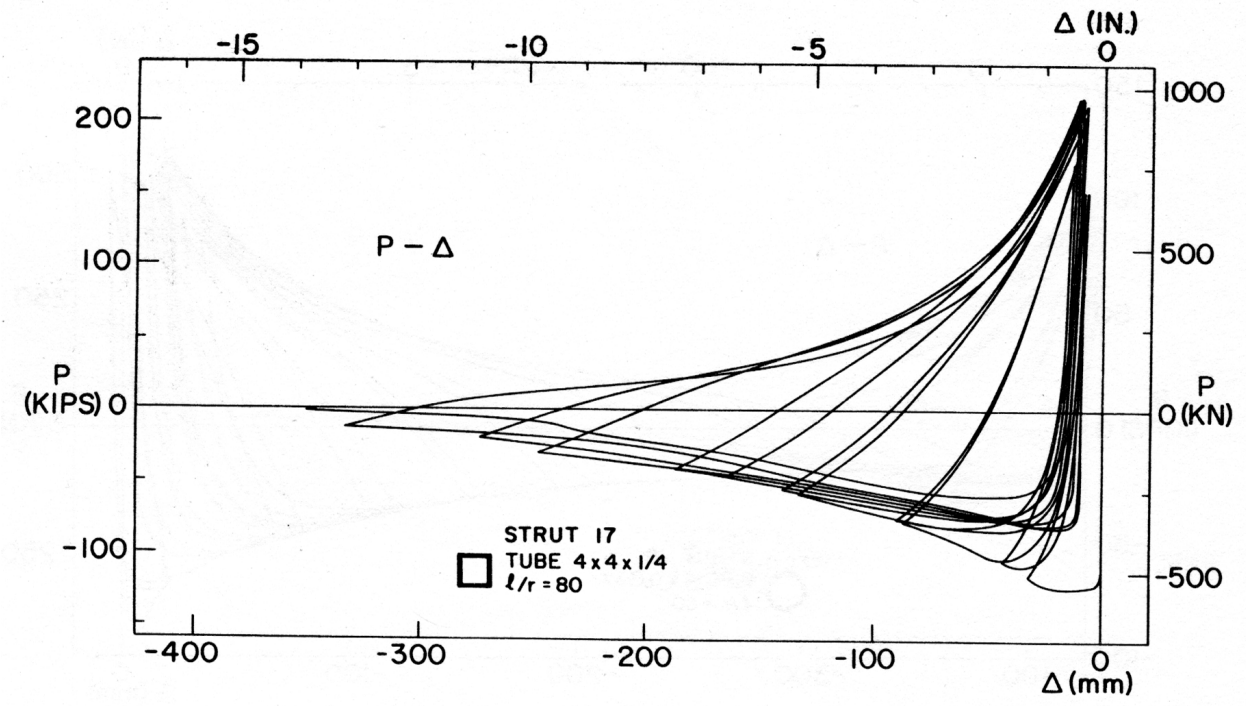

(a)

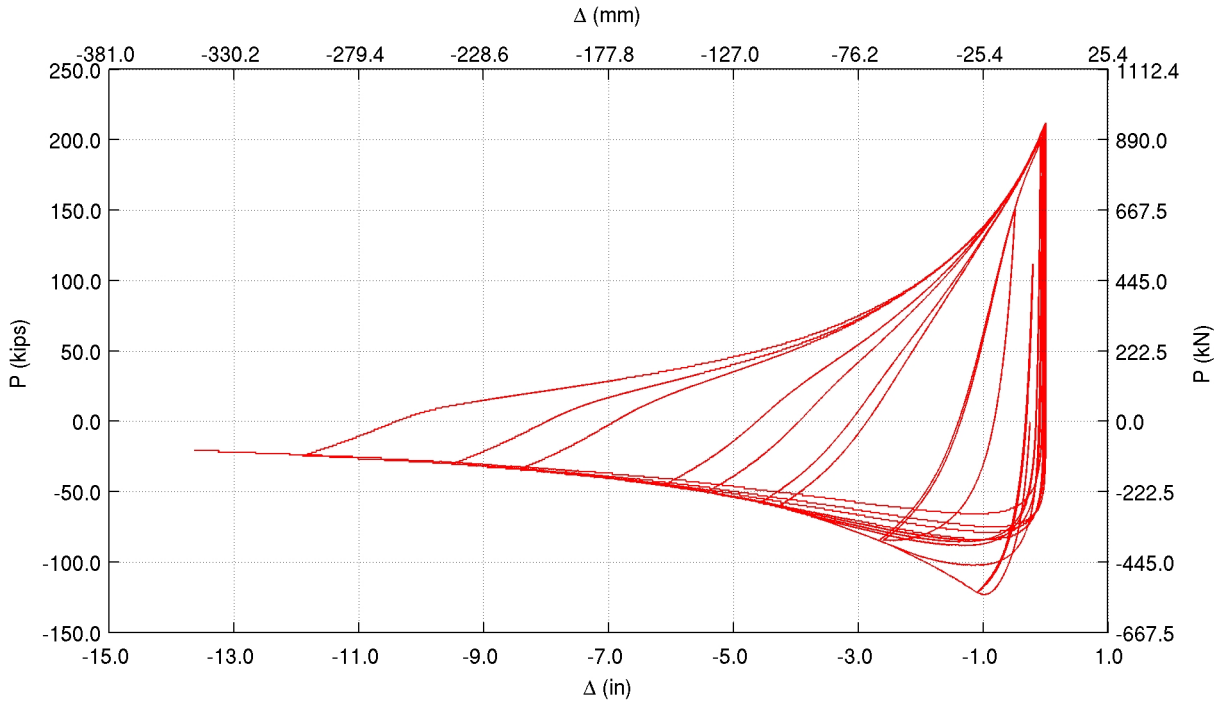

(b)

Figure B.9: Black et al. tests: Pinned ended TS4x4x1/4 strut (17) with KL/r=80, lateral displacement versus axial force history – (a) Experiment (b) Simulation.

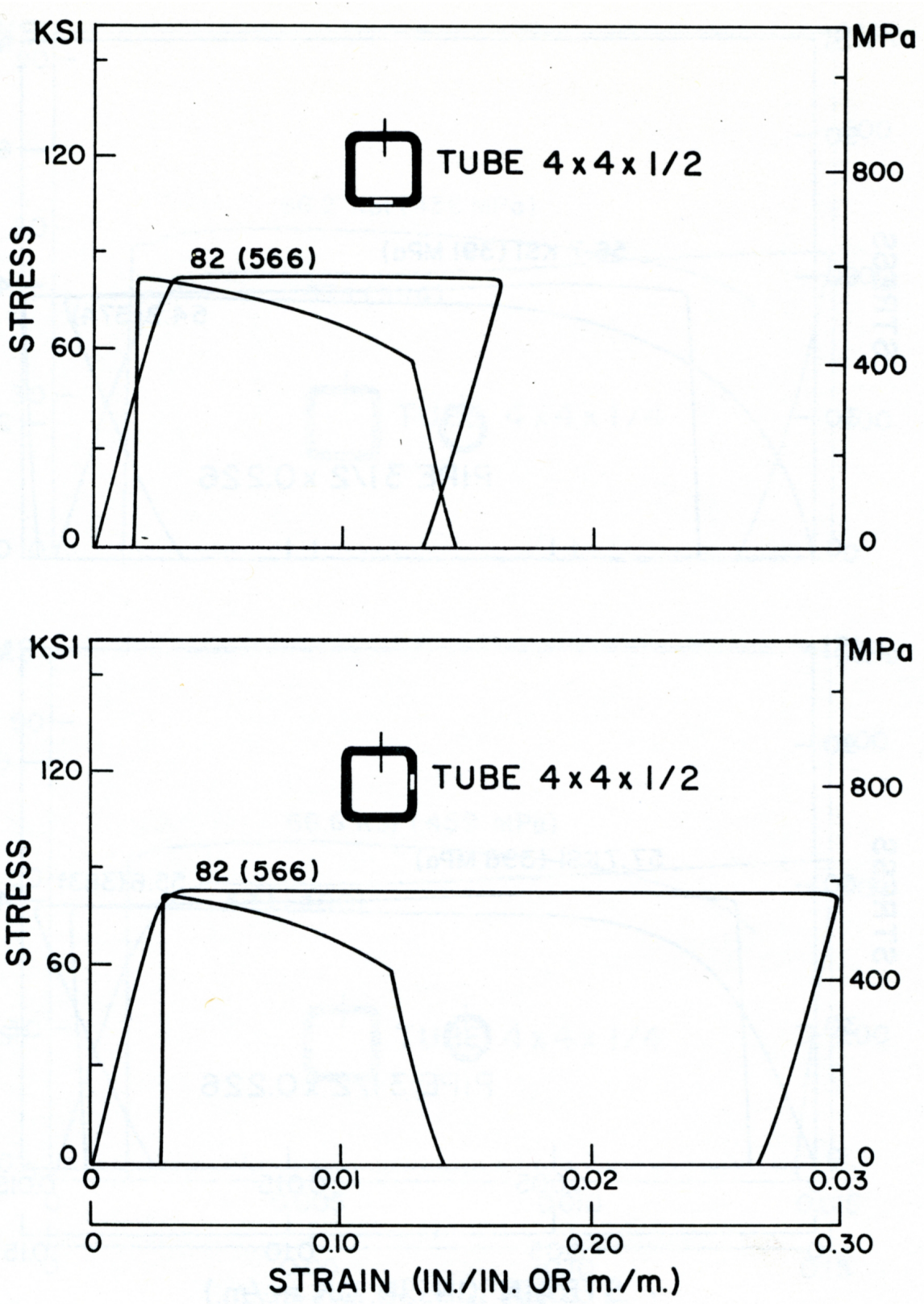

Figure B.10: Black et al. tests: TS4x4x1/2 coupon tensile loading test.

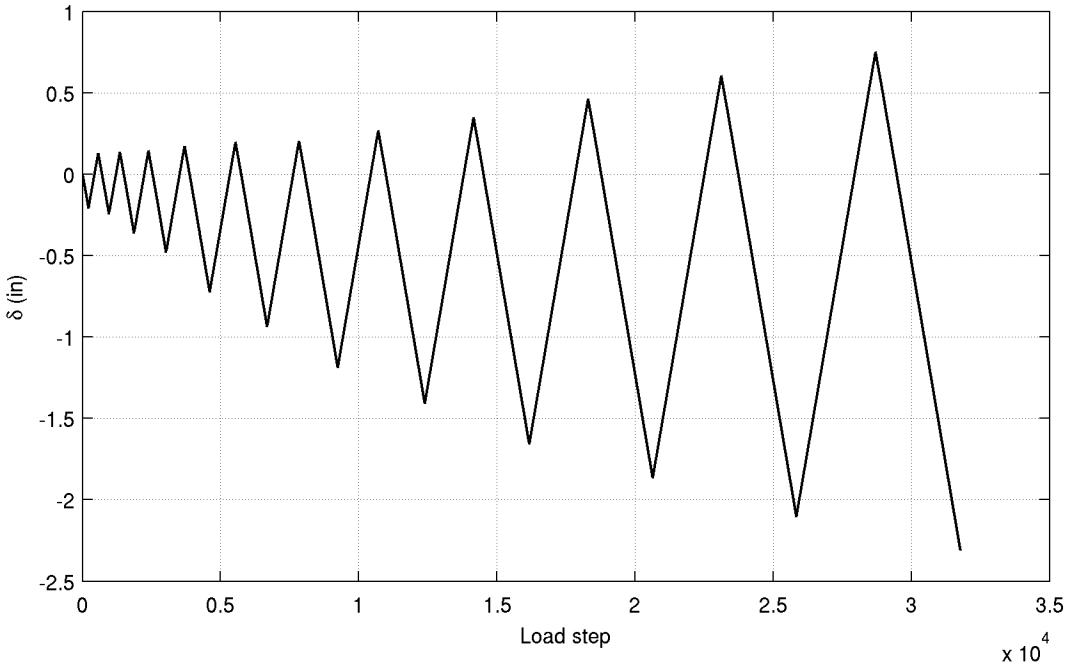

Figure B.11: Black et al. tests: Pinned ended TS4x4x1/2 strut (18) with KL/r=80 – Loading history.

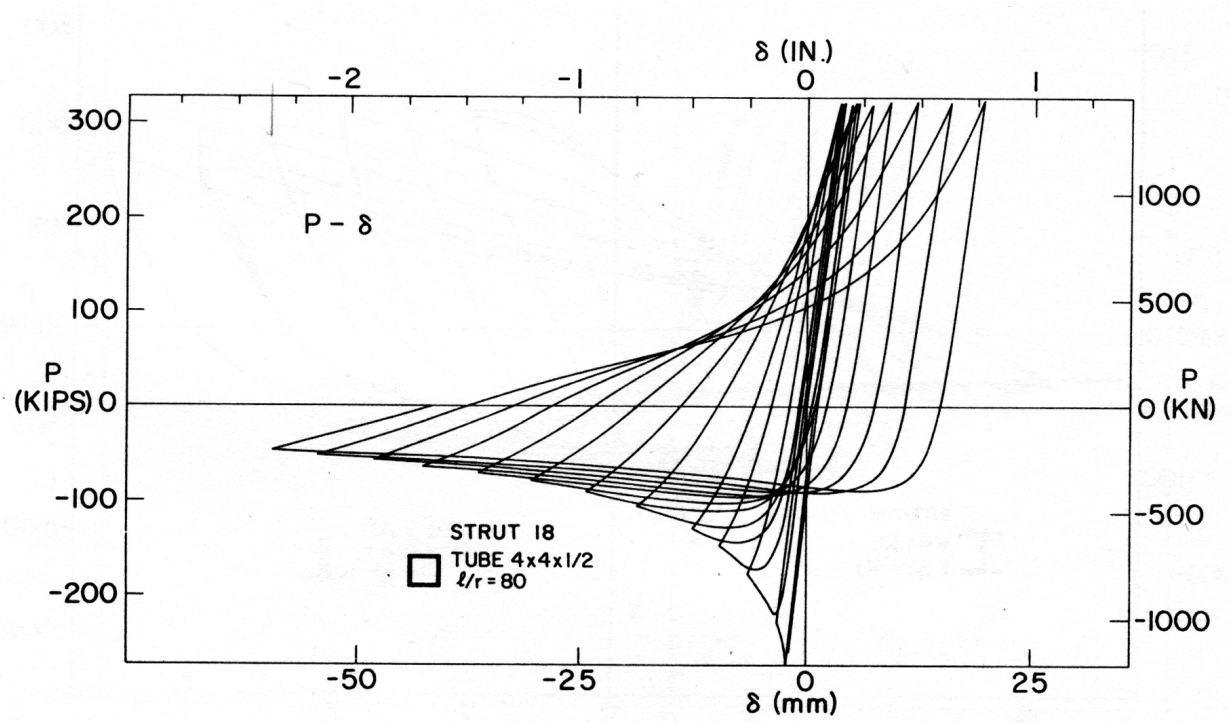

(a)

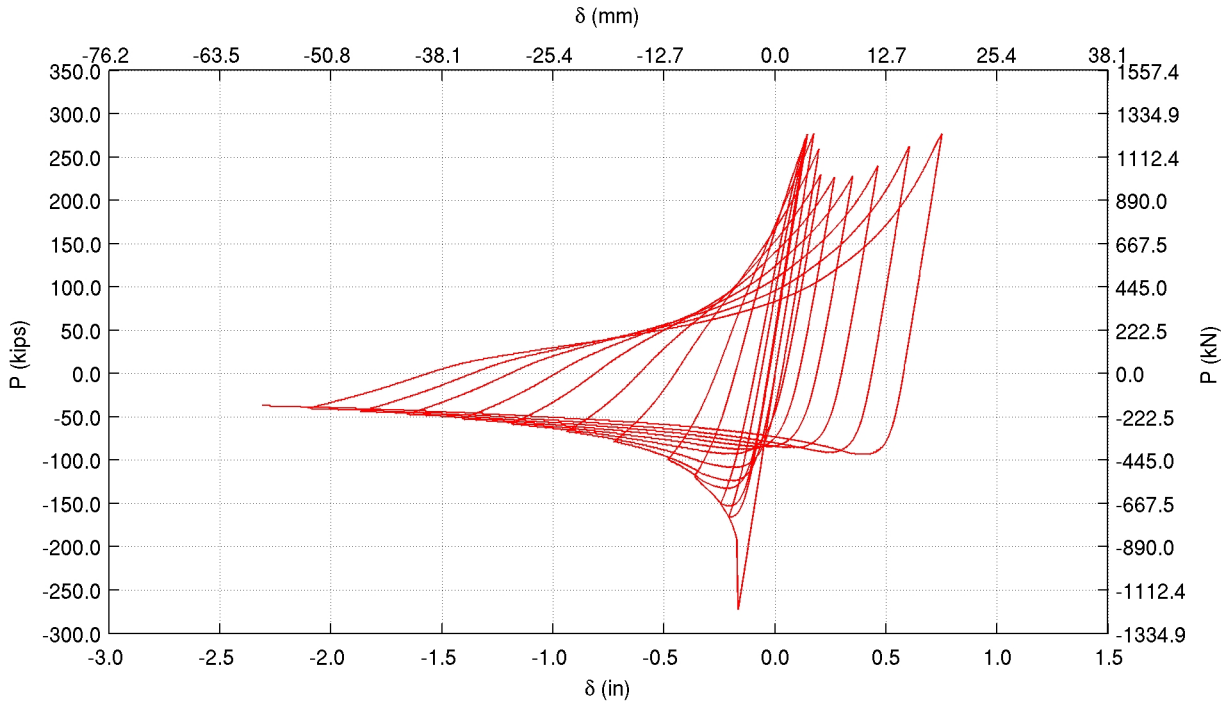

(b)

Figure B.12: Black et al. tests: Pinned ended TS4x4x1/2 strut (18) with KL/r=80, axial displacement versus axial force history – (a) Experiment (b) Simulation.

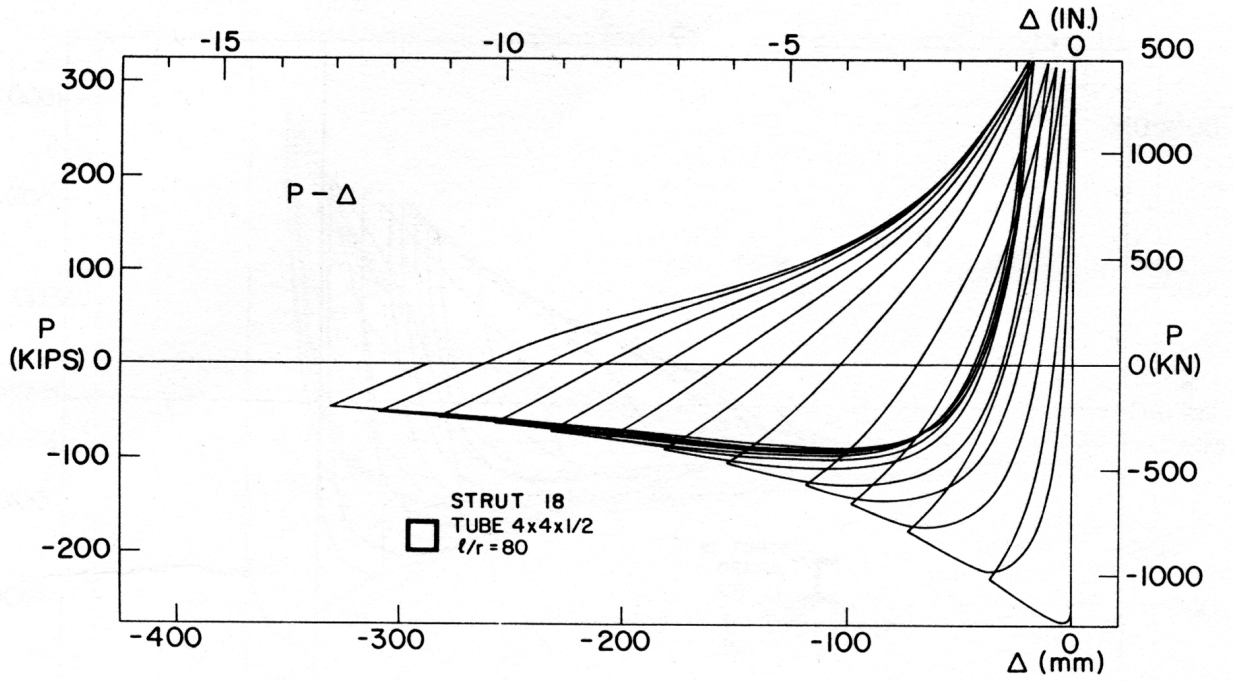

(a)

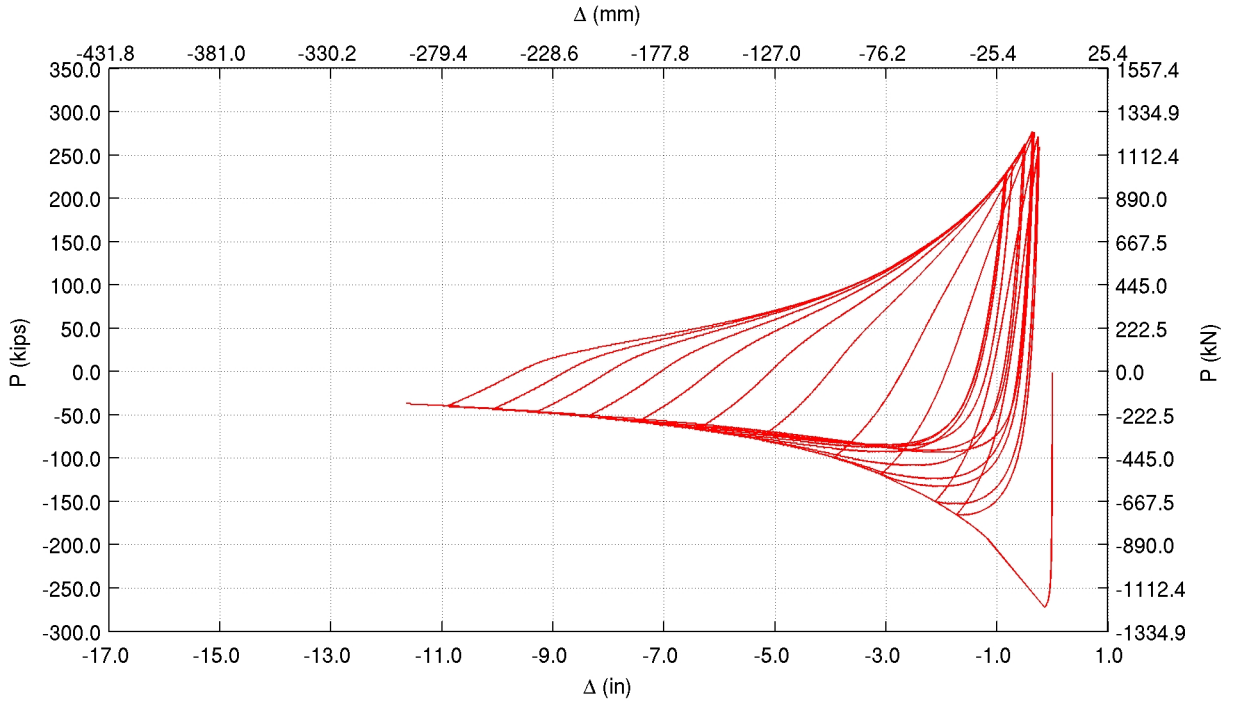

(b)

Figure B.13: Black et al. tests: Pinned ended TS4x4x1/2 strut (18) with KL/r=80, lateral displacement versus axial force history – (a) Experiment (b) Simulation.

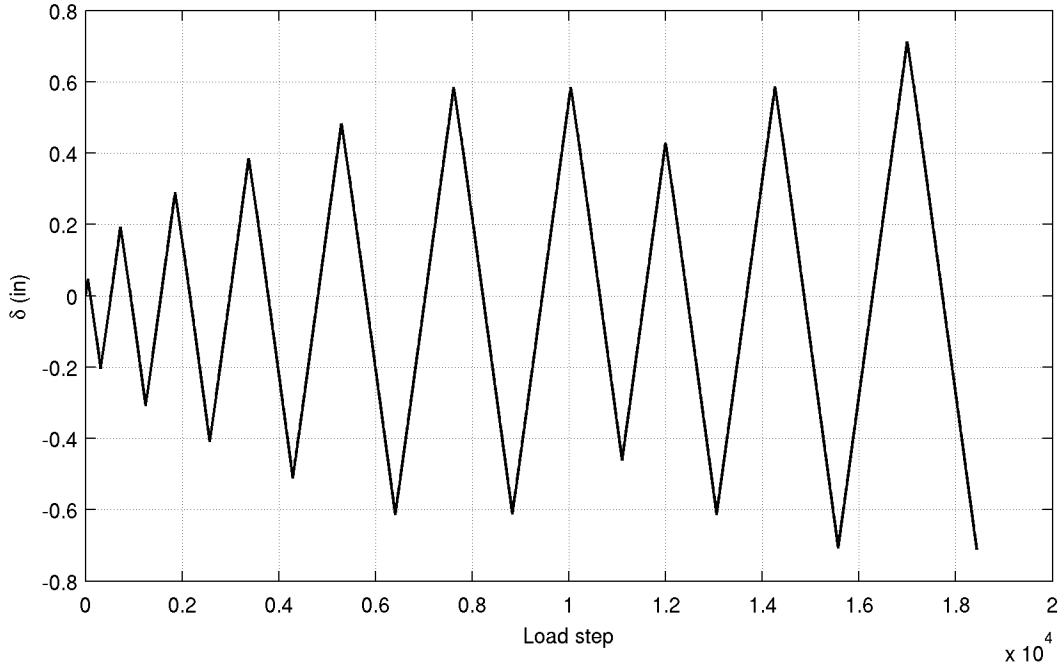

Figure B.14: Black et al. tests: W6x20 strut (19) with KL/r=40 pinned at one end and fixed at the other – Loading history.

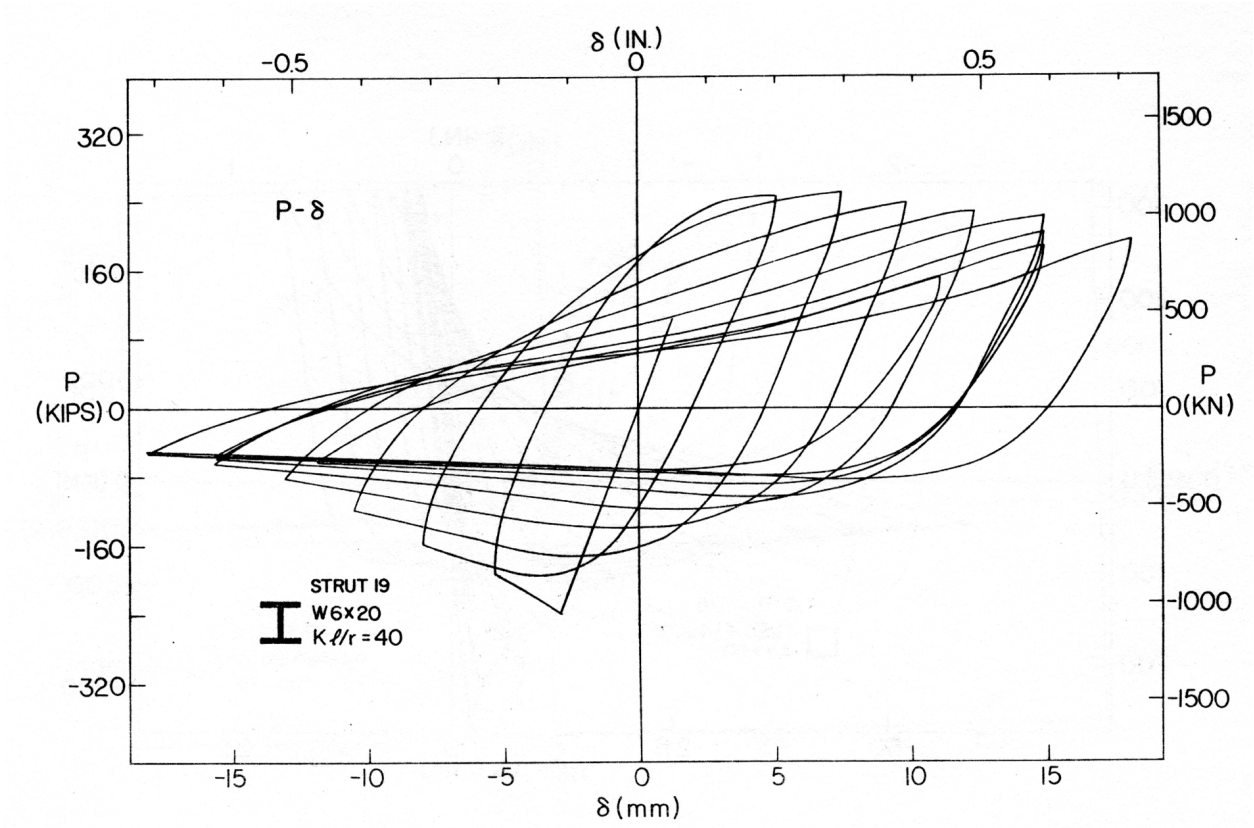

(a)

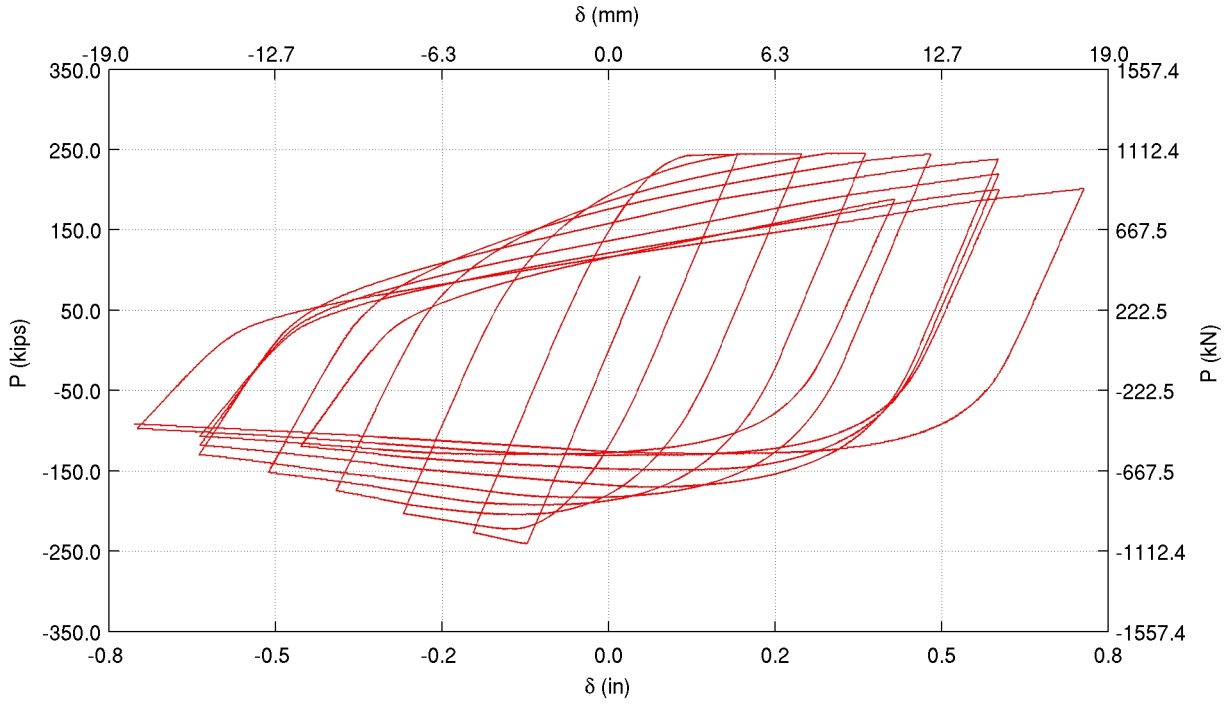

(b)

Figure B.15: Black et al. tests: W6x20 strut (19) with KL/r=40 pinned at one end and fixed at the other, axial displacement versus axial force history – (a) Experiment (b) Simulation.

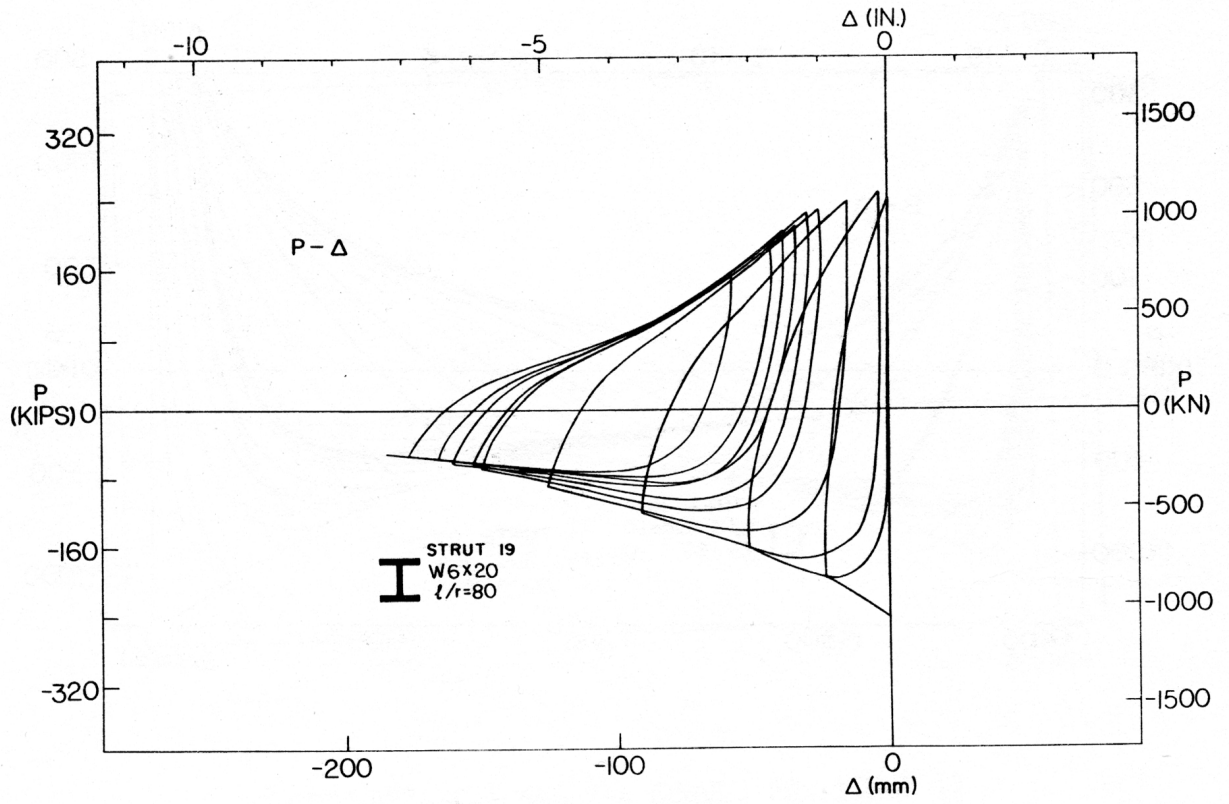

(a)

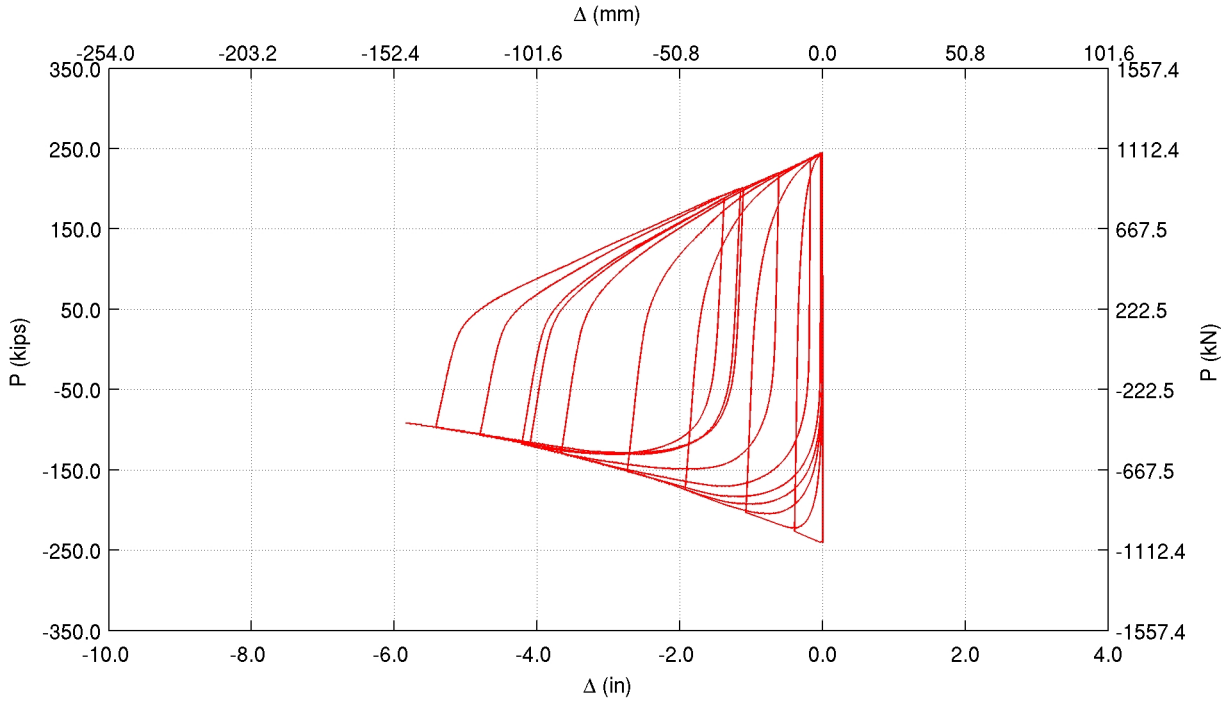

(b)

Figure B.16: Black et al. tests: W6x20 strut (19) with KL/r=40 pinned at one end and fixed at the other, lateral displacement versus axial force history – (a) Experiment (b) Simulation.

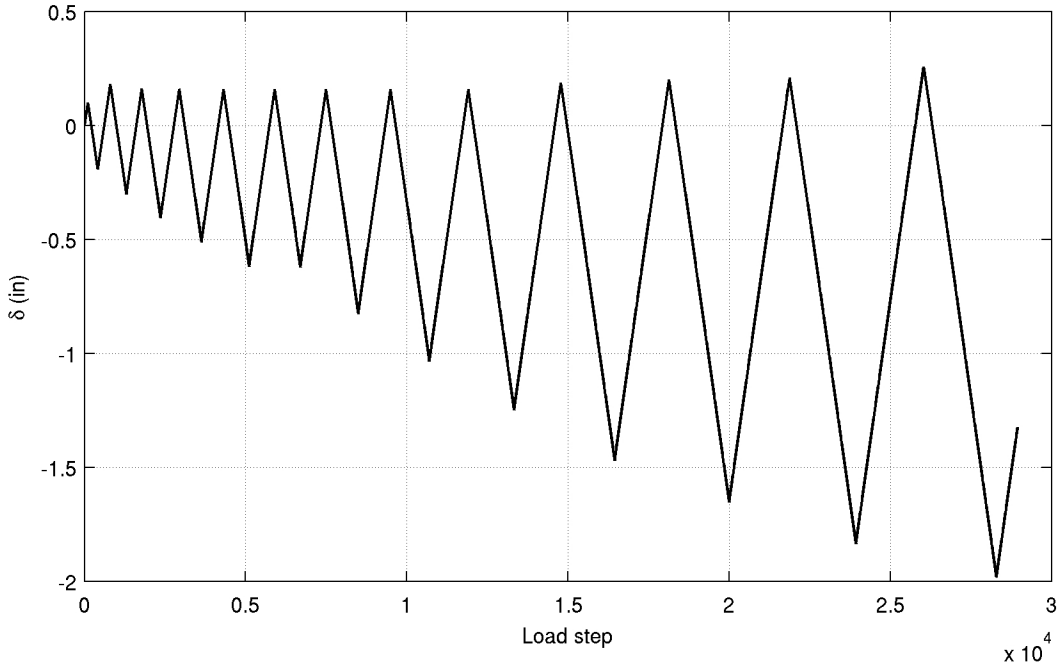

Figure B.17: Black et al. tests: Pinned ended TS4x4x1/2 strut (22) with KL/r=80 – Loading history.

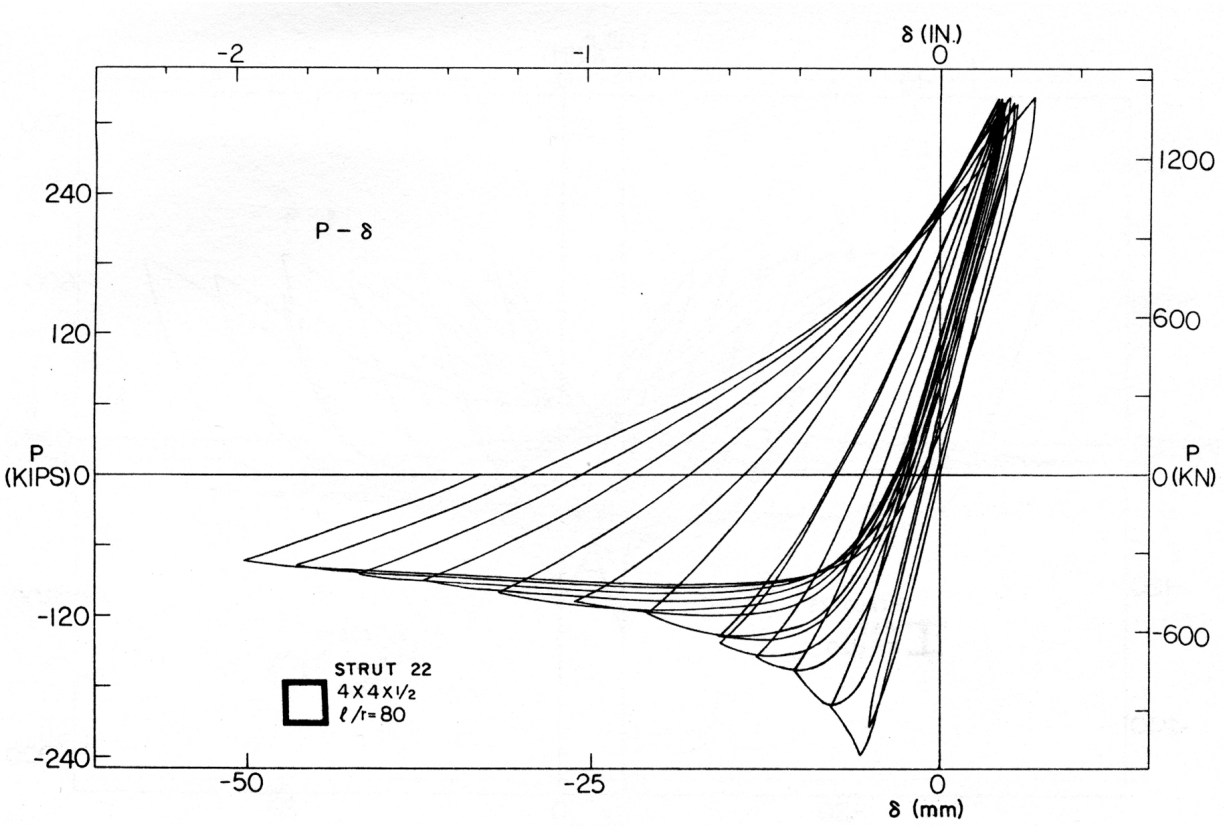

(a)

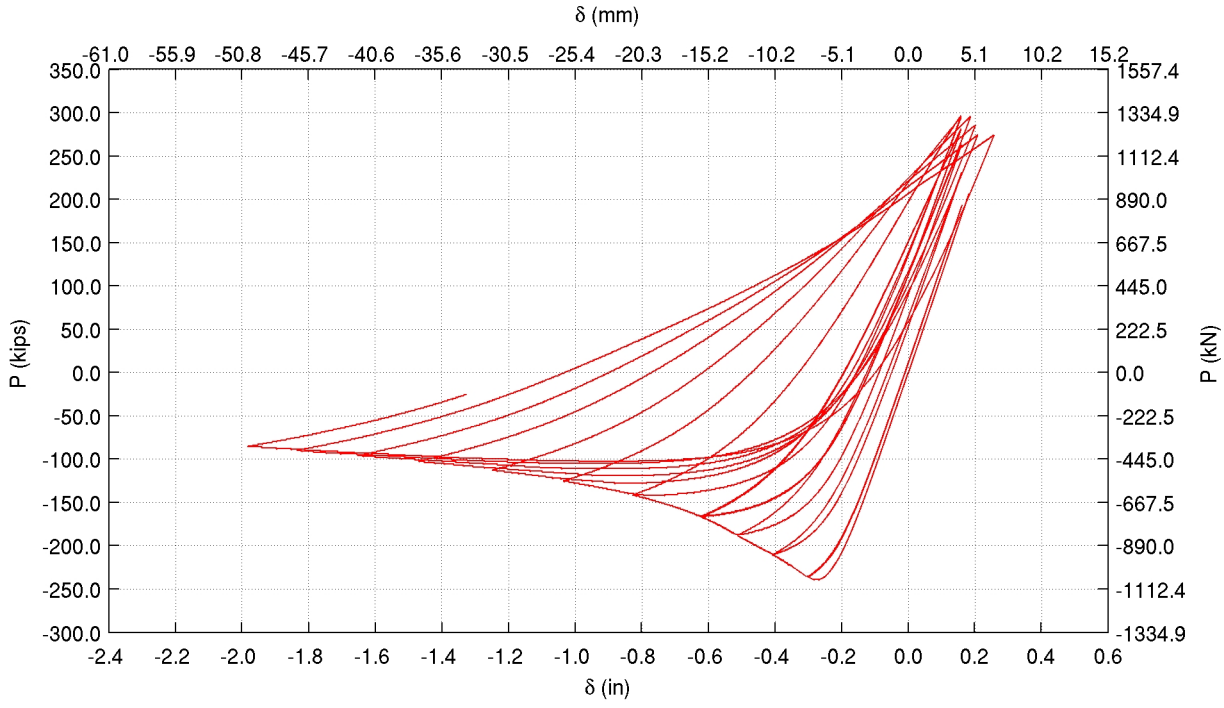

(b)

Figure B.18: Black et al. tests: TS4x4x1/2 strut (22) with KL/r=80 pinned at one end and fixed at the other, axial displacement versus axial force history – (a) Experiment (b) Simulation.

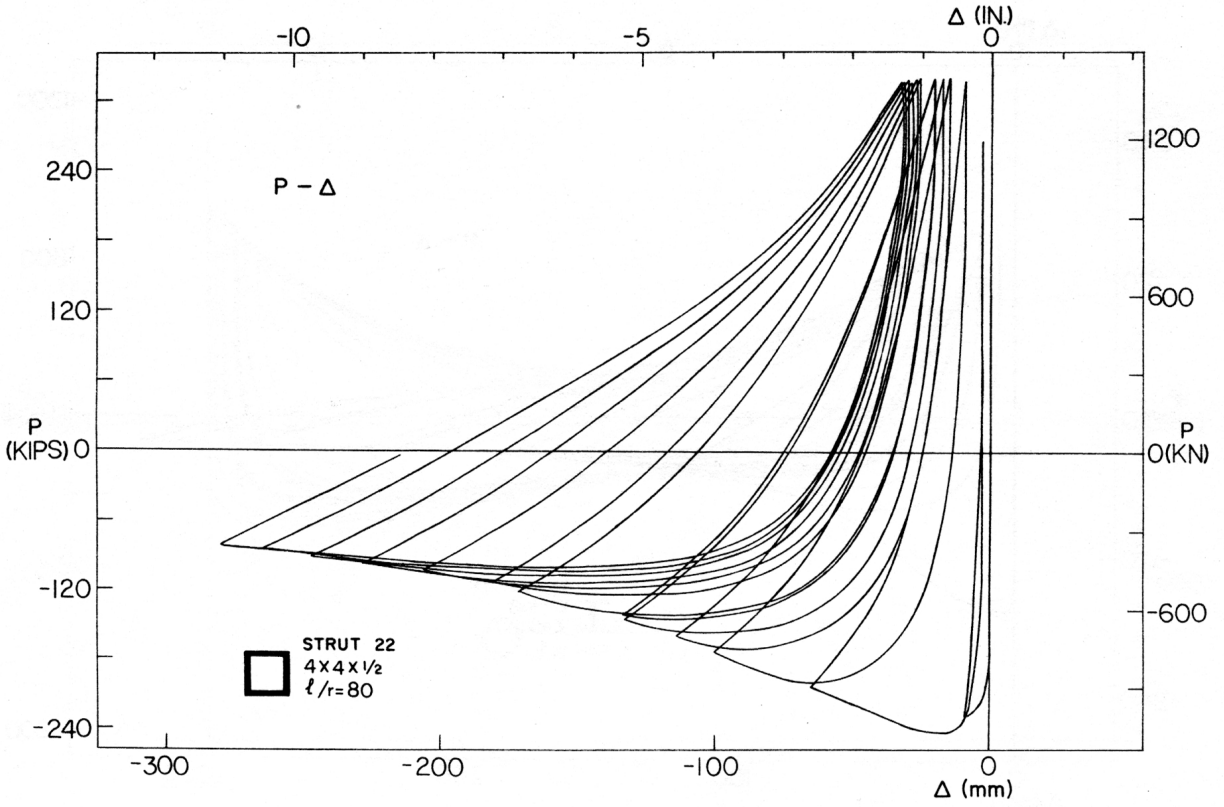

(a)

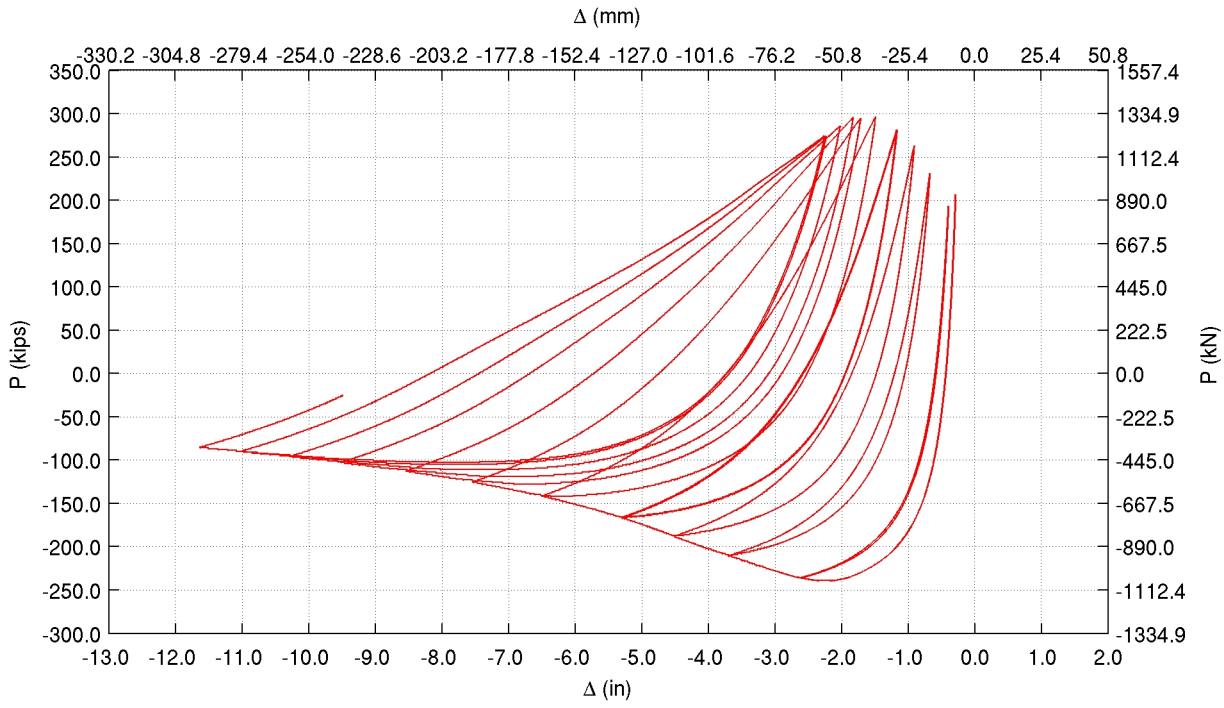

(b)

Figure B.19: Black et al. tests: TS4x4x1/2 strut (22) with KL/r=80 pinned at one end and fixed at the other, lateral displacement versus axial force history – (a) Experiment (b) Simulation.

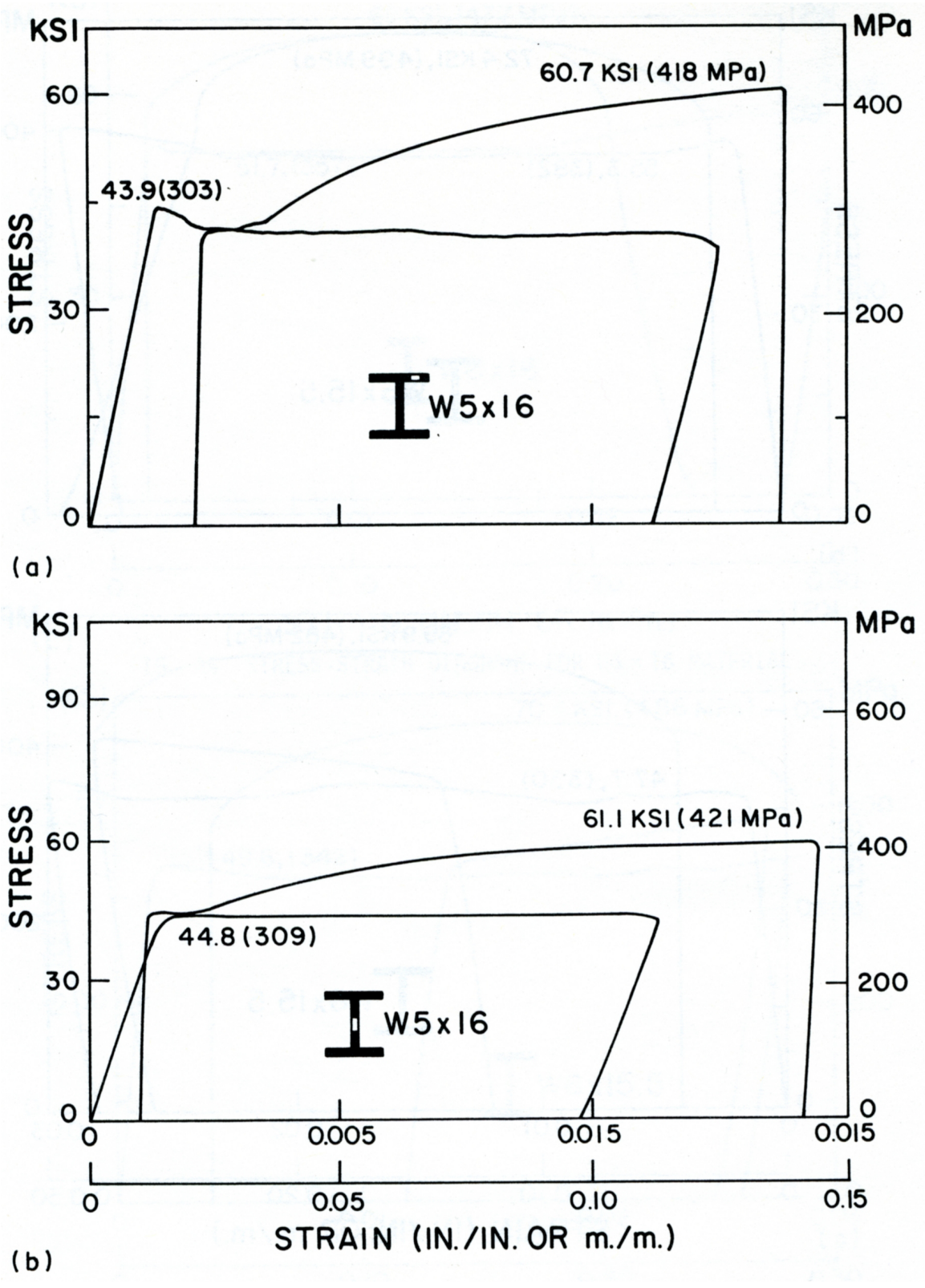

Figure B.20: Black et al. tests: W5x16 coupon tensile loading test.

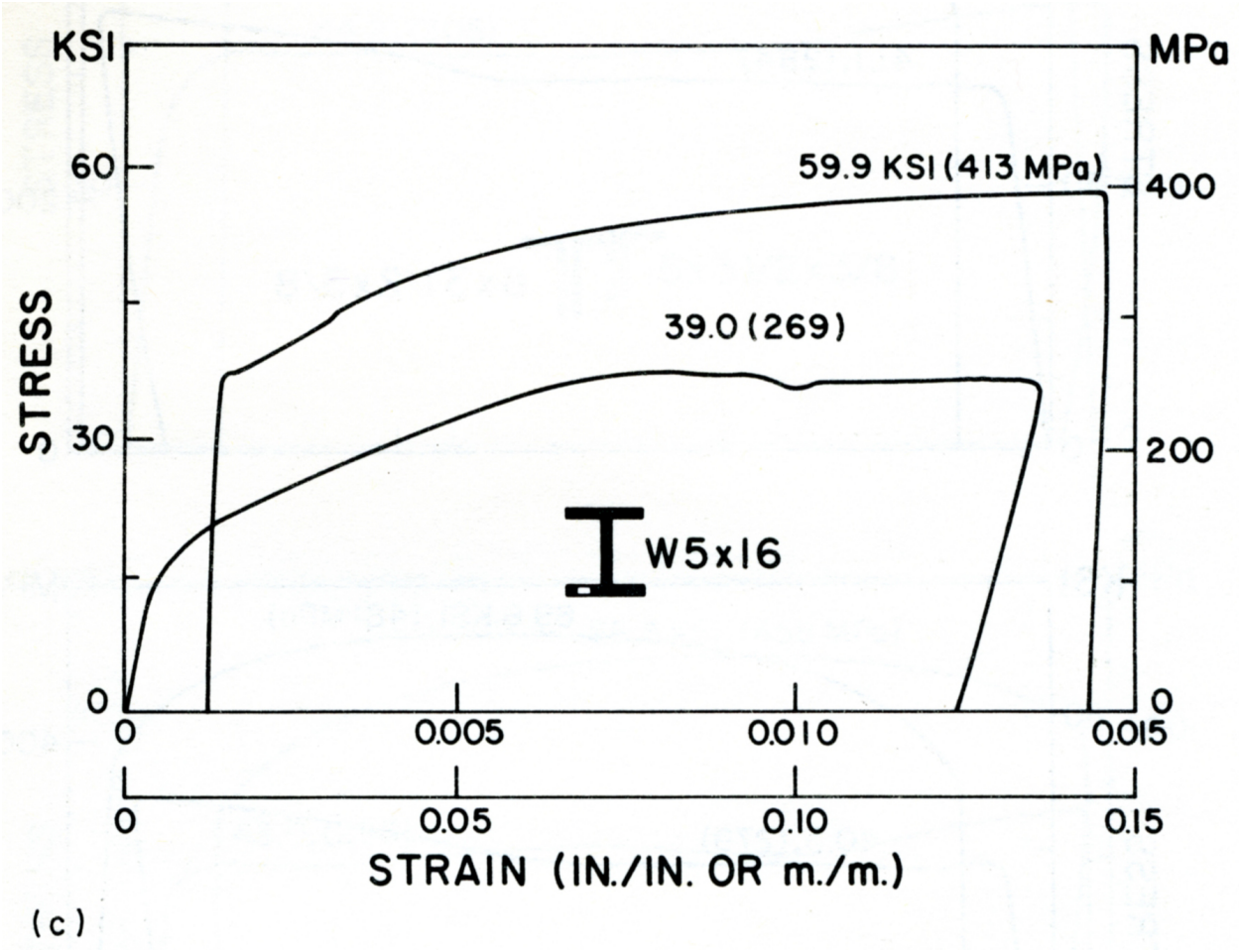

Figure B.21: Black et al. tests: W5x16 coupon tensile loading test (contd.).

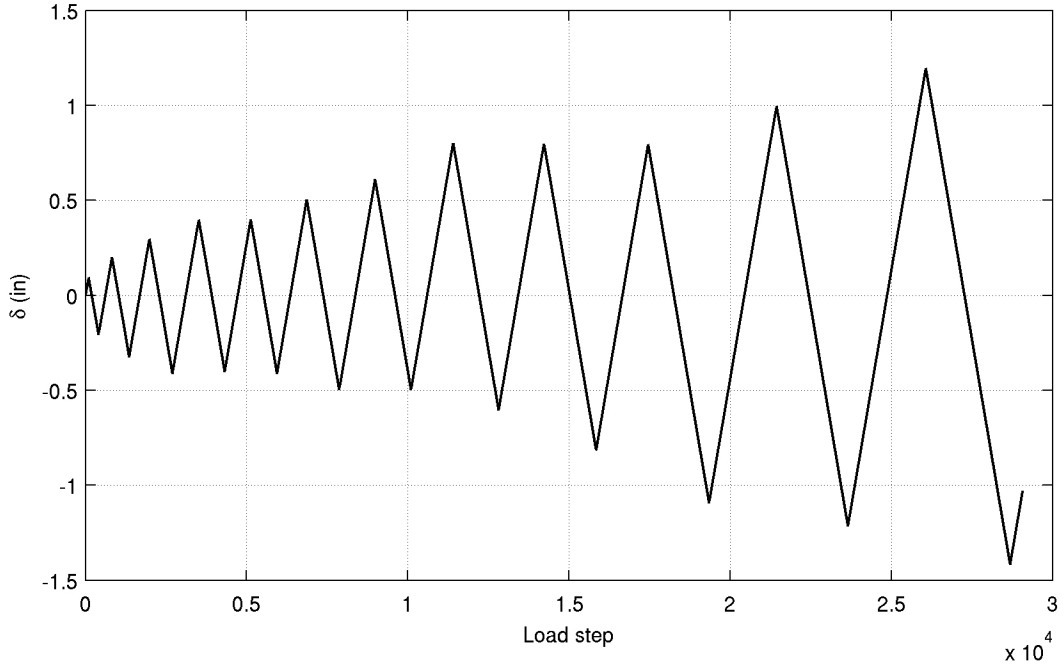

Figure B.22: Black et al. tests: W5x16 strut (23) with KL/r=80 pinned at one end and fixed at the other – Loading history.

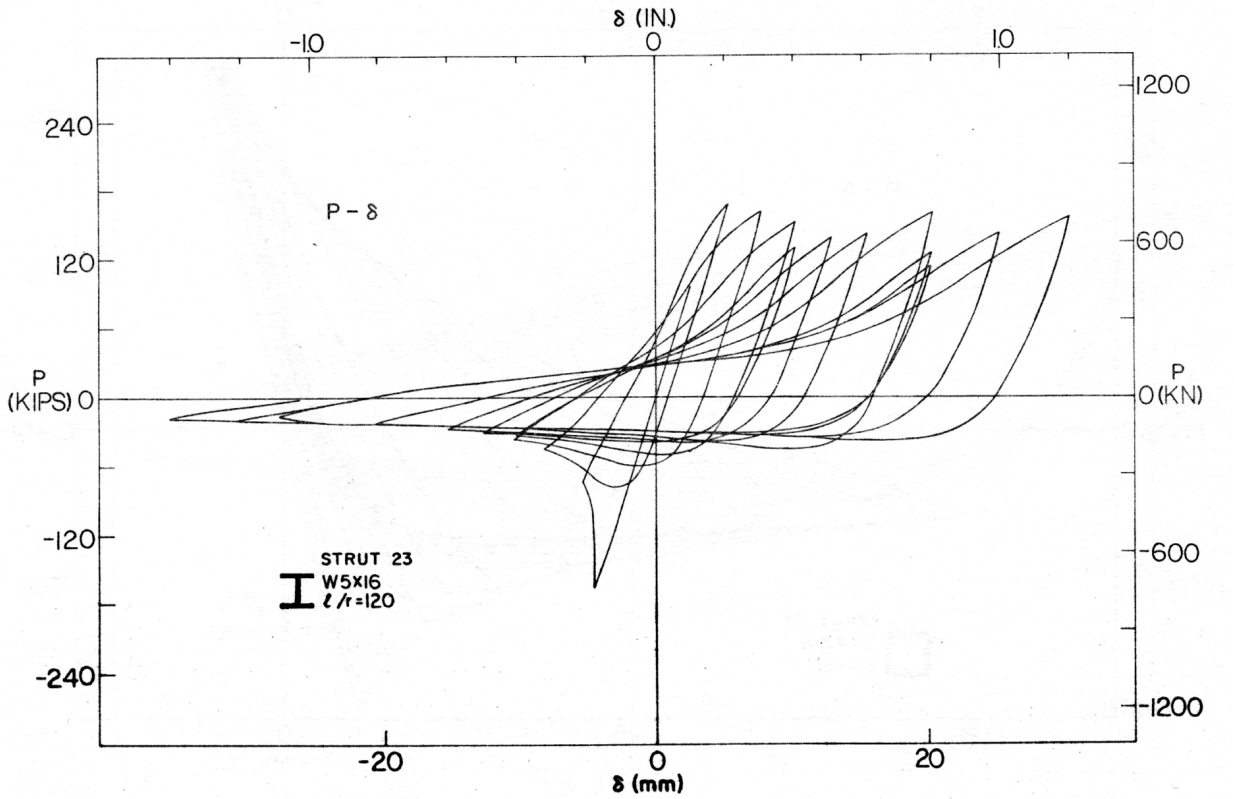

(a)

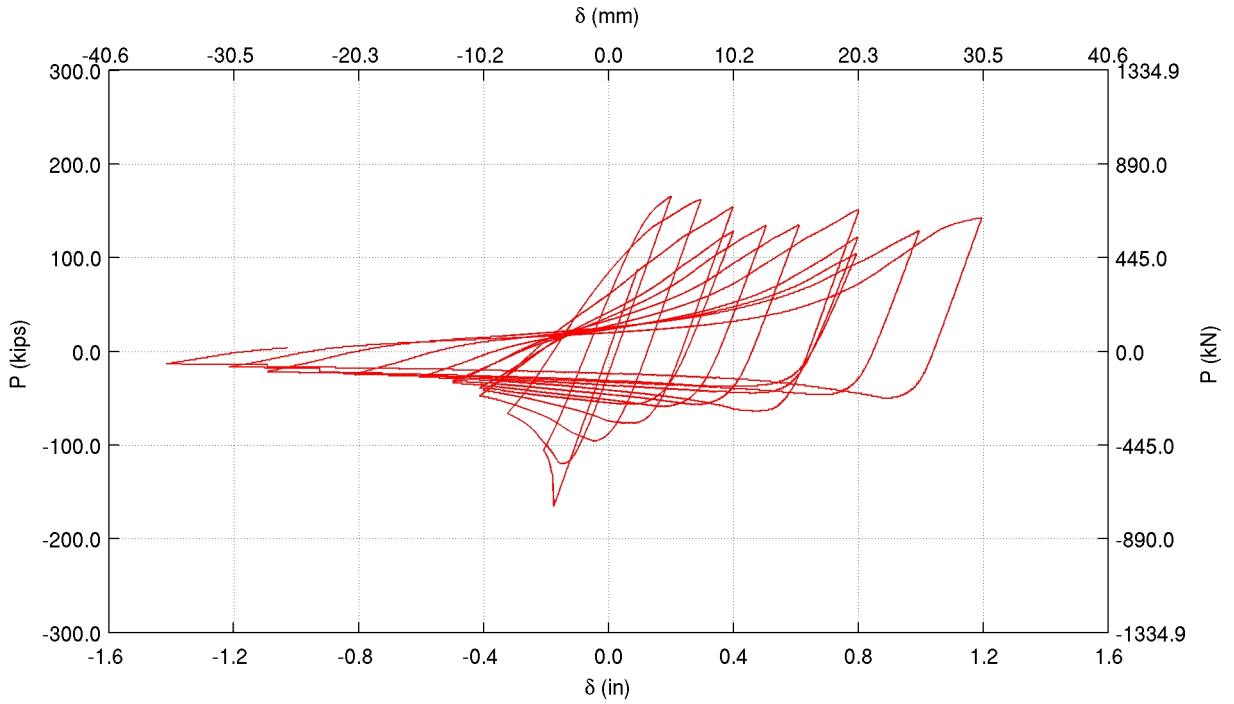

(b)

Figure B.23: Black et al. tests: W5x16 strut (23) with KL/r=80 pinned at one end and fixed at the other, axial displacement versus axial force history – (a) Experiment (b) Simulation.

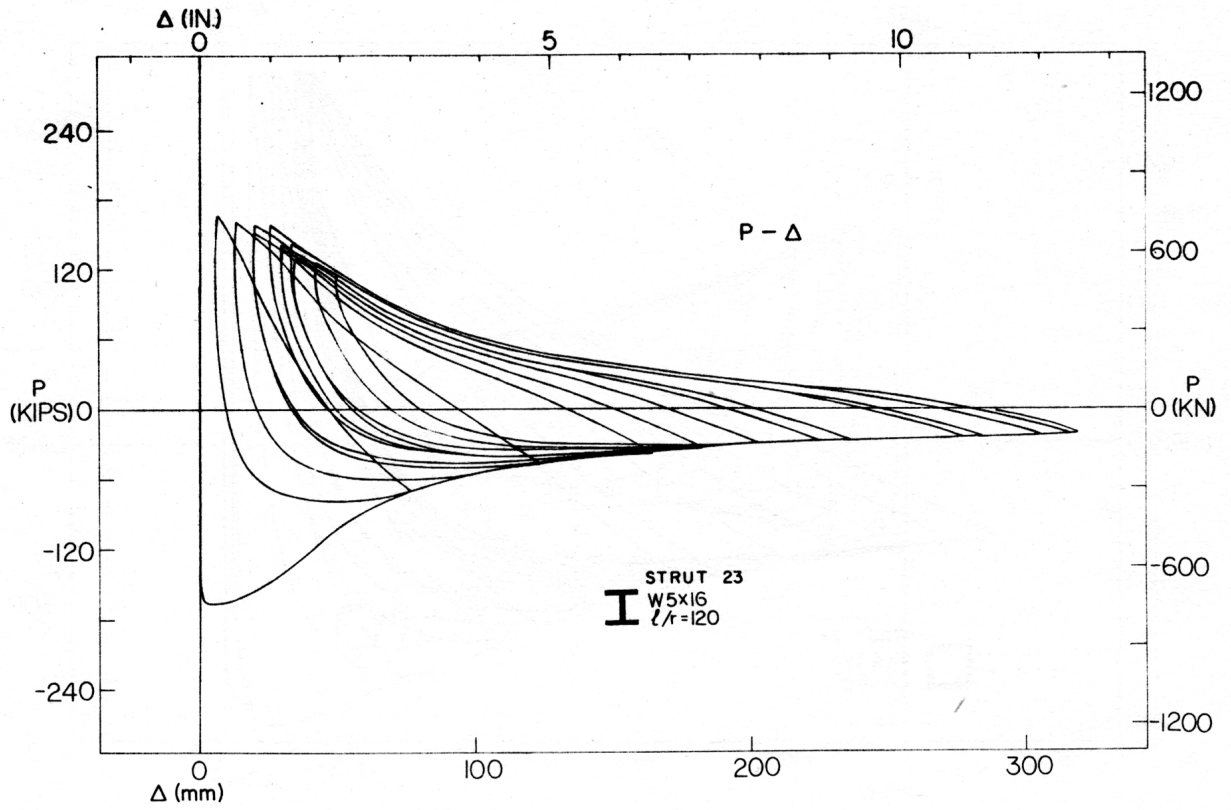

(a)

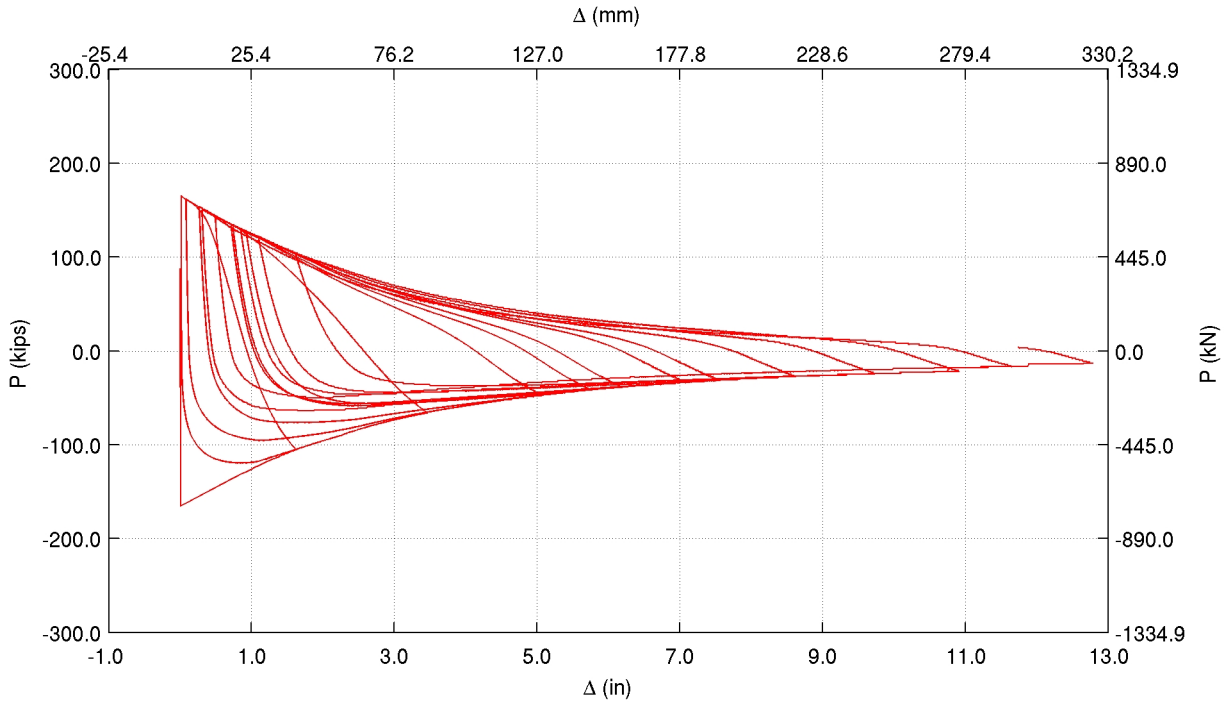

(b)

Figure B.24: Black et al. tests: W5x16 strut (23) with KL/r=80 pinned at one end and fixed at the other, lateral displacement versus axial force history – (a) Experiment (b) Simulation.

Appendix C Fell et al. Tests

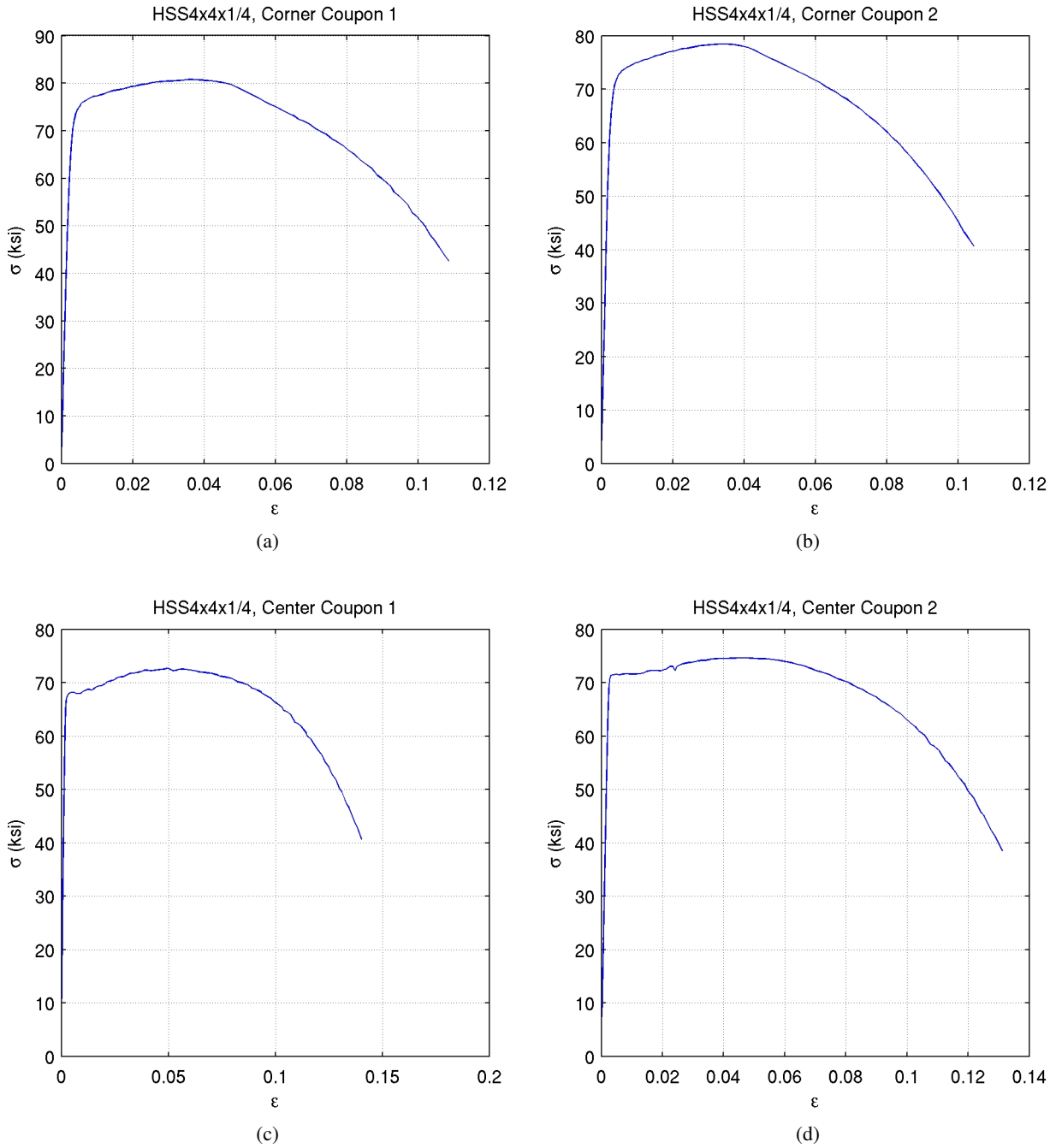

Figure C.1: NEESR project by Fell et al.: HSS4x4x1/4 coupon tensile loading test.

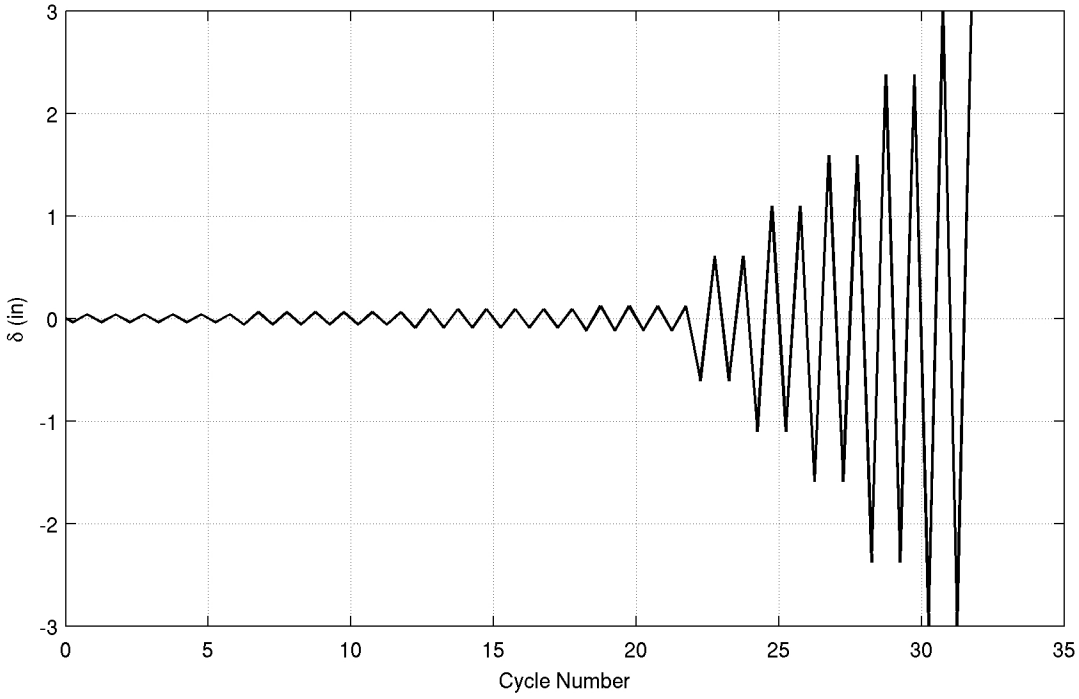

Figure C.2: Fell et al. test 1 on HSS4x4x1/4 (KL/r $\sim$ 80): Loading History

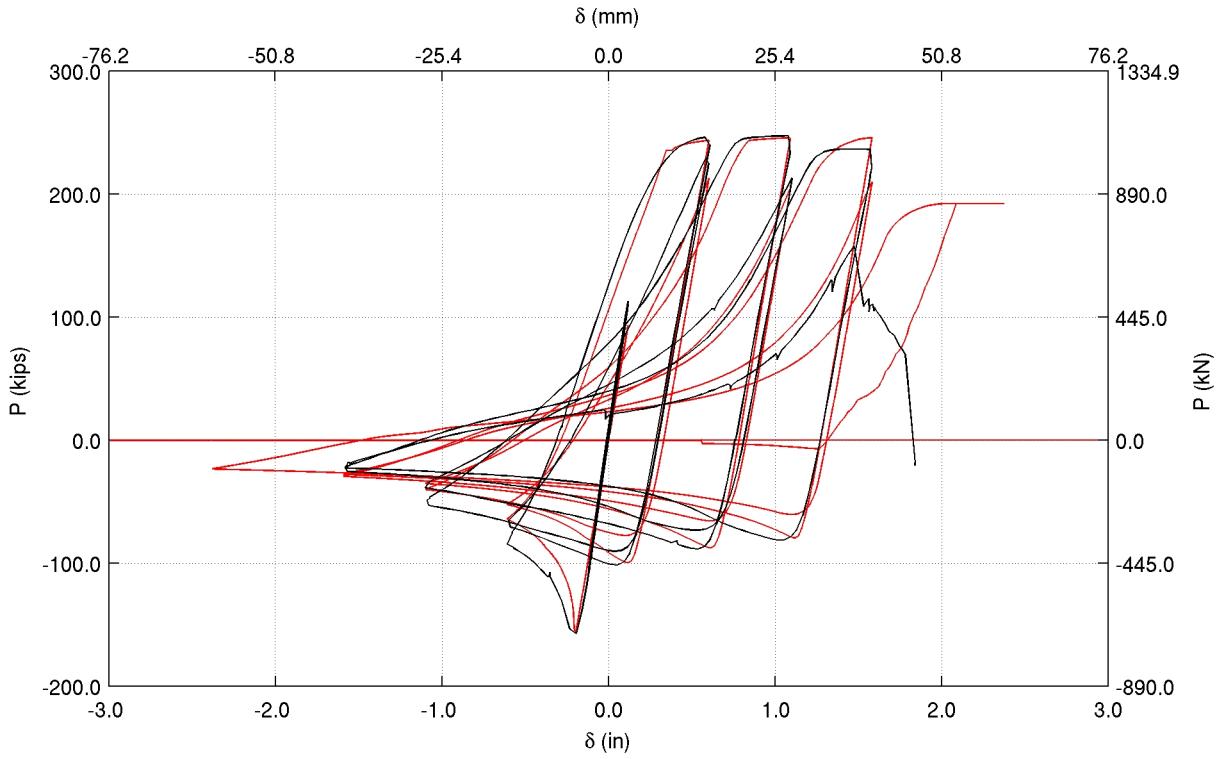

(a)

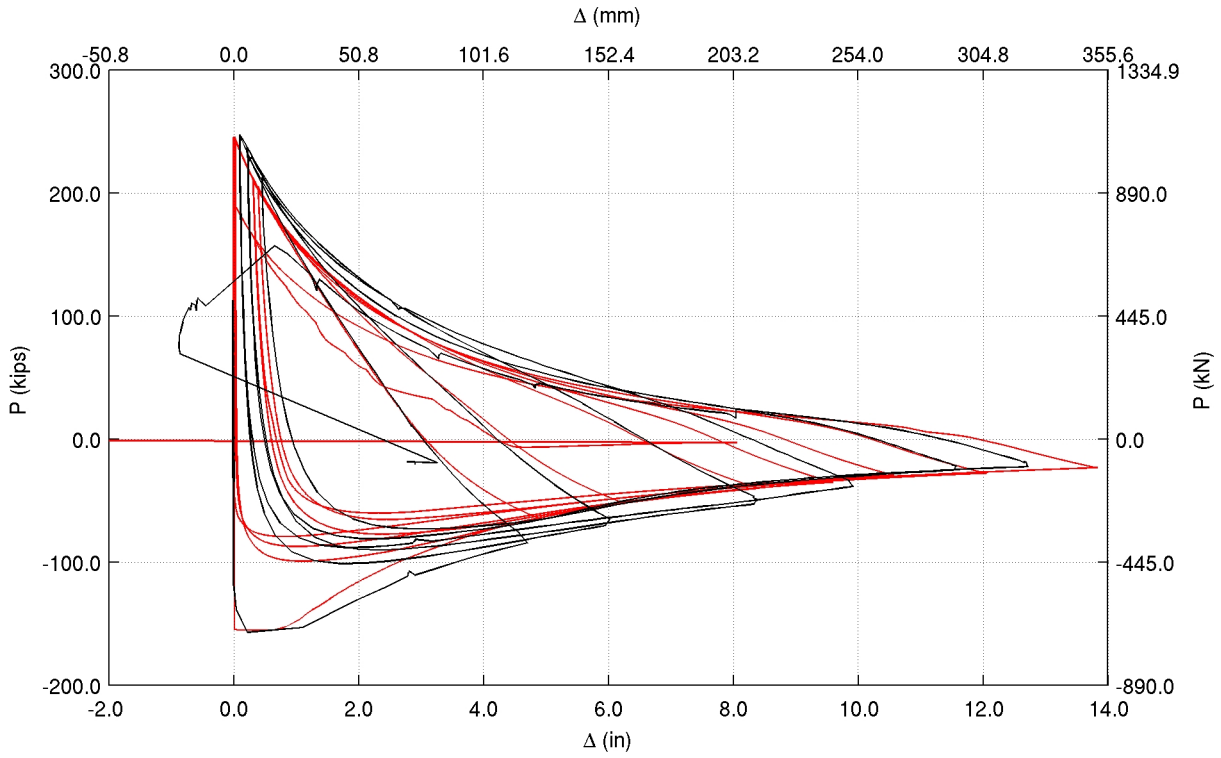

(b)

Figure C.3: Comparison of simulation against data from Fell et al. test 1 on HSS4x4x1/4 (KL/r $\sim$ 80): (a) Axial displacement versus axial force history; (b) Minor direction lateral displacement versus axial force history.

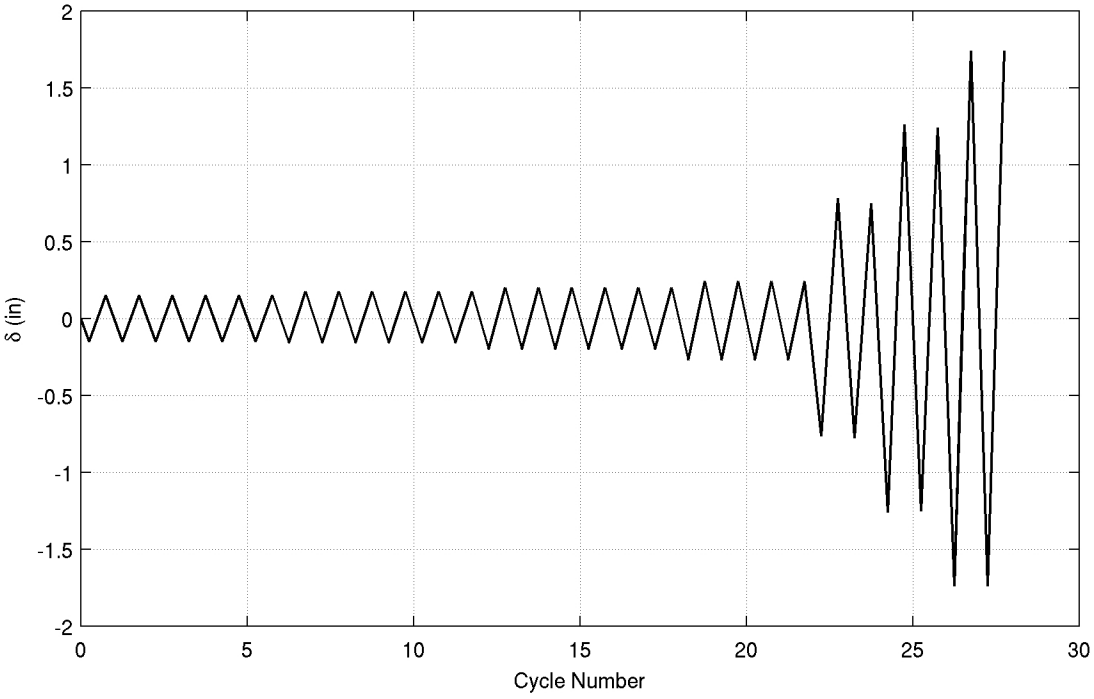

Figure C.4: Fell et al. test 3 on HSS4x4x1/4 (KL/r $\sim$ 80): Loading History

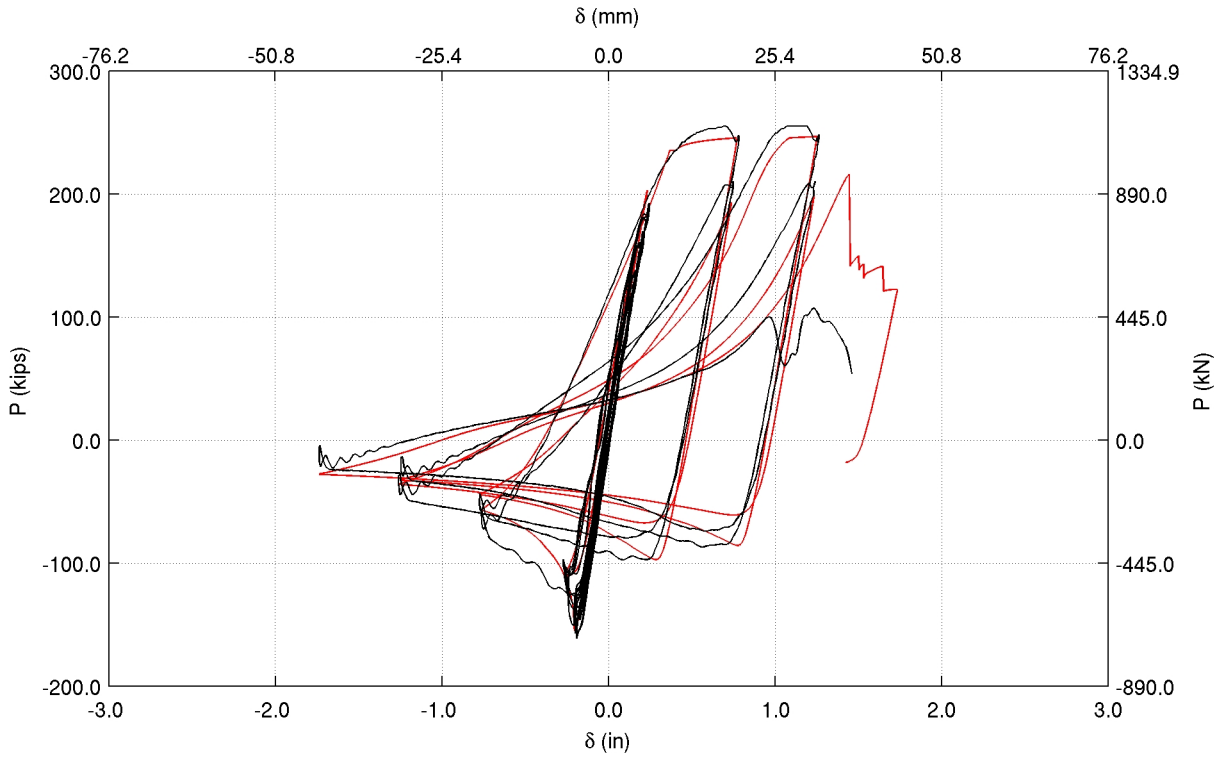

(a)

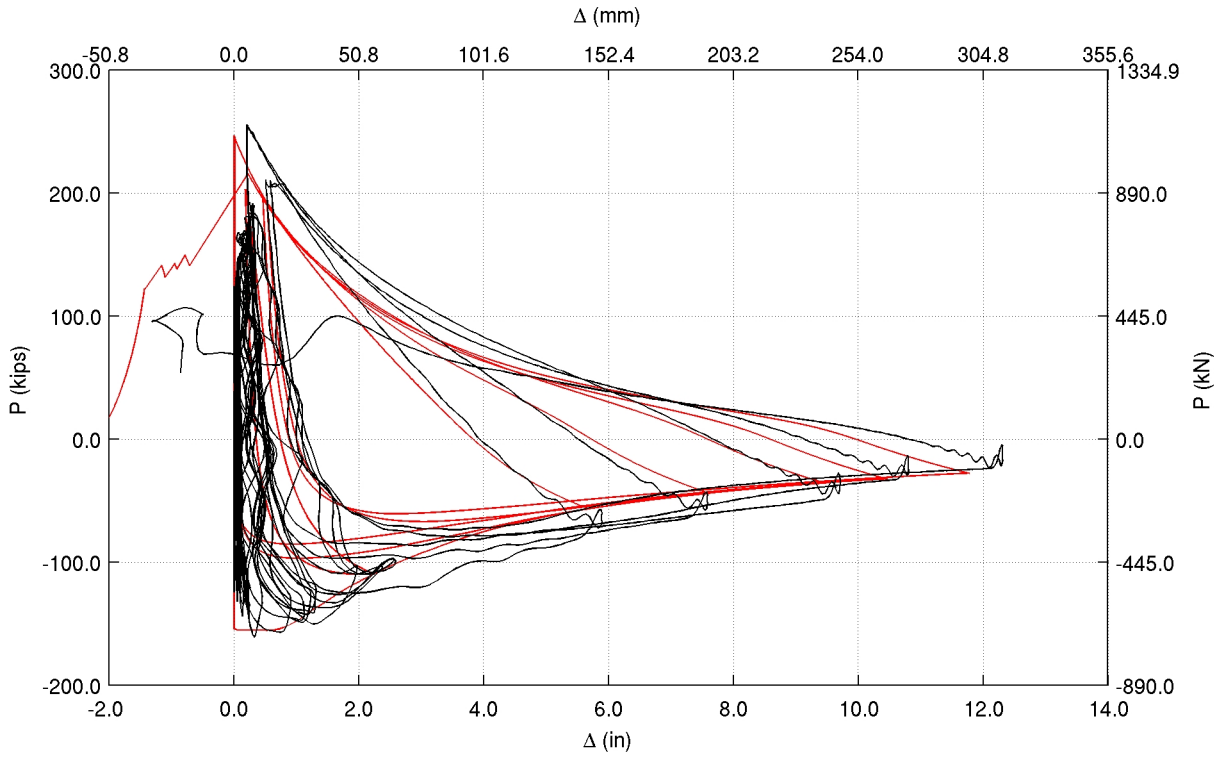

(b)

Figure C.5: Comparison of simulation against data from Fell et al. test 3 on HSS4x4x1/4 (KL/r $\sim$ 80): (a) Axial displacement versus axial force history; (b) Minor direction lateral displacement versus axial force history.

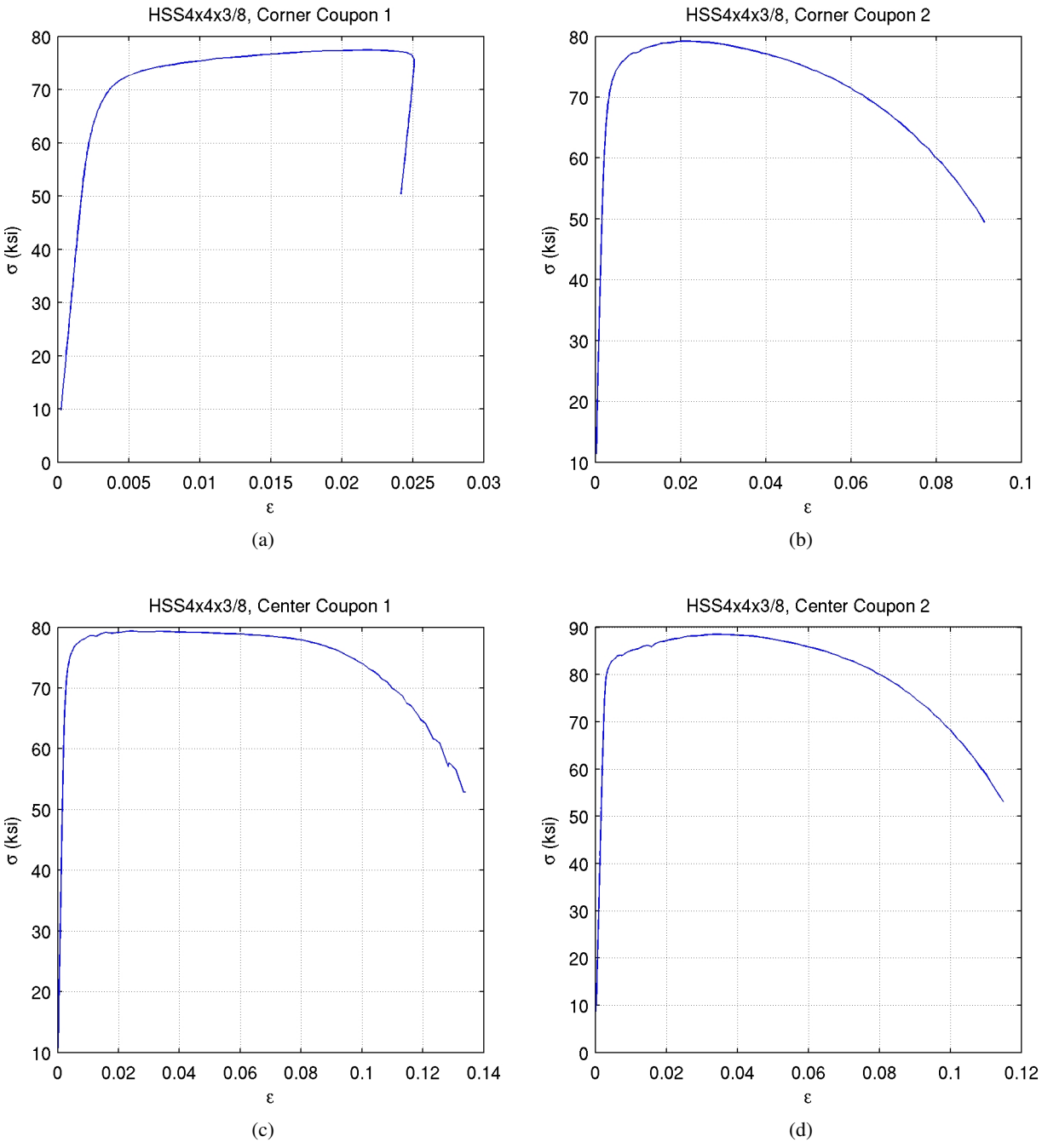

Figure C.6: NEESR project by Fell et al.: HSS4x4x3/8 coupon tensile loading test.

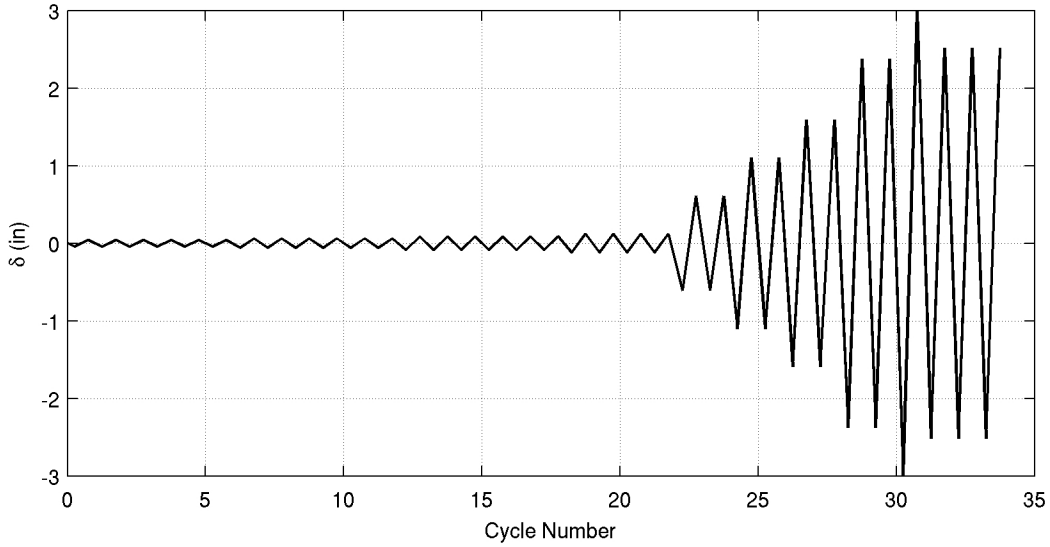

Figure C.7: Fell et al. test 4 on HSS4x4x3/8 (KL/r $\sim$ 82): Loading History

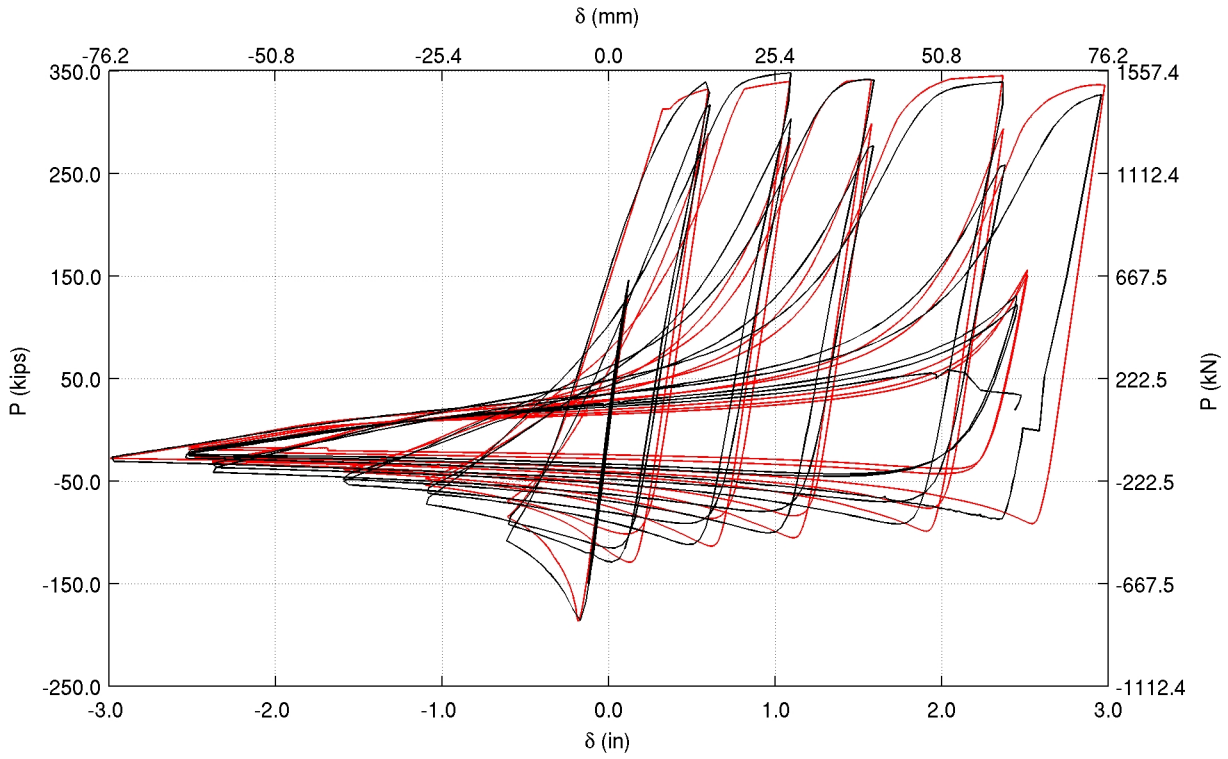

(a)

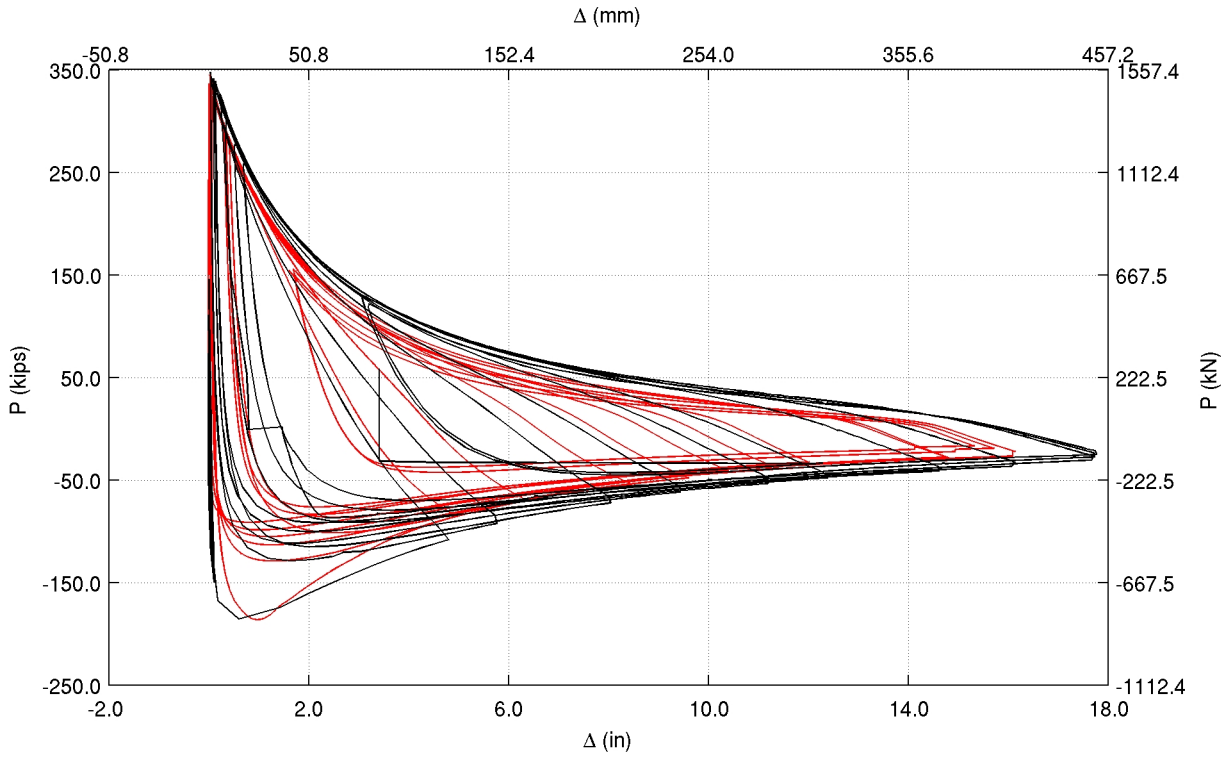

(b)

Figure C.8: Comparison of simulation against data from Fell et al. test 4 on HSS4x4x3/8 (KL/r $\sim$ 82): (a) Axial displacement versus axial force history; (b) Minor direction lateral displacement versus axial force history.

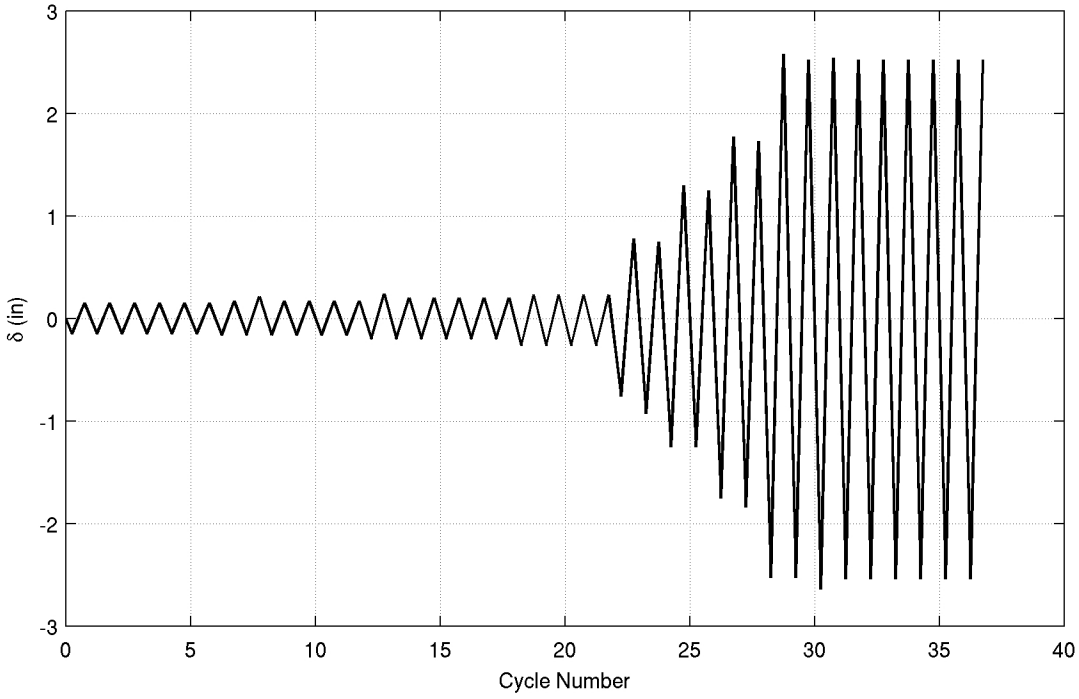

Figure C.9: Fell et al. test 5 on HSS4x4x3/8 (KL/r $\sim$ 82): Loading History

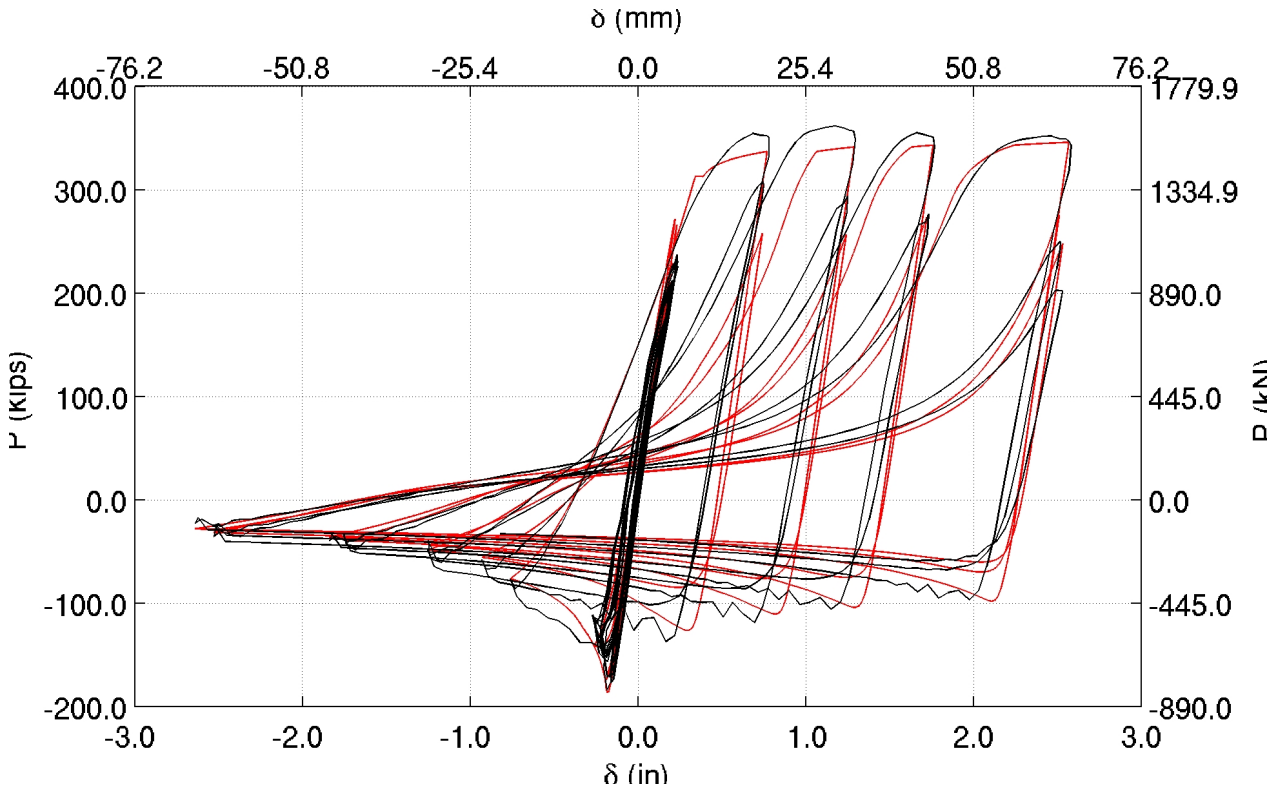

(a)

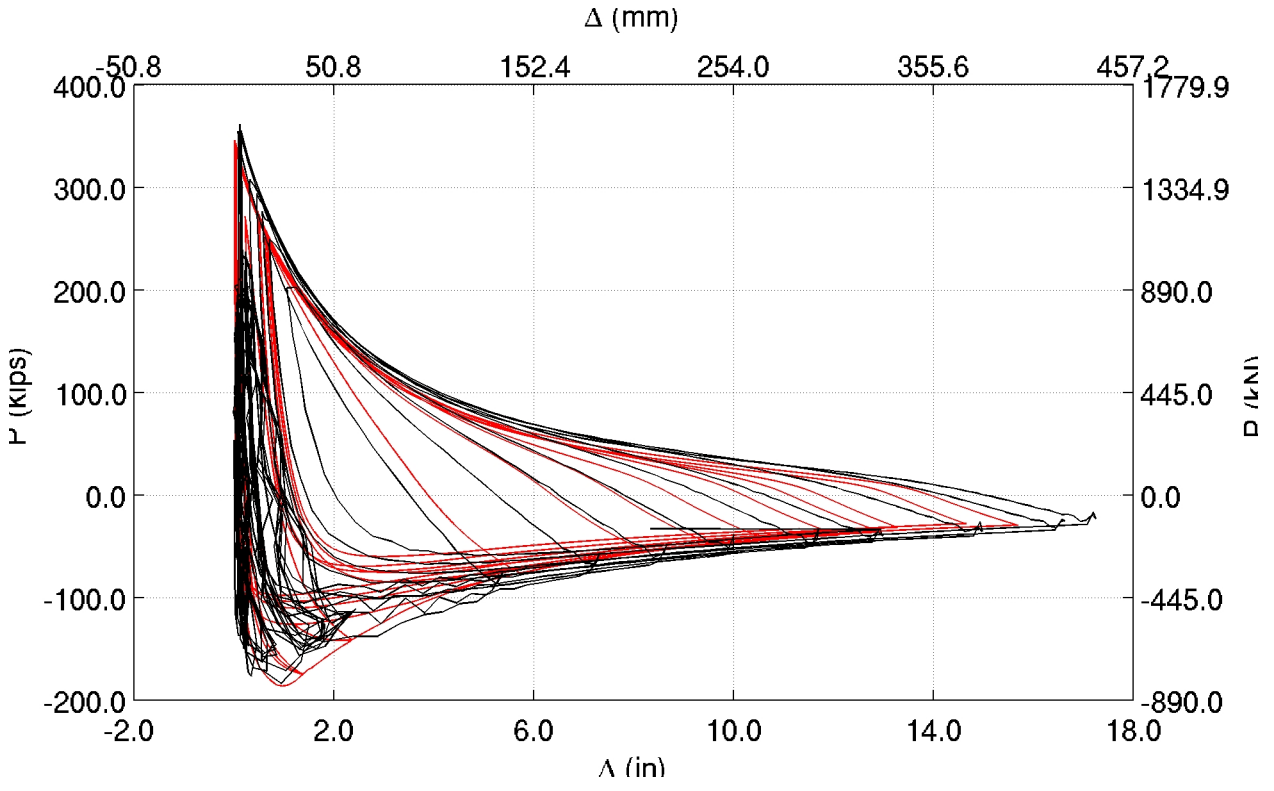

(b)

Figure C.10: Comparison of simulation against data from Fell et al. test 5 on HSS4x4x3/8 (KL/r∼82): (a) Axial displacement versus axial force history; (b) Minor direction lateral displacement versus axial force history.

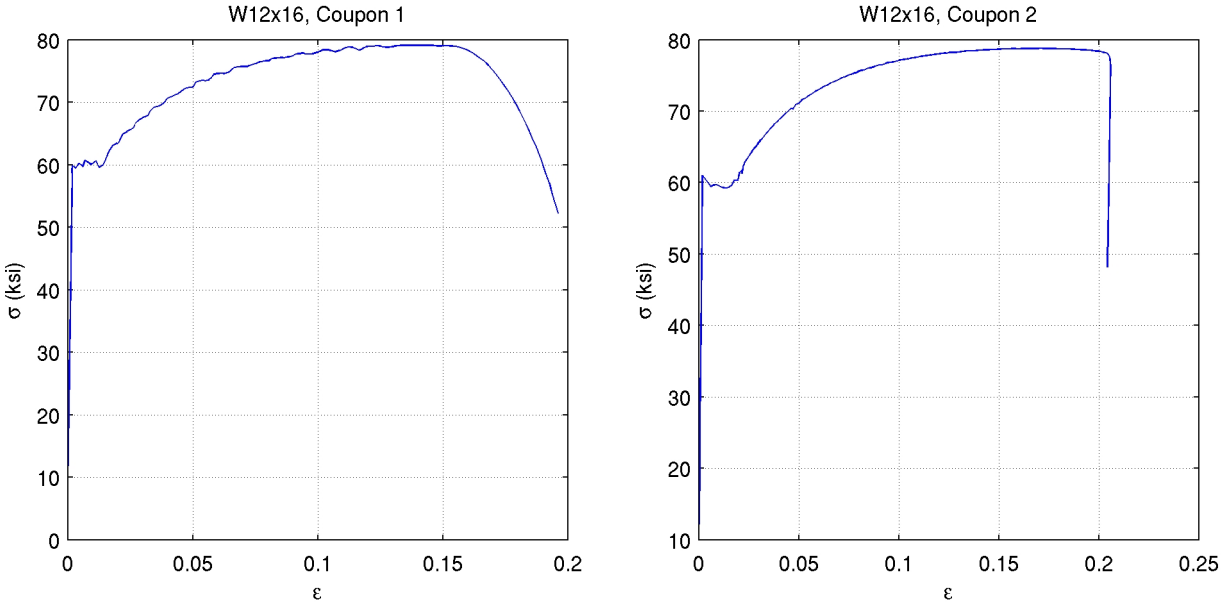

(a) (b)

Figure C.11: NEESR project by Fell et al.: W12x16 coupon tensile loading test.

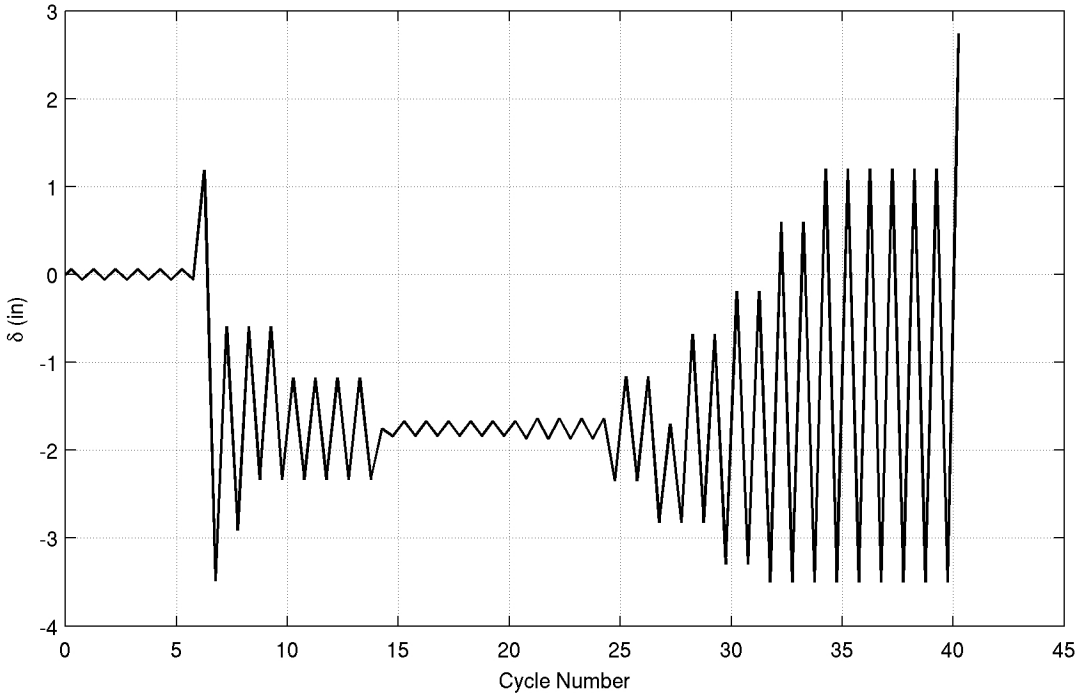

Figure C.12: Fell et al. test 14 on W12x16 (KL/r $\sim$ 159): Loading History

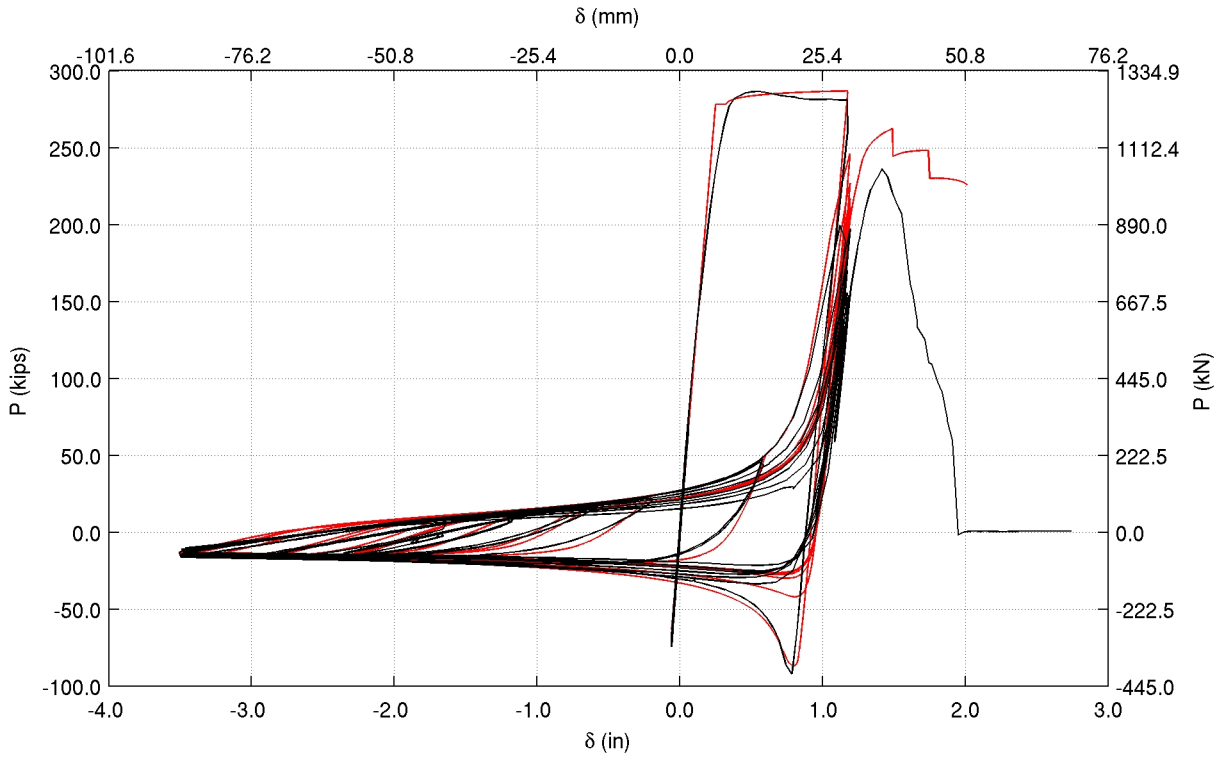

(a)

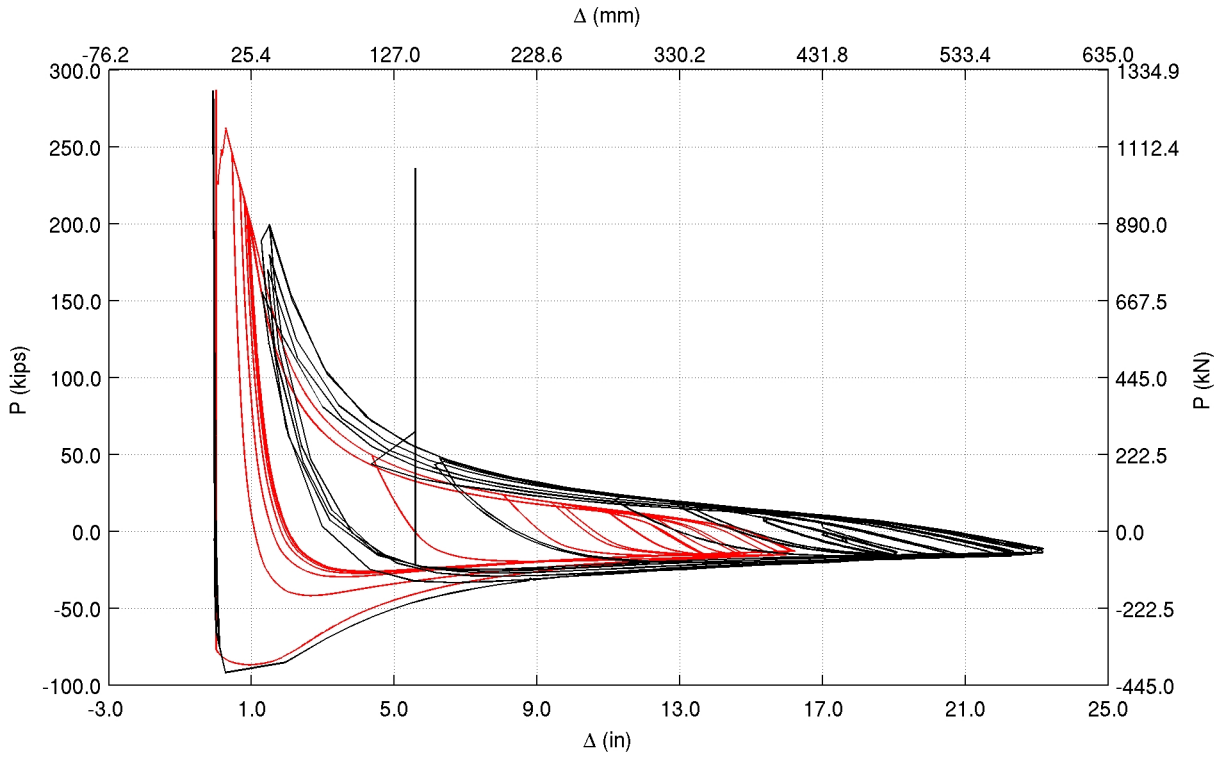

(b)

Figure C.13: Comparison of simulation against data from Fell et al. test 14 on W12x16 (KL/r $\sim$ 159): (a) Axial displacement versus axial force history; (b) Minor direction lateral displacement versus axial force history.

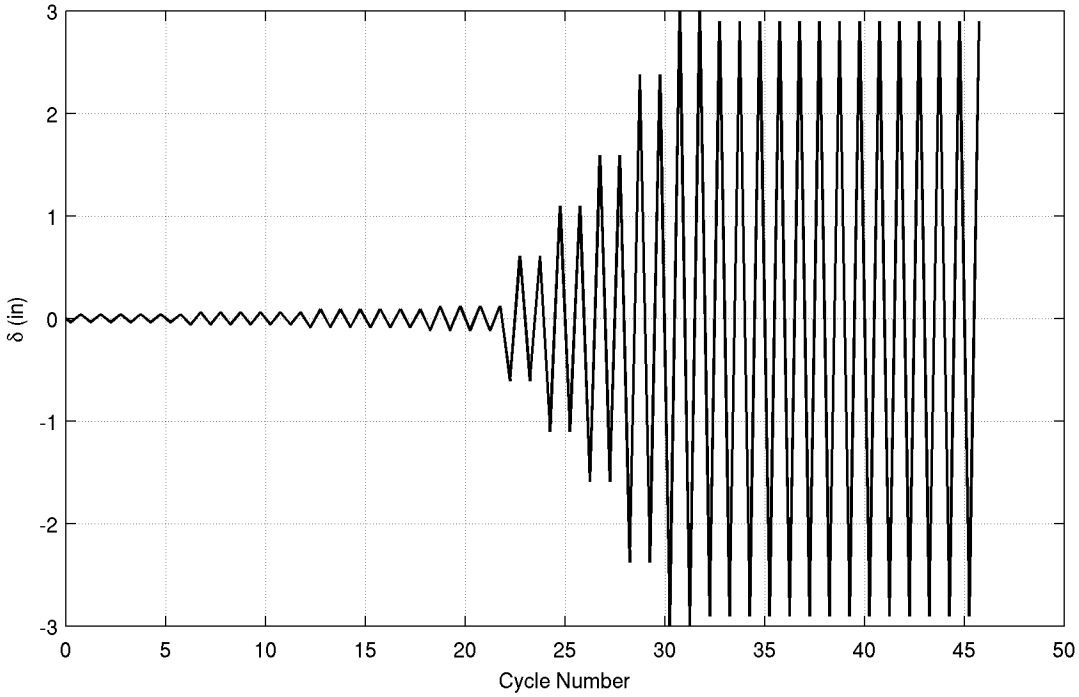

Figure C.14: Fell et al. test 15 on W12x16 (KL/r $\sim$ 159): Loading History

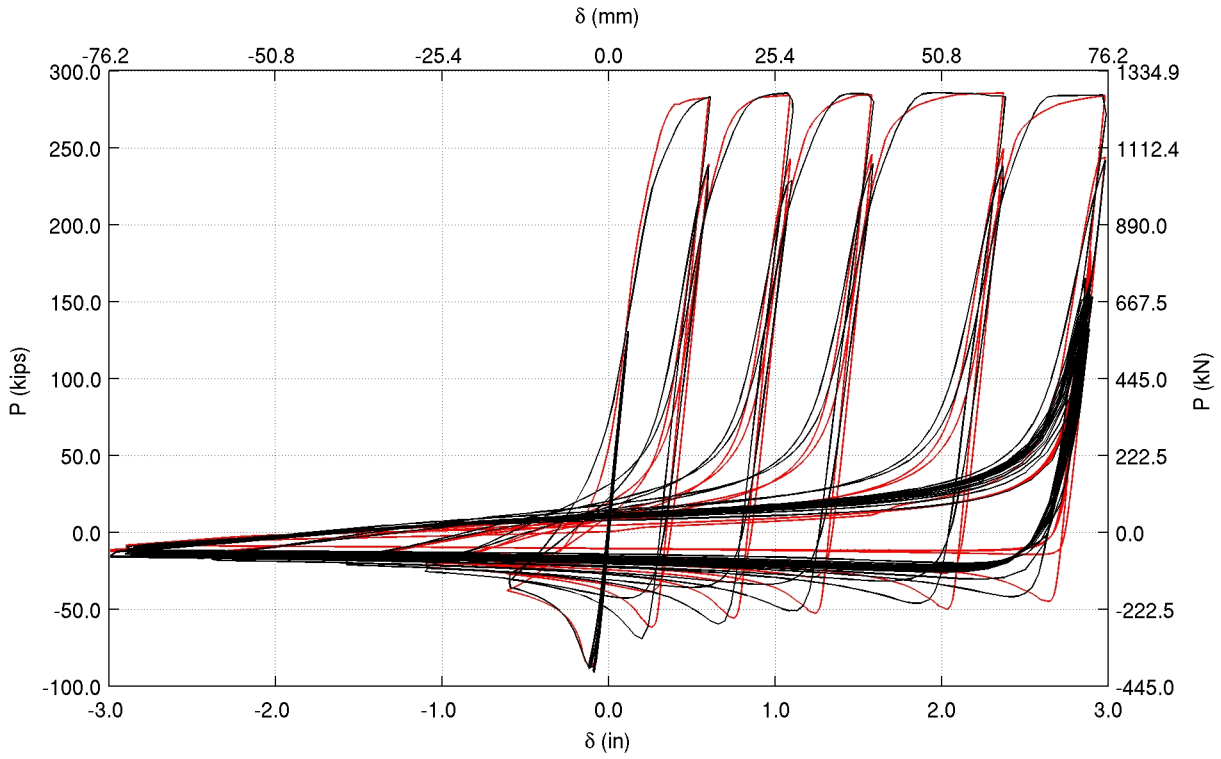

(a)

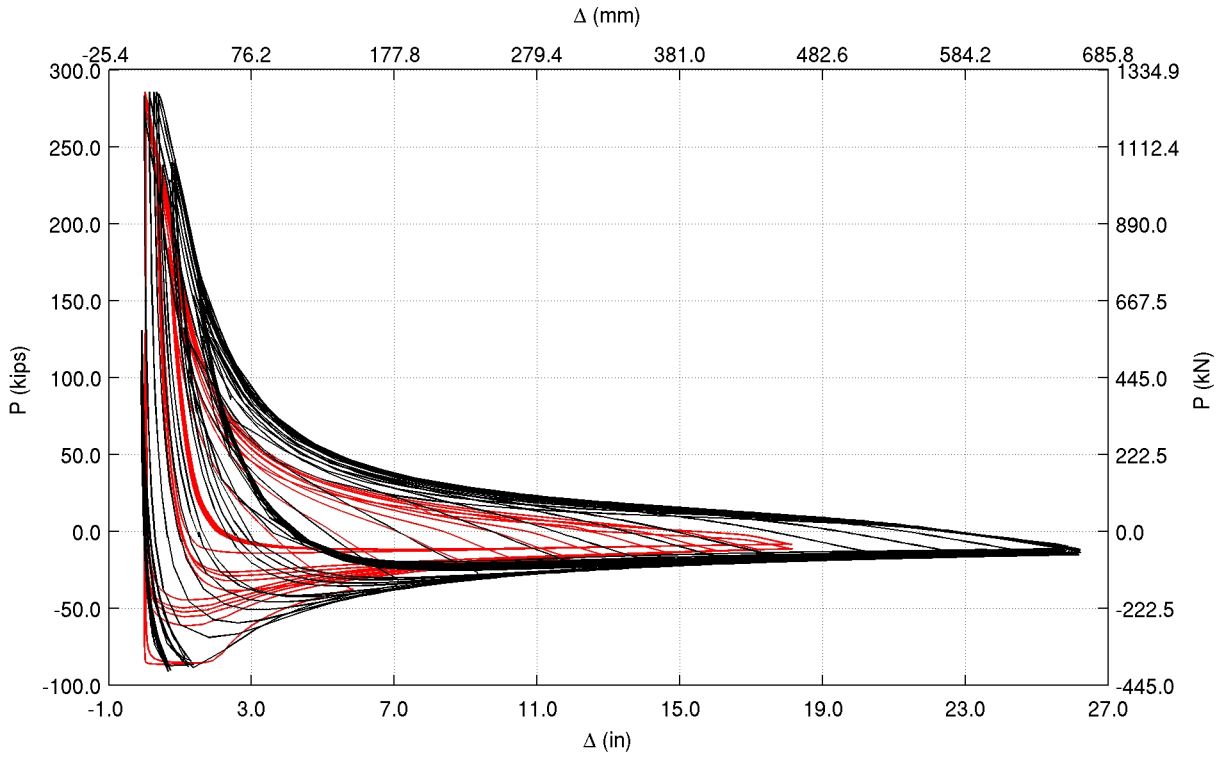

(b)

Figure C.15: Comparison of simulation against data from Fell et al. test 15 on W12x16 (KL/r $\sim$ 159): (a) Axial displacement versus axial force history; (b) Minor direction lateral displacement versus axial force history.

Appendix D Tremblay et al. Tests

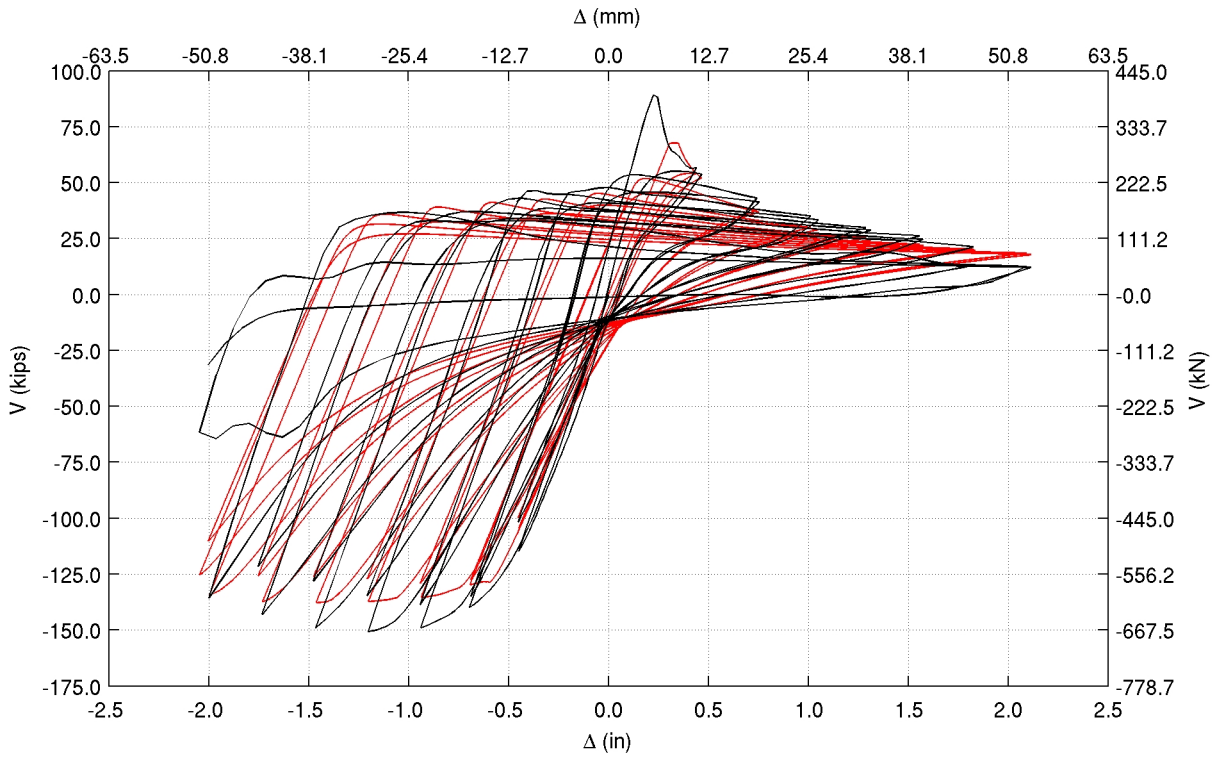

(a)

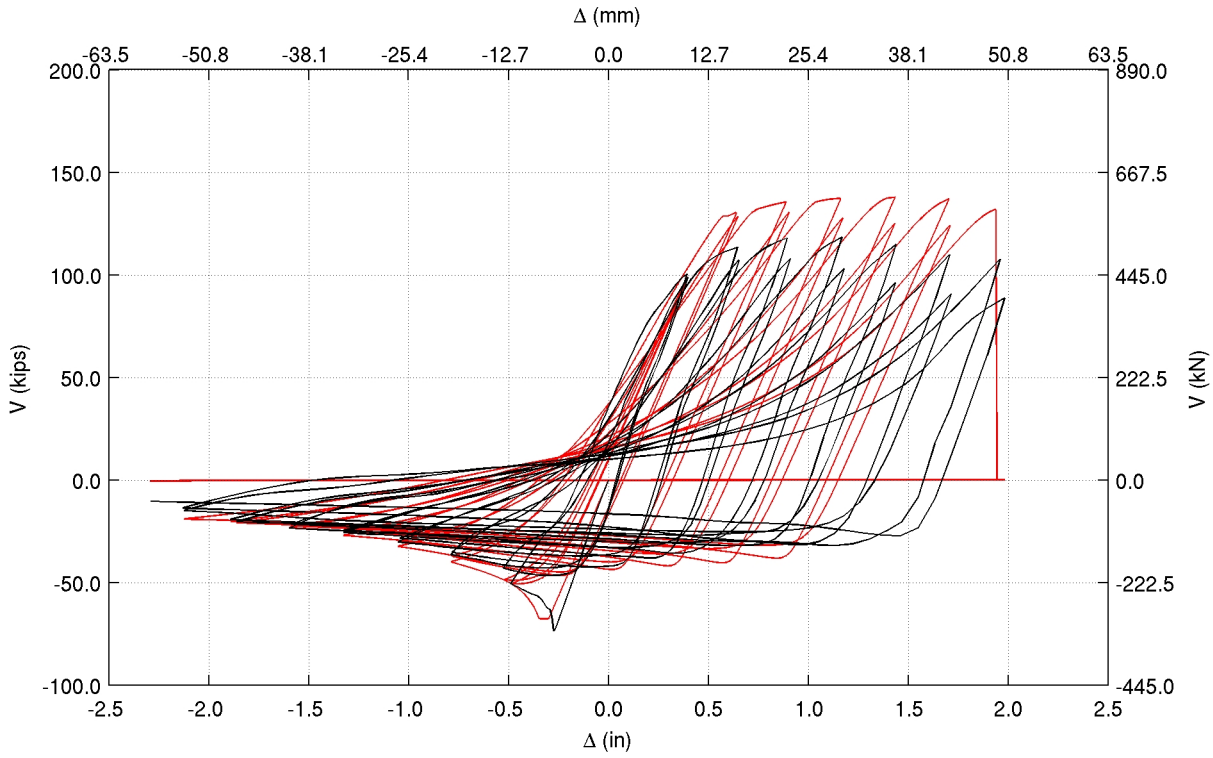

(b)

Figure D.1: Comparison of simulation against data from Tremblay et al. tests: (a) Specimen S1A and (b) Specimen S1B with RHS127x76x4.8 diagonal – frame sway versus applied lateral force history.

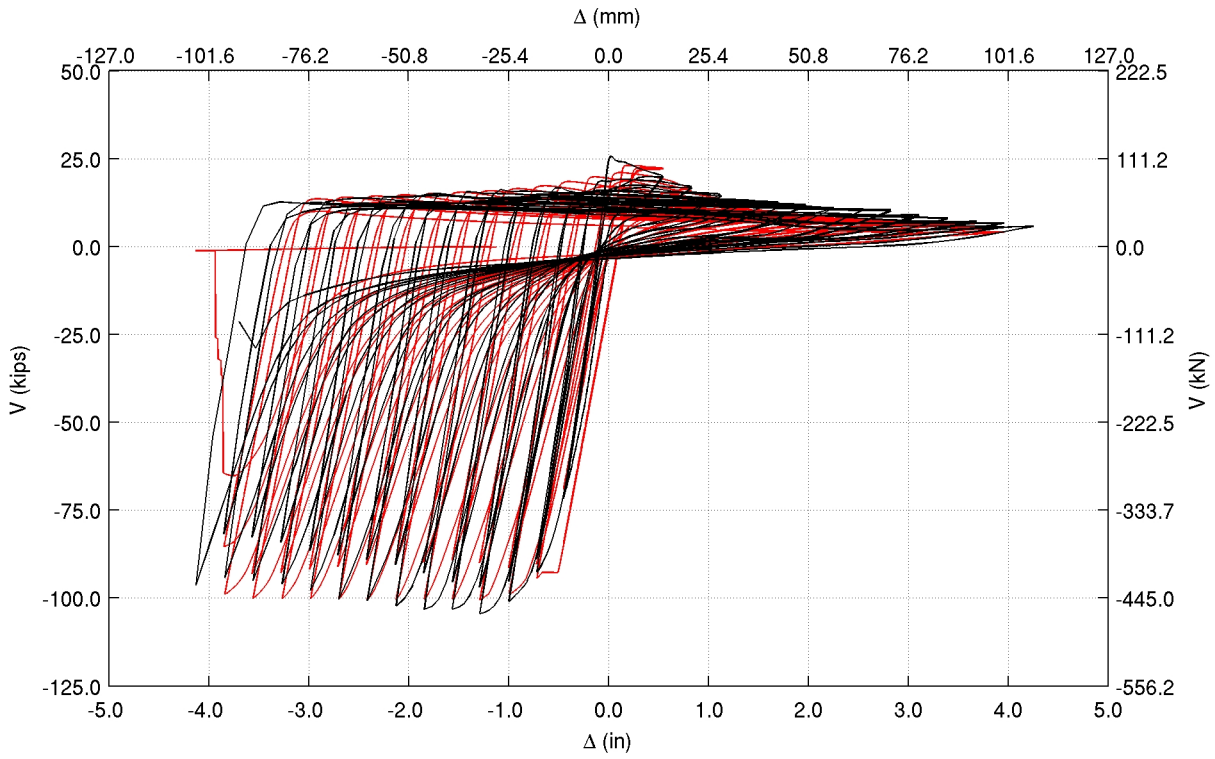

(a)

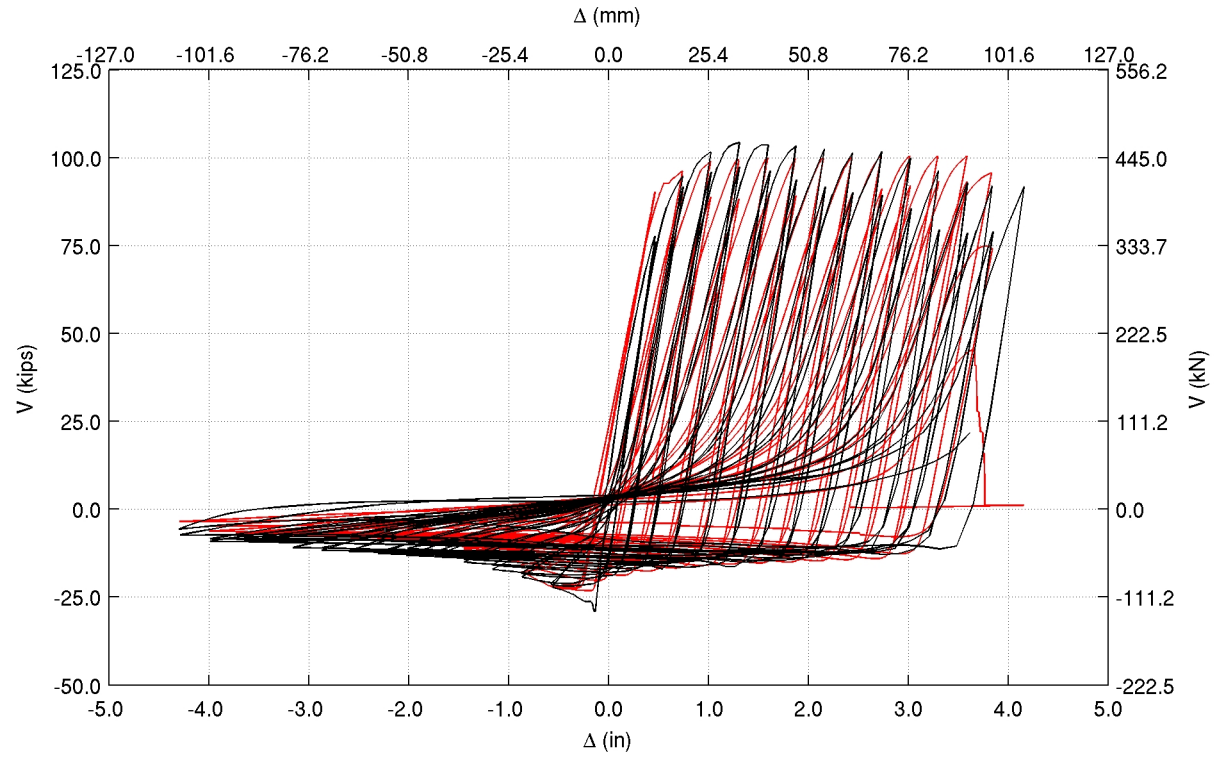

(b)

Figure D.2: Comparison of simulation against data from Tremblay et al. tests: (a) Specimen S3A and (b) Specimen S3B with RHS76x76x4.8 diagonal – frame sway versus applied lateral force history.

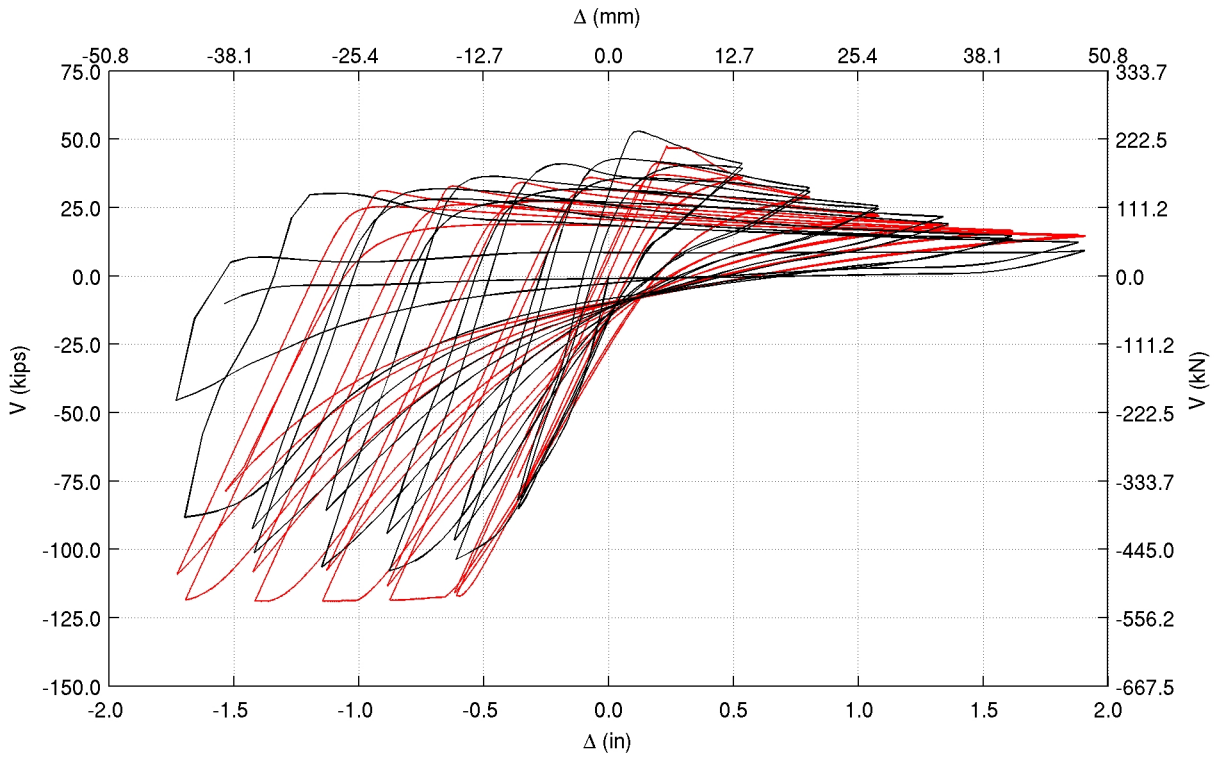

(a)

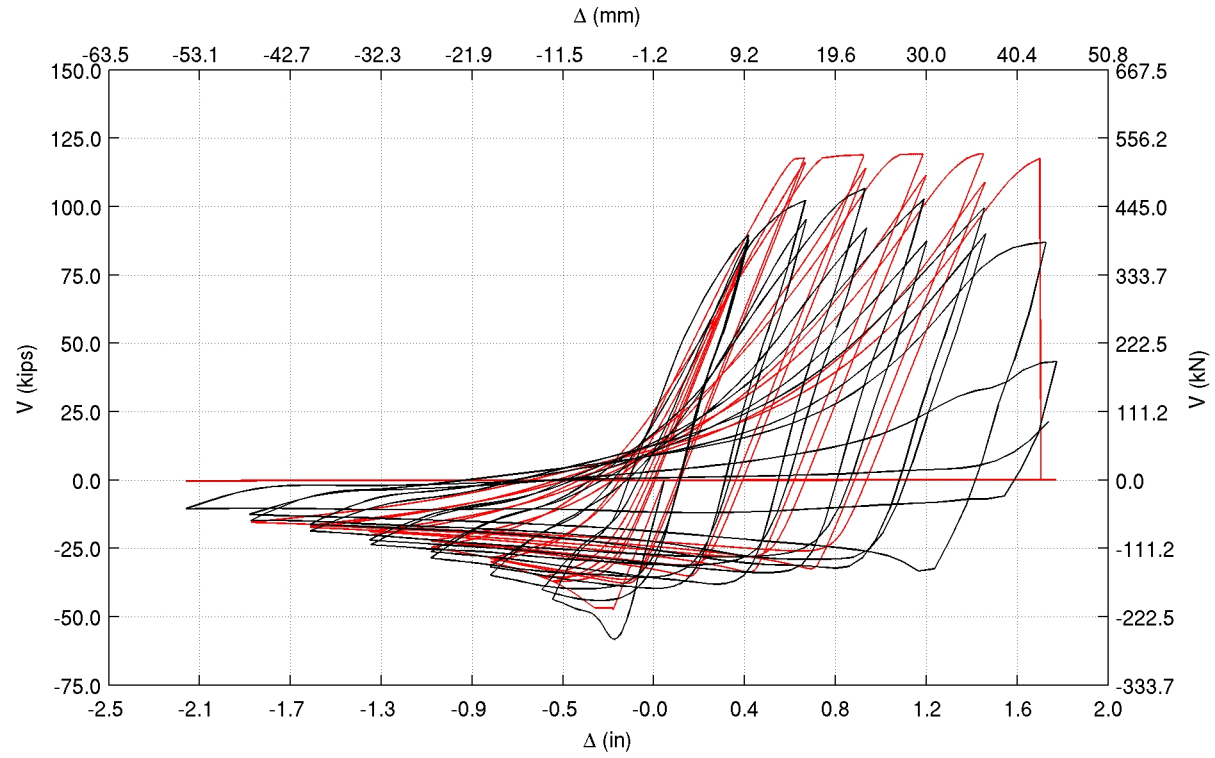

(b)

Figure D.3: Comparison of simulation against data from Tremblay et al. tests: (a) Specimen S4A and (b) Specimen S4B with RHS127x64x4.8 diagonal – frame sway versus applied lateral force history.

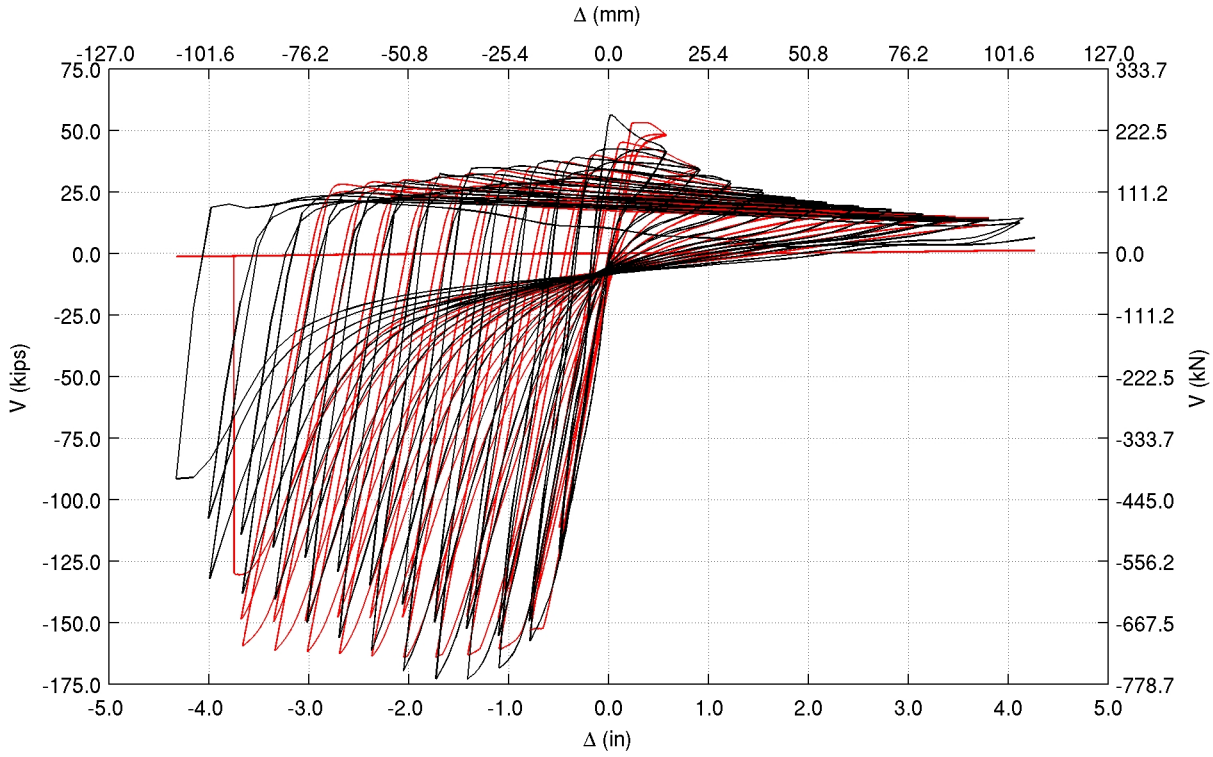

(a)

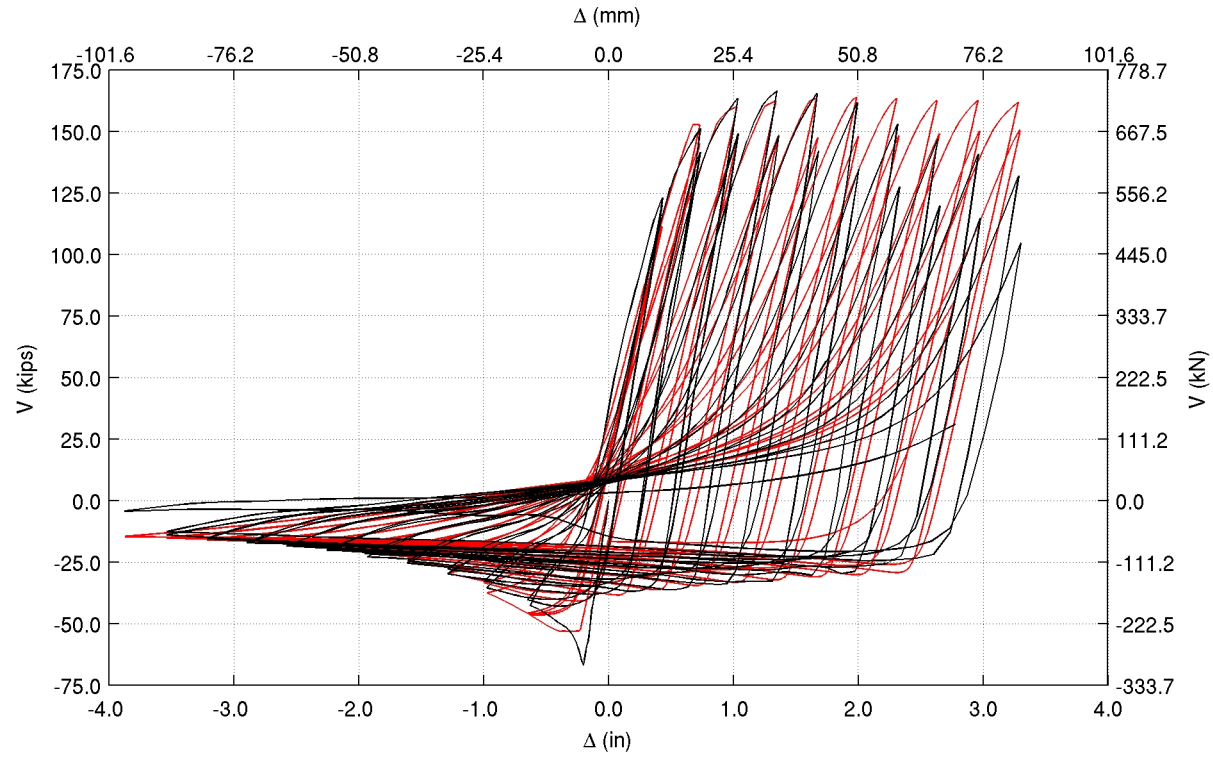

(b)

Figure D.4: Comparison of simulation against data from Tremblay et al. tests: (a) Specimen S5A and (b) Specimen S5B with RHS102x76x6.4 diagonal – frame sway versus applied lateral force history.

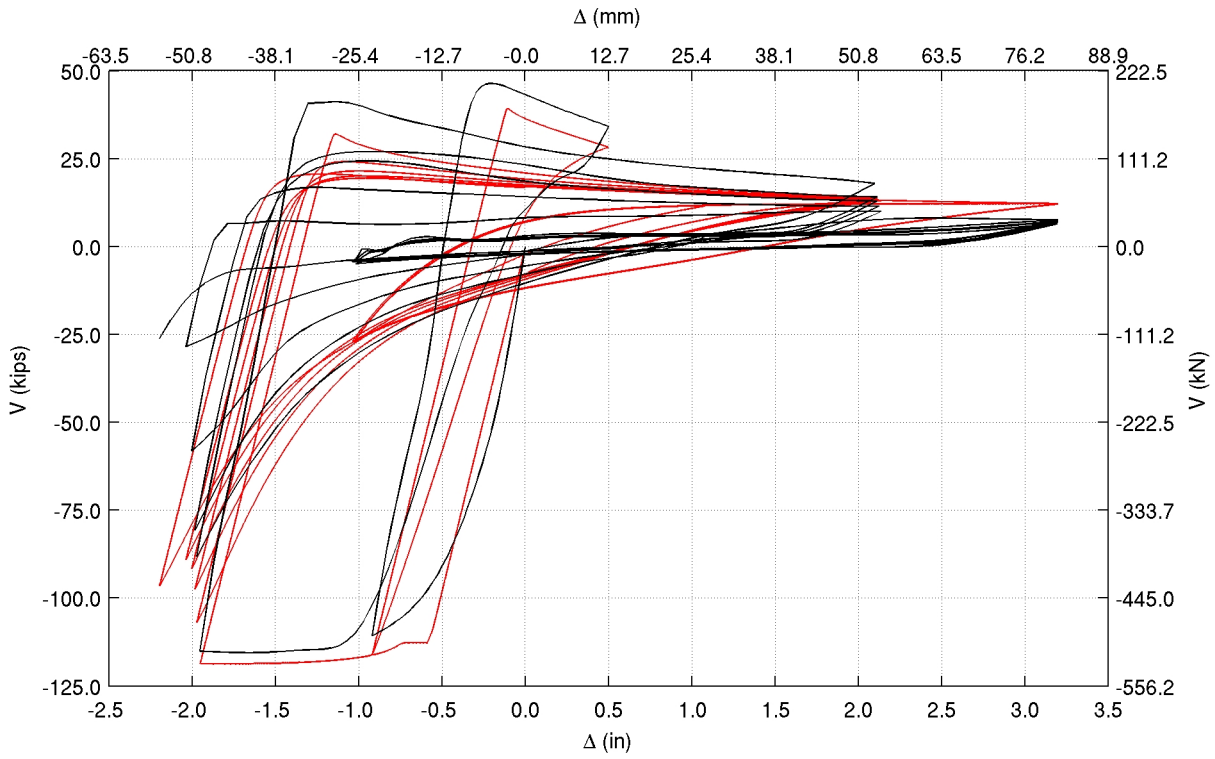

(a)

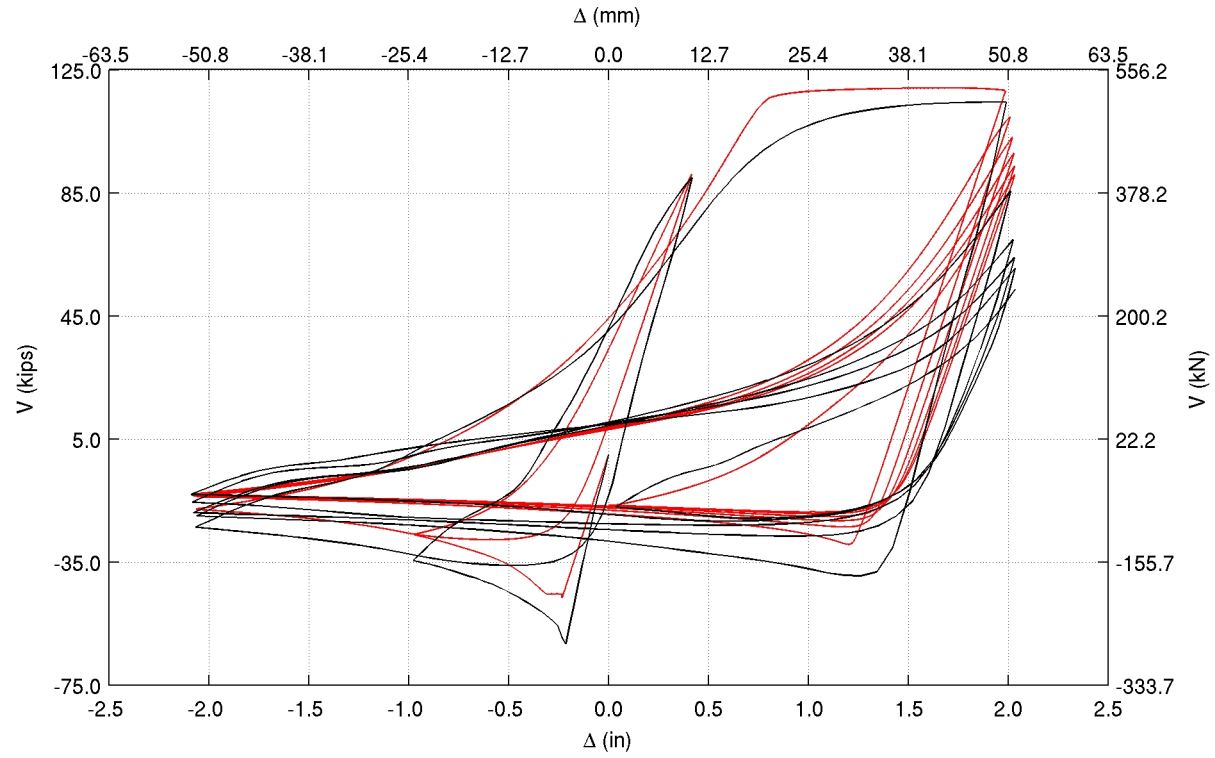

(b)

Figure D.5: Comparison of simulation against data from Tremblay et al. tests: (a) Specimen S4QA and (b) Specimen S4QB with RHS127x64x4.8 diagonal – frame sway versus applied lateral force history.

Appendix E Benchmark Problem

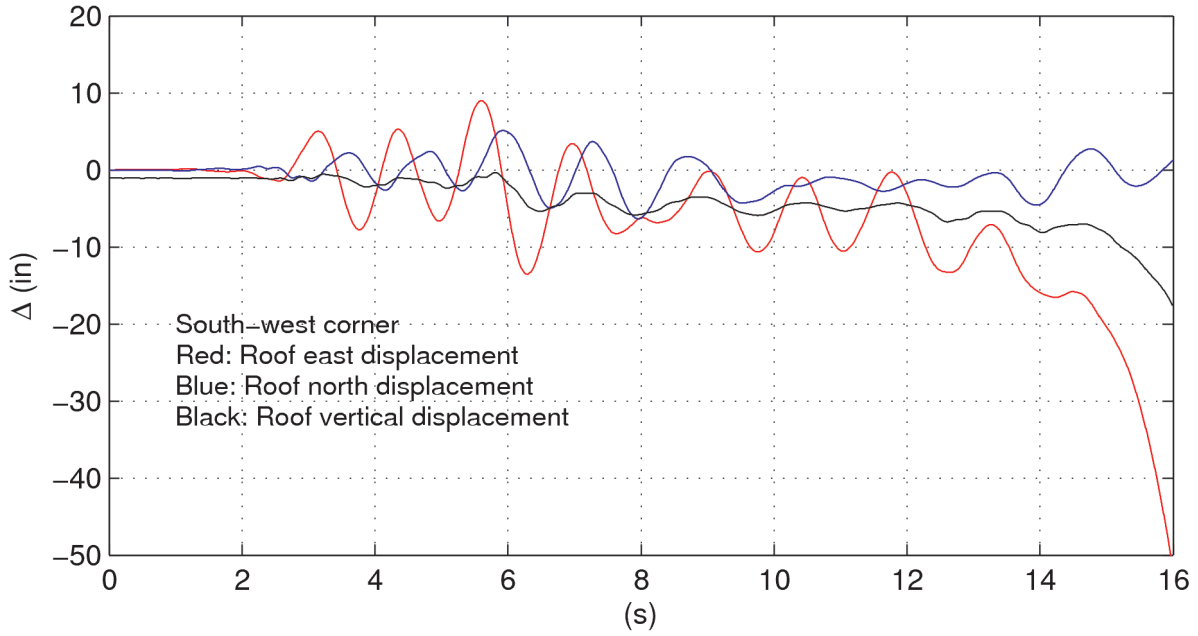

(a)

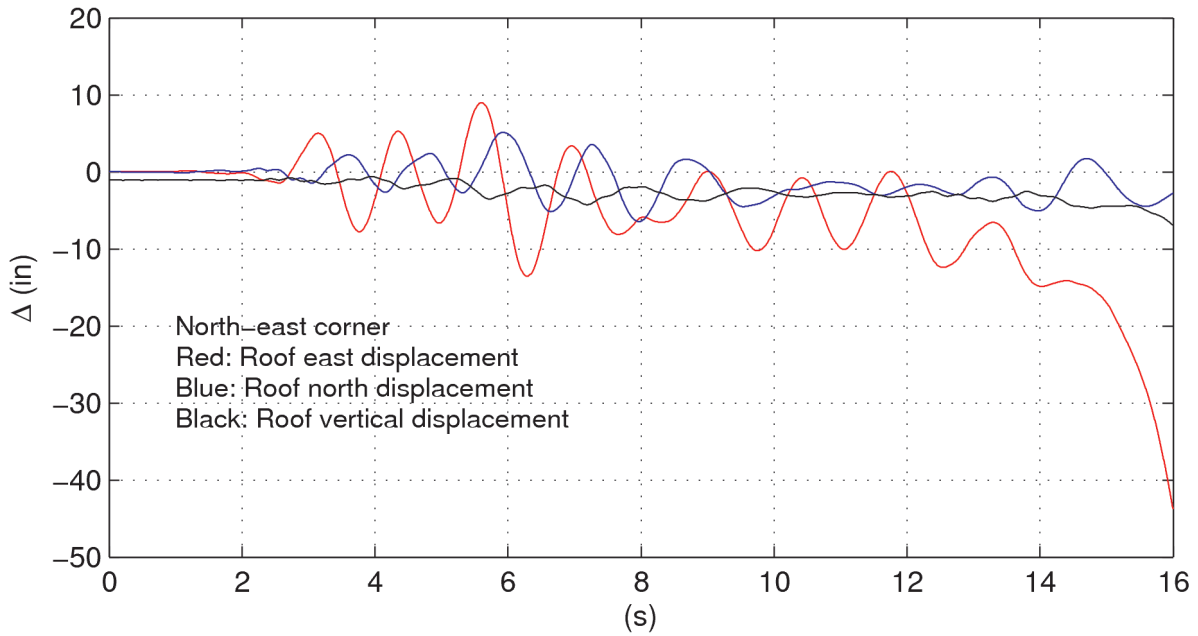

(b)

Figure E.1: Time histories of displacement at the (a) south-west and (b) north-east corners of the roof of the water-tank under the Takatori ground excitation scaled down by a factor of 0.32.

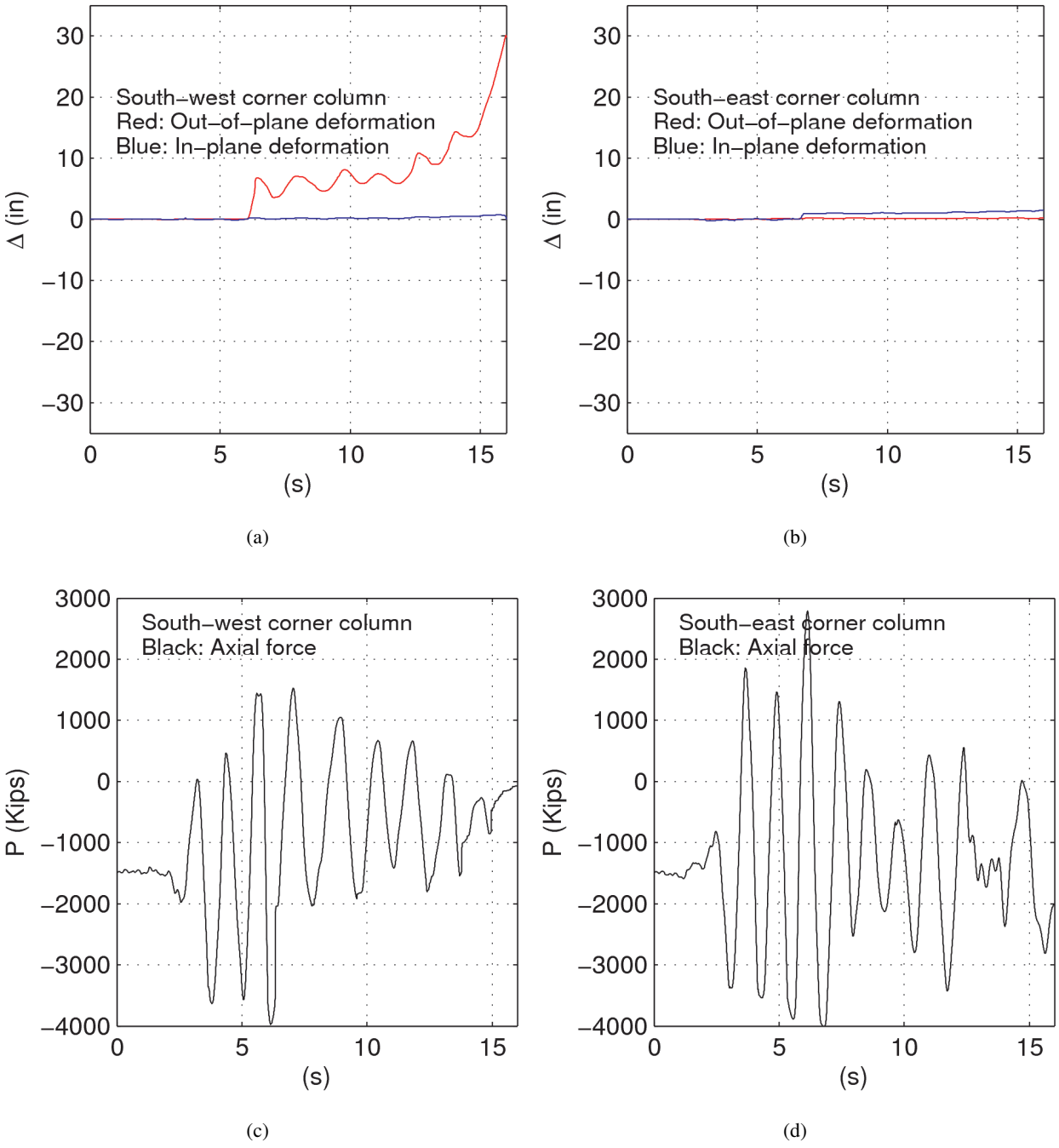

Figure E.2: Time histories of lateral deformation (a,b) and axial forces (c,d) in the base mega-columns at the south-west and south-east corners of the water-tank under the Takatori ground excitation scaled down by a factor of 0.32.

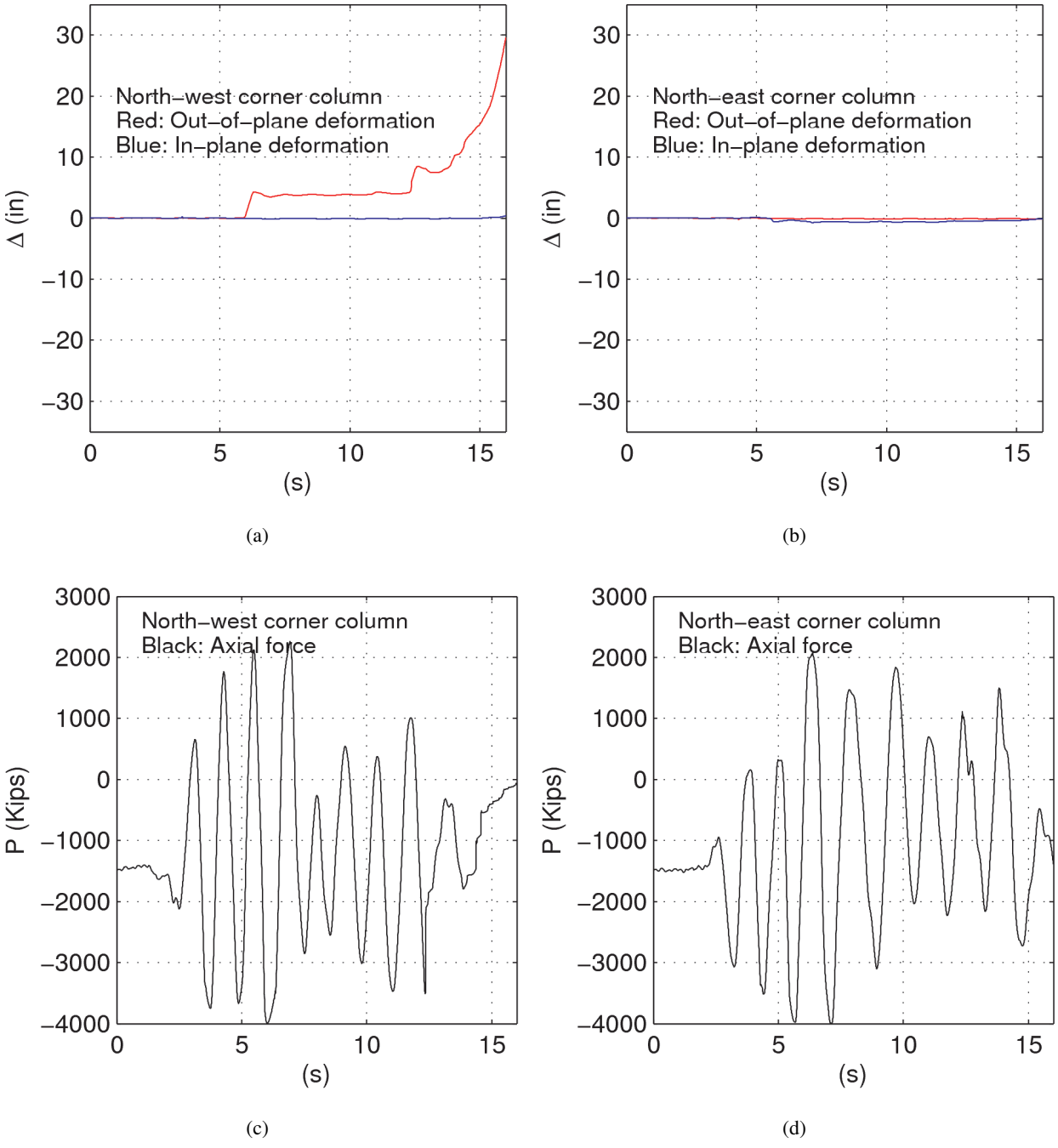

Figure E.3: Time histories of lateral deformation (a,b) and axial forces (c,d) in the base mega-columns at the north-west and north-east corners of the water-tank under the Takatori ground excitation scaled down by a factor of 0.32.

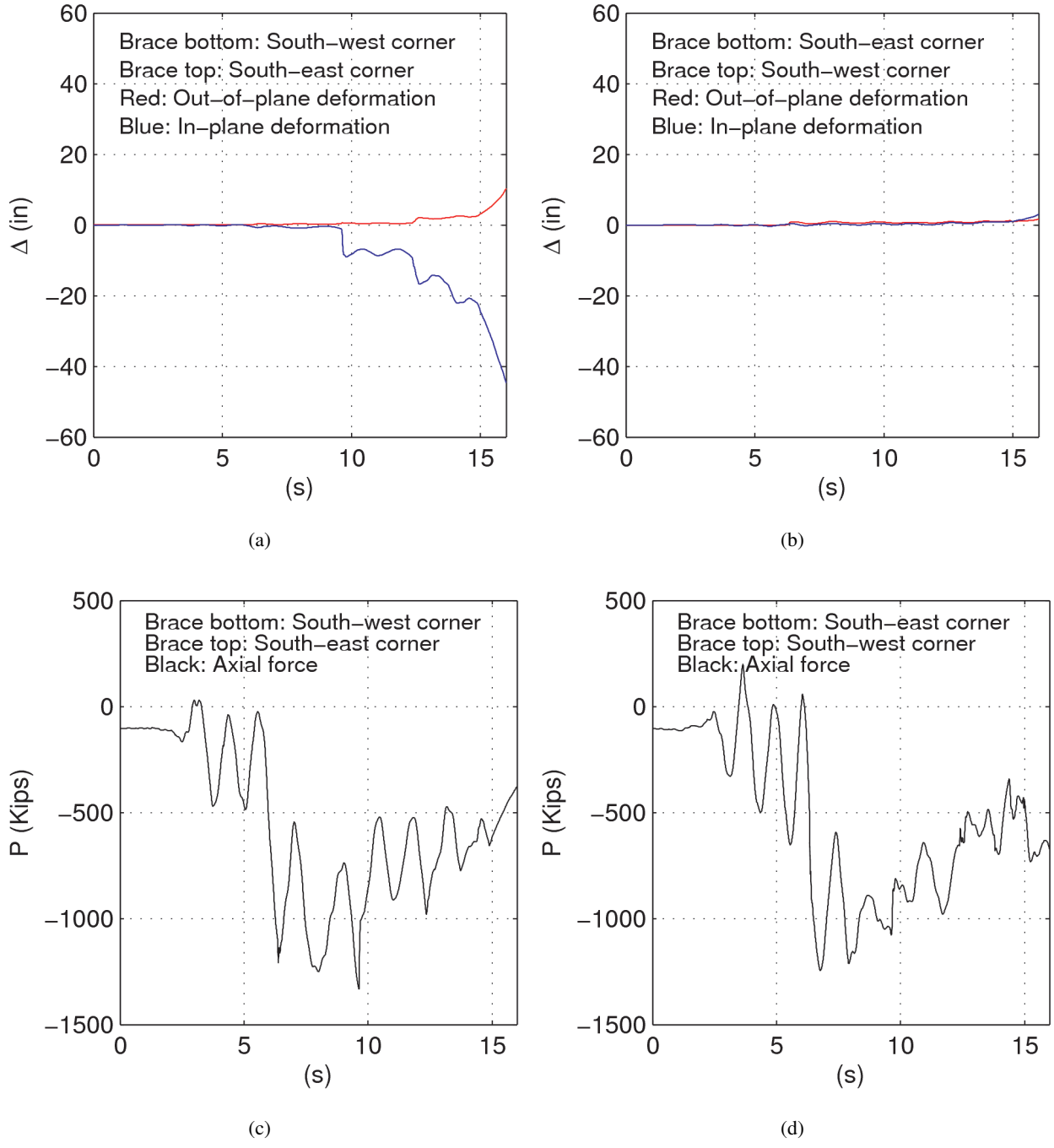

Figure E.4: Time histories of lateral deformation (a,b) and axial forces (c,d) in the bottom braces on the south face of the water-tank under the Takatori ground excitation scaled down by a factor of 0.32.

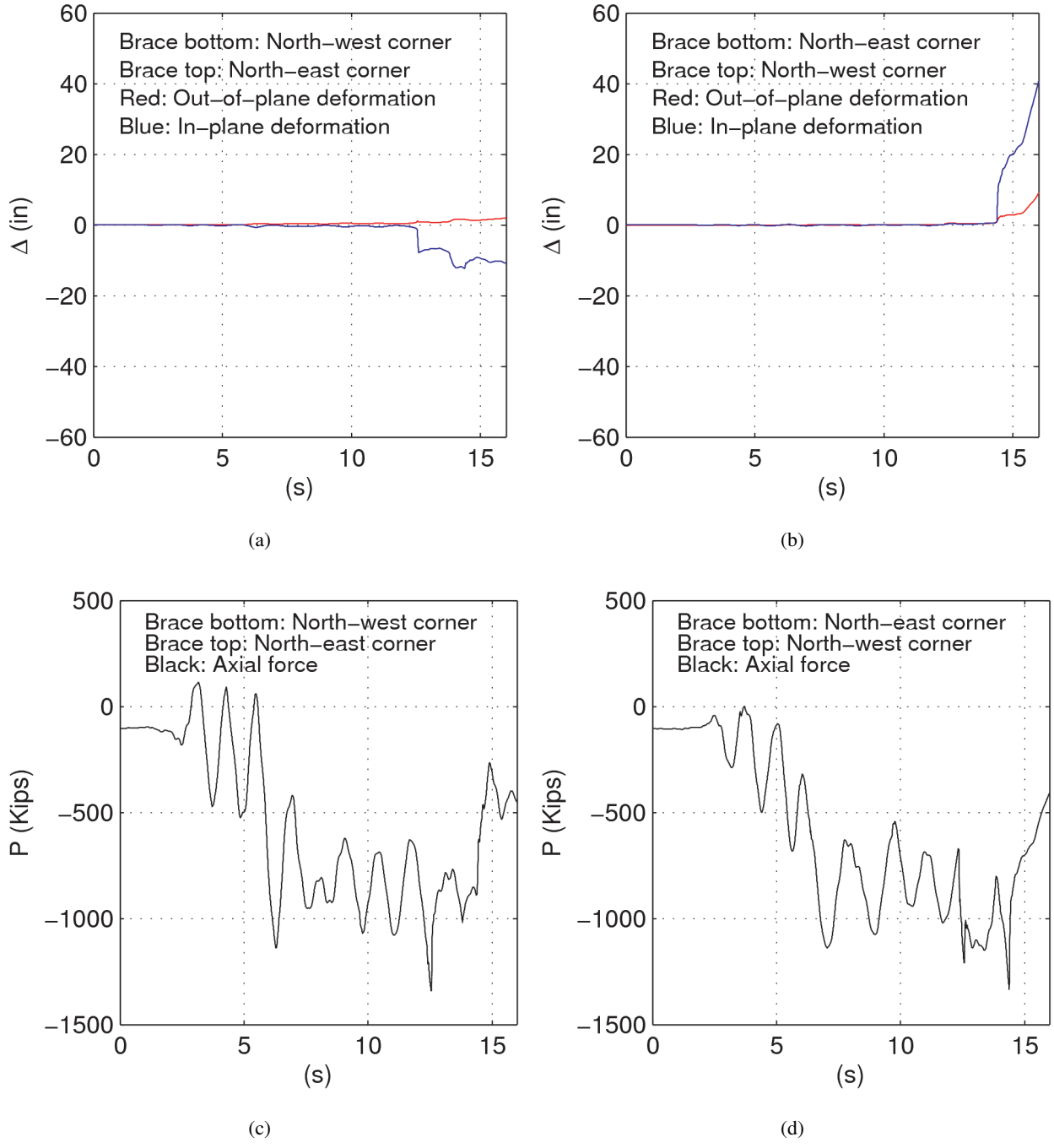

Figure E.5: Time histories of lateral deformation (a,b) and axial forces (c,d) in the bottom braces on the north face of the water-tank under the Takatori ground excitation scaled down by a factor of 0.32.

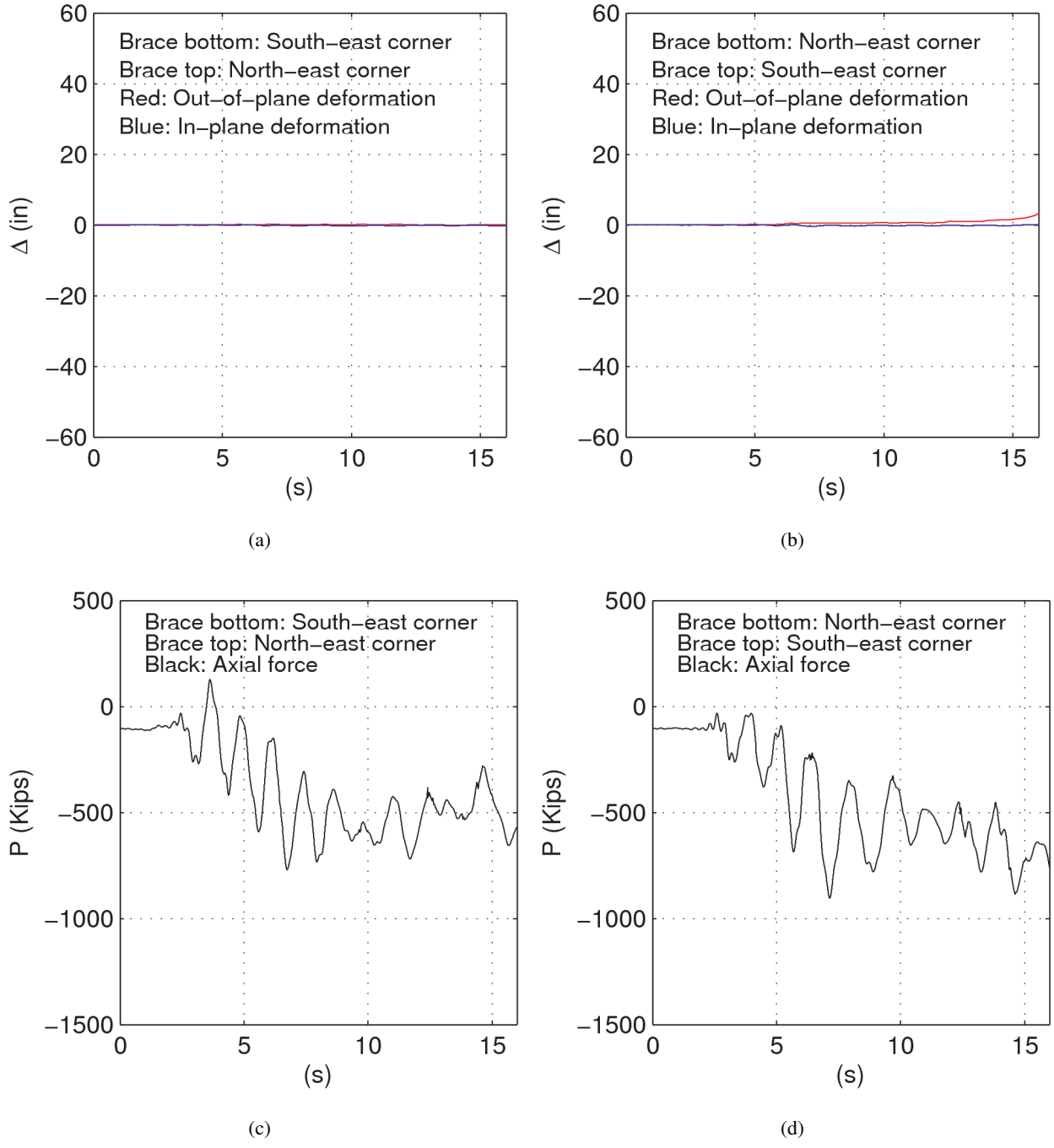

Figure E.6: Time histories of lateral deformation (a,b) and axial forces (c,d) in the bottom braces on the east face of the water-tank under the Takatori ground excitation scaled down by a factor of 0.32.

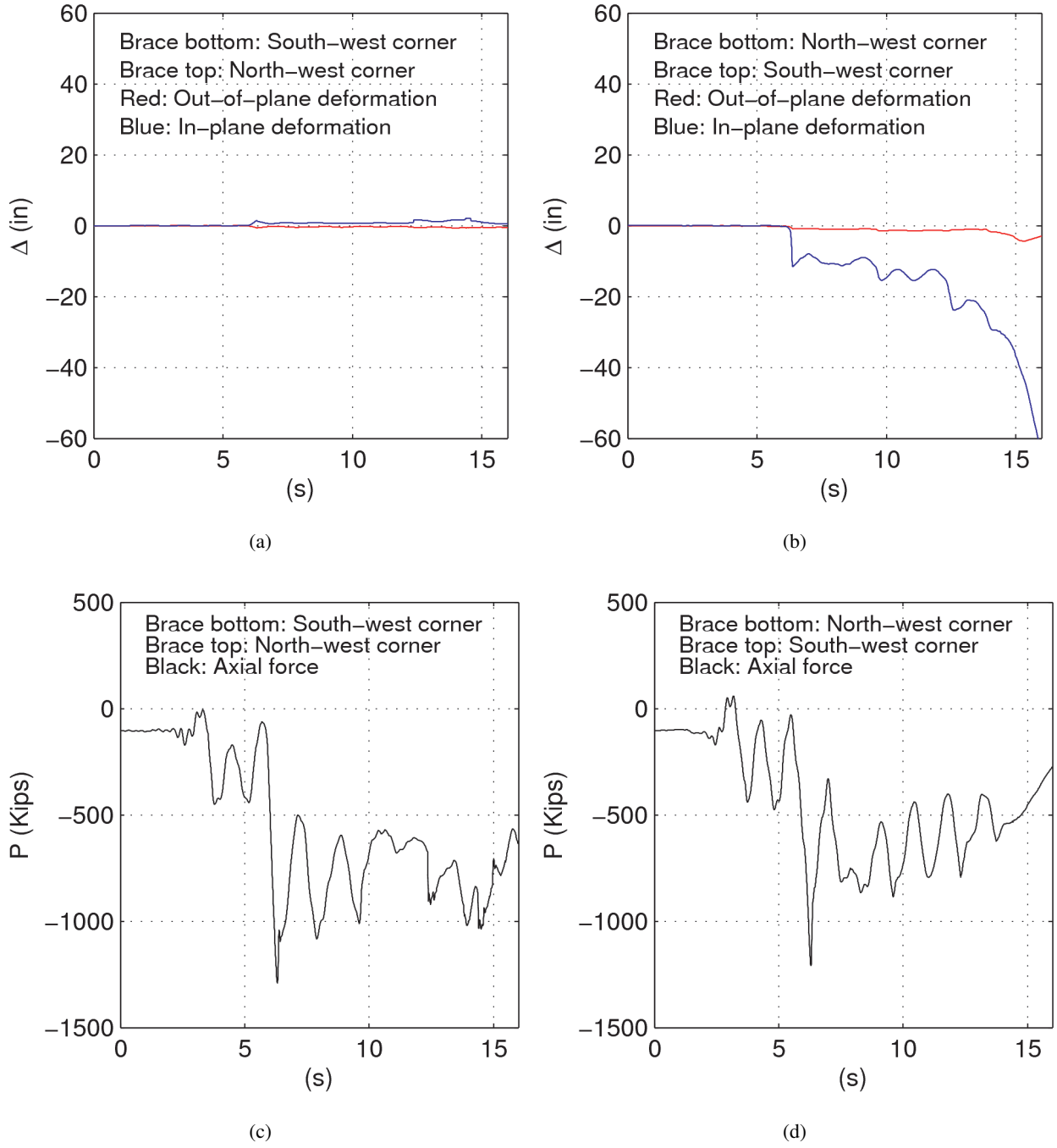

Figure E.7: Time histories of lateral deformation (a,b) and axial forces (c,d) in the bottom braces on the west face of the water-tank under the Takatori ground excitation scaled down by a factor of 0.32.

Bibliography

Aguero, A., C. Izvernari, and R. Tremblay (2006). Modeling of the seismic response of concentrically braced steel frames using the opensees analysis environment. *International Journal of Advanced Steel Construction 2*(3), 242–274.

Allahabadi, R. and G. H. Powell (1988). DRAIN-2DX user guide. Technical Report UCB/EERC-88-06, Earthquake Engineering Research Center, University of California, Berkeley, California, USA.

Bazant, Z. P. and L. Cedolin (1989). Initial post-critical analysis of asymmetric bifurcation in frames. *Journal of Structural Engineering 115*(11), 2845–2857.

Bazant, Z. P. and L. Cedolin (2003). *Stability of Structures - Elastic, Inelastic, Fracture, and Damage Theories*. Dover Publications, Inc., Mineola, New York.

Bazant, Z. P. and M. E. El Nimeiri (1973). Large-deflection spatial buckling of thin-walled beams and frames. *Journal of Engineering Mechanics Division, ASCE 99*(6), 1259–1281.

Black, G. R., W. A. Wenger, and E. P. Popov (1980). Inelastic buckling of steel struts under cyclic load reversals. Technical Report UCB/EERC-80-40, Earthquake Engineering Research Center, University of California, Berkeley, California, USA.

Challa, V. R. M. (1992). Nonlinear seismic behavior of steel planar moment-resisting frames. Technical Report EERL 92-01, Earthquake Engineering Research Laboratory, California Institute of Technology, Pasadena, California, USA.

Chopra, A. K. (1995). *Dynamics of Structures - Theory and Applications to Earthquake Engineering*. Prentice Hall.

Cook, R. D., D. S. Malkus, and M. E. Plesha (1989). *Concepts and Applications of Finite Element Analysis (Third Edition)*. John Wiley and Sons, New York.

Fell, B. V. (2008). Large-scale testing and simulation of earthquake-induced ultra low cycle fatigue in bracing members subjected to cyclic inelastic buckling. Technical Report Ph.D. Dissertation, University of California, Davis, USA.

Fell, B. V., A. M. Kanvinde, G. G. Deierlein, and A. T. Myers (2009). Experimental investigation of inelastic cyclic buckling and fracture of steel braces. *Journal of Structural Engineering 135*(1), 19–22.

Fell, B. V., A. M. Kanvinde, G. G. Deierlein, A. T. Myers, and X. Fu (2006). Buckling and fracture of concentric braces under inelastic cyclic loading. Technical Report Steel Tips: No. 94, Structural Steel Educational Council, USA.

Foutch, D. A., S. C. Goel, and C. W. Roeder (1987). Seismic testing of full-scale steel building – Part I. *Journal of Structural Engineering 113*(11), 2111–2129.

Gan, W. (1996). Earthquake response of steel braces and braced steel frames. Technical Report EERL 1996-06, Earthquake Engineering Research Laboratory, California Institute of Technology, Pasadena, California, USA.

Gan, W. and J. F. Hall (1998). Static and dynamic behavior of steel braces under cyclic displacement. *Journal of Engineering Mechanics 124*(1), 87–93.

Hall, J. F. (1995). Parameter study of the response of moment-resisting steel frame buildings to near-source ground motions. Technical Report EERL 95-08, Earthquake Engineering Research Laboratory, California Institute of Technology, Pasadena, California, USA.

Hall, J. F. (1998). Seismic response of steel frame buildings to near-source ground motions. *Earthquake Engineering and Structural Dynamics 27*(12), 1445–1464.

Hall, J. F. and V. R. M. Challa (1995). Beam-column modeling. *Journal of Engineering Mechanics 121*(12), 1284–1291.

Han, S.-W., W. T. Kim, and D. A. Foutch (2007). Seismic behavior of HSS bracing members according to width-thickness ratio under symmetric cyclic loading. *Journal of Structural Engineering 133*(2), 264–273.

Hassan, O. F. and S. C. Goel (1991). Modeling of bracing members and seismic behavior of concentrically braced steel structures. Technical Report UMCE 91-1, University of Michigan, Ann Arbor, Michigan, USA.

Ikeda, K. and S. A. Mahin (1984). Phenomenological modeling of steel braces under cyclic loading. Technical Report UCB/EERC-84-09, Earthquake Engineering Research Center, University of California, Berkeley, California, USA.

Jain, A. K. and S. C. Goel (1978). Hysteresis models for steel members subjected to cyclic buckling or cyclic end moments and buckling (User's guide for DRAIN-2D: EL9 and EL10). Technical Report UMEE 78R6, University of Michigan, Ann Arbor, Michigan, USA.

Jain, A. K., S. C. Goel, and R. D. Hanson (1978). Hysteresis behavior of bracing members and seismic response of braced frames with different proportions. Technical Report UMEE 78R3, University of Michigan, Ann Arbor, Michigan, USA.

Jain, A. K., R. D. Hanson, and S. C. Goel (1978). Inelastic response of restrained steel tubes. *Journal of the Structural Division, ASCE 104*(6), 897–910.

Jin, J. and S. El-Tawil (2003). Inelastic cyclic model for steel braces. *Journal of Engineering Mechanics 129*(5), 548–557.

Kanaan, A. E. and G. H. Powell (1973). General purpose computer program for inelastic dynamic response of plane structures. Technical Report UCB/EERC-73-06, Earthquake Engineering Research Center, University of California, Berkeley, California, USA.

Koiter, W. T. (1967). Post-buckling analysis of simple two-bar frame. In B. B. et al. (Folke Odqvist Volume) (Ed.), *Recent Progress in Applied Mechanics*, pp. 337 (Sec 2.6). Almqvist and Wiksell, Sweden.

Kounadis, A. N. (1985). An efficient simplified approach for the nonlinear buckling analysis of frames. *AIAA Journal 23*(8), 1254–1259.

Krishnan, S. (2003a). FRAME3D – A program for three-dimensional nonlinear time-history analysis of steel buildings: User guide. Technical Report EERL 2003-03, Earthquake Engineering Research Laboratory, California Institute of Technology, Pasadena, California, USA.

Krishnan, S. (2003b). Three-dimensional nonlinear analysis of tall irregular steel buildings subject to strong ground motion. Technical Report EERL 2003-01, Earthquake Engineering Research Laboratory, California Institute of Technology, Pasadena, California, USA.

Krishnan, S. (2009). FRAME3D V2.0 – A program for the three-dimensional nonlinear time-history analysis of steel structures: User guide. Technical Report EERL 2009-04, Earthquake Engineering Research Laboratory, California Institute of Technology, Pasadena, California, USA.

Krishnan, S. and J. F. Hall (2006a). Modeling steel frame buildings in three dimensions – Part I: Panel zone and plastic hinge beam elements. *Journal of Engineering Mechanics 132*(4), 345–358.

Krishnan, S. and J. F. Hall (2006b). Modeling steel frame buildings in three dimensions – Part II: Elastofiber beam element and examples. *Journal of Engineering Mechanics 132*(4), 359–374.

Mazzoni, S., F. McKenna, and G. L. Fenves (2005). OpenSees command language manual. Technical Report http://opensees.berkeley.edu, Pacific Earthquake Engineering Research (PEER), Berkeley, California, USA.

McKenna, F. (1997). Object oriented finite element programming frameworks for analysis, algorithms, and parallel computing. Technical Report Ph.D. thesis, University of California, Berkeley, California, USA.

Midorikawa, M., I. Nishiyama, and H. Yamanouchi (1989a). Analytical evaluation of K-braced structure seismic test. *Journal of Structural Engineering 115*(8), 1930–1948.

Midorikawa, M., I. Nishiyama, and H. Yamanouchi (1989b). Earthquake response analysis of full-scale six-story concentrically K-braced steel building – Part of the U.S./Japan cooperative research program. Technical Report BRI Research Paper No. 133, Building Research Institute, Ministry of Construction, Japan.

Poulsen, P. N. and L. Damkilde (1998). Direct determination of asymptotic structural postbuckling behaviour by the finite element method. *International Journal for Numerical Methods in Engineering 42*, 685–702.

Prakash, V., G. H. Powell, and S. Campbell (1993). DRAIN-2DX base program description and user guide, Version 1.10. Technical Report UCB/SEMM-93/17&18, Structural Engineering Mechanics and Materials, University of California, Berkeley, California, USA.

Rizzi, N., A. Di Carlo, and M. Pignataro (1980). A parametric postbuckling analysis of an asymmetric two-bar frame. *Journal of Structural Mechanics 8*(4), 435–448.

Roeder, C. W., D. A. Foutch, and S. C. Goel (1987). Seismic testing of full-scale steel building – Part II. *Journal of Structural Engineering 113*(11), 2130–2145.

Roorda, J. (1965). Stability of structures with small imperfections. *Journal of the Engineering Mechanics Division, ASCE 91*(EM1), 87–105.

Schachter, M. and A. Reinhorn (2007). Three-dimensional modeling of inelastic buckling in frame structures. Technical Report MCEER-07-0016, University at Buffalo, The State University of New York, Buffalo, New York, USA.

Silvestre, N. and D. Camotim (2005). Asymptotic-numerical method to analyze the postbuckling behavior, imperfection-sensitivity, and mode interaction in frames. *Journal of Engineering Mechanics 131*(6), 617–632.

Tang, X. and S. Goel (1988). DRAIN-2DM – Technical notes and user's guide. Technical Report UMEE 88-1, University of Michigan, Ann Arbor, Michigan, USA.

Tang, X. and S. C. Goel (1989). Brace fractures and analysis of Phase I structure. *Journal of Structural Engineering 115*(8), 1960–1976.

Tremblay, R. (2002). Inelastic seismic response of steel bracing members. *Journal of Constructional Steel Research 58*, 665–701.

Tremblay, R., M. H. Archambault, and A. Filiatrault (2003). Response of concentrically braced steel frames made with rectangular hollow bracing members. *Journal of Structural Engineering 129*(12), 1626–1636.

Tremblay, R. and L. Poncet (2005). Seismic performance of concentrically braced steel frames in multistory buildings with mass irregularity. *Journal of Structural Engineering 131*(9), 1363–1375.

Uang, C.-M. and V. V. Bertero (1986). Earthquake simulation tests and associated studies of a 0.3-scale model of a six-story concentrically braced structure. Technical Report UCB/EERC-86-10, Earthquake Engineering Research Center, University of California, Berkeley, California, USA.

Uriz, P., F. C. Filippou, and S. A. Mahin (2008). Model for cyclic inelastic buckling of steel braces. *Journal of Structural Engineering 134*(4), 619–628.

Yamanouchi, H., M. Midorikawa, I. Nishiyama, and M. Watabe (1989). Seismic behavior of full-scale concentrically braced steel building structure. *Journal of Structural Engineering 115*(8), 1917–1929.

Zayas, V. A., E. P. Popov, and S. A. Mahin (1980). Cyclic inelastic buckling of steel braces. Technical Report UCB/EERC-80-16, Earthquake Engineering Research Center, University of California, Berkeley, California, USA.